UNIVERSIDAD AUTÓNOMA DE MADRID

Facultad de Ciencias

Departamento de Química Inorgánica

Few-Layer Antimonene from synthesis to application

Tesis presentada por

Carlos Gibaja Palacios

para optar al grado de Doctor en Química Aplicada

Director de tesis

Prof. Félix Zamora Abanades

Madrid, Mayo de 2019

Contents

Abstract

Antimonene or Few-Layer Antimonene (FLA) are, among the recently discovered group of two-dimensional (2D) layered materials, considered as one of the most promising members due to its outstanding predicted properties that makes it a perfect candidate for a wide variety of applications, ranging from catalyst to optoelectronic devices. However, its experimental production to further characterize its properties and potential applications is still immature.

Thus, in this Thesis is described a comprehensive study of all the aspects evolving its experimental synthesis using liquid-phase exfoliation (LPE) techniques and some of its real applications.

The Introduction chapter provides a general overview of the group of 2D layered materials and the full state-of-the-art of the research carried out on antimonene, including its most interesting calculated properties, the reported production methods and the potential applications that have been theoretically or experimentally reported to date.

In Chapter 2, it is reported the first method to produce FLA nanosheets (FLAs) suspensions using LPE techniques, in a process that is assisted by sonication but does not require the addition of any surfactant. Besides, it is also described the existing dependence of the Raman signal with the thickness on the FLAs.

In Chapter 3, it is investigated the oxidation behaviour of FLAs obtained following the LPE procedure described in Chapter 2. This study has important implications with respect to antimonene based technologies due to the observed semiconducting feature upon oxidation, and might open up new avenues for surface engineering and tailoring of its properties.

Chapter 4 reports on a systematic analysis of the most significant parameters involved in the LPE process, in order to rationalize the FLAs production. For that reason, it is studied the effect in the LPE of antimony crystals of: i) the initial crystal size, ii) solvent used and iii) ultrasound parameters.

Finally, Chapter 5 describes two different potential applications in the field of energy storage where FLAs produced by LPE could be experimentally applied: it is evaluated the electrochemical capacitive performance of FLA and its successful application as a supercapacitor and it is also described the formation of a 2D/2D heterostructure with graphitic carbon nitride that enhances the optical absorption as well as charge separation under illumination.

Resumen

El Antimonene o Few-Layer Antimonene (FLA) es considerado como uno de los miembros más prometedores entre los materiales pertenecientes al grupo recientemente descubierto de los materiales laminares bidimensionales (2D) debido a sus excepcionales propiedades teóricas, lo que le convierte en un candidato perfecto para un amplio abanico de aplicaciones que van desde la catálisis hasta la fabricación de dispositivos optoelectrónicos. Sin embargo, las técnicas de producción para obtenerlo y así poder caracterizar sus propiedades y demostrar sus posibles aplicaciones siguen estando pendientes de desarrollar. Por ello, la presente tesis está centrada en la realización de un exhaustivo estudio acerca de los aspectos que afectan a la síntesis experimental de este material mediante técnicas de exfoliación en fase líquida (LPE), así como de su aplicación en distintos campos.

El capítulo introductorio trata de ofrecer una visión general del grupo de materiales laminares 2D pero centrando el foco en el Antimonene. Para ello se explican sus propiedades teóricas más interesantes, los métodos de producción existentes y las potenciales aplicaciones que han sido predichas o demostradas experimentalmente hasta la fecha.

En el capítulo 2, se describe el primer método para producir nanoláminas de FLA (FLAs) mediante técnicas LPE, mediante un proceso asistido por ultrasonidos y que no requiere del uso de surfactantes. Además, se describe también la dependencia que existe en la señal de Raman de las FLAs respecto de su espesor.

En el capítulo 3, se describe la investigación realizada sobre el proceso de oxidación que sufren las FLAs obtenidas mediante el procedimiento desarrollado en el capítulo 2. Esta investigación tiene importantes implicaciones respecto a las tecnologías basadas en el Antimonene debido a su carácter semiconductor que se ha observado tras el proceso de oxidación, lo que podría abrir una puerta a la ingeniería de superficie y a la modificación de sus propiedades.

El capítulo 4 describe el estudio sistemático realizado sobre los parámetros más importantes que controlan el proceso LPE con el fin de racionalizar la producción de FLAs. Para ello se ha procedido a estudiar el efecto que distintos factores tienen en la LPE de cristales de antimonio: i) el tamaño inicial de los cristales, ii) el disolvente utilizado y iii) los parámetros de ultrasonidos.

Por último, el capítulo 5 describe dos aplicaciones diferentes en el campo del almacenamiento de energía, donde las FLAs obtenidas mediante técnicas LPE pueden ser empleadas: se ha demostrado experimentalmente el rendimiento capacitivo de las FLAs y su aplicación como supercapacitor, así como la formación de una heteroestructura 2D/2D entre nitruro de carbono grafítico y FLA que aumenta su absorbancia óptica y la separación de cargas bajo iluminación.

Chapter 1. Introduction
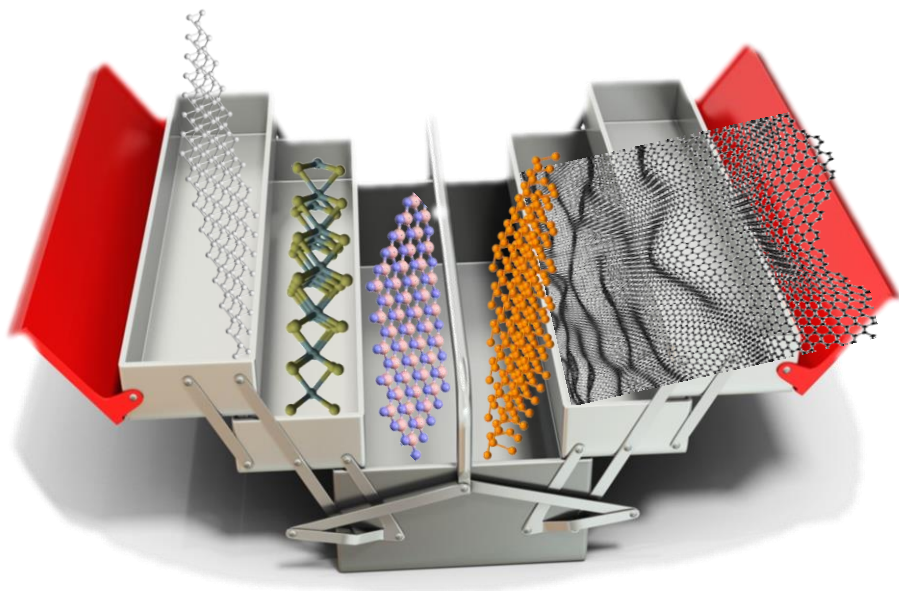
Chapter 1. Introduction

1.1 Two-dimensional layered materials

To understand what is a layered material, it's necessary to think of them as two-dimensional (2D) platelets weakly stacked to form three-dimensional (3D) structures. This kind of materials have been used since the Mayan civilization employed them to make dyes, more than 1500 years ago. Since then, other cultures and civilizations have tried to use them for different applications. More recently, it began the study of the structure and properties of these materials, as well as ways to exfoliate them until nanosheets of monoatomic thickness. Speaking about the process, exfoliation of layered solids has had a transformative effect on materials science and technology by opening up properties found in 2D exfoliated forms, not necessarily seen in their bulk counterparts.

This part of materials science reached a tremendous milestone with the discovery of graphene in 2004 by Geim and Novoselov[1]. They achieved, for the first time, to exfoliate graphite into single atomic layers of graphene and demonstrated amazing physical properties of this new material, and later the fabrication of proof-of-concept atomically thin devices[2]. An interesting point is that, graphene was always there, forming part of a stacked structure of individual sheets that gives the 3D structure to graphite, but we weren't able to isolate it[3]. However, the most interesting thing about this carbon allotrope is that only when is exfoliated down to individual sheets, the predicted remarkable properties of this 2D sheet polymer[4], could be revealed experimentally.

Since the moment that graphene was obtained experimentally and all its attributed properties were demonstrated, the scientific community working in materials science has done a tremendous effort to find new 2D materials with complementary properties to that found for graphene. Up to date, it has been discovered many different 2D layered materials that can be classified based on their structural similarities[5].

The first group includes materials whose structure is based on a hexagonal network that forms atomically thin layers. To this group belong hexagonal boron nitride (h-BN)[6], graphene[2] and graphitic carbon nitride (g-C_3N_4)[7]. The second group contains transition metal dichalcogenides (TMDs) such as molybdenum disulfide (MoS_2) and molybdenum diselenide ($MoSe_2$)[8], and also metal halides like lead diiodide (PbI_2) and magnesium dibromide ($MgBr_2$)[9]. Both compounds forming the second group have an identical structure that consist on a plane of metal atoms sandwiched between planes of halide/chalcogen atoms. The third classification, is the one formed by group 13−16 layered semiconductors such as gallium(II) selenide (GaSe) and indium(III) selenide (In_2Se_3). These are a class of layered materials with a general formula MX (M = Ga, In; X = S, Se, Te)[10]. There is also a recently new and promising fourth group formed by the MXenes, such as Ti_2C. The MXenes are a class of 2D layered transition metal carbides and/or nitride produced by selective etching of the raw MAX phases with a general formula of $M_{n+1}AX_n$ (n = 1, 2, or 3), where M is the transition metal (e.g., Ti, V, Cr, Nb, etc.), A is another element from group 13 or 14 (e.g., Al, Si, Sn, In, etc.), and X stands for carbon and/or nitrogen[11].

Another groups of 2D layered materials are: the one formed by layered metal oxides such as manganese dioxide (MnO_2) with a general formula of MO_3 (M = Mo, Ta, W, etc.)[12], the one composed by the layered double hydroxides (LDHs) like $Mg_6Al_2(OH)_{16}$, a class of materials with positively charged layers and weakly bounded charge-balancing anions or solvation molecules and interlayer water molecules[13] and the one integrated by the transition metal oxyhalides (MOX) with a layered crystal structure in which each layer is constructed by a corrugated metal−oxygen plane sandwiched by two halide layers[14].

The last group is the one formed by 2D group-15 semiconductors that derive from group-15 layered crystals (P, As, Sb and Bi), also called pnictogens. The 2D group-15 monolayer materials, are called phosphorene, arsenene, antimonene and bismuthene. Similar to group 14 silicene, germanene and stanene semiconductors, these group-15 monolayer materials are termed with suffix ''ene'', although there aren't double bonds[15].

As it has been showed, there are many different groups of 2D layered materials and each of them has a large variety of compounds with different properties and applications. This work is focused on the group-15 2D semiconductor called antimonene. To further understand the rise of antimonene we need to have a look first into other similar materials such as graphene and 2D group-15 semiconductors, for that reason a revision of those materials needs to be done.

1.1.1 Graphene

Without a doubt, the most studied and well known to date 2D layered material is graphene. Graphene is considered the basic unit of different structures of carbon, such as graphite, fullerenes or carbon nanotubes (Figure 1.1). Its structure is composed of a hexagonal close-packed carbon network, in which each atom covalently bonds to three neighbouring ones, therefore involving 3 σ+1/3 π bonds by C atom, with a C-C distance of 1.42 Å. Individual layers stack together through the van der Waals forces to form the graphite, in which the distance between adjacent layers is about 3.35 Å[16].
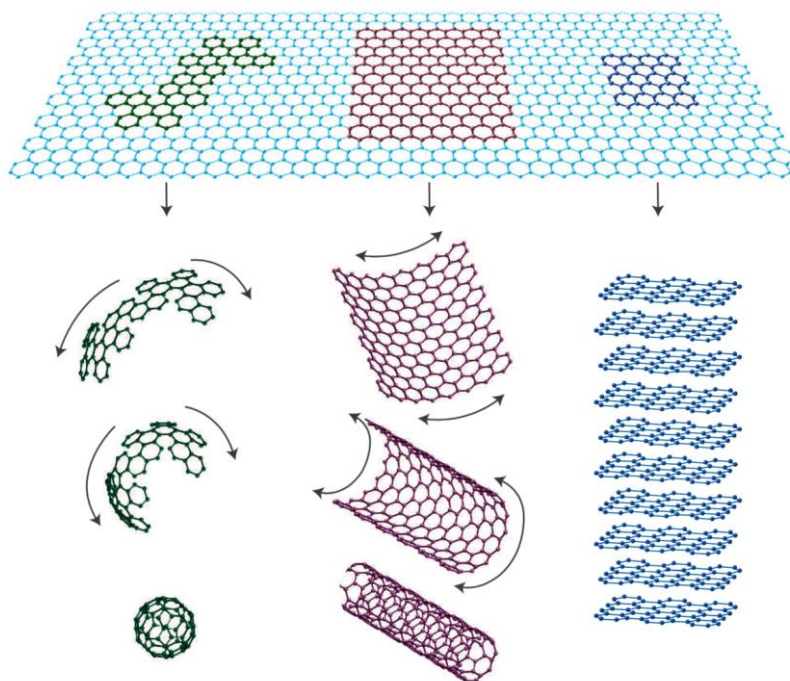
Figure 1.1. Demonstration of graphene being the basic unit of different structures of carbon. It can be wrapped up into 0D buckyballs, rolled into 1D nanotubes or stacked into 3D graphite. Adapted from Reference 2.

A single layer of graphene is the perfect example in how the properties of a material change when it is reduced to its lowest expression in one dimension, due to the electron confinement in the other two dimensions. In the case of graphene, the electron confinement gives rise to some outstanding properties such as ultrahigh room-temperature carrier mobility[1], quantum Hall effect[17], ultrahigh specific surface area[18], high Young's modulus[19], excellent optical transparency[20], and excellent electrical[1] and thermal[21] conductivities. All these properties make graphene a singular material and a leading candidate to be used in uncountable applications, including electronics/optoelectronics[22], catalysis[23], energy storage[24] and conversion[25], water remediation[26], sensors[27], biomedicine[28], among others.

Despite of these outstanding properties and applications of graphene, it is true that this remarkable new material it's not suitable for all of kind of applications. For this reason, scientific community has put too much effort investigating another similar 2D materials to complement such.

1.1.2 2D group-15 semiconductors

Very recently, it has become visible a new family of 2D crystals, derived from group-15 layered materials (P, As, Sb and Bi), with high scientific impact due to their potential practical applications[15]. The main difference with semimetallic group 14 (graphene[1], silicene[29], germanene[30] and stanene[31]) and metallic group 13 (borophene[32]) materials, is that, when their thickness is reduced to obtain 2D nanosheets, they become semiconductors with significant fundamental band gaps. This fact makes them potential candidates for future nanodevices in several (opto)electronics applications.

This group of materials in their bulk form shows a variety of stable structures. For example, phosphorus has white, red and black stable structures and several amorphous forms[33]. However, black phosphorus is its most thermodynamically stable allotropic form under ambient conditions. This allotrope of phosphorus crystallizes giving a layered orthorhombic structure with a $Cmca$ spatial group. In each individual atomic layer, every phosphorus atom is covalently bonded to three neighbouring atoms. Two of the covalent bonds are parallel to the atomic plane while the third one is almost perpendicular to it, and it's essential to connect the phosphorus atoms from upper and lower layers, forming a unique puckered structure, α phase, as shown in Figure 1.2a. To get the β phase in black phosphorus, is necessary to apply a pressure of 5 GPa[34]. This phase is characterized by a layered rhombohedral structure with a $R\bar{3}m$ space group, giving the shape of a wrinkled double-layered structure with six-membered rings, as shown in Figure 1.2b.

The case of arsenic is similar to the phosphorous, it has three common allotropes: metallic grey, yellow and black arsenic[35]. The most stable of its allotropes is grey arsenic, β phase, and it's characterized by a layered rhombohedral structure with a $R\bar{3}m$ space group, as shown in Figure 1.2b. To obtain the α phase in arsenic, it's necessary to heat it up to 370 K[36].

The third element in the group-15 semiconductors is antimony, and it also has three known allotropes: grey antimony, black antimony and explosive antimony[35]. Similar to arsenic, its most common allotrope is the grey one, β phase, and under this form it conserves the typical semimetal features.

The case of bulk bismuth is more simple, there is just one stable form with the same structure of grey arsenic and grey antimony[35]. A summary of all isolated stable phases and natural phases of this group of materials has been done in Figure 1.2c.
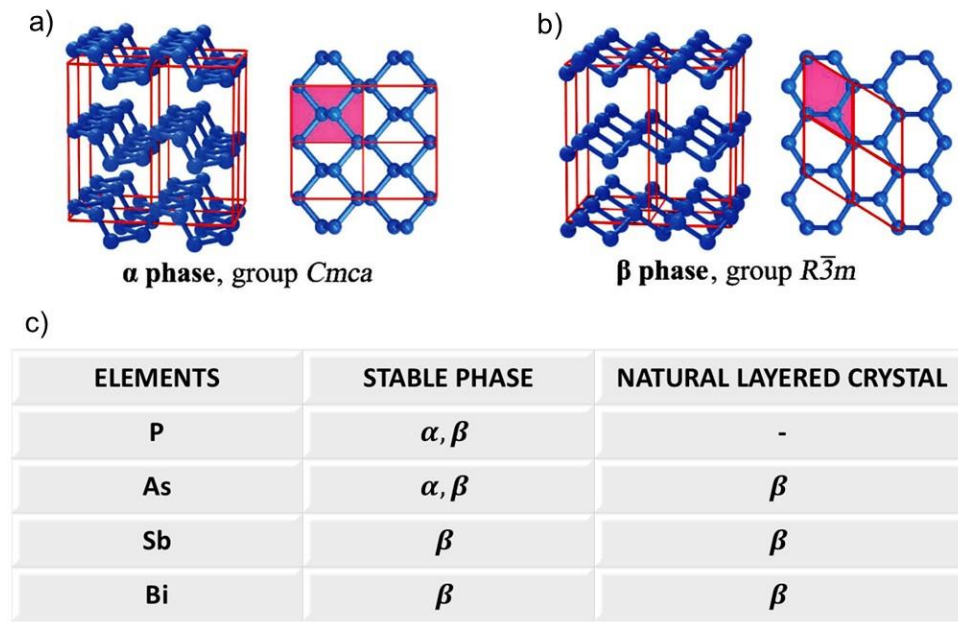
Figure 1.2. Main crystal structures of layered materials of group-15: a) parallel puckered layers with space group $Cmca$ (α phase), and b) parallel buckled layers with space group $R\bar{3}m$ (β phase). c) Summary of isolated stable phases and natural phases of layered materials of group-15. Adapted from reference 15.

Until today, phosphorene represents the most explored material of this group. It exhibits a direct band gap with a large range of tunability, from 0.3 eV in the bulk form to 2.0 eV varying its thickness to a monolayer[37], as well as high hole mobility above *ca.* 10000 cm^2 V^{-1} s^{-1} [38]. Taking this into account, Li *et al.* succeed fabricating the first phosphorene field-effect transistor (FET) in 2014[39].

In addition, the 2D shape of black phosphorus also present other promising properties, such as superior mechanical properties[40], highly anisotropic transport[38], negative Poisson's ratios[41], excellent optical[42] and thermoelectric responses[43], strain-induced conduction bands[44], and perpendicular electric-field-induced 2D topological character[33].

These unusual properties led to a large variety of studies on phosphorene, therefore being one of the most promising 2D materials for future applications in many fields. However, its reactivity under environmental conditions is significantly high. In fact, due to the high oxophilicity of phosphorous, phosphorene flakes easily uptake humidity from air and forms phosphoric acid and related species what degrades the material[45]. This degradation of the flakes can be easily detected by monitoring their topography over time[46].

Therefore, during the last few years, the rest of the members of group-15 semiconductors (arsenene, antimonene and bismuthene) have also attracted the interest of the scientific community. It was not until year 2015, that Zhang *et al.* firstly predicted and identified theoretically, novel 2D semiconducting As and Sb-monolayers, also called arsenene and antimonene. Zhang *et al.* also predicted that these two materials should exhibit wide range of band gaps, desirable stability and high carrier mobility[47]. From there on, there have been plenty of theoretical studies that support all the predicted properties of this group of materials. Even though this theoretical studies meant a great advance, their experimental obtaining implied a significant milestone on the development of new 2D materials. From this starting point, some 2D group-15 nanosheets have been obtained experimentally by mechanical exfoliation[48], liquid-phase exfoliation[49], plasma-assisted processes[50], vapour deposition techniques[51] and molecular beam epitaxy[52].

1.1.3   Antimonene

Among the rest of the group-15 2D semiconductors family, antimonene, is the most promising material due to some outstanding calculated properties and chemical stability to ambient conditions compared to phosphorene. There are several promising studies regarding antimonene that could give some light for a better understanding of this interesting material.

- *Band structure:*

As it has been already highlighted, the first theoretical work on antimonene as a promising 2D semiconductor was done by Zhang *et al.* They reported density functional theory (DFT) calculations of the band structure of monolayer β-antimonene featuring an indirect gap of 2.28 eV (Figure 1.3)[47].
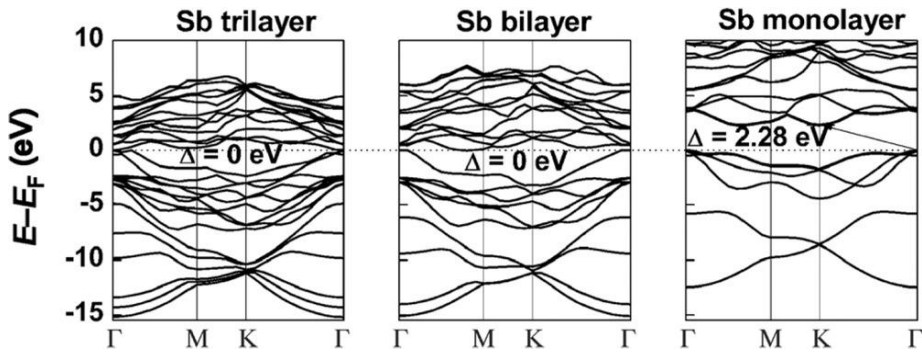

Figure 1.3 Representation of the electronic band structures of antimony trilayers, bilayers, and monolayers calculated at the HSE06 DFT functional. Adapted from reference 47.

Another parallel study was done almost at the same time, reporting and indirect gap of 0.76 eV[53]. This dispersion on the calculated band-gap values is relatively normal because of the different nature of the functionals used.

After those first approximations, another indirect gap value of 1.55 eV was calculated for single layer β-antimonene, but in this case following the discussion of Zhang *et al.* and taking into account the effect of spin-orbit coupling, which seems to play an important role[54]. More recently, a large spread of studies have been done trying to calculate the most accurate value of the antimonene band-gap using different DFT calculations and taking or not into account the effect of spin-orbit coupling[55], giving rise to a common feature in all of them that is the indirect nature of the gap. However, there is still missing an experimental evidence of this value.

- *Structural stability and allotropes:*

It is well stablished that the most stable phase for antimonene is the β structure. However, according to DFT calculations recently carried out, this is not the only feasible structure for this material. These calculations suggested that antimonene could have another possible allotropic phases such as α, γ, and δ structures (Figure 1.4)[53]. Nevertheless, among these phases the only one that seems to be stable, apart from β, is α. Indeed, α structure resembles to that of phosphorene, with some small differences: in this case the crystallographic structure corresponds to a rectangular Bravais lattice with four Sb atoms in the unit cell. The virtual stability of both phases, α and β, has been studied in terms of their cohesive energy, and their phonon free energy, suggesting that both phases could be found experimentally and their stability is comparable in terms of energy. Another difference between both phases is the band-gap.

Thus, while the case of α-antimonene is direct and its theoretical value is ~0.2 eV[56], the calculations show an indirect band-gap for the β phase.
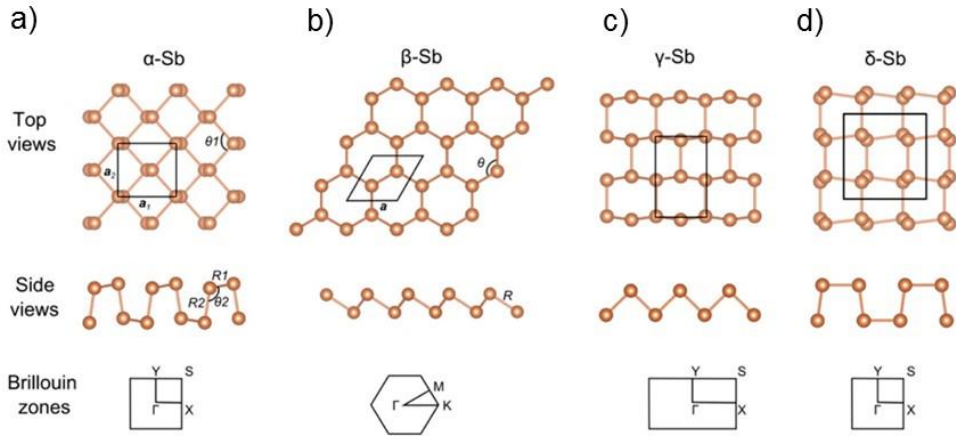
Figure 1.4 Different structural configurations of antimonene allotropes: a) α-Sb, (b) β-Sb, (c) γ-Sb, and (d) δ-Sb. Adapted from reference 53.

1.2   Properties of antimonene

Due to the fact that most of the properties of antimonene have still not been experimentally proved, in this section it will be summarized the existing theoretical and experimental results. It is necessary to point out that, in principle, physical properties of antimonene, will change significantly from the single-layer to few-layer systems (10-100 layers), being considered the monolayer as a new 2D crystal while the few-layer is expected to be a 3D topological insulator.

1.2.1   Optical properties:

Regarding the optical properties of antimonene, it has been predicted to be suitable for ultraviolet optical nanodevices, microelectronic devices and solar cells[57]. That statement can be proved by analysing the calculations carried out in terms of the dielectric functions becoming negative between 5.1 eV and 9.0 eV for α-antimonene and between 6.9 eV and 8.4 eV for β-antimonene, suggesting that antimonene behaves as a metal in the UV region of the electromagnetic spectrum. Additionally, the consequence that electron energy loss spectra (EELS) expose the plasmon energies of around 9 eV also suggests its metallic behaviour, in the UV region[56].

1.2.2   Thermal properties:

Low thermal conductivity materials are crucial for thermoelectric devices, for this reason antimonene is a good candidate for this kind of applications.

Wang *et al.* estimated using *ab initio* calculations, that antimonene has a low lattice thermal conductivity (15.1 $W \cdot m^{-1} \cdot K^{-1}$ at 300 K) due its small group velocity, its low Debye temperature and large buckling height[58]. Moreover this low thermal conductivity could be minimized by downsizing the material or by chemical functionalization[59].

1.2.3 Mechanical properties:

Recently it has been calculated, by means of strain engineering, an increase of ~25% on the Young's and shear modulus of β-antimonene compared to bulk antimony, while the hexagonal lattice constant of the monolayer decreases significantly (~5%) compared to the bulk, revealing of strong interlayer coupling. Besides, these studies also show how during the deformation process, the structural integrity of antimonene is better preserved in the armchair direction. Remarkably, under uniaxial strain in the zigzag and armchair directions reveal a direction-dependent trend in the electronic band structure. Kripalani *et al.* have found that when a strain is applied in the zigzag direction the nature of the band-gap remains unaffected, while if the strain is applied in the armchair direction activates an indirect-direct band gap transition at a critical strain of 4 %, due to a band switching mechanism[60].

1.3   Production methods of antimonene

It is crucial to know how to produce ultrathin 2D materials with specific composition, thickness, lateral dimension, crystal phase and surface characteristics, in order to study their properties and applications. There is a wide variety of methods to produce 2D materials. They could be classified in two groups attending the way to obtain the 2D layers: top-down and bottom-up approaches.

The top-down methods involve the exfoliation of van der Waals bulk crystals into thin layer 2D crystals, this process is assisted by an external force that can be supplied in different ways.

On the other hand, bottom-up methods are based on chemical reactions of selected molecular precursors under defined experimental conditions. This block also include physical methods based on the sublimation and deposition of elements, typically metallic elements. In this section, is provided a revision of the experimental methods so far reported to produce antimonene.

1.3.1 Micromechanical exfoliation

This procedure to obtain 2D materials, also known as "Scotch tape method", was the first method employed to obtain graphene by peeling repetitively graphite flakes[2].

In the case of antimonene, the situation is significantly more complex because the interlayer interactions are stronger. However, this approach has been successfully used by Ares *et al.* to isolate and characterize the first single layer of anotimonene[48]. They found out that employing the regular Scotch tape method few antimony flakes can be deposited on the substrate. For this reason, they improved the yield of the process by transferring the antimony flakes from the Scotch tape to a viscoelastic polymer and, finally, to a SiO_2/Si substrate (Figure 1.5a). Indeed, a similar method was used by Castellanos *et al.* to isolate black phosphorus[61]. This approach yielded few-layer flakes with reasonable lateral dimensions and some few single-layer antimonene flakes.

The bigger flakes could be easily identified with the optical microscope. Atomic force microscopy (AFM) allows characterization of the thinner ones (Figure 1.5b). Interestingly, Figure 1.5b shows an AFM topography image of a few-layer antimonene (FLA) flake with a folded terrace made by AFM-assisted nanomanipulation and the height of this folded terrace was about 0.4 nm (inset in Figure 1.5b and profile in Figure 1.5c) corresponding to a single-layer of a β-antimonene flake. Besides, the fact that they managed to fold the terrace of the flake without any breakage demonstrated the mechanical stability of a single-layer of antimonene.

They also demonstrated the nature and the quality of the flake by doing high resolution transmission electron microscopy (HRTEM) and X-ray energy dispersive spectroscopy (XEDS) measurements. Regarding the stability under environmental conditions of FLA, they performed AFM measurements to a pair of different thin flakes just after exfoliating them (Figure 1.5d), after two months under ambient conditions (Figure 1.5e) and then immersing the sample in water (Figure 1.5f).

It is easy to see how there are non-significant changes in the profiles of FLA flakes (FLAs) (Figure 1.5g) indicating no degradation or moisture up taking on the surface. In addition, they performed high resolution AFM measurements of the flakes demonstrating that the hexagonal periodicity suitable with the β-phase of antimony is preserved (inset Figure 1.5f).
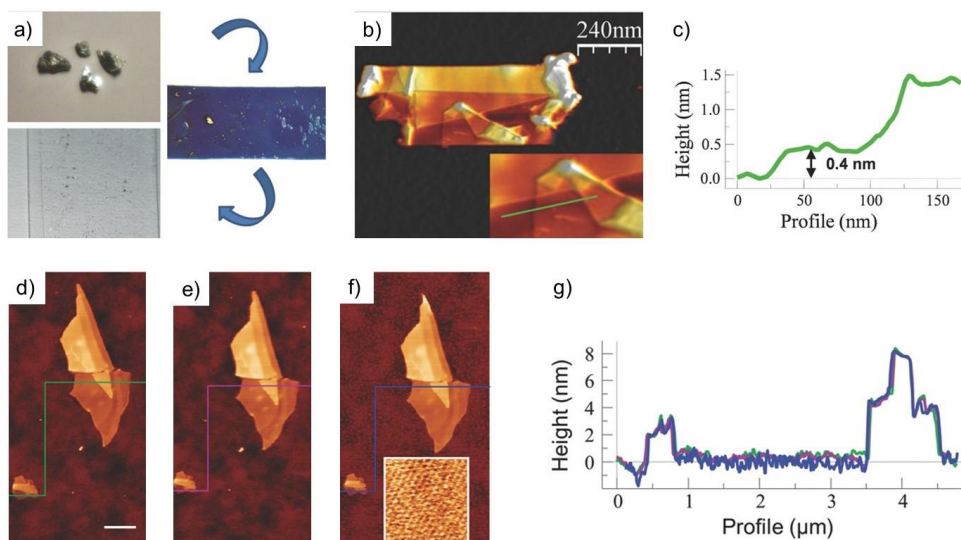
Figure 1.5 a) Top left: Sb crystals. Middle right: Adhesive tape with Sb crystals. Bottom left: Polymer on a glass slide with exfoliated Sb flakes. b) AFM image of FLA flake with folded single-layer terrace. c) Profile along the green line in the inset of (b). d) Topographic AFM image taken just after exfoliation. e) Same image as in (d) but after two months of exposing it under ambient conditions. f) Same image as in e) but after immerging the sample in water. g) Profiles taken along lines drawn in d)-f). Adapted from reference 48.

However, this production method yields low quantity of FLAs[62]. For this reason, is mainly used to study the fundamental physical properties of the materials but it is not useful to perform mass production and other potential applications.

1.3.2 Liquid-phase exfoliation (LPE)

A larger discussion will be done about this method because it is the one employed to obtain antimonene in this work. In the last section, it was said that the main problem of micromechanical exfoliation is the difficulty that it has to scale-up to mass-production.

In contrast, LPE methods are easy techniques, suitable for industrial scale-up and based on the "solubility parameters" theory. Ideally the layered material is immersed into an appropriate solvent, i.e. the surface energy of the solvent and the layered material match with each other. The amount of energy necessary to overcome the van der Waals cohesive force between the layers in the layered crystal is supplied in form of ultrasonic waves. These ultrasonic waves generates turbulence, shear forces and cavitation bubbles within the pale of the suspension. When the energy released due to the collapse of the cavitation bubbles next to the interstitial holes, along with the shear forces, is enough to overcome the van der Waals cohesive energy of the material, exfoliation occurs. After this moment, a variety of mono- and few-layer flakes are dispersed in the solvent, and comes the time for the solvent to stabilize the exfoliated flakes in order to avoid aggregation[63,64,65]. This is a simple description of the most typical procedure among the LPE methods, however, other liquid medium can be used to stabilize the suspensions like surfactants[66], molecules or polymer agents[67].

This methodology was successfully used by Hernández *et al.* in 2008 to exfoliate graphite for obtaining graphene single-layers using N-methyl-2-pyrrolidone (NMP) as a solvent[64] (Figure 1.6). Even though this methodology has notably advanced, the mechanism of exfoliation is still poorly understood. However, there is a general thought that the properties of the solvent along with the high-frequency vibration (>15 kHz) of the

sonication probe generates the environmental fluid dynamics necessary to supply the suitable amount of energy to exfoliate layered crystals, as it was described in the precedent paragraph[68,69].
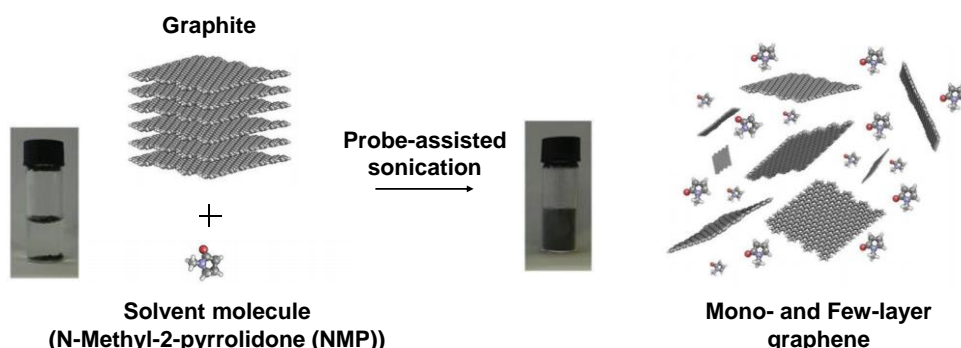
Figure 1.6 Schematic illustration of probe-assisted sonication in the liquid-phase exfoliation of graphite into graphene using NMP as a solvent. Adapted from reference 70.

One important point of using this exfoliation method instead of other, is that the final product consists of a suspension of exfoliated nanosheets which is an ideal way for processing the material afterwards. However, the strongest point that this method has is the possibility of produce industrial quantities of 2D materials in an easy way. Although this procedure to exfoliate layered crystals has a lot of advantages compared to micromechanical exfoliation, it also has several drawbacks. One is associate to the material quality, due to the production of defects during the LPE process due to the use of high energy, and the fact that the performance of the process get worse for larger volumes, when using sonication assisted exfoliation. In order to avoid part of these problems, other approaches has been developed. Paton *et al.* used a shear-mixer instead of probe sonication to obtain individual nanosheets of graphene in suspension using NMP as a solvent, and they demonstrated that with this configuration larger volumes can also be obtained[70] (Figure 1.7).
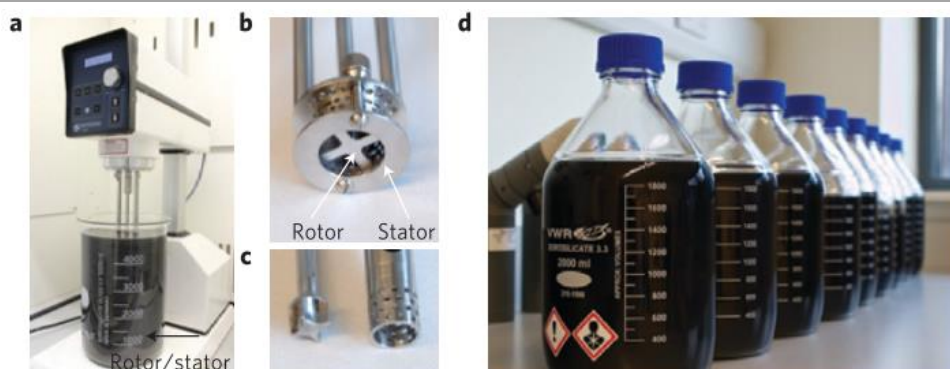
Figure 1.7 a) Configuration of the shear-mixing process to obtain graphene using NMP as a solvent and a volume of 5 L. b) Close-up view of the shear-mixing tip with a rotor-stator geometry. c) Close-up view of the rotor separated from the stator in (c). d) Graphene–NMP dispersions produced by shear exfoliation demonstrating that this process allows the production of larger volumes. Adapted from reference 71.

Even though it is true that with the shear-mixing method larger volumes of suspension can be obtained, the quantity of exfoliated flakes and the single-layer yield of the process is lower than using the probe sonication method.

To further understand the mechanism that is taking part during the exfoliation of layered materials using LPE methods, it's necessary to dive into the "solubility parameters" theory in which all of these techniques are based.

- *Solubility parameters theory:*

During the last century a huge effort was done trying to develop a solubility theory for polymers, and more specifically for their solubility parameters. Two theories were developed, the first one by Hildebrand and the second by Hansen[67,71].

The most interesting thing for us about this parameters, is that they can be applied to investigate the solubility of nanomaterials in certain solvents[64,72]. Interestingly, not all solvents are suitable to disperse every kind of material due to a mismatch of the surfaces energies between both components. For this reason, is important to understand the chemical interactions between the solvent and the nanomaterials by analysing their solubility parameters.

When two or more chemical compounds get mixed, the entropy ($\Delta\bar{S}_{mix}$) and the enthalpy ($\Delta\bar{H}_{mix}$) of the system suffer a change. This can be described by the fundamental principle of Gibbs free energy (Eq.1).

$$\Delta\bar{G}_{mix} = \Delta\bar{H}_{mix} - T\Delta\bar{S}_{mix} \qquad \text{Eq. 1}$$

To accomplish a stable dispersion, the Gibbs free energy needs to be negative. Taking into account that 2D materials tend to have lower entropy values, due to its rigid and large morphology, it's necessary to minimize the enthalpy of the system to reach a good dispersion[73]. To fully understand the thermodynamics of mixing, it is also necessary to take into account the solute-solute and solvent-solvent interactions, and not only the solute-solvent interaction.

This solubility theory is based in a typical rule of thumb, "like dissolves like". But actually, what needs to happen for a solid to be dissolved in a liquid is a breakage of some interactions or even bonds between adjacent neighbours. To get this cleavage, it is necessary to supply energy to the system (vaporization energy). Thus, for a layered crystal this energy is equal or greater to the van der Waals energy responsible to hold the 3D structure together, and the solubility parameters derived from it, are related to the "cohesive energy" of the solvent. Trying to clarify this aspect, it could be said that cohesive energy is a representation of the van der Waals energy between different molecules or nanostructures in a solvent.

Taking this into account, Hildebrand developed a solubility parameter that describes the system and it is represented by $\delta = \sqrt{E/V}$ (where E is the energy necessary to separate the molecules in the system and V is the molar volume of the solvent).

Hernández *et al.* published an expression that derives from the Hildebrand-Scatchard equation[74], for the enthalpy of mixing per unit of volume for 2D materials in a solvent (Eq.2)[75].

$$\frac{\Delta H_{mix}}{V_{mix}} \approx \frac{2}{T_{layer}}\left(\delta_{layer} - \delta_{solvent}\right)^2 \emptyset \quad \text{Eq.2}$$

Where $\delta_i = \sqrt{E_{sur}^i}$ is the square root of the component surface energy, T_{layer} is the thickness of the 2D material and $\emptyset$ is the volume fraction of the 2D material nanosheets. Therefore, in order to minimize the enthalpy of mixing of the system to favour the dispersion of the 2D material in the solvent, the surface energies of both components should match.

Even though, that the solubility parameters proposed by Hildebrand accurately describe the interaction between the solvent and the solute molecules, Hansen discovered that not just dispersive forces play a role in the dispersion mechanism.

There are different kind of interactions between solvent molecules and 2D nanosheets that should be taken into account. The most important forces are the dispersive or non-polar force (E_D), the polar force (E_P) and hydrogen bonding (E_H). The three of them are the contributions to the total cohesive energy (E) as it is shown in Eq.3.

$$E = E_D + E_P + E_H \qquad \text{Eq.3}$$

With the definition of solubility parameter given by Hildebrand ($\delta = \sqrt{E/V}$), Hansen postulated that the Hildebrand solubility parameter (δ_T) should be described again as the sum of the solubility parameters due to the different contribution forces (δ_H, δ_P, and δ_D) also called Hansen parameters (Eq.4).

$$\delta_T{}^2 = \delta_H{}^2 + \delta_P{}^2 + \delta_D{}^2 \qquad \text{Eq.4}$$

Coming back to LPE methods, since Coleman *et al.* started using them to obtain large quantities of high-quality graphene, other research groups started applying them to other layered materials such as h-BN[76], TMDs[77], TMOs[78], MOFs[79], COFs[80] and group-VA semiconductors[81], with promising results.

Regarding the production of antimonene, in 2016 our group was the first one that experimentally demonstrated that high-quality FLAs could be obtained using LPE methods[49]. This issue would be discussed in detail in Chapter 2 of this manuscript. This work paved the way for antimonene production using LPE techniques by other groups. Later on Gu *et al.* developed another LPE method to obtain FLAs using an isopropanol solution with a constant concentration of NaOH[82]. In this work, they employed 30 h of sonication followed by centrifugation at 2000 rpm to eliminate aggregates and the obtained FLAs had minimum thicknesses comprised in the 3.0–4.3 nm range.

Recently, Wang *et al.* also prepared FLA including a pre-grinding process followed by sonication-assisted LPE using 2-Butanol as a solvent. This approach is also based on other of our experimental works where we improved the exfoliation yield by including a pre-grinding process using a ball-mill reactor[83]. This issue will be discussed in detail in Chapter 4.

Additionally, LPE techniques have demonstrated the obtaining of antimonene "quantum dots" (AMQDs) by Tao *et al.* combining both types of sonication (bath assisted and probe-assisted) and coating the particles with polyethylene glycol (PEG)[84].
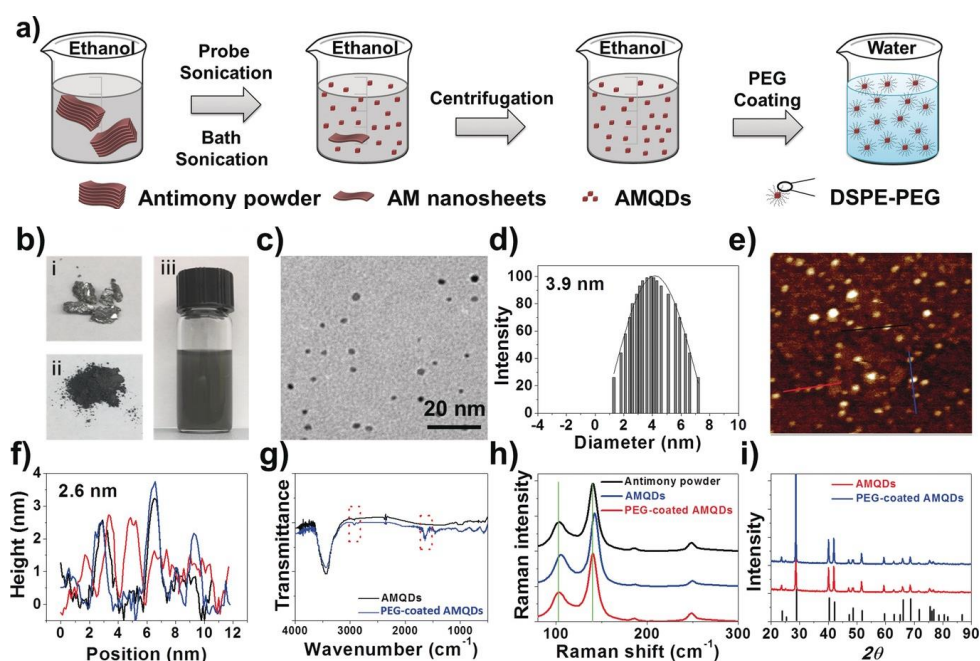
Figure 1.8 a) Scheme of production of PEG-coated AMQDs. b) Photos of bulk antimony, antimony powder, and AQDs solution during the preparation process. c), d), e), f) TEM image, diameter distribution, topographic AFM image and thickness of the PEG-coated AMQDs. g), h), i) FTIR spectrum, Raman spectrum, and XRD spectrum of AMQDs and PEG-coated AMQDs. Adapted from reference 84.

A similar procedure but changing the solvent was also investigated by Lu et al. to obtain AMQDS, in this case they used NMP as a solvent, and they observed that the production yield experiments an enhancement[85].

Gusmão *et al.* reported the obtention of antimonene using other kind of LPE technique employing kitchen blenders[86]. In this case, spinning blades produce turbulence and collisions of the particles within the pale of the suspension, rending to a lateral shear force that is enough energetic to exfoliate antimony crystals. A deeper study regarding the different variables that affects the LPE technique in the production of FLA will be described in Chapter 4 of this manuscript.

1.3.3 Epitaxial growth

This set of techniques belongs to the "bottom-up" group, and are considered as the best-known scalable methods to produce high-quality 2D materials[87,88,89]. In the case of growing single-layer antimonene, two methods are the most employed among this group of techniques: molecular beam epitaxy (MBE) and van der Waals beam epitaxy (vdWE). Regarding vdWE technique, its principal feature relies in the use of substrates without dangling bonds on their surface. After the growing step, the epitaxial-grown layers are linked to the substrate by means of weak van der Waals forces. In this way, different crystalline symmetries of layered materials can grow on the substrate[90].

In 2016, Ji *et al.* achieved for the first time the growth of antimonene polygons on different substrates   using vdWE[51]. In this work, they also showed the atomic structure of β-antimonene flakes (Figure 1.9). The synthesis takes part inside a two-zone oven (Figure 1.9a), where antimony powder is first heated (T1) to produce antimony vapour and then is transferred to the substrate (T2) through an Ar/H_2 flow. Thus, crystallization of the Sb atoms from vapour phase on mica substrate takes place (Figure 1.9b).

The subsequent antimonene flakes have lateral dimensions about 5-10 µm and heights of 4 nm (Figure 1.9c).They have also found a small structure, with irregular shape, assigned to a single-layer of antimonene (Figure 1.9d). They also investigated the stability of antimonene flakes by measuring Raman spectra of one flake right after its preparation and after one month of aging in air (Figure 1.9e) without seeing any new signature in the spectra. Topography AFM images recorded after one month for the same flake do not show any significant change. In addition, the stability of the antimonene flakes confirmed by X-ray energy-dispersive spectroscopy (XEDS) (Figure 1.9f).
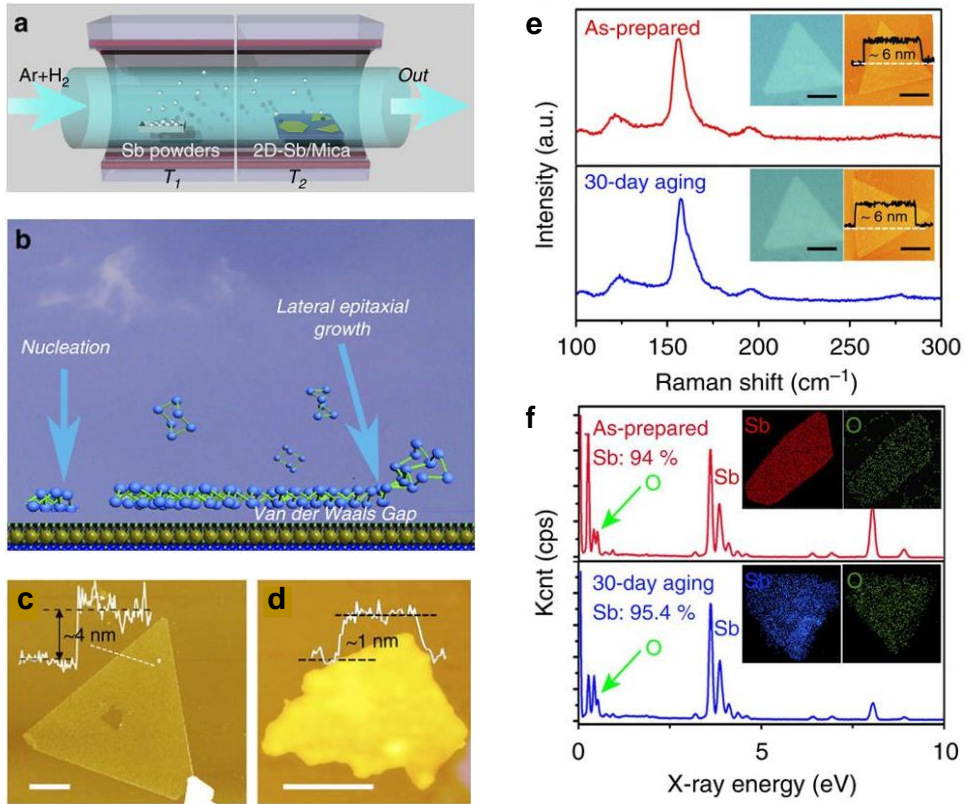
Figure 1.9 a) Schematic image of the synthesis of the sample. b) Diagram of van der Waals epitaxy process. c), d) AFM images of antimonene flakes on mica (scale bar equal to 50 nm). e) Optical images, AFM images, and Raman spectra of antimonene before and after a 30-day aging period (scale bar equal to 2 µm). f) XEDS analysis of antimonene before and after aging for 30 days. Adapted from reference 51.

In 2016, Lei *et al.* reported the growth of antimonene on Bi_2Te_3 (111) and Sb_2Te_3 (111) substrates with a small lattice mismatch using MBE[91]. After this study, other groups achieved the growth of antimonene by MBE on different substrates.

Thus, Wu *et al.* have used PdTe$_2$ to grow a single-layer of antimonene[52] (Figure 1.10a) with an almost perfect (111) orientation, a graphene-like honeycomb with no major defects and an apparent height of 0.28 nm (Figure 1.10b-c). They also demonstrated the stability in air of an antimonene flake.

More recently, Fortin-Deschênes *et al.* used MBE to grow antimonene on a Ge (111) substrate, optimizing the growth with *in-situ* electron microscopy[92] (Figure 1.10d). They also obtained single-layer antimonene, stable under ambient conditions and weakly bonded with the substrate (Figure 1.10e-f).

More recently, Shao *et al.* reported the growth of a single-layer antimonene onto an Ag (111) substrate[93]. They confirmed using scanning tunnelling microscopy (STM) the formation of the single-layer with the typical honeycomb structure and a height of 2.2 Å (Figure 1.10g-i).
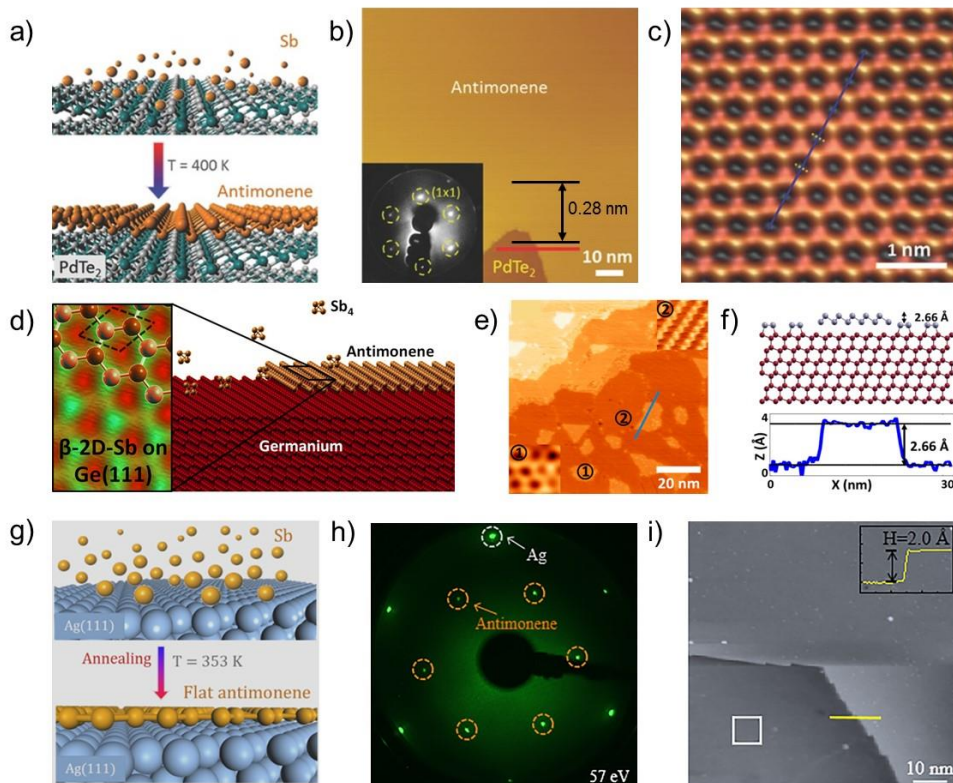
Figure 1.10 a) Scheme of the fabrication of an antimonene monolayer on a PdTe$_2$ substrate. b) STM image of antimonene on PdTe$_2$ (Inset: Low-energy electron-diffraction pattern of the same area). Height profile along the red line. c) Atomic-resolution STM image of antimonene. d) Scheme of the fabrication of an antimonene monolayer on a Ge (111) substrate. e) STM image of single-layer antimonene f) (Image top) model of a single-layer antimonene on bare Ge (111) surrounded by Ge (2×1)-Sb chains. (Bottom) STM height profile measured along the blue line in (e). g) Scheme of the fabrication of an antimonene monolayer on an Ag (111) substrate. h) LEED pattern of antimonene on Ag (111), presenting an Ag (111)-($\sqrt{3} \times \sqrt{3}$) superstructure. i) Large scale STM image of monolayer antimonene on the Ag (111) substrate (Inset: Height profile of the antimonene single-layer along the yellow line at the terrace edge).

1.3.4 Electrochemical exfoliation

Recently, different groups have prepared different 2D materials using electrochemical exfoliation, such as graphene[94], MoS_2[95] and phosphorene[96] among others. This method seems to be useful to decrease the costs of large-scale 2D materials production, and also avoids the use of several chemicals[97].

Lu *et al.* have published the isolation of FLA using electrochemical exfoliation[85]. The procedure they carry out was quite simple, they placed an antimony crystal between the conducting wire of a DC power supply and the counter electrode made of platinum, within the pale of a Na_2SO_4 used as electrolyte (Figure 1.11a). To avoid contamination from the conducting wire and the possibility of having electrolysis, the antimony crystal and the platinum wire were partially placed into the electrolyte. An -6 eV constant voltage, ensure full intercalation and exfoliation of Na ions inside the cathodic antimony. After that step, the resulting electrolyte containing the exfoliated antimony nanosheets was centrifuged at 6000 rpm and 30 min and then sonicated in deionized water for 10 min. The resulting suspension was then vacuum dried and re-dispersed in NMP.

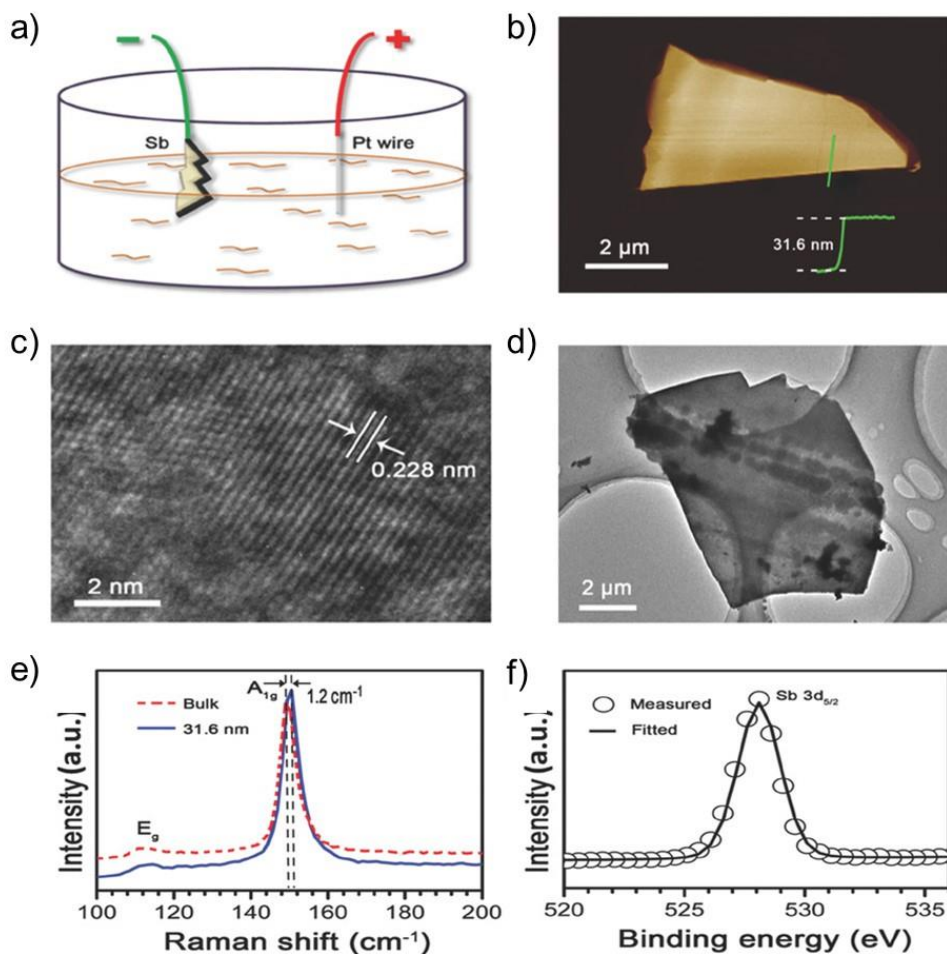**Figure 1.11** a) Scheme of the electrochemical exfoliation of antimony crystals using a two electrode configuration and Na_2SO_4 as electrolyte. b) Topographic AFM image of a FLA flake with its height profile along the green line. c) HRTEM and d) TEM images of a FLA flake. e) Raman spectra of bulk antimony and FLA flake showed in (b). f) XPS spectrum of the Sb $3d_{5/2}$ peak of exfoliated FLA. Adapted from reference 85.

Figure 1.11b shows a topographic AFM image of an individual FLA flake, with a thickness of ~ 31.6 nm and several microns of lateral dimension, further confirmed by TEM (Figure 1.11c-d). High-resolution TEM measurements also confirmed the inter-distance of the lattice fringes ~ 0.228 nm what is in good agreement with the (100) interplanar distance of β-antimonene structure (0.225 nm)[48]. The Raman spectra of FLA show the similar vibration modes to that found for bulk antimony, E_g and A^1_g vibrations modes (red dashed line in Figure 1.11e), but blue-shifted to higher wavenumber values (blue dashed line in Figure 1.11e) in agreement with exfoliation to nanometer thickness. X-ray photoelectron spectroscopy (XPS) was used to check the stability of the FLA under ambient conditions, confirming no oxidization. To sum up, Lu *et al.* have achieved the development of an electrochemical approach to exfoliate antimony crystals to produce stable FLAs with large lateral dimensions. However, this technique needs to be quite improved in order to increase the exfoliation yield and the exfoliation grade.

In summary, it has been described the *pros* and *cons* of the so far reported production methods of antimonene or FLA. From the point of view of mass-production, it seems clear that LPE methods are the most promising among all the reviewed techniques, due to their high exfoliation yield, low cost of production and simplicity. However, there is still a long way to find the best experimental conditions to obtain high-quality antimonene using LPE methods. This is the reason way, large part of this thesis focused on these issues (Chapter 2-4). A better understanding of the LPE process, would rend to better results regarding the production of high-quality antimonene and then applications.

1.4   Applications of antimonene

Nowadays, the state of art regarding applications where antimonene can be suitable is still emerging. However, there are some works related to this issue where several groups published some good results in a wide variety of real and potential applications for antimonene.

1.4.1   Electronic devices

It has been demonstrated that group-15 semiconductors are suitable materials for the construction of next-generation field effect transistor (FETs)[98]. Their atomically thin thickness enhances geometric scaling behaviour and gate electrostatics, and their free-dangling-bond smooth surface provides the high carrier mobility.

In 2016, Pizzi *et al.* presented a detailed multiscale simulation of using monolayer arsenene and antimonene as channels for the construction of a FET[99]. These simulations provided for the very first time an estimation of the upper limits for the electron and hole mobilities and demonstrated that devices in the sub-10 nm scale showed a performance that is appropriate for industry demands.

More recently, Chang *et al.* have moved by the thickness dependent semiconductor to metal transition, proposed to use a lateral mono-layer/multi-layer heterostructure of antimonene for constructing a tunnelling field effect transistor (TFETs)[100]. The proposed device consisted of a source made with a semiconducting antimonene monolayer and a small metallic multilayer region between the source and the channel.

The fact that there is a multilayer region between the source and the channel introduces gapless metallic states which induces an enhancement of the tunnelling probability and in consequence a large current. This work was carried out using *ab initio* electronic structure and quantum transport calculations for different conformations of the TFETs. Simulation revealed that even ~ 1 nm scale nanostructured multilayer increases the current and enables abrupt device switching. They concluded that according to the simulations antimonene seems to be better candidate than phosphorene for TFETs fabrication, due to the tunnelling barrier absence.

In 2018, Sun *et al.* have investigated the performance of mono-layer antimonene and arsenene for FETs fabrication in the sub-5 nm using *ab initio* quantum transport simulation[101]. They have revealed that the configuration of sub-5 nm double gate single-layer antimonene and arsenene metal oxide semiconductor FETs, also known as MOSFETs, could accomplish the low power requirements of the International Technology Roadmap for semiconductors in 2028, with a better performance than MoS_2 MOSFETs in terms of On-Current.

Ji *et al.* have reported the first experimental transistor using antimonene [51]. They fabricated the devices directly on mica substrates after synthesising antimonene by van der Waals beam epitaxy, using as top gate dielectric HfO_2 (Figure 1.12a). The contacts were made of a 10 nm thick layer of Cr and a 30 nm thick layer of Au. Then a 15 nm thick layer of HfO_2 was growth on the top of them by atomic layer deposition followed by another 50 nm thick layer of Au as the top gate electrode (Figure 1.12b). The I-V curves of three different devices made with different antimonene thicknesses showed good ohmic behaviour (Figure 1.12c).

They also calculated the electric resistance of the thinnest antimonene device, obtaining a value of 600 Ω, and the electrical conductivity of the synthesized antimonene flake with a result of 1.6 x 10^{-4} S·m^{-1}. This conductivity is in good agreement with the typical semimetal values and also is consistent with the predictions. This means that exists a strong dependence on the thickness for the semimetal-semiconductor transition. The devices also exhibited high flexibility and no major changes were observed regarding the conductivity after bending the device 100 times (Figure 1.12d). They also checked the transparency of the obtained antimonene by measuring its transmittance. They observed that the transmittance of antimonene flakes is almost independent of the applied wavelength, within the range from 400 to 700 nm (Figure 1.12e-f). This is an interesting result and could lead to applications in the transparent conductive electrode related areas.
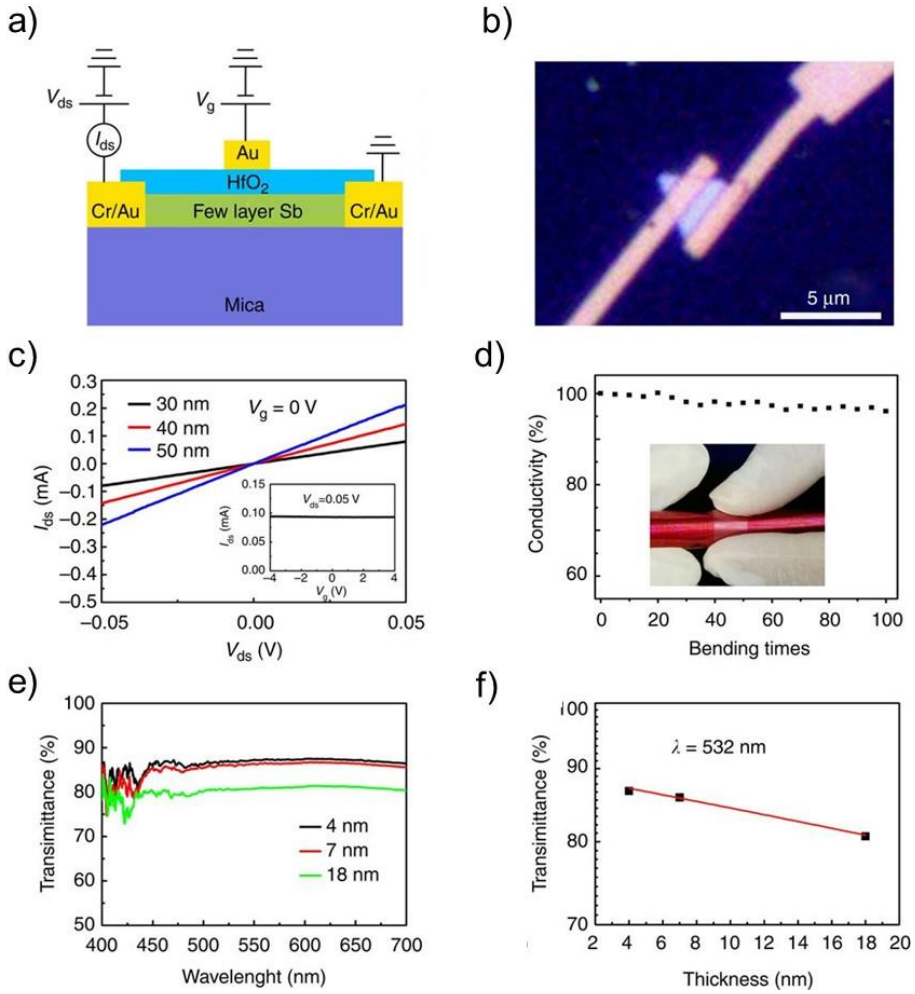
Figure 1.12 a) Scheme of a top-gated antimonene thin film transistor. b) Optical image of the transistor made of antimonene. c) I_{ds}–V_{ds} curves of three tested devices acquired at V_g=0 V (Inset: I_{ds}–V_g curve of the 30-nm thick antimonene device acquired at 0.05 V bias voltage). d) Conductivity of the tested device after bending it 100 times (Inset: Photograph of bended antimonene device on mica substrate). e) Transmittance spectra of three typical antimonene flakes of 4, 7 and 18 nm thicknesses, respectively. f) Transmittance of antimonene flakes versus sample thickness. Adapted from reference 51.

1.4.2 Optoelectronic devices

This kind of devices and applications need materials with specific band-gap values and high-carrier mobility[102]. For that reason, 2D forms of group-15 semiconductors and, especially, antimonene has been studied as a suitable material for such applications. Zeng *et al.* calculated that the thickness reduction from bulk antimony to a single-layer produce a change from a semi-metal to a semiconductor with a broad band-gap of 2.28 eV[98]. Besides, they stated that antimonene oxides behave also as semiconductors with a direct tunable band-gap and high carrier mobility when varying their quantity of oxygen. This fact could convert this antimonene oxides into a suitable materials for optoelectronic devices[103].

In the meantime, Wang *et al.* used *ab initio* methods to investigate the carrier mobility, many-body effect and the device performance of single-layer antimonene. They came up with some interesting results regarding the optical and quasi-particle band-gaps, 1.5 eV and 2.38 eV respectively, and also they concluded that sub-10 nm antimonene could be used to produce a FET with a good performance[55].

Additionally, using DFT calculations Xie *et al.* suggested the use of a bi-layer of antimonene to fabricate thermophotovoltaic (TPV) devices. This approach supplied an energy conversion efficiency about ~ 31 %, which is significantly larger than those found for related materials typically used for this specific application[104].

Regarding the practical application of antimonene in the fabrication of optoelectronic devices, in 2018 Wang *et al.* experimentally proved the use of antimonene as hole transport layer (HTL) material in the fabrication of a perovskite solar cell[105]. It was the first experimentally use of antimonene for manufacturing this kind of devices (Figure 1.12).

One of the most interesting things of this work is that they obtain antimonene using LPE, and then experimentally proving that this technique is suitable for subsequent applications of antimonene. Interestingly, they found out that the energy level of the LPE antimonene matched with the one of $MAPbI_3$ and that provides a likely hole extraction driving force (Figure 1.13a). They also fabricated an HTL-free device (device 1) in order to compare it with the one fabricated using antimonene as a HTL (device 2). This new device (Figure 1.13b) exhibited a higher power conversion efficiency and higher J_{sc} (increased from 11.2 to 14.6 mA/cm^2). Besides, within the visible light range, the external quantum efficiency (EQE) of Device 2 was 55-60 %, what was in accord with the results from the JV-curves (Figure 1.13c-d). It's easy to see how this work pave the way for future projects regarding the application of antimonene in optoelectronic applications.

Immediately after Zhang *et al.* experimentally studied the semiconductor properties of single-layer antimonene. They demonstrated that semiconducting antimonene nanosheets (SANs) exhibited a photoluminescence bandgap of ~ 2.33 eV and a photoluminescence lifetime of 4.3 ns. Besides, in this work they also employed the obtained SANs for the hole extraction layer in a planar inverted perovskite solar cell (PVSCs), enhancing the device performance due to fast hole extraction and efficient hole transfer at the perovskite/hole transport layer interface[106].
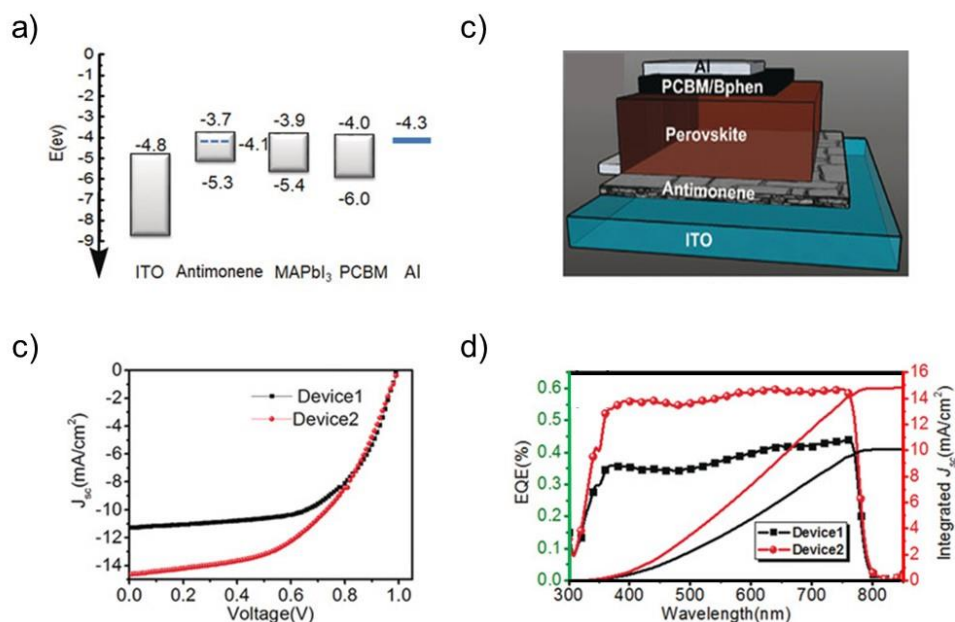
Figure 1.13 a) Comparison of energy levels between different components of the device (Fermi level of antimonene is represented by the dashed line. b) Scheme of the different components included in the perovskite solar-cell. c) Current density–voltage (J–V) curves of devices with different configuration. d) External quantum efficiency (EQE) spectra together with EQE-data-based integrated short-circuit current densities (J_{sc}) for the two different device configuration. Adapted from reference 102.

Furthermore, antimonene not only has been used for constructing solar cells. In 2017, Lu *et al.* studied the non-linear refractive index of antimonene using spatial self-phase modulation (SSPM)[85], and they obtained a value of ~ 10^{-5} cm²·W⁻¹ using visible light. They also found out that this index was larger for FLA than AMQDs. They stated that with these results, antimonene could be considered as a new kind of promising optical Kerr material with enhanced stability. Taking into account this work, antimonene seems to be useful for developing photonic devices, since it fulfil the gap that graphene and phosphorene could not.

Additionally, in 2017 Song *et al.* experimentally explored the broadband non-linear optical response of FLA, by measuring with an open-aperture Z-scan laser[107]. They also demonstrated the possibility of fabricate a FLA decorated microfiber (Figure 1.14c) to be used as an optical saturated absorber for ultrafast photonics and also as a stable all-optical pulse thresholder that can effectively suppress the transmission noise, boost the signal-to-noise ratio (SNR), and reshape the deteriorated input signal. In 2018, this same research group experimentally demonstrated the all-optical signal processing based on the high optical nonlinearity of antimonene[108]. They used the same FLA decorated microfiber but they applied it as an all-optical Kerr switcher with an extinction ratio up to 12 dB and a wavelength conversion of modulated high-speed signals with a frequency as high as 18 GHz (Figure 1.14 a-b). These two studies suggest that FLA could be used for the applications of high-speed optical communication.
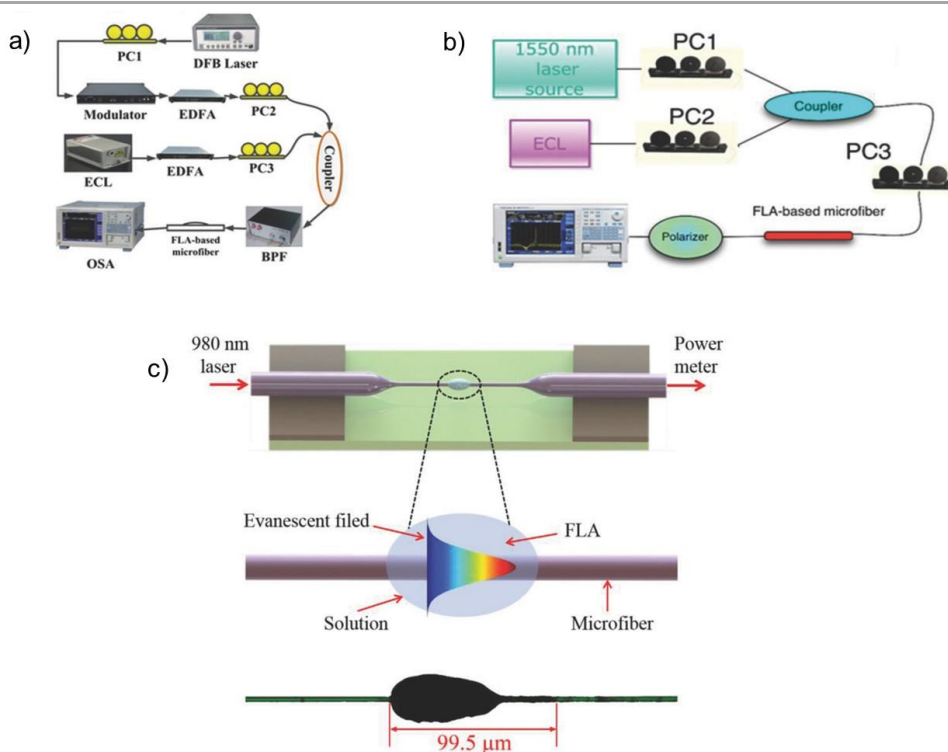
Figure 1.14 a) Experimental setup on four-wave mixing wavelength converter based on the FLA-decorated microfiber (DFB laser: distributed feedback laser; BPF: band-pass filter; PC: polarization controller; EDFA: erbium-doped fiber amplifier; ECL: external cavity laser; OSA: optical spectrum analyser). b) Scheme of the all-optical Kerr switcher in the FLA nonlinear fiber optical device. c) Scheme of the FLA deposition process onto the microfiber. Adapted from reference 107 and 108.

1.4.3 Electrocatalysis

Recently, a wide variety of 2D materials have been employed as useful in electrocatalytic CO_2 reduction reaction (CO_2RR), due to their improved electron hopping, enlarged surface area and the increase of defects and active sites[109].

Concerning group-15 semiconductors, bismuth has already exhibited good catalytic activity in the CO_2RR[110]. For this reason, different research groups have explored this direction using antimonene instead.

Thus, Li *et al.* reported for the first time the possibility of using FLAs in the CO_2 reduction reaction (CO_2RR)[111]. They found out clear differences between using FLA to fabricate the electrode and using bulk antimony. Thus, FLA produced a lower onset potential and a clear enhancement of the catalytic current density compared to the bulk antimony. Besides, the electrode made with FLA generated a broad peak around -1.06 V in the CO_2 saturated solution which is an indicator of the CO_2 reduction (Figure 1.15a). They also discovered that the selectivity of FLA towards H_2 and formate was dependent on the applied potential. The faradaic efficiency (FE) towards formate reached for the system had a maximum of ~ 84 % at -1.06 V, while for CO was almost constant independently of the applied potential (Figure 1.15b).

The hypothesis that the catalytic activity was increased due to the greater number of active sites after the cathodic exfoliation and the liquid-phase exfoliation processes, was confirmed analysing the peak at the polarization curve (I_{mass}), where the curve obtained with larger antimony nanosheets (SbNS) was found to be 3.6 times lower than the one obtained with the smaller ones (Figure 1.15c). In this work, Li *et al.* also produced a composite of antimonene and graphene by means of *in situ* cathodic exfoliation replacing the Pt anode with a graphite rod (Figure 1.15d). Interestingly, the antimonene-graphene (FLA-G) composite exhibited a greater selectivity and I_{mass} for producing fromate at lower potentials (Figure 1.15e).

Besides, the FLA-G composite showed a partial current density towards formate 1.5 times higher compared to the FLA, and 16 times higher compared to bulk antimony at -1.07 V (Figure 1.15f). They also explained that the enhancement of the catalytic activity of the FLA-G composite compared to the FLA is due to the strong electronic interaction between both materials, and not just because the greater number of active sites exposure in the FLA-G composite.

There has been also studies regarding the electrocatalytic activity of antimonene focused in the possibility of use it as an anode material in batteries and supercapacitors. In 2017, Sengupta *et al.* reported *ab initio* studies about the lithium and sodium adsorption of single-layer antimonene[112]. Their calculations showed the possibility of using single-layer antimonene for anode material in sodium ion batteries (SIB) with a theoretical capacity of 320 mAh·g^{-1}, an open circuit voltage up to 1.22 V and a small diffusion barrier of 0.114 eV.
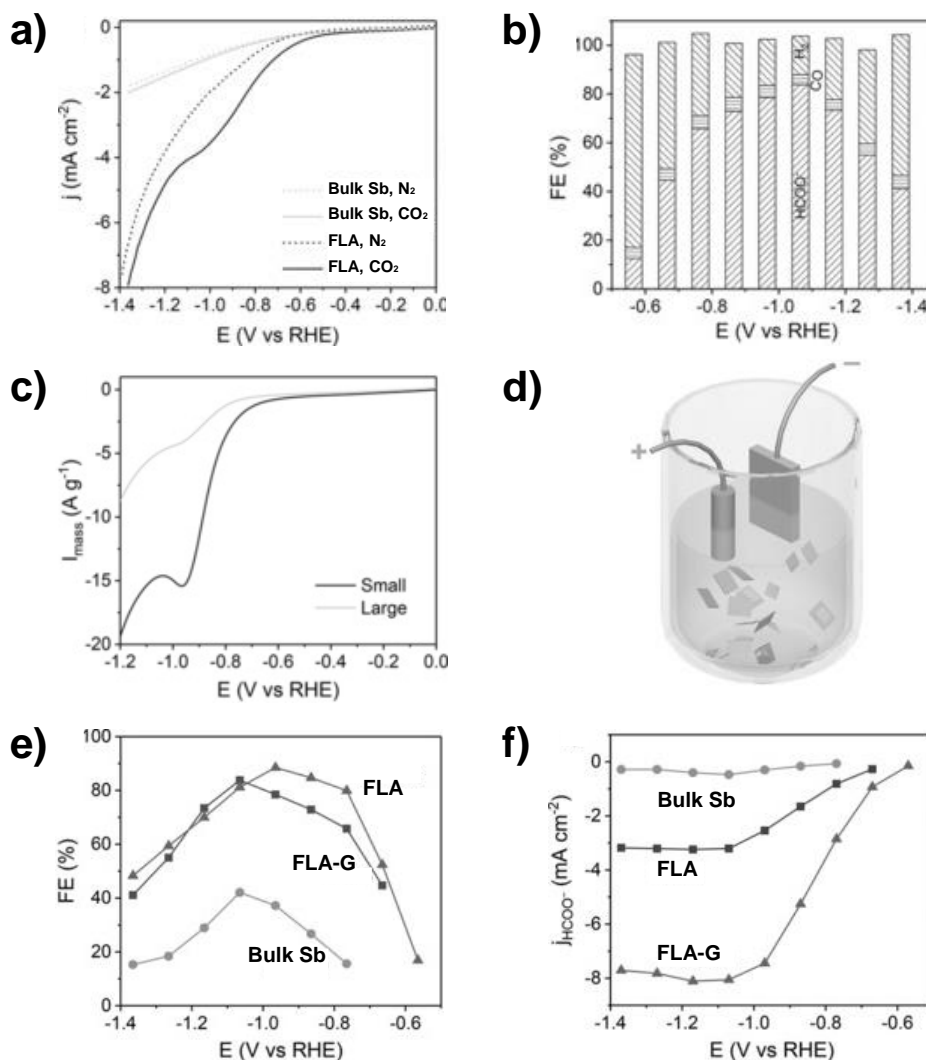
Figure 1.15 a) LSV curves of bulk antimony and FLA in N_2-saturated and CO_2-saturated solutions (pH values 8.5 and 7.2, respectively). b) FE for H_2, CO, and formate on the FLA electrode at different applied potentials. c) Polarization curves of small and large FLA-modified GCEs in CO_2-saturated solution. The mass loading of antimony was measured by inductively coupled plasma mass spectrometry (ICP-MS). d) Schematic illustration of the electrochemical cell for the in situ formation of the composite. e) FE for formate at different applied potentials on bulk Sb, FLAs, and FLA-G. f) Partial current density for the same cases than (e). Adapted from reference 111.

1.4.4 Catalysis

Historically, elements of the group-15 have not been frequently used for chemical catalysis. The reason why is associated to the existing difficulties when preparing stable materials from this group of elements. However, with the appearance of stable 2D forms new opportunities to apply them in catalysis have been opened.

In 2019, Lloret *et al.* reported on the synthesis of few-layer phosphorene and antimonene using LPE methods[113]. They used ionic liquid as media to exfoliate the bulk materials, rending into highly exfoliated and zero oxidized flakes, with the native atoms eluding any aqueous degradation and ready to act as catalysts for the alkylation of nucleophiles with esters. Thanks to ionic liquids on the top of the flakes, the obtained few-layer pnictogens avoid the extremely severe conditions that normally take part in superacid-catalyzed alkylations. This inhibition is due to an alternative mechanism that takes part in the surface of the exfoliated flakes, where the aromatic nucleofile and ester are activated, allowing acid sensitive molecules to be alkylated (Figure 1.16). This experimental study was the first one regarding the utilization of FLA and FL-phosphorene as catalyst in organic synthesis[113].

Equation rates

FL-P or Sb:
$v_0 = k_{app1}$ [P or Sb] [1] [2]

HOTf: $v_0 = k_{app2}$ [H$^+$] [2]

Chirality test

OAc — 13 → HOTf (0.1 mol%) or FL-BP (10 mol%), MeOH (10 equiv.), bmim-BF$_4$ (1 M), 75 °C, 20 h → OMe (14a, 15-20%) + OH (14b, 10-15%) + 13, 65-70%

Ph / Me

Competitive test

1 + 15 (with OH, 9) + 2 (1 equiv.) (As in 4B) → 3 + 16 (Me—O^{t}Bu, 9)

Catalyst	v_0 (3/16)	Yield of 3 (%)	Yield of 16 (%)
FL-BP or Sb	10.0	67	14
HOTf	1.7	42	29

Proposed reaction mechanism

2D FL pnictogen catalysis — 2D FL pnictogen-stabilized carbocation and NuH

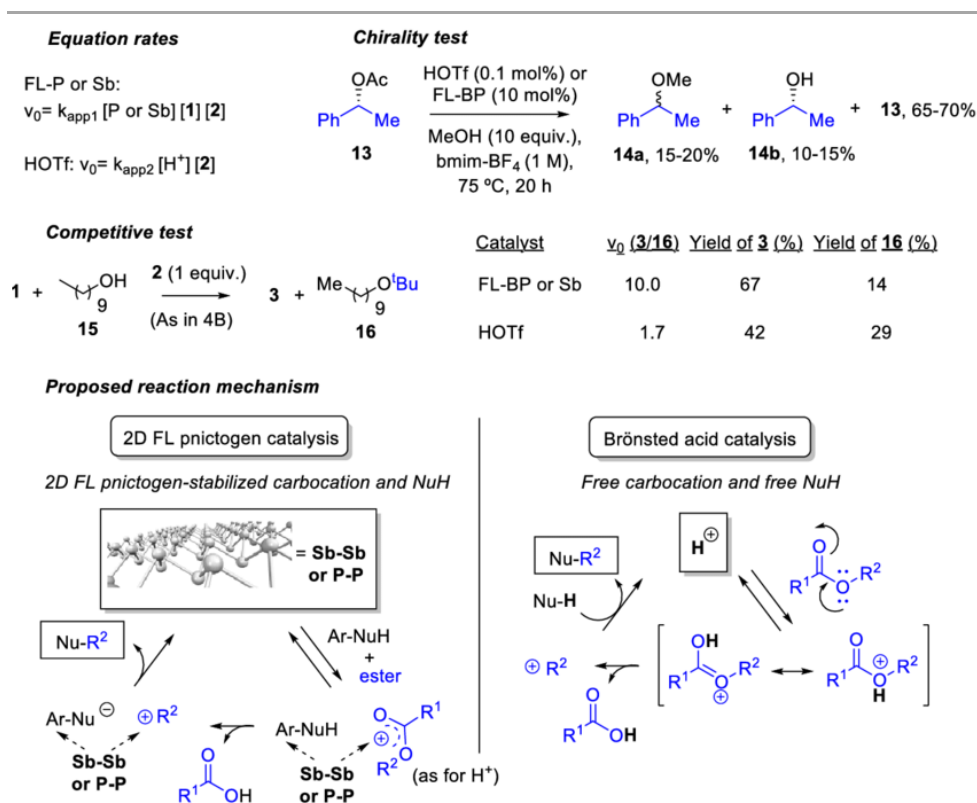Brönsted acid catalysis — Free carbocation and free NuH

Figure 1.16 Experimental evidences and proposed mechanisms for FL-phosphorene, FLA and HOTf catalyzed–alkylation of nucleophiles with esters in the ionic liquid, bmim–BF$_4$. Adapted from reference 113.

55

1.4.5 Energy storage

Currently, the finding of a sustainable, cheap and efficient energy storage system is one of the main scientific topic[114]. Among the wide variety of energy storage technologies that it could be found, Na-ion batteries (SIBs) have attracted a lot of interest due to the fact that Na is an abundant element in nature, the cost of producing the batteries is relatively low and they are environmentally friendly[115]. Regarding this specific group of batteries, it has been demonstrated that antimonene could also be used as an anode in Na storage, due to its theoretical capacity of 660 mAh/g towards Na storage and its low discharge potential of ~ 0.5 V (Na$^+$/Na)[116].

Recently, Gu *et al.* have proposed a modification of the LPE approach that our group developed for obtaining FLA, but using a constant concentration of sodium hydroxide, they called them SbNS). They also reported the fabrication of composite films made of SbNS and graphene (SbNS-G). These composite films were proved to have high volumetric capacity, ~1226 mAh·cm^{-3}, compared to that found for graphene films, 80 mAh/cm^3 and Sb/C composites, 100-300 mAh/cm^3 previously reported (Figures 1.17a and 1.17b, respectively). Besides, they also exhibited high rate capabilities for Na storage even at the highest applied current density (4.0 mA·cm^{-2}). At this value of current density the charge and discharge volumetric capacities were kept at 216 mAh·cm^{-3} (Figure 1.17c-d) and after 100 cycles the composite film still presented a stable capacity of 110 mAh·cm^{-3} (Figure 1.17e)[82].
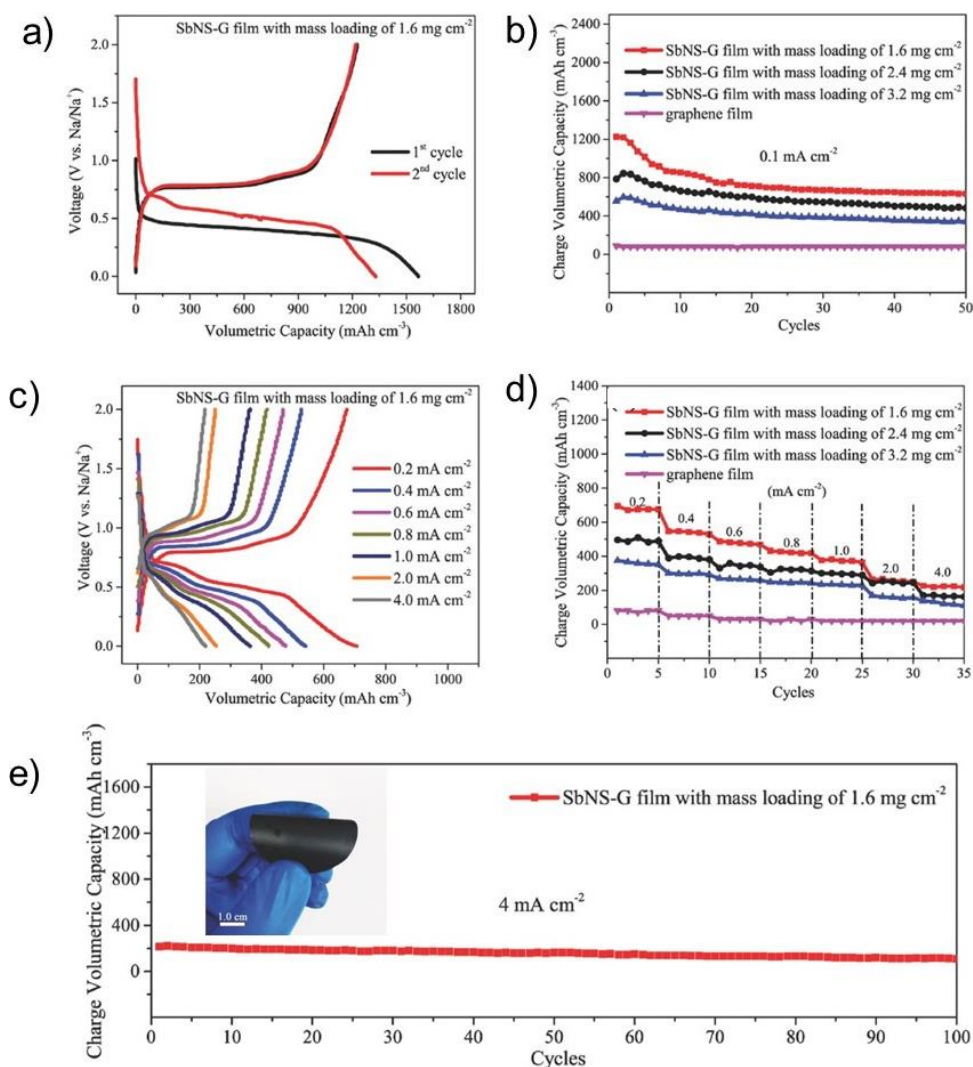
Figure 1.17 a) Charge-discharge curves of the first and second cycle for the SbNS-G composite at a current density of 0.1 mA·cm⁻². b) Comparison of the cyclic performances of the SbNS-G composite film with different mass loads and graphene at a current density of 0.1 mA·cm⁻². c) Charge–discharge curves of SbNS-G film (mass load equal to 1.6 mg cm⁻²) at different current densities from 0.2 to 4.0 mA·cm⁻². d) Rate performances of SbNS-G and graphene films at the same current densities than (c). e) Cyclic performances of SbNS-G film at a fixed current density of 4.0 mA cm⁻² (Inset: image of the SbNS-G composite film). Adapted from reference 82.

Few months later, Tian *et al.* found out that the storage of Na in FLA occurred through sodiation/desodiation mechanism, characterised by a fast insertion of the Na^+ and the following in-plane alloying reaction, due to the small Na-ion diffusion barrier of FLA, 0.14 eV [117]. They performed *in situ* synchrotron X-ray diffraction to further confirm that FLA experienced reversible crystalline phase evolution (Sb ⇋ NaSb ⇋ Na_3Sb)[118]. Figure 1.18a shows this phenomenon, where the (003) and (001) planes corresponding to the peaks in the FLA diffractogram are both shifted to smaller and larger angles during the sodiation/desodiation process. Taking into account that theoretical capacity of antimonene is 660 mAh·g^{-1} and that they obtained an experimentally measured capacity value of 620 mAh·g^{-1}, they conclude that *ca.* 93.9 % of Sb atoms participate in the process for over 150 cycles (Figure 1.18c).

Furthermore, our group firstly reported the possibility of using FLA as an electrode material in supercapacitors[83]. This issue will be discussed deeply in Chapter 5. In summary, these studies show antimonene as a promising material for different kind of energy storage applications.
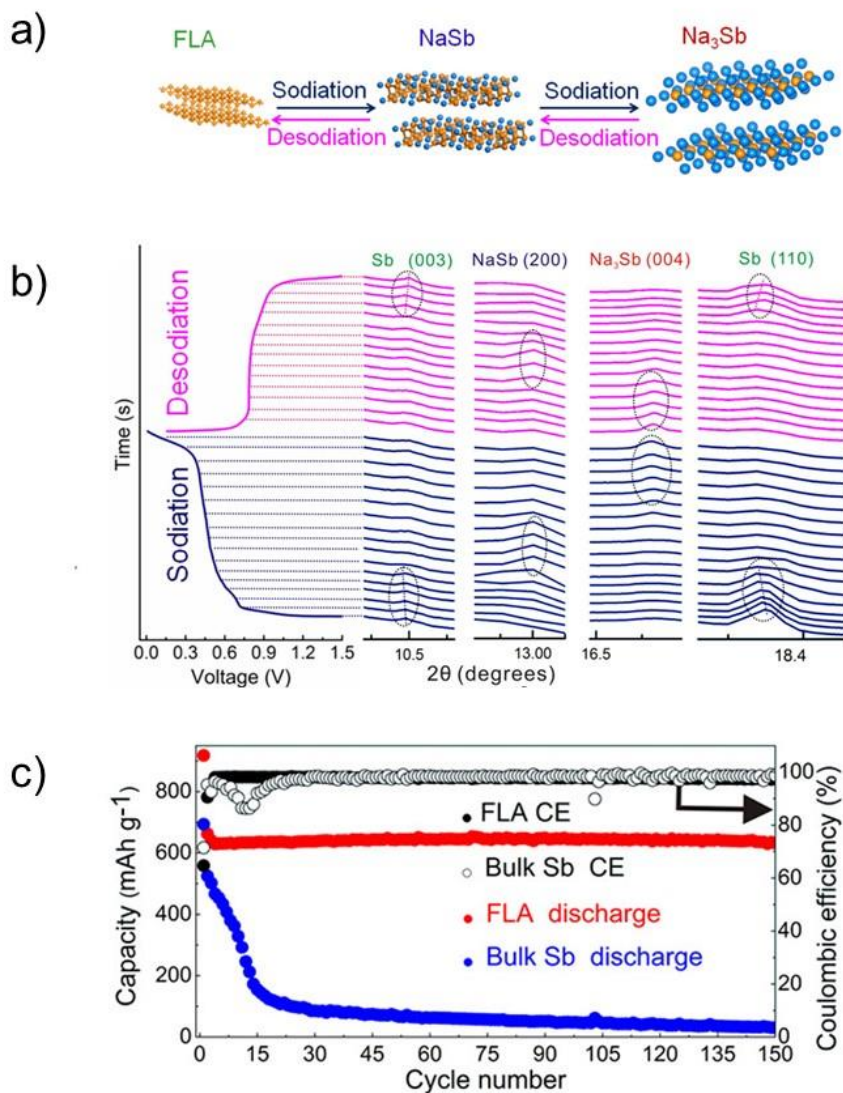
Figure 1.18 a) Schematic diagram of the crystalline phase evolution (Sb ⇆ NaSb ⇆ Na₃Sb) during the sodiation/desodiation process. b) *In situ* X-Ray diffraction pattern evolution of FLA anodes during the third sodiation/desodiation process at a current of 0.2 C c) Long-term cycling performance and Coulombic efficiency (CE) of the FLA and bulk Sb powder at a rate of 0.5 C. Adapted from reference 117.

1.4.6 Cancer therapy

From the existing group of techniques related to cancer therapy, photothermal therapy (PTT) has been recently considered as one of the most promising strategies. The growing interest in this specific therapy is due to the is a slight invasiveness and high efficiency approach[119]. For this reason, is necessary to develop new photothermal agents (PTAs) that improve the biocompatibility and the photothermal conversion efficiency (PTCEs).

Thus, Tao *et al.* have developed a novel PTAs using AMQDs coated with PEG[84]. Regarding the photothermal heating curves, they have observed that there is a clear dependence of the photothermal effect with the concentration (Figure 1.19a). Interestingly, this novel PTA reaches PTCE values of 45.5 % (Figure 1.19b), therefore a significant enhancement in comparison to related PTAs[120]. They have also measured the *in vitro* cytotoxicity of the PEG-coated AMQDs and obtained that samples had a good biocompatibility (Figure 1.19c). Besides, they have also observed that when the concentration of AMQDs increased under near-infrared (NIR) irradiation, the cellular viability decreased, down to 10 % of viable cells at a concentration of 200 mg/mL (Figure 1.19d). Figure 1.19e shows a clear separation between the living cells (green) and dead cells (red), confirming that cancer cells could be killed by using AMQDs as a PTA under NIR irradiation. Additionally, they have performed *in vivo* therapeutic studies on a MCF-7 tumour bearing in a mice, confirming that using NIR irradiation combined with an intratumour injection of PEG-coated AMQDs the tumour is ablated (Figure 1.19f). These results suggest that PTT using PEG-coated AMQDs as PTA, can show an excellent efficacy *in vivo*.
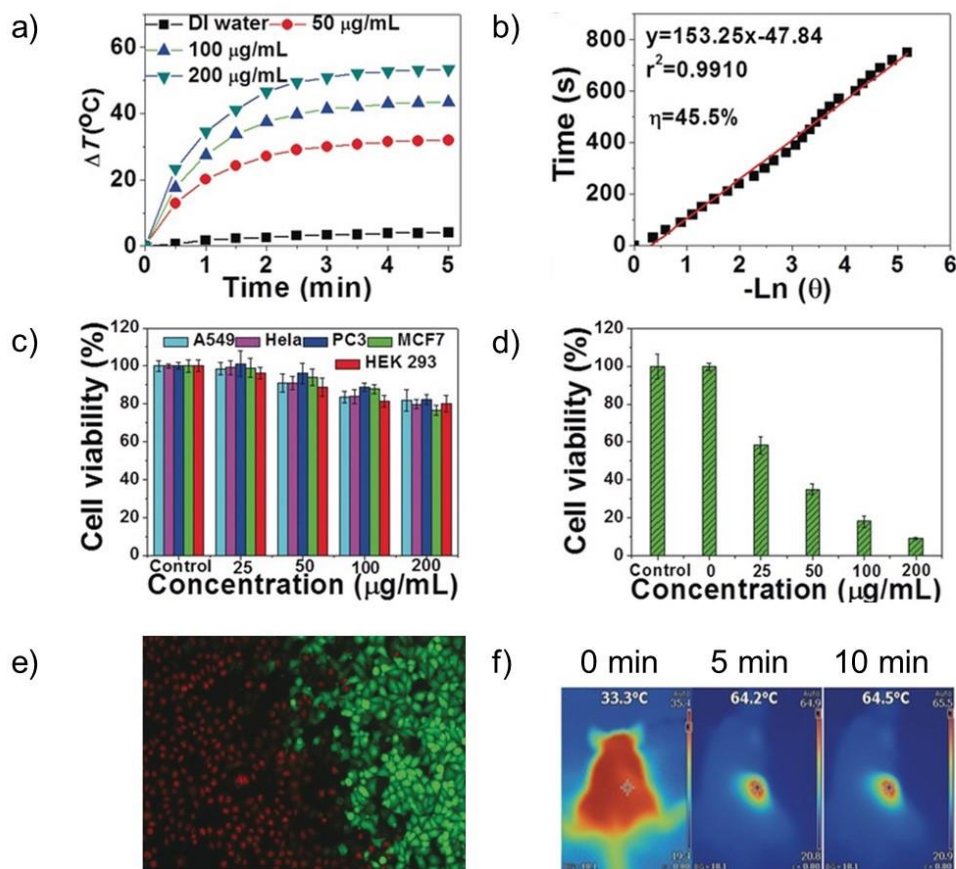
Figure 1.19 a) Time-dependent temperature change under irradiation (808 nm, 2 W/cm^2). b) PTCE of PEG-coated AMQDs. c) Cell viability after incubation with PEG-coated AMQDs. d) Cell viability of MCF-7 cells treated with PEG-coated AMQDs under NIR irradiation (808 nm, 1 W/cm^2) for 5 min. e) Confocal images of live cells (green) and dead cells (red), co-stained MCF- 7 cells after exposure to NIR irradiation (808 nm, 1 W/cm^2). f) IR images of MCF-7 tumour-bearing mice at different times after using PEG-coated AMQDs + NIR; 808 nm, 1 W/cm^2). Adapted from reference 84.

One year later, the same research group developed a photonic drug-delivery platform using FLAs, or as they called them AMNSs[121]. Figure 1.20a shows a scheme of the synthetic procedure for PEGylated AMNSs and its drug loading.

This novel platform has multiple advances compared to those typically used (Figure 1.20b), such as excellent photothermal properties, spatiotemporally controlled drug release activated by near-infrared (NIR) light and moderate acidic pH, high drug-loading capacity, deep tumour penetration by extrinsic and intrinsic stimuli and substantial inhibition of tumour growth with no apparent side effects and potential degradability. In this work, they have also revealed the intracellular fate of AMNSs for the first time, driving to a better understanding of the bio-interactions of 2D materials. This work represents the first study that related antimonene with cancer theranostics, opening up a new field of research where antimonene could be applied.
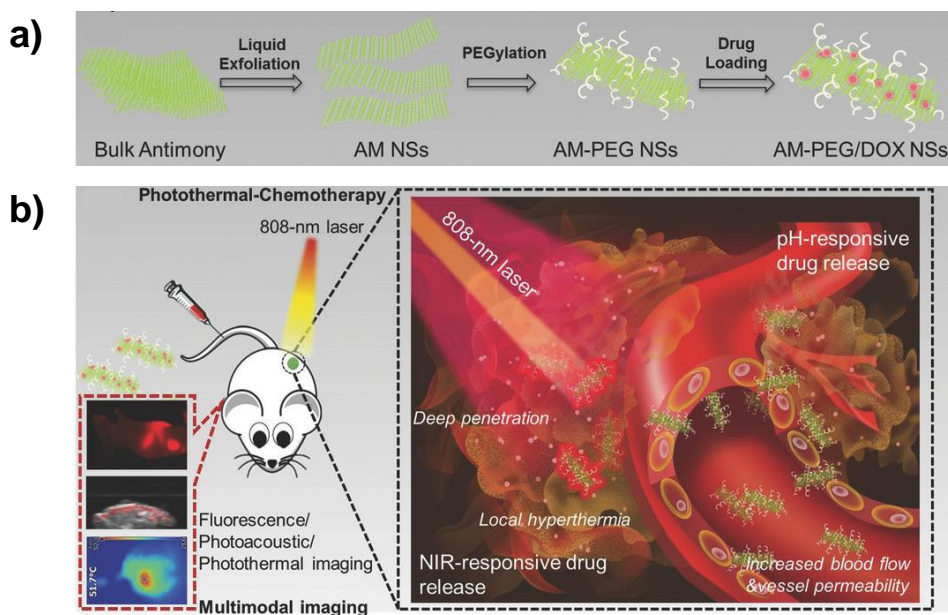

Figure 1.20 a) Schematic representation of the preparation of 2D AM-PEG/DOX NSs. b) Scheme of the systemic administration of AMNSs-PEG/DOX as photonic nanomedicines for multimodal-imaging-guided cancer theranostics. Adapted from reference 121.

1.4.7 Biosensor

The employment of 2D materials for biomedical and environmental application has recently gained interest. Particularly, the fabrication of biosensors based on these materials is the one of the main topics in this field[122]. A revision in the literature confirms that the most studied 2D materials for biosensing applications are: graphene[123], TMDs[124] and BP[125]. Following the growing interest in BP for the fabrication of biosensor, other group-15 semiconductors have attracted interest due to their higher stability under ambient conditions.

The first group that exploring the possibility to use related group-15 elements instead of BP for biosensing was Mayorga-Martínez *et al.* They optimized and implemented a phenol enzymatic biosensor, using exfoliated group-15 semiconductors, including antimonene, as a platform that enhances the electron transfer[126]. Interestingly, among the whole group-15 elements, antimonene showed the best analytical performance in terms of sensitivity, selectivity and reproducibility. They used the shear-exfoliation method (Figure 1.21a) to exfoliate the different materials, and in order to fabricate the device they used a layer-by-layer method (Figure 1.21b). The so-formed biosensor was used to detect phenol through the electroreduction of o-quinone to catechol (Figure 1.21c). This seminal work opened up a new field of research regarding the application of antimonene for biosensing.
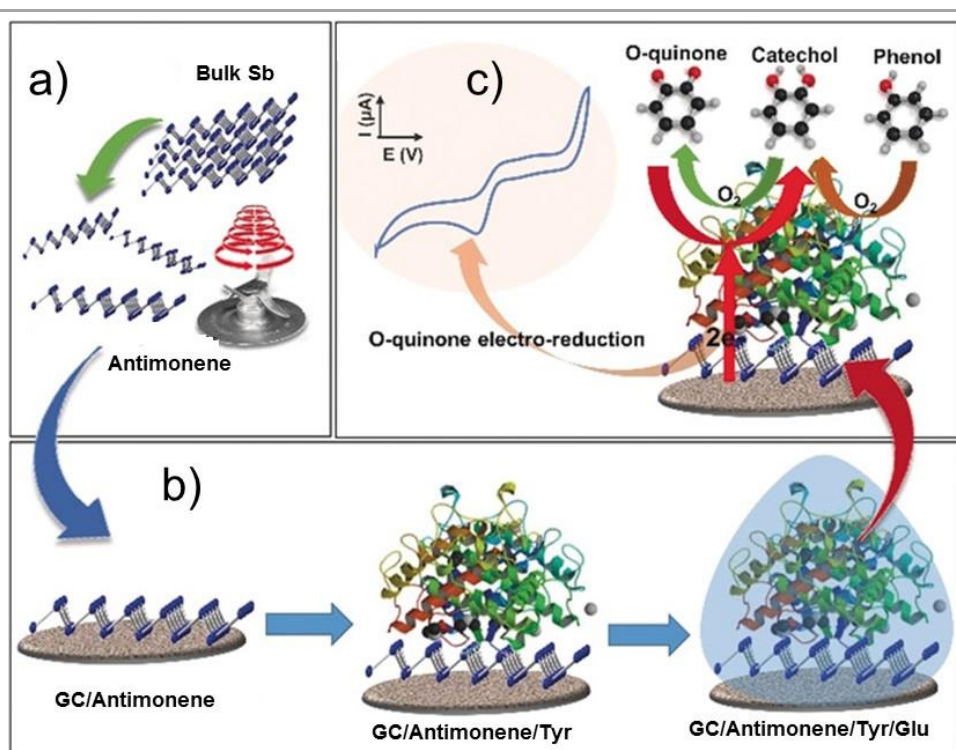
Figure 1.21 a) Schematic representation of antimonene production using shear mixing. b) Layer-by-layer method to fabricate the biosensor drop-casting: antimonene, tyrosinase (Tyr), and glutaraldehyde (Glu) onto a glassy carbon (GC) electrode. c) Chemical mechanism of phenol detection by biosensor. Adapted from reference 126.

Recently, Xue *et al.* have published another study where they build up an antimonene biosensor[127]. They managed to develop a surface plasmon resonance sensor with FLA. The scope of this biosensor is the label-free detection of significant biomarkers such as miRNA-21 and miRNA-155 (Figure 1.22a). They also performed first-principles energetic calculations in order to expose that antimonene has significantly stronger interaction with ssDNA than graphene due to the more delocalized 5s/5p in antimonene. This work has shown that the limit of detection (LOD) experimented an enhancement using this biosensor of 10,000 times compared to existing miRNA sensors (Figure 1.22b).

Interestingly, this technique for detecting nucleic acid with antimonene, holds intriguing potential for the development of multiplexed lab-on-chip platforms, which can be further applied for clinical purposes.
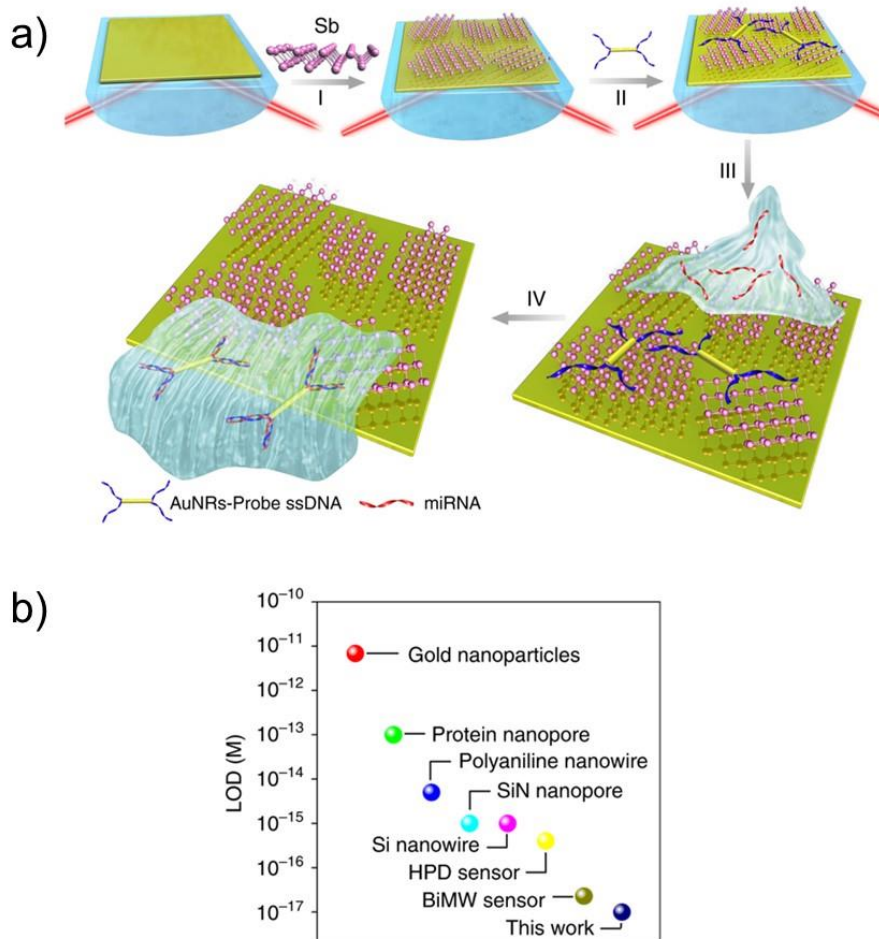
Figure 1.22 a) Scheme of the detection process of antimonene-miRNA hybridization events: I) antimonene is assembled on the surface of Au film, II) AuNR-ssDNAs were adsorbed on antimonene, III) miRNA solution flowed through the surface of antimonene, and paired up to form a double-strand with complementary AuNR-ssDNA, IV) The interaction between miRNA with AuNR-ssDNA results in release of the AuNR-ssDNA from antimonene. b) Comparison of the LOD of the antimonene miRNA SPR sensor with that of state-of-the-art sensors. Adapted from Reference 127.

1.5 Closing remarks

In this introduction chapter, it has summarized the state-of-the-art of a new 2D material of the group-15 elements known as antimonene. A revision of its outstanding properties and applications has been carried out, showing its differences with graphene and other related 2D materials as BP.

Despite antimonene represents the latter element incorporated to the 2D materials, the remarkable properties already found suggest that antimonene or FLA is a perfect candidate for a large variety of applications within different technological areas, such as electronics, optoelectronics, catalysis, electrocatalysis, energy storage, biomedical treatments and (bio)sensing.

In order to overcome the bottleneck that production methods can represent towards real applications, it is necessary to develop high yield production methods to obtain high-quality FLAs. This fact represented the main motivation of this Thesis, the development of industrial scalable methods to obtain high-quality FLA and the concept proofs of its applicability in several areas. Therefore, the next four chapters tries to gain knowledge in these issues.

1.6   References

(1)   Novoselov, K. S. Electric Field Effect in Atomically Thin Carbon Films. *Science* **2004**, *306* (5696), 666–669.

(2)   Geim, A. K.; Novoselov, K. S. The Rise of Graphene. *Nat. Mater.* **2007**, *6* (3), 183–191.

(3)   Hirsch, A. The Era of Carbon Allotropes. *Nat. Mater.* **2010**, *9* (11), 868–871.

(4)   Semenoff, G. W. Condensed-Matter Simulation of a Three-Dimensional Anomaly. *Phys. Rev. Lett.* **1984**, *53* (26), 2449–2452.

(5)   Nicolosi, V.; Chhowalla, M.; Kanatzidis, M. G.; Strano, M. S.; Coleman, J. N. Liquid Exfoliation of Layered Materials. *Science* **2013**, *340* (6139), 1226419–1226419.

(6)   Golberg, D.; Bando, Y.; Huang, Y.; Terao, T.; Mitome, M.; Tang, C.; Zhi, C. Boron Nitride Nanotubes and Nanosheets. *ACS Nano* **2010**, *4* (6), 2979–2993.

(7)   Thomas, A.; Fischer, A.; Goettmann, F.; Antonietti, M.; Müller, J. O.; Schlögl, R.; Carlsson, J. M. Graphitic Carbon Nitride Materials: Variation of Structure and Morphology and Their Use as Metal-Free Catalysts. *J. Mater. Chem.* **2008**, *18* (41), 4893–4908.

(8)   Wang, Q. H.; Kalantar-Zadeh, K.; Kis, A.; Coleman, J. N.; Strano, M. S. Electronics and Optoelectronics of Two-Dimensional Transition Metal Dichalcogenides. *Nat. Nanotechnol.* **2012**, *7* (11), 699–712.

(9)   Coleman, C. C.; Goldwhite, H.; Tikkanen, W. A Review of Intercalation in Heavy Metal Iodides. *Chem. Mater.* **1998**, *10* (10), 2794–2800.

(10)   Afzaal, M.; O'Brien, P. Recent Developments in II-VI and III-VI Semiconductors and Their Applications in Solar Cells. *J. Mater. Chem.* **2006**, *16* (17), 1597–1602.

(11)   Naguib, M.; Mochalin, V. N.; Barsoum, M. W.; Gogotsi, Y. 25th Anniversary Article: MXenes: A New Family of Two-Dimensional Materials. *Adv. Mater.* **2014**, *26* (7), 992–1005.

(12)   Osada, M.; Sasaki, T. Exfoliated Oxide Nanosheets: New Solution to Nanoelectronics. *J. Mater. Chem.* **2009**, *19* (17), 2503–2511.

(13) Ma, R.; Sasaki, T. Nanosheets of Oxides and Hydroxides: Ultimate 2D Charge-Bearing Functional Crystallites. *Adv. Mater.* **2010**, *22* (45), 5082–5104.

(14) Kalidindi, S. B.; Oh, H.; Hirscher, M.; Esken, D.; Wiktor, C.; Turner, S.; Van Tendeloo, G.; Fischer, R. A. Metal@COFs: Covalent Organic Frameworks as Templates for Pd Nanoparticles and Hydrogen Storage Properties of Pd@COF-102 Hybrid Material. *Chem. - A Eur. J.* **2012**, *18* (35), 10848–10856.

(15) Zhang, S.; Guo, S.; Chen, Z.; Wang, Y.; Gao, H.; Gómez-Herrero, J.; Ares, P.; Zamora, F.; Zhu, Z.; Zeng, H. Recent Progress in 2D Group-VA Semiconductors: From Theory to Experiment. *Chem. Soc. Rev.* **2018**, *47* (3), 982–1021.

(16) Allen, M. Honeycomb Carbon -- A Study of Graphene. *Am. Chem. Soc.* **2009**, 184.

(17) Zhang, Y.; Tan, Y. W.; Stormer, H. L.; Kim, P. Experimental Observation of the Quantum Hall Effect and Berry's Phase in Graphene. *Nature* **2005**, *438* (7065), 201–204.

(18) Stoller, M. D.; Park, S.; Zhu, Y.; An, J.; Ruoff, R. S. Graphene-Based Ultracapacitors. *Nano Lett.* **2008**, *8* (10), 3498–3502.

(19) Lee, C.; Wei, X.; Kysar, J. W.; Hone, J. Measurement of the Elastic Properties and Intrinsic Strength of Monolayer Graphene. *Science* **2008**, *321* (5887), 385–388.

(20) Nair, R. R.; Blake, P.; Grigorenko, A. N.; Novoselov, K. S.; Booth, T. J.; Stauber, T.; Peres, N. M. R.; Geim, A. K. Fine Structure Constant Defines Visual Transparency of Graphene. *Science* **2008**, *320* (5881), 1308.

(21) Balandin, A. a; Ghosh, S.; Bao, W.; Calizo, I.; Teweldebrhan, D.; Miao, F.; Lau, C. N. Superior Thermal Conductivity of Single-Layer Graphene 2008. *Nano Lett.* **2008**, *8*, 902–907.

(22) Bonaccorso, F.; Sun, Z.; Hasan, T.; Ferrari, A. C. Graphene Photonics and Optoelectronics. *Nat. Photonics* **2010**, *4* (9), 611–622.

(23) Zheng, Y.; Jiao, Y.; Li, L. H.; Xing, T.; Chen, Y.; Jaroniec, M.; Qiao, S. Z. Toward Design of Synergistically Active Carbon-Based Catalysts for Electrocatalytic Hydrogen Evolution. *ACS Nano* **2014**, *8* (5), 5290–5296.

(24)   Wang, H.; Zhang, C.; Liu, Z.; Wang, L.; Han, P.; Xu, H.; Zhang, K.; Dong, S.; Yao, J.; Cui, G. Nitrogen-Doped Graphene Nanosheets with Excellent Lithium Storage Properties. *J. Mater. Chem.* **2011**, *21* (14), 5430–5434.

(25)   Ferrari, A. C.; Bonaccorso, F.; Fal'ko, V.; Novoselov, K. S.; Roche, S.; Bøggild, P.; Borini, S.; Koppens, F. H. L.; Palermo, V.; Pugno, N.; et al. Science and Technology Roadmap for Graphene, Related Two-Dimensional Crystals, and Hybrid Systems. *Nanoscale* **2015**, *7* (11), 4598–4810.

(26)   Santhosh, C.; Velmurugan, V.; Jacob, G.; Jeong, S. K.; Grace, A. N.; Bhatnagar, A. Role of Nanomaterials in Water Treatment Applications: A Review. *Chem. Eng. J.* **2016**, *306*, 1116–1137.

(27)   He, Q.; Wu, S.; Yin, Z.; Zhang, H. Graphene-Based Electronic Sensors. *Chem. Sci.* **2012**, *3* (6), 1764–1772.

(28)   Yang, K.; Feng, L.; Shi, X.; Liu, Z. Nano-Graphene in Biomedicine: Theranostic Applications. *Chem. Soc. Rev.* **2013**, *42* (2), 530–547.

(29)   Ni, Z.; Liu, Q.; Tang, K.; Zheng, J.; Zhou, J.; Qin, R.; Gao, Z.; Yu, D.; Lu, J. Tunable Bandgap in Silicene and Germanene. *Nano Lett.* **2012**, *12* (1), 113–118.

(30)   Bianco, E.; Butler, S.; Jiang, S.; Restrepo, O. D.; Windl, W.; Goldberger, J. E. Stability and Exfoliation of Germanane: A Germanium Graphane Analogue. *ACS Nano* **2013**, *7* (5), 4414–4421.

(31)   Zhu, F.; Chen, W.; Xu, Y.; Gao, C.; Guan, D.; Liu, C.; Qian, D.; Zhang, S.-C.; Jia, J. Epitaxial Growth of Two-Dimensional Stanene. *Nat. Mater.* **2015**, *14* (10), 1020–1025.

(32)   Feng, B.; Zhang, J.; Liu, R. Y.; Iimori, T.; Lian, C.; Li, H.; Chen, L.; Wu, K.; Meng, S.; Komori, F.; et al. Direct Evidence of Metallic Bands in a Monolayer Boron Sheet. *Phys. Rev. B* **2016**, *94* (4), 2–6.

(33)   Hultgren, R.; Gingrich, N. S.; Warren, B. E. The Atomic Distribution in Red and Black Phosphorus and the Crystal Structure of Black Phosphorus. *J. Chem. Phys.* **1935**, *3* (6), 351–355.

(34)   Bridgman, P. W. Two New Modifications of Phosphorus. *J. Am. Chem. Soc.* **1914**, *36* (7), 1344–1363.

(35)   *Chemistry of Arsenic, Antimony and Bismuth*; Norman, N. C., Ed.; Springer Netherlands, 1998.

(36) Xu, J. H.; Wang, E. G.; Ting, C. S.; Su, W. P. Tight-Binding Theory of the Electronic Structures for Rhombohedral Semimetals. *Phys. Rev. B* **1993**, *48* (23), 17271–17279.

(37) Fei, R.; Yang, L. Strain-Engineering the Anisotropic Electrical Conductance of Few-Layer Black Phosphorus. *Nano Lett.* **2014**, *14* (5), 2884–2889.

(38) Qiao, J.; Kong, X.; Hu, Z. X.; Yang, F.; Ji, W. High-Mobility Transport Anisotropy and Linear Dichroism in Few-Layer Black Phosphorus. *Nat. Commun.* **2014**, *5*, 1–7.

(39) Li, L.; Yu, Y.; Ye, G. J.; Ge, Q.; Ou, X.; Wu, H.; Feng, D.; Chen, X. H.; Zhang, Y. Black Phosphorus Field-Effect Transistors. *Nat. Nanotechnol.* **2014**, *9* (5), 372–377.

(40) Jiang, J. W.; Park, H. S. Mechanical Properties of Single-Layer Black Phosphorus. *J. Phys. D. Appl. Phys.* **2014**, *47* (38), 14–17.

(41) Jiang, J.-W.; Park, H. S. Negative Poisson's Ratio in Single-Layer Black Phosphorus. *Nat. Commun.* **2014**, *5*, 1–7.

(42) Low, T.; Rodin, A. S.; Carvalho, A.; Jiang, Y.; Wang, H.; Xia, F.; Castro Neto, A. H. Tunable Optical Properties of Multilayer Black Phosphorus Thin Films. *Phys. Rev. B* **2014**, *90* (7), 075434.

(43) Qin, G.; Yan, Q. B.; Qin, Z.; Yue, S. Y.; Cui, H. J.; Zheng, Q. R.; Su, G. Hinge-like Structure Induced Unusual Properties of Black Phosphorus and New Strategies to Improve the Thermoelectric Performance. *Sci. Rep.* **2014**, *4*, 1–8.

(44) Huang, L.; Li, Y.; Wei, Z.; Li, J. Strain Induced Piezoelectric Effect in Black Phosphorus and MoS2 van Der Waals Heterostructure. *Sci. Rep.* **2015**, *5* (1), 16448.

(45) Huang, Y.; Qiao, J.; He, K.; Bliznakov, S.; Sutter, E.; Chen, X.; Luo, D.; Meng, F.; Su, D.; Decker, J.; et al. Interaction of Black Phosphorus with Oxygen and Water. *Chem. Mater.* **2016**, *28* (22), 8330–8339.

(46) Abellán, G.; Wild, S.; Lloret, V.; Scheuschner, N.; Gillen, R.; Mundloch, U.; Maultzsch, J.; Varela, M.; Hauke, F.; Hirsch, A. Fundamental Insights into the Degradation and Stabilization of Thin Layer Black Phosphorus. *J. Am. Chem. Soc.* **2017**, *139* (30), 10432–10440.

(47) Zhang, S.; Yan, Z.; Li, Y.; Chen, Z.; Zeng, H. Atomically Thin Arsenene and Antimonene: Semimetal-Semiconductor and Indirect-Direct Band-Gap Transitions. *Angew. Chemie Int. Ed.* **2015**, *54* (10), 3112–3115.

(48) Ares, P.; Aguilar-Galindo, F.; Rodríguez-San-Miguel, D.; Aldave, D. A.; Díaz-Tendero, S.; Alcamí, M.; Martín, F.; Gómez-Herrero, J.; Zamora, F. Mechanical Isolation of Highly Stable Antimonene under Ambient Conditions. *Adv. Mater.* **2016**, 6332–6336.

(49) Gibaja, C.; Rodriguez-San-Miguel, D.; Ares, P.; Gómez-Herrero, J.; Varela, M.; Gillen, R.; Maultzsch, J.; Hauke, F.; Hirsch, A.; Abellán, G.; et al. Few-Layer Antimonene by Liquid-Phase Exfoliation. *Angew. Chemie Int. Ed.* **2016**, *55* (46), 14345–14349.

(50) Tsai, H. S.; Chen, C. W.; Hsiao, C. H.; Ouyang, H.; Liang, J. H. The Advent of Multilayer Antimonene Nanoribbons with Room Temperature Orange Light Emission. *Chem. Commun.* **2016**, *52* (54), 8409–8412.

(51) Ji, J.; Song, X.; Liu, J.; Yan, Z.; Huo, C.; Zhang, S.; Su, M.; Liao, L.; Wang, W.; Ni, Z.; et al. Two-Dimensional Antimonene Single Crystals Grown by van Der Waals Epitaxy. *Nat. Commun.* **2016**, *7* (1), 13352.

(52) Wu, X.; Shao, Y.; Liu, H.; Feng, Z.; Wang, Y. L.; Sun, J. T.; Liu, C.; Wang, J. O.; Liu, Z. L.; Zhu, S. Y.; et al. Epitaxial Growth and Air-Stability of Monolayer Antimonene on PdTe2. *Adv. Mater.* **2017**, *29* (11).

(53) Wang, G.; Pandey, R.; Karna, S. P. Atomically Thin Group v Elemental Films: Theoretical Investigations of Antimonene Allotropes. *ACS Appl. Mater. Interfaces* **2015**, *7* (21), 11490–11496.

(54) Aktürk, O. Ü.; Özçelik, V. O.; Ciraci, S. Single-Layer Crystalline Phases of Antimony: Antimonenes. *Phys. Rev. B* **2015**, *91* (23), 235446.

(55) Wang, Y.; Huang, P.; Ye, M.; Quhe, R.; Pan, Y.; Zhang, H.; Zhong, H.; Shi, J.; Lu, J. Many-Body Effect, Carrier Mobility, and Device Performance of Hexagonal Arsenene and Antimonene. *Chem. Mater.* **2017**, *29* (5), 2191–2201.

(56) Xu, Y.; Peng, B.; Zhang, H.; Shao, H.; Zhang, R.; Zhu, H. First-Principle Calculations of Optical Properties of Monolayer Arsenene and Antimonene Allotropes. *Ann. Phys.* **2017**, *529* (4), 1–9.

(57)   Singh, D.; Gupta, S. K.; Sonvane, Y.; Lukačević, I. Antimonene: A Monolayer Material for Ultraviolet Optical Nanodevices. *J. Mater. Chem. C* **2016**, *4* (26), 6386–6390.

(58)   Wang, S.; Wang, W.; Zhao, G. Thermal Transport Properties of Antimonene: An Ab Initio Study. *Phys. Chem. Chem. Phys.* **2016**, *18* (45), 31217–31222.

(59)   Zhang, T.; Qi, Y.-Y.; Chen, X.-R.; Cai, L.-C. Predicted Low Thermal Conductivities in Antimony Films and the Role of Chemical Functionalization. *Phys. Chem. Chem. Phys.* **2016**, *18* (43), 30061–30067.

(60)   Kripalani, D. R.; Kistanov, A. A.; Cai, Y.; Xue, M.; Zhou, K. Strain Engineering of Antimonene by a First-Principles Study: Mechanical and Electronic Properties. *Phys. Rev. B* **2018**, *98* (8), 1–10.

(61)   Castellanos-Gomez, A.; Vicarelli, L.; Prada, E.; Island, J. O.; Narasimha-Acharya, K. L.; Blanter, S. I.; Groenendijk, D. J.; Buscema, M.; Steele, G. A.; Alvarez, J. V; et al. Isolation and Characterization of Few-Layer Black Phosphorus. *2D Mater.* **2014**, *1* (2), 025001.

(62)   Hong, G.; Zhou, M.; Zhang, R.; Hou, S.; Choi, W.; Woo, Y. S.; Choi, J. Y.; Liu, Z.; Zhang, J. Separation of Metallic and Semiconducting Single-Walled Carbon Nanotube Arrays by "Scotch Tape." *Angew. Chemie - Int. Ed.* **2011**, *50* (30), 6819–6823.

(63)   Coleman, J. N. Liquid-Phase Exfoliation of Nanotubes and Graphene. *Adv. Funct. Mater.* **2009**, *19* (23), 3680–3695.

(64)   Hernandez, Y.; Nicolosi, V.; Lotya, M.; Blighe, F. M.; Sun, Z.; De, S.; McGovern, I. T.; Holland, B.; Byrne, M.; Gun'Ko, Y. K.; et al. High-Yield Production of Graphene by Liquid-Phase Exfoliation of Graphite. *Nat. Nanotechnol.* **2008**, *3* (9), 563–568.

(65)   Khan, U.; O'Neill, A.; Lotya, M.; De, S.; Coleman, J. N. High-Concentration Solvent Exfoliation of Graphene. *Small* **2010**, *6* (7), 864–871.

(66)   Bergin, S. D.; Sun, Z.; Streich, P.; Hamilton, J.; Coleman, J. N. Supporting Information for : New Solvents for Nanotubes : Matching the Dispersability of Surfactants. *J. Phys. Chem. C* **2010**, *3* (C), 1–8.

(67) Hughes, J. M.; Aherne, D.; Coleman, J. N. Generalizing Solubility Parameter Theory to Apply to One- and Two-Dimensional Solutes and to Incorporate Dipolar Interactions. *J. Appl. Polym. Sci.* **2013**, *127* (6), 4483–4491.

(68) Hennrich, F.; Krupke, R.; Arnold, K.; Stütz, J. A. R.; Lebedkin, S.; Koch, T.; Schimmel, T.; Kappes, M. M. The Mechanism of Cavitation-Induced Scission of Single-Walled Carbon Nanotubes. *J. Phys. Chem. B* **2007**, *111* (8), 1932–1937.

(69) Ciesielski, A.; Samorì, P. Graphene via Sonication Assisted Liquid-Phase Exfoliation. *Chem. Soc. Rev.* **2014**, *43* (1), 381–398.

(70) Paton, K. R.; Varrla, E.; Backes, C.; Smith, R. J.; Khan, U.; O'Neill, A.; Boland, C.; Lotya, M.; Istrate, O. M.; King, P.; et al. Scalable Production of Large Quantities of Defect-Free Few-Layer Graphene by Shear Exfoliation in Liquids. *Nat. Mater.* **2014**, *13* (6), 624–630.

(71) Detriche, S.; Zorzini, G.; Colomer, J.-F.; Fonseca, A.; Nagy, J. B. Application of the Hansen Solubility Parameters Theory to Carbon Nanotubes. *J. Nanosci. Nanotechnol.* **2008**, *8* (11), 6082–6092.

(72) Bergin, S. D.; Nicolosi, V.; Streich, P. V.; Giordani, S.; Sun, Z.; Windle, A. H.; Ryan, P.; Niraj, N. P. P.; Wang, Z. T. T.; Carpenter, L.; et al. Towards Solutions of Single-Walled Carbon Nanotubes in Common Solvents. *Adv. Mater.* **2008**, *20* (10), 1876–1881.

(73) Tomba, J. P. Understanding Chemical Equilibrium: The Role of Gas Phases and Mixing Contributions in the Minimum of Free Energy Plots. **2017**.

(74) Miller-Chou, B. A.; Koenig, J. L. A Review of Polymer Dissolution. *Prog. Polym. Sci.* **2003**, *28* (8), 1223–1270.

(75) Hernandez, Y.; Lotya, M.; Rickard, D.; Bergin, S. D.; Coleman, J. N. Measurement of Multicomponent Solubility Parameters for Graphene Facilitates Solvent Discovery. *Langmuir* **2010**, *26* (5), 3208–3213.

(76) Lin, Y.; Williams, T. V.; Connell, J. W. Soluble, Exfoliated Hexagonal Boron Nitride Nanosheets. *J. Phys. Chem. Lett.* **2010**, *1* (1), 277–283.

(77) Coleman, J. N.; Lotya, M.; O'Neill, A.; Bergin, S. D.; King, P. J.; Khan, U.; Young, K.; Gaucher, A.; De, S.; Smith, R. J.; et al. Two-Dimensional Nanosheets Produced by Liquid Exfoliation of Layered Materials. *Science* **2011**, *331* (6017), 568–571.

(78) Hanlon, D.; Backes, C.; Higgins, T. M.; Hughes, M.; O'Neill, A.; King, P.; McEvoy, N.; Duesberg, G. S.; Mendoza Sanchez, B.; Pettersson, H.; et al. Production of Molybdenum Trioxide Nanosheets by Liquid Exfoliation and Their Application in High-Performance Supercapacitors. *Chem. Mater.* **2014**, *26* (4), 1751–1763.

(79) Gao, H.; Hu, Y.; Xuan, Y.; Li, J.; Yang, Y.; Martinez, R. V.; Li, C.; Luo, J.; Qi, M.; Cheng, G. J. Metal-Organic Framework Nanosheets as Building Blocks for Molecular Sieving Membranes. *Science* **2014**.

(80) Berlanga, I.; Ruiz-González, M. L.; González-Calbet, J. M.; Fierro, J. L. G.; Mas-Ballesté, R.; Zamora, F. Delamination of Layered Covalent Organic Frameworks. *Small* **2011**, *7* (9), 1207–1211.

(81) Brent, J. R.; Savjani, N.; Lewis, E. A.; Haigh, S. J.; Lewis, D. J.; O'Brien, P. Production of Few-Layer Phosphorene by Liquid Exfoliation of Black Phosphorus. *Chem. Commun.* **2014**, *50* (87), 13338–13341.

(82) Gu, J.; Du, Z.; Zhang, C.; Ma, J.; Li, B.; Yang, S. Liquid-Phase Exfoliated Metallic Antimony Nanosheets toward High Volumetric Sodium Storage. *Adv. Energy Mater.* **2017**, *7* (17), 1–8.

(83) Martínez-Periñán, E.; Down, M. P.; Gibaja, C.; Lorenzo, E.; Zamora, F.; Banks, C. E. Antimonene: A Novel 2D Nanomaterial for Supercapacitor Applications. *Adv. Energy Mater.* **2018**, *8* (11), 1702606.

(84) Tao, W.; Ji, X.; Xu, X.; Islam, M. A.; Li, Z.; Chen, S.; Saw, P. E.; Zhang, H.; Bharwani, Z.; Guo, Z.; et al. Antimonene Quantum Dots: Synthesis and Application as Near-Infrared Photothermal Agents for Effective Cancer Therapy. *Angew. Chemie - Int. Ed.* **2017**, *56* (39), 11896–11900.

(85) Lu, L.; Tang, X.; Cao, R.; Wu, L.; Li, Z.; Jing, G.; Dong, B.; Lu, S.; Li, Y.; Xiang, Y.; et al. Broadband Nonlinear Optical Response in Few-Layer Antimonene and Antimonene Quantum Dots: A Promising Optical Kerr Media with Enhanced Stability. *Adv. Opt. Mater.* **2017**, *5* (17), 1–9.

(86) Gusmão, R.; Sofer, Z.; Bouša, D.; Pumera, M. Pnictogen (As, Sb, Bi) Nanosheets for Electrochemical Applications Are Produced by Shear Exfoliation Using Kitchen Blenders. *Angew. Chemie - Int. Ed.* **2017**, *56* (46), 14417–14422.

(87) Yang, W.; Chen, G.; Shi, Z.; Liu, C. C.; Zhang, L.; Xie, G.; Cheng, M.; Wang, D.; Yang, R.; Shi, D.; et al. Epitaxial Growth of Single-Domain Graphene on Hexagonal Boron Nitride. *Nat. Mater.* **2013**, *12* (9), 792–797.

(88) Pan, M.; Zhu, Y. X.; Wu, K.; Chen, L.; Hou, Y. J.; Yin, S. Y.; Wang, H. P.; Fan, Y. N.; Su, C. Y. Epitaxial Growth of Hetero-Ln-MOF Hierarchical Single Crystals for Domain- and Orientation-Controlled Multicolor Luminescence 3D Coding Capability. *Angew. Chemie - Int. Ed.* **2017**, *56* (46), 14582–14586.

(89) Li, C.; Zhang, S.; Zhang, B.; Liu, J.; Zhang, W.; Solovev, A. A.; Tang, R.; Bao, F.; Yu, J.; Zhang, Q.; et al. Local-Curvature-Controlled Non-Epitaxial Growth of Hierarchical Nanostructures. *Angew. Chemie - Int. Ed.* **2018**, *57* (14), 3772–3776.

(90) Yang, T.; Zheng, B.; Wang, Z.; Xu, T.; Pan, C.; Zou, J.; Zhang, X.; Qi, Z.; Liu, H.; Feng, Y.; et al. Van Der Waals Epitaxial Growth and Optoelectronics of Large-Scale WSe2/SnS2vertical Bilayer p-n Junctions. *Nat. Commun.* **2017**, *8* (1), 1–9.

(91) Lei, T.; Jin, K.-H.; Zhang, N.; Zhao, J.-L.; Liu, C.; Li, W.-J.; Wang, J.-O.; Wu, R.; Qian, H.-J.; Liu, F.; et al. Electronic Structure Evolution of Single Bilayer Bi(1 1 1) Film on 3D Topological Insulator Bi 2 Se x Te 3− x Surfaces. *J. Phys. Condens. Matter* **2016**, *28* (25), 255501.

(92) Fortin-Deschênes, M.; Waller, O.; Menteş, T. O.; Locatelli, A.; Mukherjee, S.; Genuzio, F.; Levesque, P. L.; Hébert, A.; Martel, R.; Moutanabbir, O. Synthesis of Antimonene on Germanium. *Nano Lett.* **2017**, *17* (8), 4970–4975.

(93) Shao, Y.; Liu, Z. L.; Cheng, C.; Wu, X.; Liu, H.; Liu, C.; Wang, J. O.; Zhu, S. Y.; Wang, Y. Q.; Shi, D. X.; et al. Epitaxial Growth of Flat Antimonene Monolayer: A New Honeycomb Analogue of Graphene. *Nano Lett.* **2018**, *18* (3), 2133–2139.

(94) Su, C. Y.; Lu, A. Y.; Xu, Y.; Chen, F. R.; Khlobystov, A. N.; Li, L. J. High-Quality Thin Graphene Films from Fast Electrochemical Exfoliation. *ACS Nano* **2011**, *5* (3), 2332–2339.

(95) Liu, N.; Kim, P.; Kim, J. H.; Ye, J. H.; Kim, S.; Lee, C. J. Large-Area Atomically Thin MoS2nanosheets Prepared Using Electrochemical Exfoliation. *ACS Nano* **2014**, *8* (7), 6902–6910.

(96)   Shimizu, M.; Usui, H.; Yamane, K.; Sakata, T.; Nokami, T.; Itoh, T.; Sakaguchi, H. Electrochemical Na-Insertion/Extraction Properties of Phosphorus Electrodes in Ionic Liquid Electrolytes. *Int. J. Electrochem. Sci.* **2015**, *10* (12), 10132–10144.

(97)   Yu, P.; Lowe, S. E.; Simon, G. P.; Zhong, Y. L. Electrochemical Exfoliation of Graphite and Production of Functional Graphene. *Curr. Opin. Colloid Interface Sci.* **2015**, *20* (5–6), 329–338.

(98)   Zhang, S.; Yan, Z.; Li, Y.; Chen, Z.; Zeng, H. Atomically Thin Arsenene and Antimonene: Semimetal-Semiconductor and Indirect-Direct Band-Gap Transitions. *Angew. Chemie - Int. Ed.* **2015**, *54* (10), 3112–3115.

(99)   Pizzi, G.; Gibertini, M.; Dib, E.; Marzari, N.; Iannaccone, G.; Fiori, G. Performance of Arsenene and Antimonene Double-Gate MOSFETs from First Principles. *Nat. Commun.* **2016**, *7*, 1–9.

(100) Chang, J. Novel Antimonene Tunneling Field-Effect Transistors Using an Abrupt Transition from Semiconductor to Metal in Monolayer and Multilayer Antimonene Heterostructures. *Nanoscale* **2018**, *10* (28), 13652–13660.

(101) Sun, X.; Song, Z.; Liu, S.; Wang, Y.; Li, Y.; Wang, W.; Lu, J. Sub-5 Nm Monolayer Arsenene and Antimonene Transistors. *ACS Appl. Mater. Interfaces* **2018**, *10* (26), 22363–22371.

(102) Baugher, B. W. H.; Churchill, H. O. H.; Yang, Y.; Jarillo-Herrero, P. Optoelectronic Devices Based on Electrically Tunable P-n Diodes in a Monolayer Dichalcogenide. *Nat. Nanotechnol.* **2014**, *9* (4), 262–267.

(103) Zhang, S.; Zhou, W.; Ma, Y.; Ji, J.; Cai, B.; Yang, S. A.; Zhu, Z.; Chen, Z.; Zeng, H. Antimonene Oxides: Emerging Tunable Direct Bandgap Semiconductor and Novel Topological Insulator. *Nano Lett.* **2017**, *17* (6), 3434–3440.

(104) Xie, M.; Zhang, S.; Cai, B.; Gu, Y.; Liu, X.; Kan, E.; Zeng, H. Van Der Waals Bilayer Antimonene: A Promising Thermophotovoltaic Cell Material with 31% Energy Conversion Efficiency. *Nano Energy* **2017**, *38* (December), 561–568.

(105) Wang, X.; He, J.; Zhou, B.; Zhang, Y.; Wu, J.; Hu, R.; Liu, L.; Song, J.; Qu, J. Bandgap-Tunable Preparation of Smooth and Large Two-Dimensional Antimonene. *Angew. Chemie - Int. Ed.* **2018**, *57* (28), 8668–8673.

(106) Zhang, F.; He, J.; Xiang, Y.; Zheng, K.; Xue, B.; Ye, S.; Peng, X.; Hao, Y.; Lian, J.; Zeng, P.; et al. Semimetal-Semiconductor Transitions for Monolayer Antimonene Nanosheets and Their Application in Perovskite Solar Cells. *Adv. Mater.* **2018**, *1803244*, 1803244.

(107) Song, Y.; Liang, Z.; Jiang, X.; Chen, Y.; Li, Z.; Lu, L.; Ge, Y.; Wang, K.; Zheng, J.; Lu, S.; et al. Few-Layer Antimonene Decorated Microfiber: Ultra-Short Pulse Generation and All-Optical Thresholding with Enhanced Long Term Stability. *2D Mater.* **2017**, *4* (4).

(108) Song, Y.; Chen, Y.; Jiang, X.; Liang, W.; Wang, K.; Liang, Z.; Ge, Y.; Zhang, F.; Wu, L.; Zheng, J.; et al. Nonlinear Few-Layer Antimonene-Based All-Optical Signal Processing: Ultrafast Optical Switching and High-Speed Wavelength Conversion. *Adv. Opt. Mater.* **2018**, *6* (13), 1–10.

(109) Miao, P.; Zhang, Z.; Sun, J.; Walasik, W.; Longhi, S.; Litchinitser, N. M.; Feng, L. Nanostructured Transition Metal Dichalcogenide Electrocatalysts for CO2 Reduction in Ionic Liquid. *Science* **2016**, *353* (6298), 467–470.

(110) Medina-Ramos, J.; Pupillo, R. C.; Keane, T. P.; Dimeglio, J. L.; Rosenthal, J. Efficient Conversion of CO_2 to CO Using Tin and Other Inexpensive and Easily Prepared Post-Transition Metal Catalysts. *J. Am. Chem. Soc.* **2015**, *137* (15), 5021–5027.

(111) Li, F.; Xue, M.; Li, J.; Ma, X.; Chen, L.; Zhang, X.; MacFarlane, D. R.; Zhang, J. Unlocking the Electrocatalytic Activity of Antimony for CO 2 Reduction by Two-Dimensional Engineering of the Bulk Material. *Angew. Chemie Int. Ed.* **2017**, *56* (46), 14718–14722.

(112) Sengupta, A.; Frauenheim, T. Lithium and Sodium Adsorption Properties of Monolayer Antimonene. *Mater. Today Energy* **2017**, *5*, 347–354.

(113) Lloret, V.; Rivero-Crespo, M. Á.; Vidal-Moya, J. A.; Wild, S.; Doménech-Carbó, A.; Heller, B. S. J.; Shin, S.; Steinrück, H.; Maier, F.; Hauke, F.; et al. Few Layer 2D Pnictogens Catalyze the Alkylation of Soft Nucleophiles with Esters. *Nat. Commun.* **2019**, *10* (1), 509.

(114) Dunn, B.; Kamath, H.; Tarascon, J. M. Electrical Energy Storage for the Grid: A Battery of Choices. *Science* **2011**, *334* (6058), 928–935.

(115) Wang, L.; Lu, Y.; Liu, J.; Xu, M.; Cheng, J.; Zhang, D.; Goodenough, J. B. A Superior Low-Cost Cathode for a Na-Ion Battery. *Angew. Chemie - Int. Ed.* **2013**, *52* (7), 1964–1967.

(116) Li, Z.; Tan, X.; Li, P.; Kalisvaart, P.; Janish, M. T.; Mook, W. M.; Luber, E. J.; Jungjohann, K. L.; Carter, C. B.; Mitlin, D. Coupling in Situ TEM and Ex Situ Analysis to Understand Heterogeneous Sodiation of Antimony. *Nano Lett.* **2015**, *15* (10), 6339–6347.

(117) Tian, W.; Zhang, S.; Huo, C.; Zhu, D.; Li, Q.; Wang, L.; Ren, X.; Xie, L.; Guo, S.; Chu, P. K.; et al. Few-Layer Antimonene: Anisotropic Expansion and Reversible Crystalline-Phase Evolution Enable Large-Capacity and Long-Life Na-Ion Batteries. *ACS Nano* **2018**, *12* (2), 1887–1893.

(118) Kong, B.; Zu, L.; Peng, C.; Zhang, Y.; Zhang, W.; Tang, J.; Selomulya, C.; Zhang, L.; Chen, H.; Wang, Y.; et al. Direct Superassemblies of Freestanding Metal-Carbon Frameworks Featuring Reversible Crystalline-Phase Transformation for Electrochemical Sodium Storage. *J. Am. Chem. Soc.* **2016**, *138* (50), 16533–16541.

(119) Shi, J.; Kantoff, P. W.; Wooster, R.; Farokhzad, O. C. Cancer Nanomedicine: Progress, Challenges and Opportunities. *Nat. Rev. Cancer* **2017**, *17* (1), 20–37.

(120) Sun, Z.; Xie, H.; Tang, S.; Yu, X. F.; Guo, Z.; Shao, J.; Zhang, H.; Huang, H.; Wang, H.; Chu, P. K. Ultrasmall Black Phosphorus Quantum Dots: Synthesis and Use as Photothermal Agents. *Angew. Chemie - Int. Ed.* **2015**, *54* (39), 11526–11530.

(121) Tao, W.; Ji, X.; Zhu, X.; Li, L.; Wang, J.; Zhang, Y.; Saw, P. E.; Li, W.; Kong, N.; Islam, M. A.; et al. Two-Dimensional Antimonene-Based Photonic Nanomedicine for Cancer Theranostics. *Adv. Mater.* **2018**, *1802061*, 1802061.

(122) Chen, Y.; Tan, C.; Zhang, H.; Wang, L. Two-Dimensional Graphene Analogues for Biomedical Applications. *Chem. Soc. Rev.* **2015**, *44* (9), 2681–2701.

(123) Kurapati, R.; Kostarelos, K.; Prato, M.; Bianco, A. Biomedical Uses for 2D Materials Beyond Graphene: Current Advances and Challenges Ahead. *Adv. Mater.* **2016**, 6052–6074.

(124) Toh, R. J.; Mayorga-Martinez, C. C.; Sofer, Z.; Pumera, M. 1T-Phase WS2 Protein-Based Biosensor. *Adv. Funct. Mater.* **2017**, *27* (5), 1–8.

(125) Gusmão, R.; Sofer, Z.; Pumera, M. Black Phosphorus Rediscovered: From Bulk Material to Monolayers. *Angew. Chemie - Int. Ed.* **2017**, *56* (28), 8052–8072.

(126) Pumera, M. Pnictogens Based Biosensor: Phosphorene, Arsenene, Antimonene, and Bismuthene. *Angew. Chemie Int. Ed.* **2018**, 134–138.

(127) Xue, T.; Liang, W.; Li, Y.; Sun, Y.; Xiang, Y.; Zhang, Y.; Dai, Z.; Duo, Y.; Wu, L.; Qi, K.; et al. Ultrasensitive Detection of MiRNA with an Antimonene-Based Surface Plasmon Resonance Sensor. *Nat. Commun.* **2019**, *10* (1), 28.

Chapter 2: Few-Layer Antimonene obtained by Liquid-Phase Exfoliation
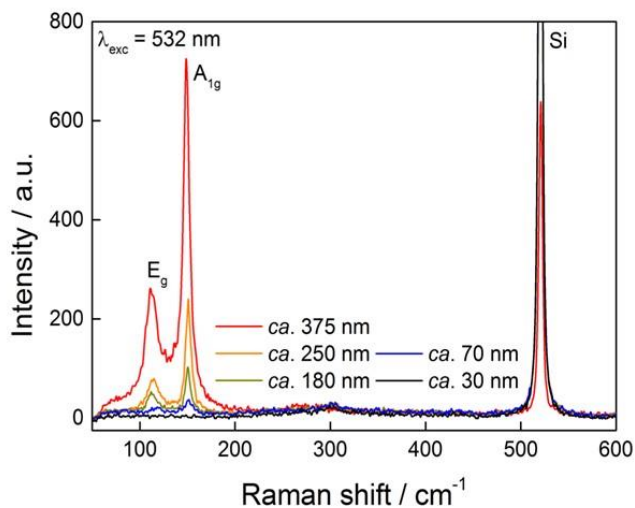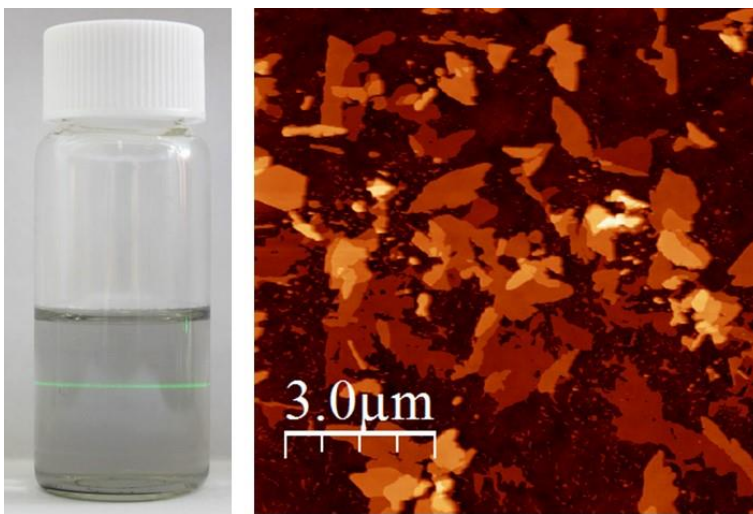
Chapter 2: Few-Layer Antimonene obtained by Liquid-Phase Exfoliation

2.1. Introduction

The production methods of 2D nanomaterials with specific and desired features, such as chemical composition and morphology, are of singular importance for the further study of their properties, as well as for the exploration of potential applications.

LPE technique has become one of the most promising methods for the production of 2D nanosheets in large quantities. The versatility of this method has been proved by the variety of 2D materials obtained using it. Besides, the resulting suspensions can be fully characterized to analyse the properties of the suspended nanosheets[1].

This technique is a top-down route to obtain single-layer and few-layer nanosheets by means of sonication[2] or shearing[3] layered crystals in appropriate liquid media, such as organic solvents[4], surfactants[5], stabilizers or polymer solutions[6]. In all the cases, the liquid media reduce the net amount of energy necessary to exfoliate the crystals into nanosheets, and stabilise them against aggregation, by means of its interaction with the surface of the nanosheets.

In this chapter, it is reported the first method to produce FLA suspensions using LPE techniques, in a process that is assisted by sonication but does not require the addition of any surfactant.

2.2. Results and Discussion

In this work, is demonstrated the exfoliation of bulk antimony crystals (see Figure 2.1a) in a 4:1 mixture of 2-propanol/H_2O without the addition of any surfactants, to produce stable suspensions containing micrometre large FLAs (Figure 2.1b). The exfoliation procedure was carried out using tip sonication of ground antimony crystals for 40 min at 400 W and 24 kHz, that gives a light grey suspension showing Faraday-Tindall effect (Figure 2.1c). To remove the unexfoliated antimony, centrifugation was applied for 3 min at 3000 rpm (746 g), giving a final concentration of FLA nanosheets in suspension of 1.74×10^{-3} gL^{-1}, determined by atomic absorption spectroscopy (AAS).
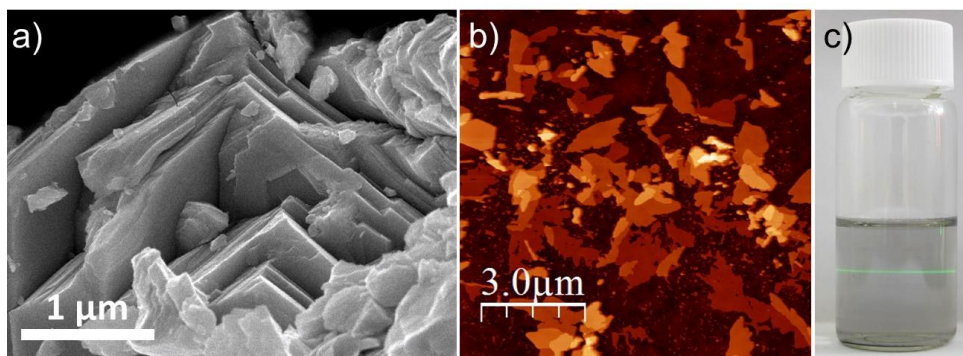

Figure 2.1 a) SEM image of a layered antimony crystal. b) Topographic AFM image of several FLA nanosheets drop-casted onto SiO_2 showing micrometer lateral dimensions. c) Image of a light grey suspension of exfoliated antimonene showing the Faraday–Tyndall effect.

It is also worth to highlight that the procedure described is the result of a previous optimization of the experimental LPE parameters involved, such as: liquid media, initial concentration and sonication time (see Appendix A2.3.1 for further information, page 197).

Finally, it was observed that the most suitable conditions to exfoliate bulk antimony crystals were 40 minutes, an initial concentration of 0.1 g/L and as liquid media a 4:1 mixture of 2-propanol/H_2O.

FLAs were firstly characterized by AFM in order to know their morphology and topography. Figure 2.2a shows a typical topographic image of FLAs isolated onto a SiO_2 substrate. From this image it can be easily extracted that the system is quite heterogeneous, speaking about the morphology of the nanosheets. Even though the shape of FLAs resembles similar, there are not two equal flakes. The statistic treatment gives a height histogram like the one in Figure 2.2b, where it can be extracted a periodic step height multiple of about 4 nm in the nanosheets.

It is well stablished that the apparent AFM height of a nanosheet obtained by LPE, can be overestimated because of residual solvent[7] or due to other effects such as capillary and adhesion forces[8]. For this reason, the real height of the flakes could be lower. On the other hand, the overall lateral size of the isolated nanosheets was greater than 1–3 μm^2.

The morphological features of the FLAs were further confirmed by TEM measurements, see Figure 2.2c and Figure 2.2d. The FLAs depicted in these images have the same morphology observed in AFM measurements.
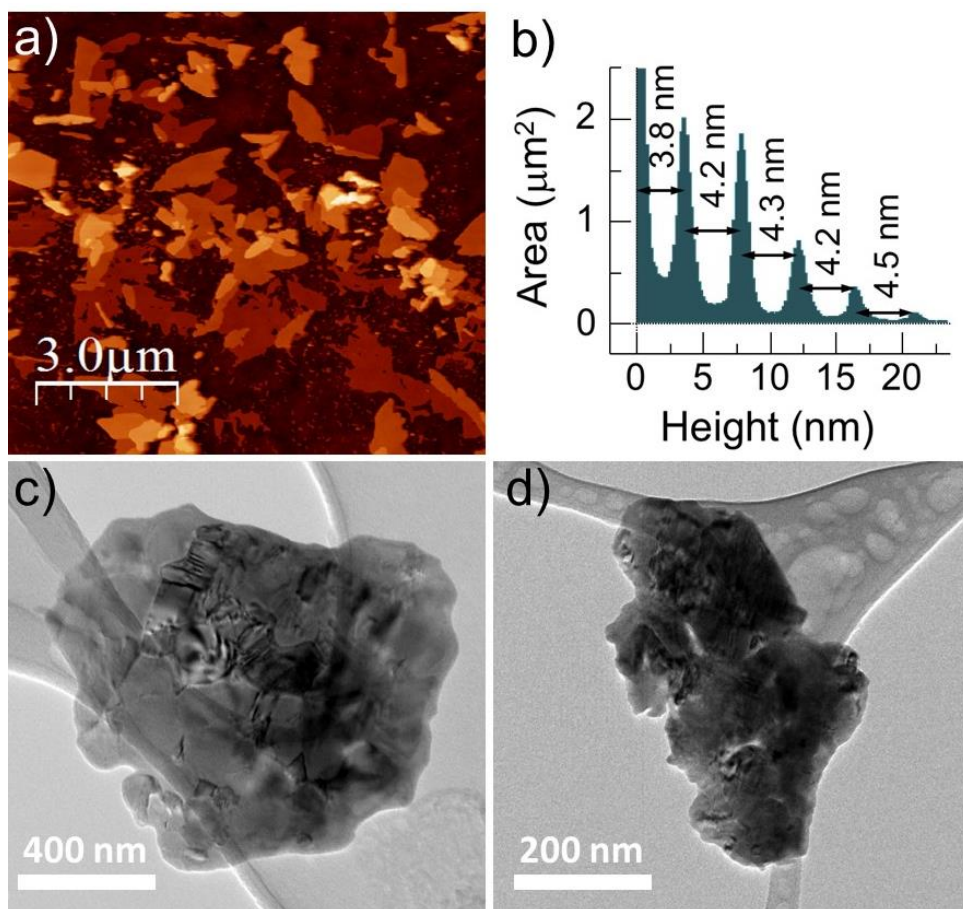
Figure 2.2 a) Topographic AFM image of several FLAs drop-casted onto SiO_2 showing micrometer lateral dimensions. b) Height histogram of the image in (a) where the different thicknesses of the terraces can be readily seen. For the sake of clarity, the substrate peak has been cut to 2.5 μm^2. The constant minimum thickness of about 4 nm can be easily observed. c), d) TEM images of different FLAs.

To corroborate the atomic structure of the obtained FLAs, a high-resolution AFM topographic image of an isolated flake was taken (Figure 2.3a). The flake exhibits in its lowest terrace an atomic periodicity in line with that expected for the β-phase of antimony (Figure 2.3c).

Besides, the Fourier transform was also obtained from the AFM topographic image, to confirm the atomic structure of the β-phase of antimony (Figure 2.3d). It revealed a hexagonal symmetry as expected for this phase of antimony, indicating an excellent crystal quality.
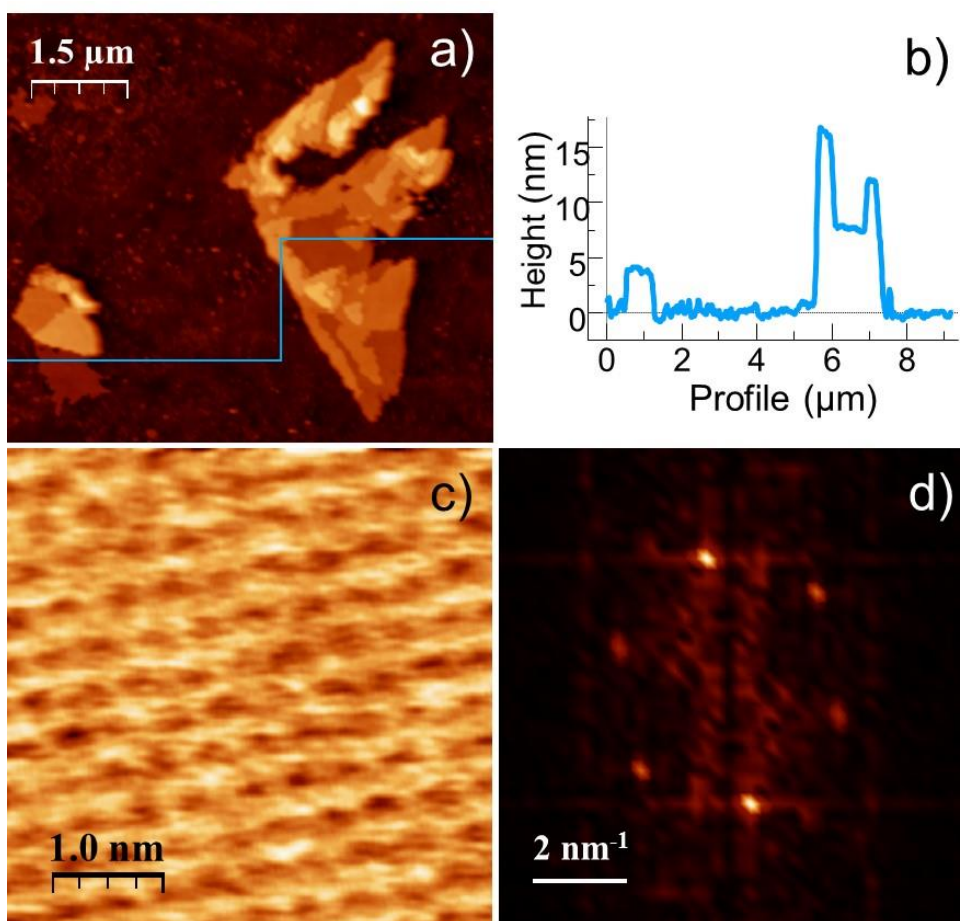

Figure 2.3 a) Topographic AFM image of two FLAs with different height terraces. b) Height profile along the blue line of the image in (a) where the different thicknesses of the terraces can be seen. The minimum step height is about 4.0 nm. c) Atomic resolution AFM image showing the atom periodicity of right flake in (a). d) Fast Fourier transform (FFT) image taken from (c), showing the agreement with a hexagonal lattice as expected for $\boldsymbol{\beta}$-antimony.

Antimonene was supposed to be stable under ambient conditions, to confirm this fact, an AFM measurement is repeated after exposing the same flake under ambient conditions for more than two weeks (Figure A2.2, page 200). Results further confirm the stability under normal conditions of the exfoliated FLAs. These results are in good agreement with other real-space measurements done with atomic resolution. In Figure 2.4 there is a TEM image of a FLA nanosheet, electron diffraction pattern is obtained from a magnification spot of this thin flake, confirming the hexagonal symmetry.
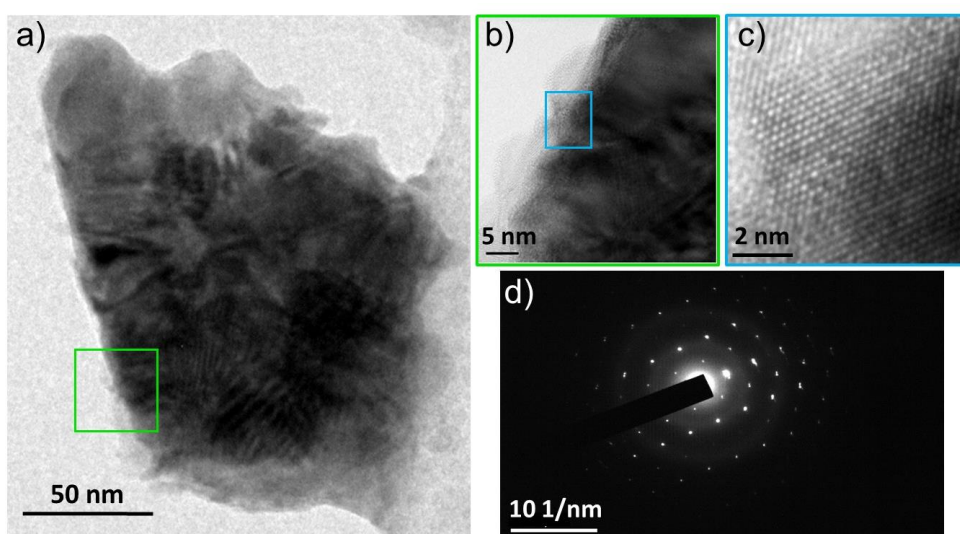

Figure 2.4 a) TEM image of a FLA nanosheet. b) Magnification of the green area in (a). c) Digital magnification of the blue region in (b). d) Electron diffraction pattern, showing the hexagonal symmetry.

The local structure and the chemical composition of FLAs are investigated using aberration-corrected scanning transmission electron microscopy (STEM) merged with electron energy loss spectroscopy (EELS).

Figure 2.5a shows a low-magnification high angle annular dark field (HAADF) image of an isolated FLA nanosheet (top left) along the [0 1 -2] direction with an atomic-resolution image of the crystal structure, both obtained at an acceleration voltage of 80 kV to prevent beam-induced damage. The structure shown in the image, agrees with the previous atomic resolution AFM measurements of the β-phase of antimony.

These results also show that the exfoliated FLAs were crystalline, and no major atomic defects were observed. To prove the chemical composition of the samples, compositional maps are obtained from the EELS spectra including the C K, Ca $L_{2,3}$, O K, and Sb $M_{4,5}$ absorption edges (Figure 2.5b). The maps show little chemical heterogeneity within the FLAs, the edges of the flake appear to be somewhat damaged. In Figure 2.5b it can be observed a homogenously distributed Sb signal all around the analysed area of the flake. However, it can also be seen that a certain degree of contamination is present considering the significant C signal within a few nanometres of the sample edge. Likewise, traces of O and Ca are detected within tens of nanometres from the edges, which is very likely due to the same reason (the presence of Ca is probably because of solvent contamination).
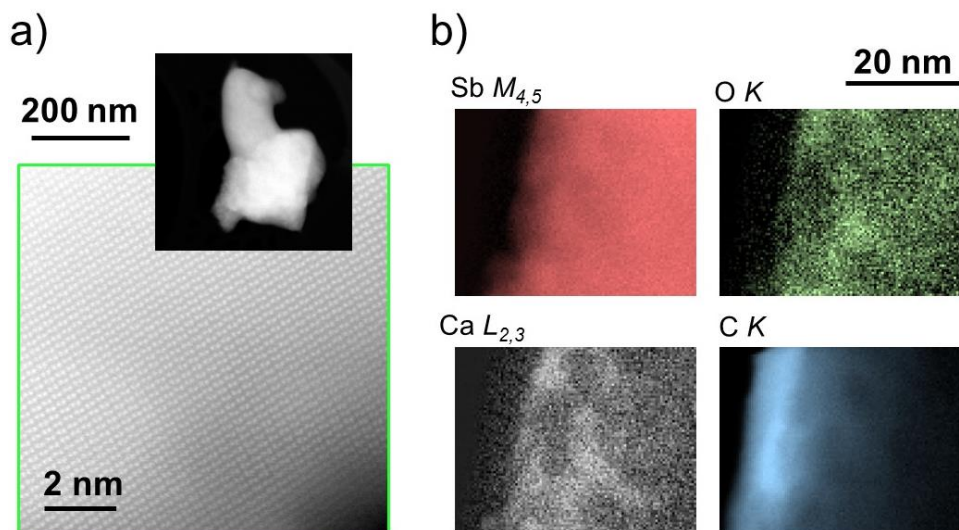
Figure 2.5 a) Low-magnification HAADF image of a FLAs (top left) along with an atomic-resolution image (image taken along the [0 1 -2] direction). b) Two-dimensional EELS maps acquired near the edge of the flake, showing the signals below the Sb $M_{4,5}$ (red) and O K (green) absorption edges.

Nowadays one of the most adequate techniques to characterize 2D materials is Raman spectroscopy. Bulk antimony present a Raman spectrum that exhibits two distinguished phonon peaks: A_{1g} mode at 149.8 cm^{-1} and E_g mode at 110 cm^{-1}, when excited with a green laser (λ = 532 nm)[9].

A correlation between the AFM images of the FLAs in a polydisperse sample and scanning Raman microscopy (SRM) is carried out to get more insights about the samples. The results show that the Raman signal of FLA is extremely dependent with the thickness of the nanosheets. It was impossible to find any Raman signal in FLAs with an apparent thickness below 30 nm (Figure 2.6). These results are in good agreement with those reported previously from micromechanically exfoliated flakes of antimony[10].

Figure 2.6 shows the decrease on the intensity of Raman signal when single-point spectra are acquired in nanosheets with a decreasing thickness.
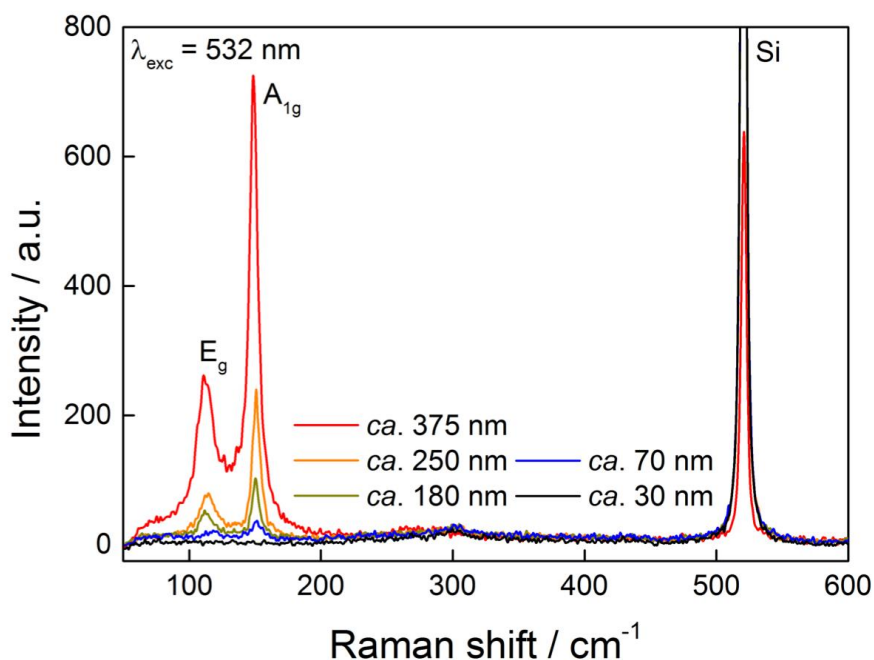

Figure 2.6 Single-point spectra of FLA measured at different thicknesses.

In order to study the influence of the laser excitation wavelength on the samples, a thin antimony flake (*ca.* 10 nm), obtained by micromechanical exfoliation, was measured with different lasers wavelengths (Figure 2.7) obtaining the same results as previous for thin flakes, *i.e.* no Raman signal.
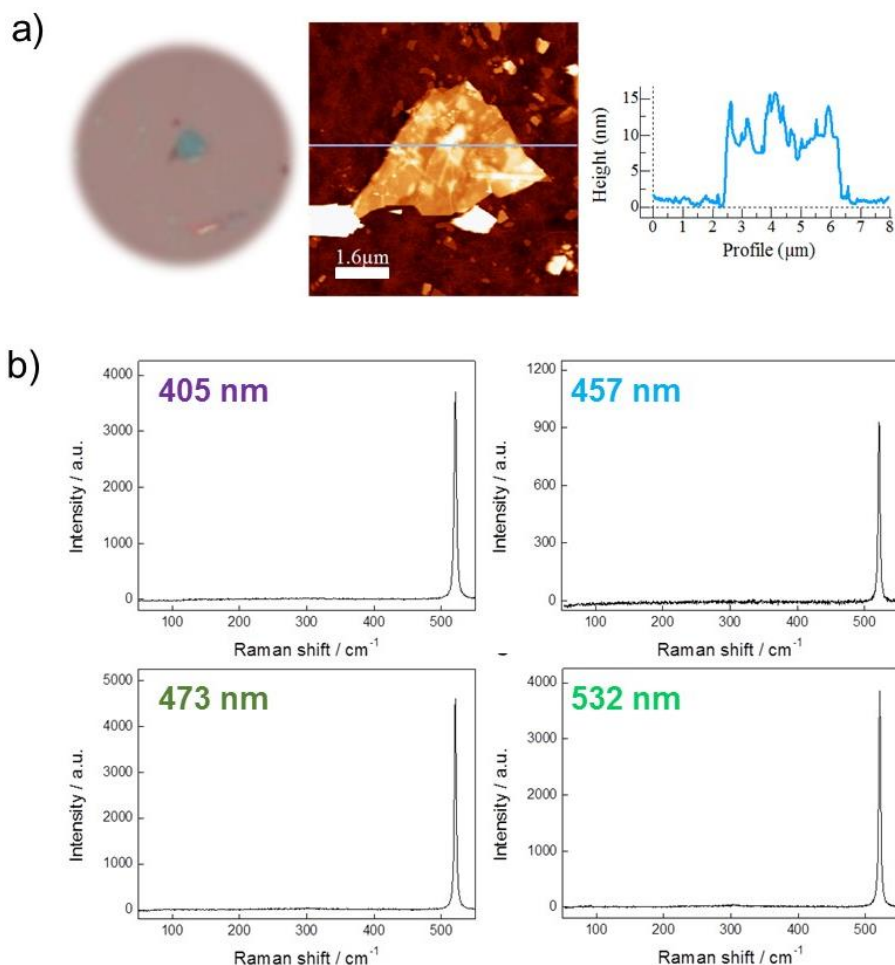
Figure 2.7 Micromechanically exfoliated FLA measured with different laser excitation wavelengths.

Although it was impossible to detect Raman signal of thinner flakes of antimony, they can be located using SRM by monitoring the decrease in the silicon characteristic peak about 521 cm^{-1} (Figure 2.8).
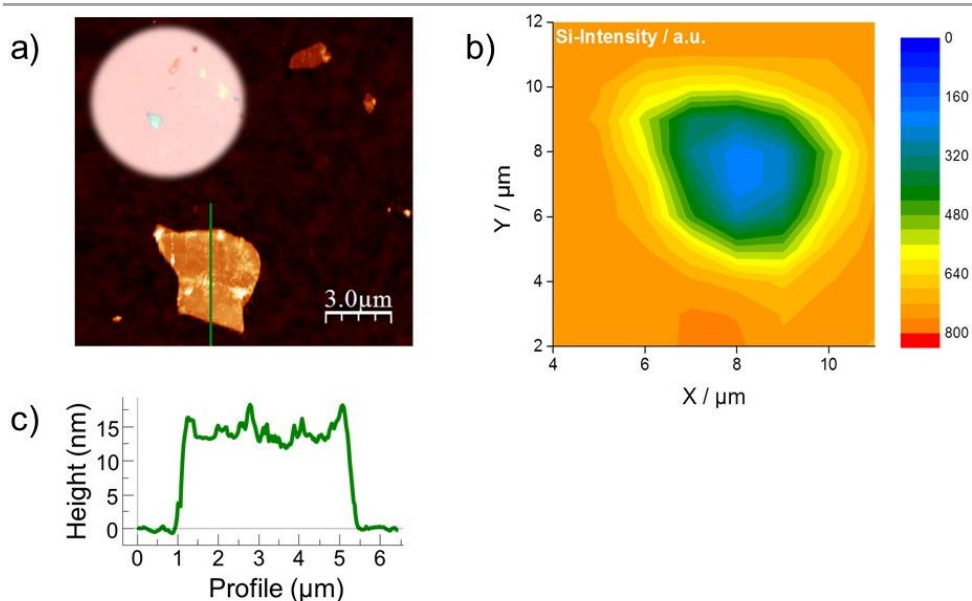
Figure 2.8 Detection of thin flakes monitoring the Silicon intensity. (a) AFM image of a micrometric antimony flake obtained by michromecanical exfoliation, and its corresponding profile showing a thickness of *ca.* 15 nm. The inset corresponds to the optical micrograph of the same area. (b) Silicon intensity Raman map showing a decrease in the 521 cm^{-1} signal that clearly reveals the morphology of the flake.

To further confirm these experimental results, the theoretical phonon spectra of bulk antimony and FLA was obtained by DFT calculations. For the calculations is taken into account that the β-phase of antimony consists of a buckled quasi-2D layers in an ABC-type sequence (space group $R\bar{3}m$). As it was experimentally observed, calculations confirm a strong influence of simulated Raman signal with the thickness of the flakes, which suffers a drop of three orders of magnitude from bulk to single-layer antimony (Figure 2.9). Therefore, these results explain what is experimentally observed for the thinnest flakes (Figure 2.6).
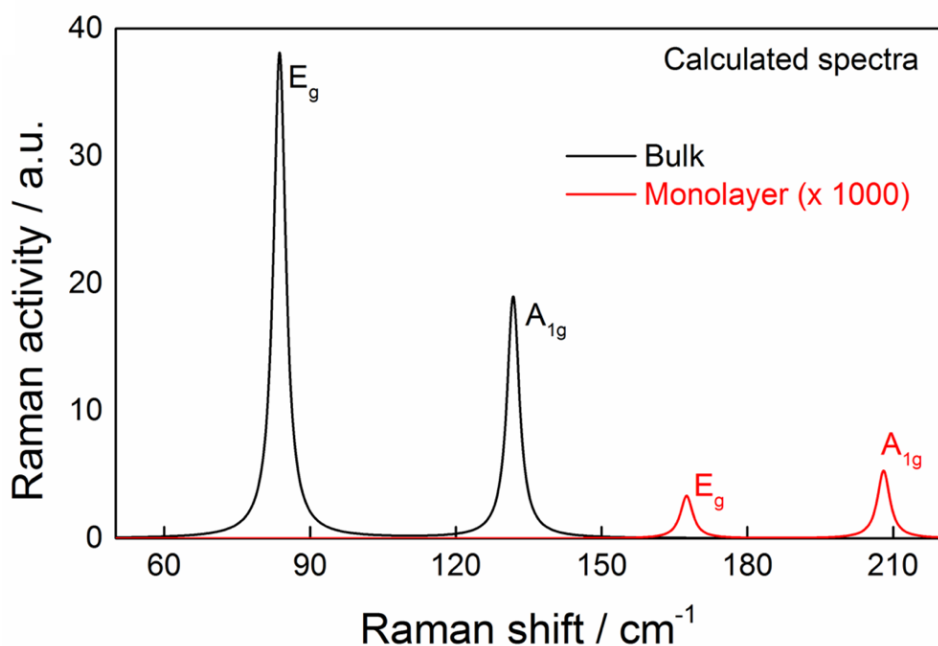
Figure 2.9 Calculated Raman spectra for bulk antimony and single-layer antimonene. According to the experimental observations, Raman for a monolayer exhibits a very low intensity (>1000 times less Raman activity than the bulk counterpart), precluding its detection.

This behaviour fully contrast with other 2D materials, as BN, where there is a weak dependence of the predicted Raman tensor with the number of layers. The main hypothesis is that the vanishing of the Raman signal in thinner flakes is due to a qualitative change in light–phonon coupling produced by the decrease on layer number.

94

To sum up the results related to the Raman measurements, the isolated flakes produced by LPE should consist of only few-layers of antimonene. Taking that into account, it could be understood why it has been impossible to see their Raman signal, not even in flakes with an apparent AFM height bellow 30 nm (*ca.* 60 layers). Thus, if the calculations indicate that the Raman signal of antimonene suffers a drop of three orders of magnitude from the bulk to single-layer, the obtained FLAs with thicknesses *ca.* 4 nm could correspond to a bi- or single-layer of antimonene.

2.3. Conclusions

The present work presents the first evidence of a procedure to generate stable suspensions of high-quality FLAs using LPE techniques. The use of green-solvents such as 2-propanol or water, and the low energy consumption due to the short sonication time endow the process with the characteristic of being environmentally friendly. Besides, it has been described the existing dependence of the Raman signal with the thickness on the FLAs.

2.3.1. Future prospects

In addition to being environmentally friendly, the process is also scalable due to its simplicity and the soft conditions that needs to be carried out. These two characteristics will pave the way for the development of new antimonene-based technologies. Despite of the process achieve the goal of obtaining FLAs using a LPE technique, is needed a deepest analysis of the rest of parameters involved in this approach in order to optimise it, as well as, a further study of the exfoliation procedure is taking part within the antimony crystals.

2.4. References

(1)   Backes, C.; Higgins, T. M.; Kelly, A.; Boland, C.; Harvey, A.; Hanlon, D.; Coleman, J. N. Guidelines for Exfoliation, Characterization and Processing of Layered Materials Produced by Liquid Exfoliation. *Chem. Mater.* **2017**, *29* (1), 243–255.

(2)   Coleman, J. N.; Lotya, M.; O'Neill, A.; Bergin, S. D.; King, P. J.; Khan, U.; Young, K.; Gaucher, A.; De, S.; Smith, R. J.; et al. Two-Dimensional Nanosheets Produced by Liquid Exfoliation of Layered Materials. *Science (80-.).* **2011**, *331* (6017), 568–571.

(3)   Paton, K. R.; Varrla, E.; Backes, C.; Smith, R. J.; Khan, U.; O'Neill, A.; Boland, C.; Lotya, M.; Istrate, O. M.; King, P.; et al. Scalable Production of Large Quantities of Defect-Free Few-Layer Graphene by Shear Exfoliation in Liquids. *Nat. Mater.* **2014**, *13* (6), 624–630.

(4)   Cunningham, G.; Lotya, M.; Cucinotta, C. S.; Sanvito, S.; Bergin, S. D.; Menzel, R.; Shaffer, M. S. P.; Coleman, J. N. Solvent Exfoliation of Transition Metal Dichalcogenides: Dispersibility of Exfoliated Nanosheets Varies Only Weakly between Compounds. *ACS Nano* **2012**, *6* (4), 3468–3480.

(5)   Smith, R. J.; King, P. J.; Lotya, M.; Wirtz, C.; Khan, U.; De, S.; O'Neill, A.; Duesberg, G. S.; Grunlan, J. C.; Moriarty, G.; et al. Large-Scale Exfoliation of Inorganic Layered Compounds in Aqueous Surfactant Solutions. *Adv. Mater.* **2011**, *23* (34), 3944–3948.

(6)   May, P.; Khan, U.; Hughes, J. M.; Coleman, J. N. Role of Solubility Parameters in Understanding the Steric Stabilization of Exfoliated Two-Dimensional Nanosheets by Adsorbed Polymers. *J. Phys. Chem. C* **2012**, *116* (20), 11393–11400.

(7)   Hanlon, D.; Backes, C.; Doherty, E.; Cucinotta, C. S.; Berner, N. C.; Boland, C.; Lee, K.; Harvey, A.; Lynch, P.; Gholamvand, Z.; et al. Liquid Exfoliation of Solvent-Stabilized Few-Layer Black Phosphorus for Applications beyond Electronics. *Nat. Commun.* **2015**, *6*, 8563.

(8)   Nemes-Incze, P.; Osváth, Z.; Kamarás, K.; Biró, L. P. Anomalies in Thickness Measurements of Graphene and Few Layer Graphite Crystals by Tapping Mode Atomic Force Microscopy. *Carbon N. Y.* **2008**, *46* (11), 1435–1442.

(9)   Wang, X.; Kunc, K.; Loa, I.; Schwarz, U.; Syassen, K. Effect of Pressure on the Raman Modes of Antimony. *Phys. Rev. B - Condens. Matter Mater. Phys.* **2006**, *74* (13), 1–10.

(10)   Ares, P.; Aguilar-Galindo, F.; Rodríguez-San-Miguel, D.; Aldave, D. A.; Díaz-Tendero, S.; Alcamí, M.; Martín, F.; Gómez-Herrero, J.; Zamora, F. Mechanical Isolation of Highly Stable Antimonene under Ambient Conditions. *Adv. Mater.* **2016**, 6332–6336.

Chapter 3: Unveiling the oxidation tendency of Liquid-Phase Exfoliated Few-Layer Antimonene
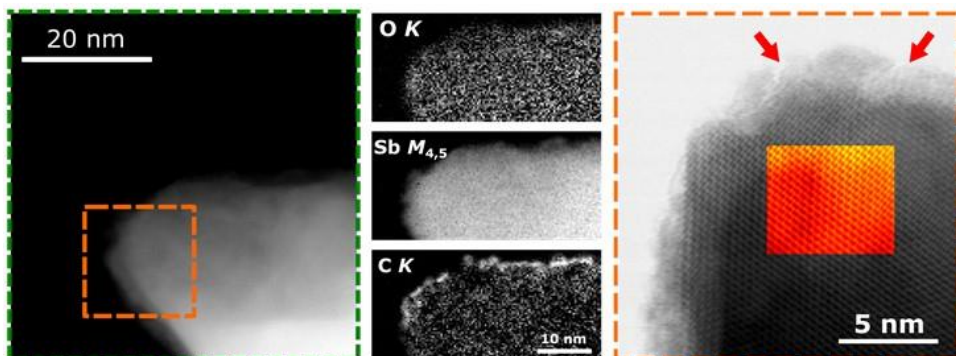
Chapter 3: Unveiling the oxidation tendency of Liquid-Phase Exfoliated Few-Layer Antimonene

3.1. Introduction

Contrarily to the low stability of black phosphorous, antimonene has been proven as air-stable material under ambient conditions. This stability is likely due to the shorter out-of-plane atom-to-atom distances, the lone-pair electrons of the antimony atoms terminating the surfaces of the layers and the absence of dangling bonds in the perfect crystalline structure[1,2]. Remarkably, theoretical calculations revealed a high oxidation tendency of antimonene that surpasses even that of black phosphorus[3]. Therefore, it is expected that antimonene could easily undergo oxidation during the course of its synthesis under ambient conditions[4], which is in good consistency with recent reports on experimental preparation of antimonene where oxygen species are always detected on its surface [5,6]. Unlikely black phosphorus, the resulting surface oxidation layer is thought to act as a passivation layer, shielding the material from further structural decomposition. Otherwise, an oxidized antimonene surface might also alter the physical properties of the material and bring about either beneficial or detrimental effects, affecting its potential applications[7].

In this context, and whilst the surface chemistry of several 2D-materials and their oxygen-sensitivity have been addressed[8], the oxidation tendency of antimonene remains poorly investigated.

It is then crucial to fully understand the oxidation behaviour of antimonene prepared by top-down approaches, from both fundamental and experimental point of view, as a necessary step towards developing a controlled preparation method of function-driven high-quality material.

In this work, it has been studied the oxidation behaviour of FLAs prepared by the LPE process described in Chapter 2. Using a set of top-notch analytical techniques, effect of the sonication time on the surface chemistry of prepared FLAs has been demonstrated. Additionally, it is performed quantum mechanical calculations to shed light on the observed antimonene oxide formation, predicting a dynamic behaviour. Analysing the obtained results, it can be seen that the oxidation process taking part has a dynamic behaviour, which upon annealing at moderate temperature (210 °C) resulted in a semiconducting feature with a bandgap of *ca.* 1 eV measured by Ultraviolet photoelectron spectroscopy (UPS).

3.2. Results and Discussion

FLA suspensions are prepared by LPE following the process described in Chapter 2. Thus, an initial antimony concentration of 0.1 g·L^{-1} is mixed with a 4:1 mixture of IPA/H$_2$O. Then, the mixture is sonicated using a tip sonicator for 40 min at 400 W and 24 kHz developing the ultrasound power in pulses of 0.5 s long every 1 s. After the tip sonication the suspensions are centrifuged for 3 min at 3000 rpm. In this work, a pre-processing step of bulk antimony crystals via ball-milling for 180 min at 30 Hz, is carried out in order to increase the efficiency of the exfoliation process[9]. Obtained FLAs are then casted on clean SiO$_2$/Si wafers and subjected to an exhaustive characterization with respect to structure, morphology and chemical composition.

The morphological features of synthesized FLAs are first analysed by AFM. Figure 3.1a shows a representative topological large area AFM image of the as-exfoliated FLAs. To obtain insights about the thickness and size distribution of the obtained nanosheets, statistical AFM analysis is performed. Figure 3.1b exhibits the average height distribution acquired by AFM considering 150 sheets. Almost 56 % of the measured nanosheets are thinner than 15 nm and that most of their lateral size is below 200 nm. Besides, it is found that nanosheets with a matching thickness ranging between 3 – 20 nm and a lateral sizes of less than 200 nm are predominantly present in the sample, *ca.* 75 % (see Figure 3.1c), hence demonstrating that bulk antimony crystals underwent successful lateral exfoliation along the layer surfaces as well as considerable longitudinal downsizing. It is worth it to point out that the noticeable big chunks in Figure 3.1a, do not correspond to a single nanosheet, but rather to an aggregate of FLAs as can be clearly seen in the magnified image shown in Figure 3.1d. Typical FLAs with a range of heights between 3.5 and 5.3 nm are depicted in Figure 3.1d.
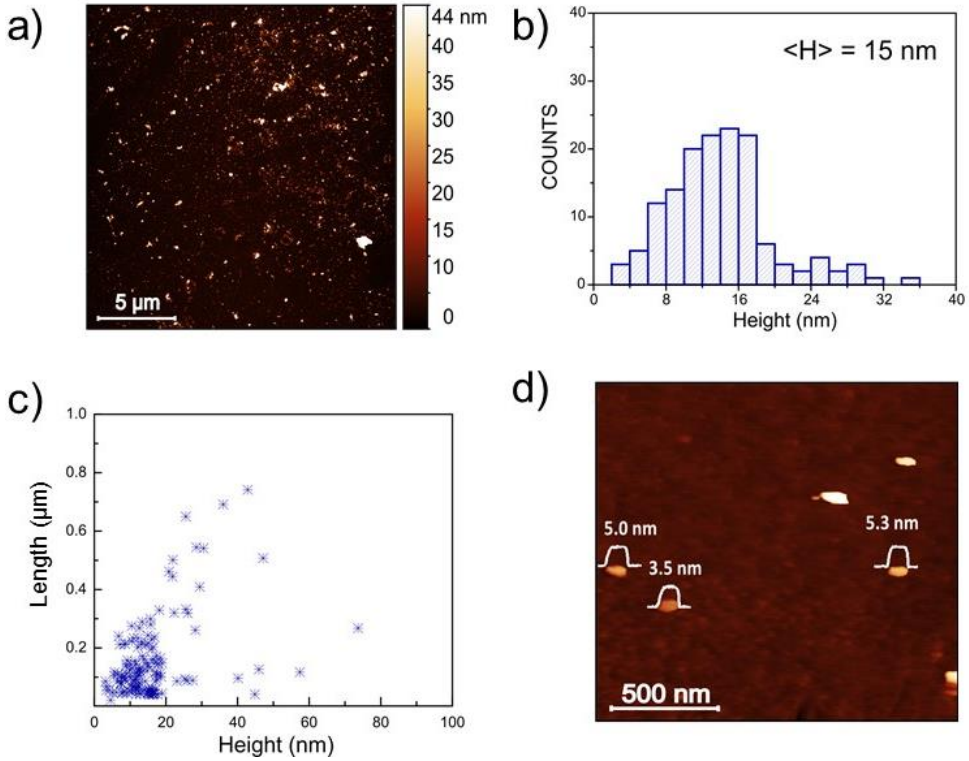
Figure 3.1 a) Large-scan AFM topography image of the exfoliated FLAs drop-casted onto SiO$_2$ wafers, b) Height distribution obtained from statistical analysis of AFM height profiles extracted from 150 individual FLAs, c) Plot of the length as a function of the height of 150 individual FLAs, d) Small-area AFM scan of typical FLAs with corresponding apparent thicknesses.

To further characterize the material properties and provide the structural fingerprint to identify FLAs, SRM measurements are driven as an adequate technique. As shown in Figure 3.2, bulk antimony crystals exhibit the typical E$_g$ (112.2 cm^{-1}) and A^1_g (150.1 cm^{-1}) peaks ascribed to the in-plane and out-of-plane vibrational modes, respectively, when excited by a green laser (λ_{exc} = 532 nm).

Upon exfoliation, a drastic decrease in the intensity of the A^1_g peak accompanied with a slight blue shift by ca. 2.3 cm^{-1} is observed, while a change in the E_g cannot be detected, which follows well to Raman results presented in Chapter 2 on FLA obtained by LPE techniques.

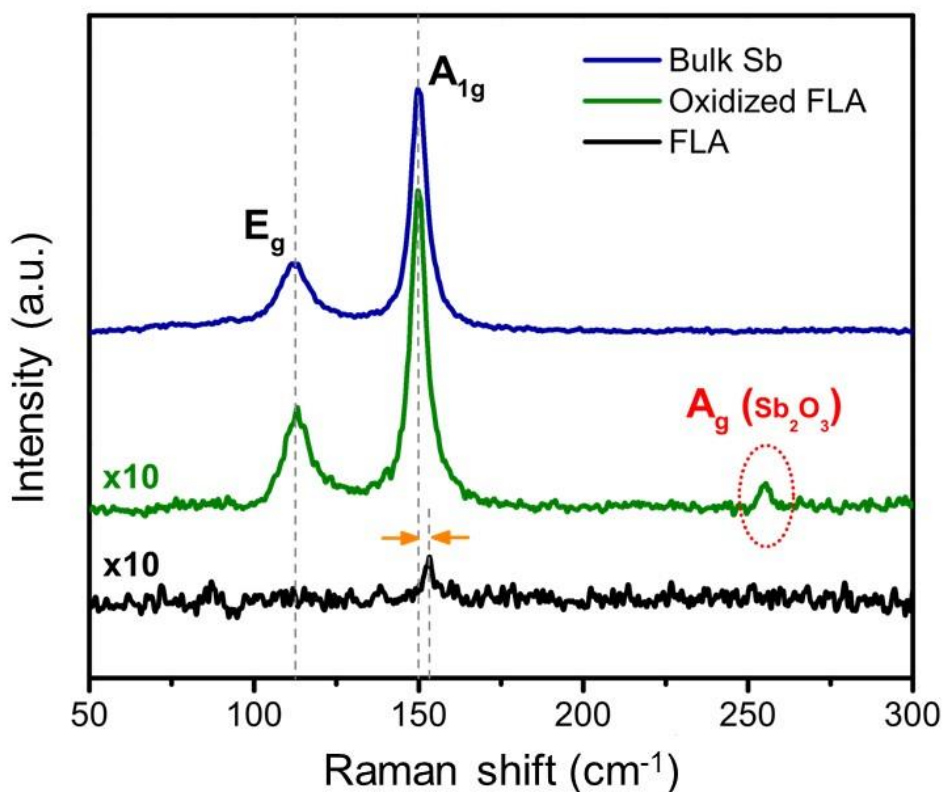**Figure 3.2** Raman spectra of bulk antimony (blue), exfoliated FLAs (black) and oxidized-FLAs exhibiting Sb$_2$O$_3$ Raman fingerprint at 254.6 cm^{-1} (green).

Figure 3.3a shows an optical microscopy image of the exact same area scanned by AFM in Figure 3.3b. Raman mapping of the A^1_g peak intensity is recorded over this spot in order to get a correlation between the three techniques (Figure 3.3c).

The obtained A^1_g map, which is constituted by 10,000 single spectra with a spatial resolution of 0.2 µm, unambiguously confirm the successful exfoliation of bulk antimony crystals into FLAs.
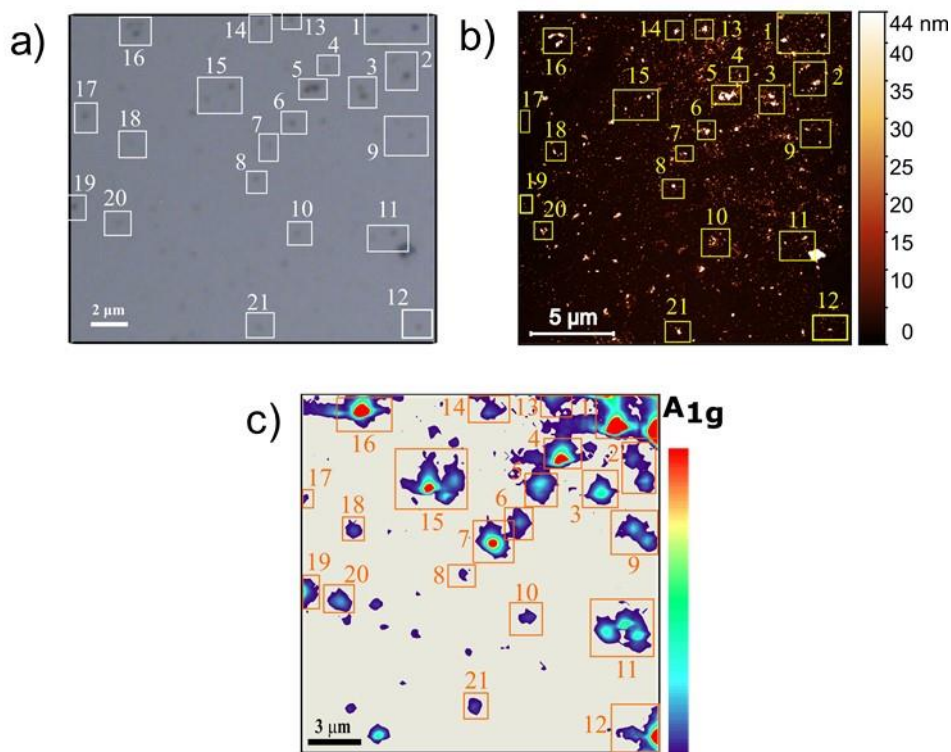

Figure 3.3 a) Optical microscopy image, b) topographic AFM image and c) Raman mapping of A^1_g, obtained over the exact same area. To simplify the correlation between the three images, each spot of is highlighted with numbered squares, unambiguously confirming the successful exfoliation of FLAs.

Furthermore, it can be clearly seen that for most of the thinner nanosheets observed by AFM, no Raman signal can be detected due to its drastic dependence with the thickness of the FLAs, what is in good agreement with theoretical and experimental predictions presented in Chapter 2.

However, it is important to point out that, when conducting Raman measurements; special care needs to be taken with respect to the laser intensity and acquisition time employed. Indeed, high power density laser will considerably increase the local spot temperature which might consequently induce several damages to the sample, such as oxidation or decomposition[10,11,12]. Nonetheless, to avoid such accidental damage to our samples, all Raman data presented in this work are acquired using laser intensities as low as 1.6 mW and exposure times not exceeding 5 s.

Moreover, an earlier oxidation of the sample, most probably during the course of the LPE process, might be the underlying reason behind the noticed attenuation of Raman intensities of FLAs. Such effect has been also observed in transition metal dichalcogenides[13]. Interestingly, it is observed that Raman spectra of some FLAs exhibited additional peaks at 190.5 cm^{-1} and 254.6 cm^{-1} that matches well those of antimony oxide (α-Sb_2O_3), as can be clearly seen in Figure 3.2. The statistical analysis carried out over Raman spectra of one hundred FLAs, shows that only *ca*. 3% present Raman signature of Sb_2O_3. Therefore, discarding the possibility of laser-induced oxidation during the measurement and suggesting the possibility of being partially oxidized during the LPE process while preserving structural integrity.

To further investigate the morphology and microstructure of the prepared FLAs there are performed STEM measurements. Figure 3.4a displays a low-magnification HAADF image of a sub-micron FLA nanosheet with an irregular shape, hanging on the edge of the C support acquired with an acceleration voltage of 80 kV to avoid any electron beam-induced damage as is the case with very thin nanosheets. Chemical composition of the nanosheet is solved by EELS over the green-dashed area in Figure 3.4a which allowed the construction of Sb, O and C elemental mappings shown in Figure 3.4b.

The analysed nanosheet is mainly composed of Sb and a noticeable
amount of oxygen mostly located at its surface and edges. Additionally,
minor C signal is also detected on the very edges of the nanosheet, most
probably as a result of contamination from remaining solvent. It is noticed
that the reduced contrast in the middle of the sheet in the Sb map is due
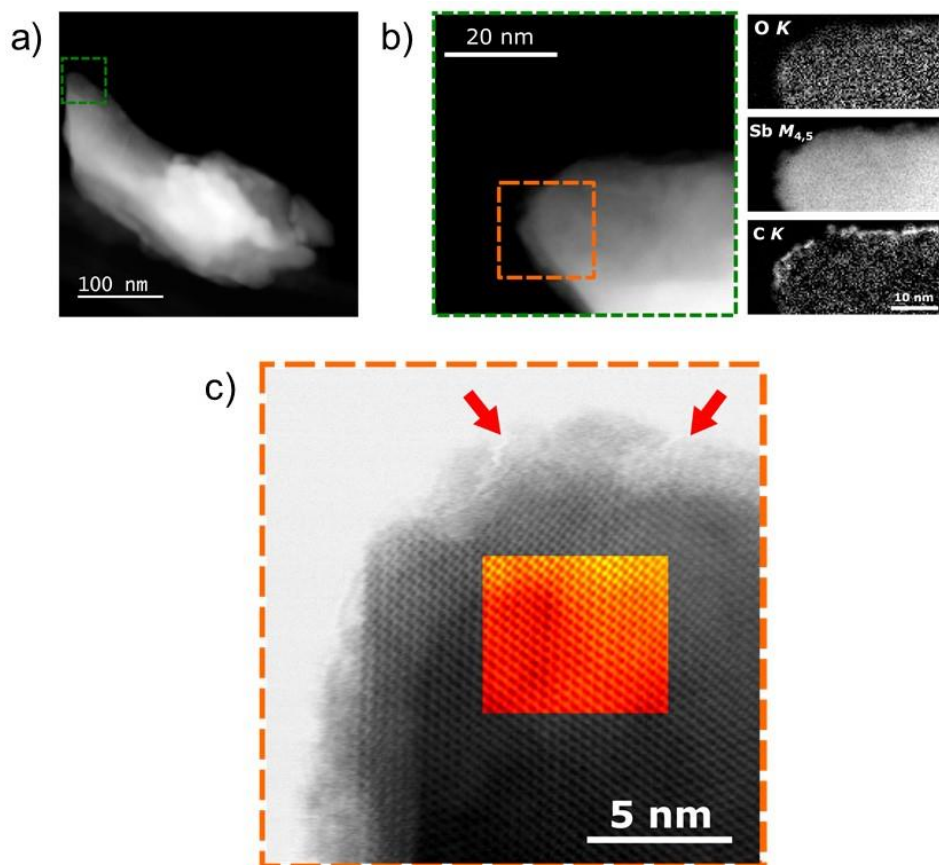to its relatively large thickness.

Figure 3.4 a) HAADF image of sub-nanometric FLA nanosheet acquired using 80 kV
acceleration voltage, b) magnified image corresponding to the green-dashed area in (f) and
elemental composition derived from EELS maps and c)

A HAADF image of the area dashed in orange in Figure 3.4b near the edge of the sheet is displayed in Figure 3.4c along with an overlaid noise-free Fourier-transformed image, which clearly demonstrates the high degree of crystallinity within the nanosheet with no major defects. Moreover, another feature that can also be clearly seen in this image is the characteristic "washboard" structure and a corresponding ABC-type of stacking which agrees well with that of rhombohedral β-phase of antimony. Furthermore, as pointed out by the red arrows in Figure 3.4c, it can be easily notice the presence of an approximately 2 nm-thick amorphous layer covering the crystalline sheet, which in combination with EELS maps, reveals that it consists of Sb and O. This loss of crystallinity at the top surface and edges pointed towards the formation of an oxidation layer around the nanosheet, while the inner structure is still preserved.

In order to examine even further the surface chemistry and oxidation state of Sb in the obtained FLAs, X-ray photoelectron spectroscopy (XPS) is employed as a highly surface-sensitive technique to the samples deposited on a clean HOPG substrate. Figure 3.5 displays the obtained XPS spectra of the 3d region of the as-prepared FLA, where the large peak near 532 eV contains contributions from both Sb $3d_{5/2}$ and O 1s, while the peak near 541 eV only contains Sb $3d_{3/2}$ components. A more detailed analysis of the peaks led to the deconvolution of the large peak at 532 eV into five components. Peak 1 (orange) at 528.6 eV corresponding to metallic Sb, peak 2 (green) of oxidized Sb with a binding energy of 531.3 eV close to that of Sb_2O_3, peak 3 (light-blue) at 531.8 eV ascribed to Sb in a higher oxidation state, most probably to Sb_2O_5, and peak 4 at 532.3 eV assigned to O 1s. An additional peak 5 (pink), of the O 1s component is observed and is found to be compatible with hydroxide species present at the surface. Note that all components are more clearly seen in the $3d_{3/2}$ emission spectrum at 541 eV, in particular peak 3, as it almost coincides with O 1s component in the Sb $3d_{5/2}$ region.
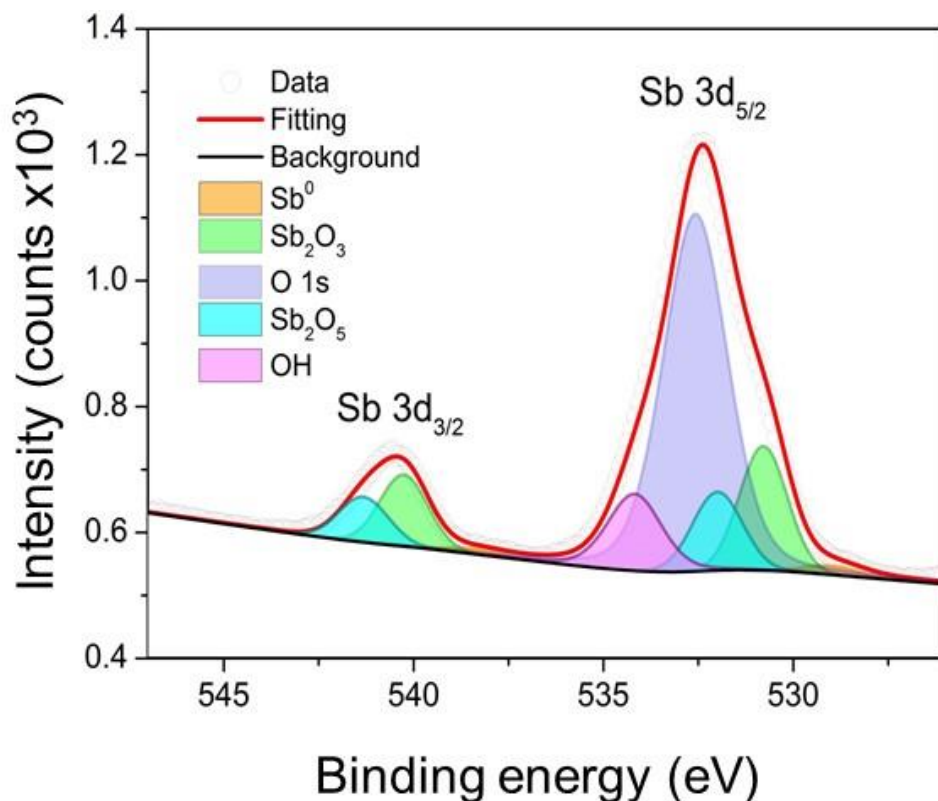
Figure 3.5 Typical XPS line spectra of Sb $3d_{5/2}$ and $3d_{3/2}$ region for as-exfoliated FLAs (after 40 min sonication) showing contribution from both metallic and oxidized Sb components.

The XPS data unambiguously revealed that the as-prepared FLAs exhibits a considerable contribution from antimony oxide, thus corroborating the earliest observation in Raman microscopy and STEM-EELS measurements. In fact, it is not a surprise that the surface of the obtained FLAs exhibited in most cases some form of oxygen species, as it has been also reported by many recent experimental outcomes.

For instance, Lloret *et al.* have carried out a remarkable experiment in which they highlighted the high oxidation tendency of FLA exfoliated in liquid media using 1-butyl-3-methylimidazolium tetrafluoroborate (bmim-BF4), which is an ionic-liquid well known for its excellent oxidation protection behavior[14]. In that work, they have shown by means of XPS that upon exposing a FLA nanosheet to air for several hours, after removing the ionic liquid protective layer by heating under ultra-high vacuum (UHV) conditions, there is a concurrent severe decrease in the intensity of metallic Sb component and increase of oxidized Sb species compared to those of ionic-liquid protected samples. This result provide strong experimental evidence of the high tendency of antimonene to oxidize under ambient conditions, which is also in good agreement with recent theoretical predictions[3]. Unlike phosphorene, it has been experimentally proved that antimonene exhibits a high thermodynamic stability under ambient conditions for over months[15], probably due to the generated surface oxidation layer acting as a passivation layer, thus preventing oxygen from diffusing inwards into the inner layers and protecting them from further structural degradation. The first hypothesis made in this work is that the partial surface oxidation that suffer prepared FLAs, occurs during the course of LPE process, most likely as a result of the energy bursts provided by the ultrasonic waves in the liquid media.

Addressing this issue, there have carried out a set of LPE experiments increasing the sonication time, ranging from 5 min to 45 min. It is worth it to point out that at shorter times, no considerable exfoliation is expected, but the main objective is to examine the oxidation degree at early stages of exfoliation. The obtained FLAs are analysed using XPS, and the obtained spectra corresponding to samples sonicated for 5, 20 and 40 min are deconvoluted (Figure 3.6). An overview of all XPS spectra as function of time is also displayed in Figure A3.1 (page 205).

A closer examination of the spectra corresponding to the 5 min sample in Figure 3.6a reveals the existence of peaks corresponding to oxidized Sb and O 1s, in addition to the peak corresponding to metallic Sb. Indeed, this is a proof that the surface of antimony crystals undergo oxidized fairly quickly as a result of the sonication tip processing that only took 5 min, though the degree of exfoliation is still not substantial at this stage.
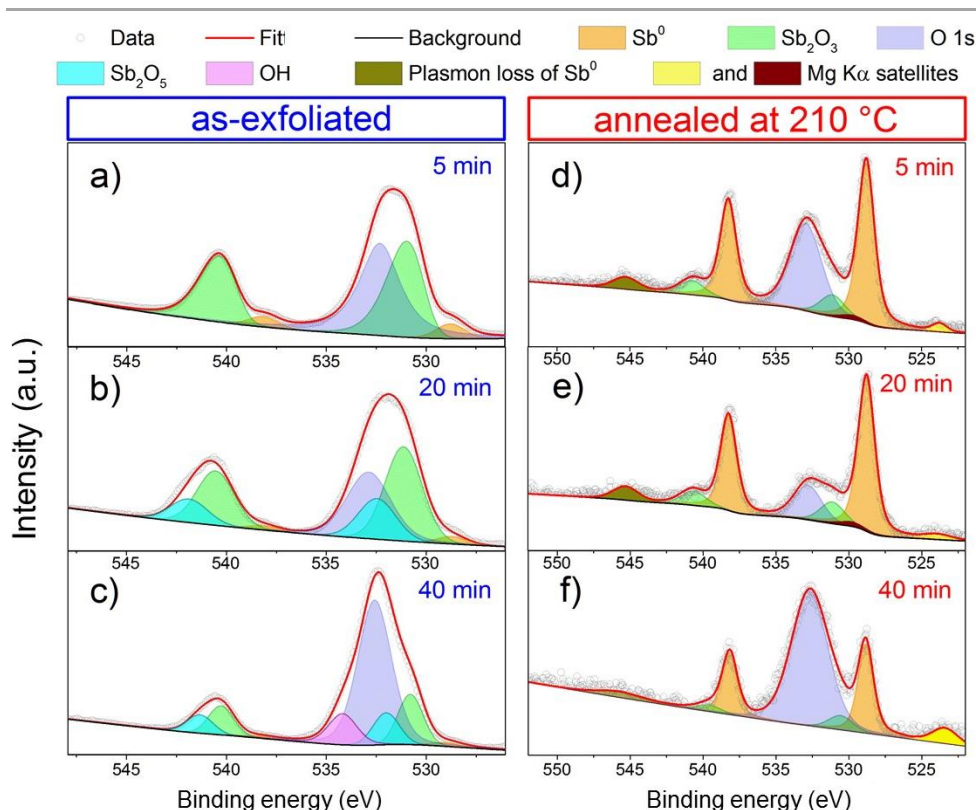

Figure 3.6 XPS line spectrum with peaks deconvoluted in the 3d region of FLAs obtained by LPÊ: (a) 5 min, (b) 20 min, and (c) 40 min. High resolution XPS spectra of the same set of samples sonicated for (d) 5 min, (e) 20 min, and (f) 40 min, measured using synchrotron radiation after annealing for 90 min at 210 °C.

In addition, the oxidation of the 5 min sample is also depicted by EELS compositional mapping shown in Figure 3.7, where a considerable amount of oxygen is noticed on the surface and edges of the nanosheet.
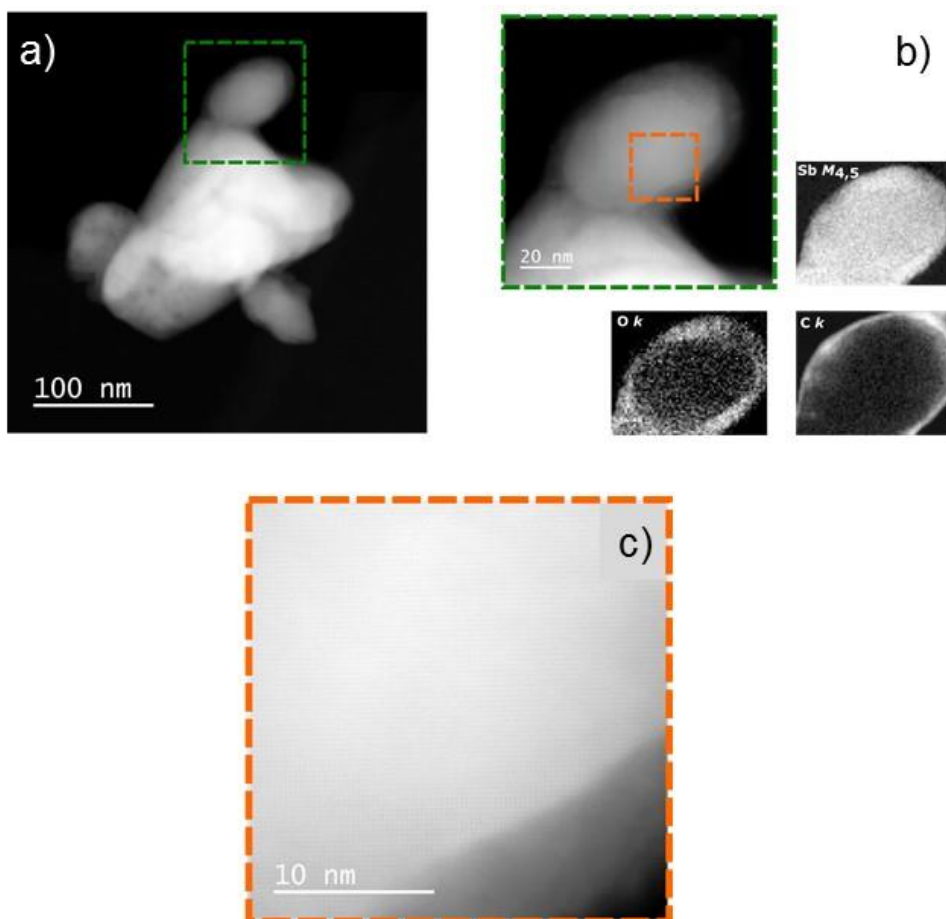

Figure 3.7 a) HAADF image of a thick FLA nanosheet obtained after sonication for 5 minutes in IPA/H$_2$O, b) magnified image of the green-dashed area in (a) and corresponding elemental mapping images of Sb, O-s and C-k lines, c) high magnification image of the rectangular orange-dashed area in (b) depicting the crystallinity of the lattice.

Remarkably for this sample, there is only one oxidized Sb component, of which the binding energy is close to Sb_2O_3. In contrast, for the sample processed for 20 min, Sb component related to higher oxidation states arises (peak 4), and its relative weight has grown with time as evidently depicted in Figure 3.6c. Next, while keeping in mind the above-discussed analysis of the XPS line spectra obtained for the sample processed for 40 min, it seems that as sonication time increases the resulting FLAs undergo progressive oxidation.

First, at 5 min it is noticed the appearance of an oxidized Sb component consisting of Sb_2O_3 followed by the formation of Sb_2O_5 corresponding to a higher oxidation degree after 20 min (Figure 3.6b). Subsequently, as the oxidized Sb signal reaches saturation and grows no more after 40 min, surface oxygen species such as adsorbed oxygen and hydroxides become predominant (Figure 3.6c). In addition, the XPS data as a function of sonication time clearly shows the progressive decrease in intensity of metallic Sb (peak 1). This is expected, since as sonication time increases, the exfoliation proceeds to a higher extent, thus producing thinner flakes with higher surface area which renders them more likely to oxidation. A more detailed analysis revealed that the intensity ratio I_{532eV}/I_{540eV} of both main peaks is not constant and is increasing with time. Since the ratio between Sb components is fixed, the observed difference is only due to the O 1s intensity. Moreover, calculation of the O 1s /Sb 3d ratio reveals that it is far from any oxide stoichiometry, thus indicating that either most of the oxygen is not bound to Sb, or the development of a different form of antimonene oxide layer at the surface of the flake, which fits quite well with our earlier remarks using STEM-EELS.

In the following step, the samples are subjected to thermal annealing at 210 °C under UHV for 90 min, in order to remove any possible adlayer impurities and gain further insight into the nature of the previously observed amorphous layer. Then, the samples are measured in-situ by XPS using synchrotron Mg Kα line with lower pass energy of 20 eV. The obtained spectra are shown in Figure 3.6d- f, corresponding to samples sonicated for 5, 20 and 40 min, respectively. It can be easily seen that after the annealing process they are better resolved, and also that the intensity of metallic Sb component is much larger than for the samples prepared without annealing. Besides, it is also remarkable the absence of the oxidized component, corresponding to Sb_2O_5, in the spectra of 20 min sample and the almost total absence of oxidized Sb components for 40 min sample, even though the intensity of the O 1s component increases drastically. Interestingly for the 40 min sample, since this O 1s is not bound to Sb, it is possible that either the oxygen layer is thicker and is not completely removed by the annealing, or the oxygen is bound in a different way to the surface. Furthermore, an additional peak 6 (dark yellow) is also observed next to 544 eV, and it corresponds to the plasmon loss of metallic Sb, whose presence is a good sign of metallicity. It can be concluded that annealing under this conditions not only removes the previously observed surface adlayer, thus exposing more non-oxidized Sb, but also modifies the ratio of remaining Sb oxides present at the sample. Therefore, it is possible that this dynamic process observed upon annealing leaves behind an exotic heterostructure of type antimonene oxide/antimonene at the surface of the flakes.

To gain further understanding about the antimonene oxide surface layer from the structural point of view, there are performed DFT calculations. It is started from the recently proposed structure of antimonene oxides single layers, where the oxygen atoms form double bonds perpendicularly to the monolayer plane[16].

Calculations of the phonon dispersion show vibrational modes with negative frequencies in a widespread range of the Brillouin zone, indicating that this structure is meta-stable and suffers a phase transition at room temperature, where the oxygen atoms move into the plane, forming Sb-O-Sb bonds (Figure 3.8a-b). By adding more oxygen atoms to the system, it is found a two-dimensional Sb_2O_3 structure, which is stable under environmental conditions and displays characteristic Raman modes in the range 250-400 cm^{-1} that are absent for antimonene and the previously suggested oxide geometry. In combination with the experimental data, this suggests the possibility of formation of layered heterostructures of FLA cores sandwiched by two-dimensional Sb_2O_3 layers from surface oxidation (Figure 3.8c).
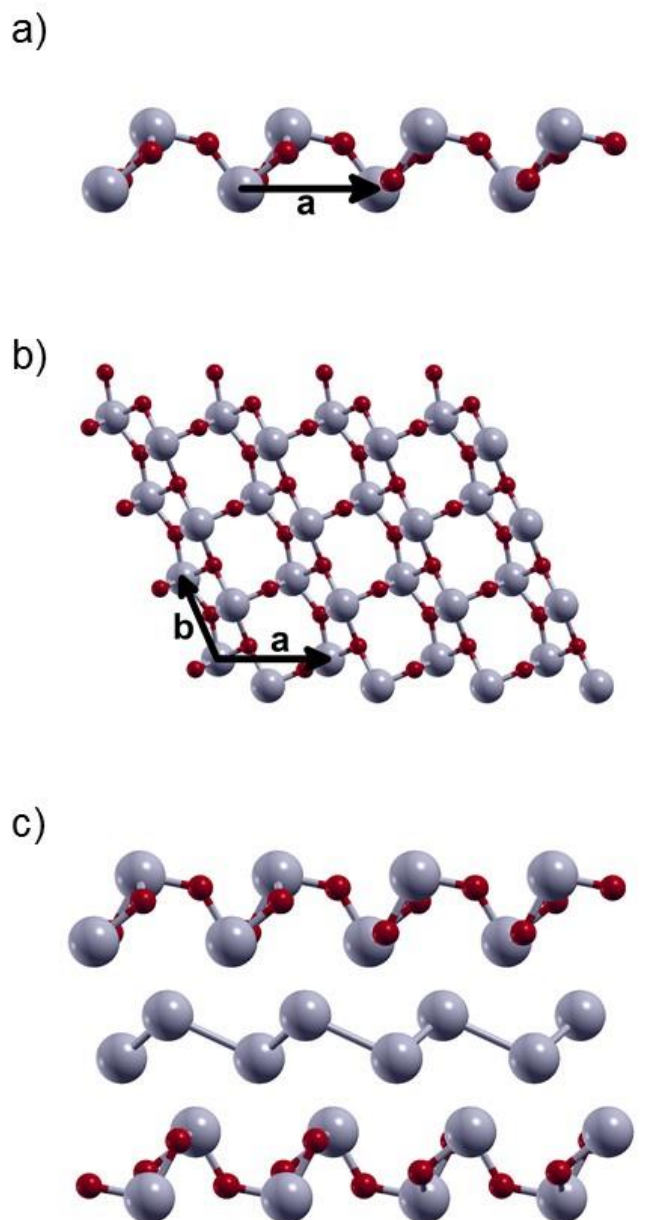
Figure 3.8 Relevant views from the calculated antimonene oxide surface layer structure: a) Side view, b) Top view. c) Side view of the layered heterostructure of FLAs sandwiched by 2D antimonene oxide surface layer.

Attending to the results so far reported, it is legitimate to expect that the oxidation layer might induce changes in the electronic properties of the prepared FLAs. For this purpose, are explored the surface electronic properties of the three samples prepared by LPE for 5, 20 and 40 min of sonication time, by means of UPS using synchrotron radiation. In fact, the main advantage offered by making use of the ultraviolet light is the low photon energy which allows a detailed investigation of the valence levels. Obtained photoemission spectra, before and after annealing at 210ºC under UHV for 90 min, of the three samples are shown in Figure 3.9.
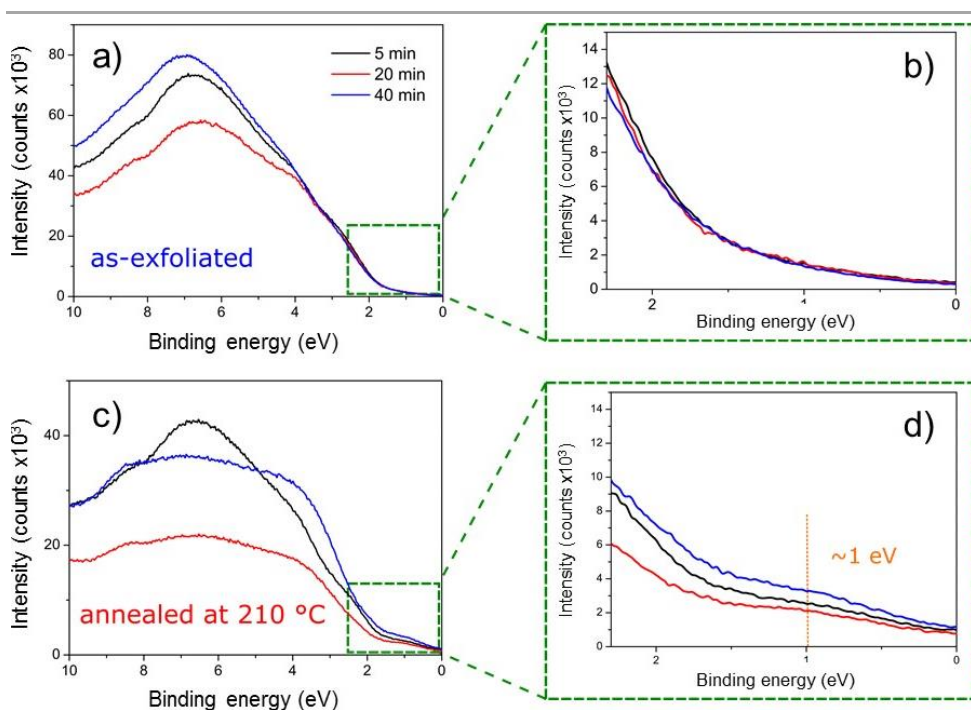

Figure 3.9 a) Valence band of the FLAs obtained by LPE for 5, 20 and 40 min measured by UPS, b) enlarged view of the square-dashed area in (a), c) valence band for 210 °C post-annealed sample and d) enlarged view of the green-dashed area in (c) showing a peak near 1 eV ascribed to antimonene oxide.

Significant changes are observed after annealing process. Thus, while the shape of the valence band of the 5 min sample remained almost unchanged, the valence band of 20 and 40 min samples undergo significant change and exhibited a different shape (Figure 3.8c). Remarkably, the enlarged view of the valence band of the three samples after the annealing process displayed in Figure 3.5d, shows a peak at *ca.* 1 eV of binding energy. In view of the fact that XPS data has revealed the presence of both metallic and oxidized Sb in those samples, the observed peak at 1 eV can be ascribed to the antimonene oxide. Moreover, the intensity enhancement noticed near 0.5 eV is due to the onset of the valence band of an otherwise semiconducting material. Considering the fact that earliest theoretical computations predicted a direct bandgap for antimonene oxide[7], it comes as no surprise that the so-formed antimonene oxide layer observed in our samples induced such modification in the electronic band structure.

3.3. Conclusions

In this work, has been investigated the oxidation behaviour of FLAs obtained following the LPE procedure described in Chapter 2. Obtained results revealed the formation of an antimonene oxide layer (Sb_2O_3-like) on the surface of the nanosheets as a result of the LPE of bulk antimony crystals.

Furthermore, it has been performed quantum mechanical calculations for the sake of clarity of the observed antimonene oxide formation. This calculations suggests that the formation of layered heterostructures of FLA cores sandwiched by two-dimensional Sb_2O_3 layers from surface oxidation, is feasible. It has been also demonstrated, by means of XPS and UPS measurements, that the oxide layer could be partially removed upon annealing at moderate temperatures, leaving behind a Sb_2O_3-like/antimonene heterostructure with a band gap of *ca.* 1 eV.

3.3.1. Future prospects

Results derived from this work, have important implications with respect to applications based on antimonene due to the observed semiconducting feature upon oxidation, and might open up new avenues for surface engineering and tailoring of its properties.

3.4. References

(1)   Zhang, S.; Yan, Z.; Li, Y.; Chen, Z.; Zeng, H. Atomically Thin Arsenene and Antimonene: Semimetal-Semiconductor and Indirect-Direct Band-Gap Transitions. *Angew. Chem., Int. Ed.* **2015**, *54* (10), 3112–3115.

(2)   Abellán, G.; Ares, P.; Wild, S.; Nuin, E.; Neiss, C.; Miguel, D. R.-S.; Segovia, P.; Gibaja, C.; Michel, E. G.; Görling, A.; et al. Noncovalent Functionalization and Charge Transfer in Antimonene. *Angew. Chem., Int. Ed.* **2017**, *56* (46), 14389–14394.

(3)   Kistanov, A. A.; Cai, Y.; Kripalani, D. R.; Zhou, K.; Dmitriev, S. V.; Zhang, Y. W. A First-Principles Study on the Adsorption of Small Molecules on Antimonene: Oxidation Tendency and Stability. *J. Mater. Chem. C* **2018**, *6* (15), 4308–4317.

(4)   Gusmão, R.; Sofer, Z.; Bouša, D.; Pumera, M. Pnictogen (As, Sb, Bi) Nanosheets for Electrochemical Applications Are Produced by Shear Exfoliation Using Kitchen Blenders. *Angew. Chem., Int. Ed.* **2017**, *56* (46), 14417–14422.

(5)   Ji, J.; Song, X.; Liu, J.; Yan, Z.; Huo, C.; Zhang, S.; Su, M.; Liao, L.; Wang, W.; Ni, Z.; et al. Two-Dimensional Antimonene Single Crystals Grown by van Der Waals Epitaxy. *Nat. Commun.* **2016**, *7* (1), 13352.

(6)   Wang, X.; He, J.; Zhou, B.; Zhang, Y.; Wu, J.; Hu, R.; Liu, L.; Song, J.; Qu, J. Bandgap-Tunable Preparation of Smooth and Large Two-Dimensional Antimonene. *Angew. Chem., Int. Ed.* **2018**, *57* (28), 8668–8673.

(7)   Zhang, S.; Zhou, W.; Ma, Y.; Ji, J.; Cai, B.; Yang, S. A.; Zhu, Z.; Chen, Z.; Zeng, H. Antimonene Oxides: Emerging Tunable Direct Bandgap Semiconductor and Novel Topological Insulator. *Nano Lett.* **2017**, *17* (6), 3434–3440.

(8)   Abellán, G.; Wild, S.; Lloret, V.; Scheuschner, N.; Gillen, R.; Mundloch, U.; Maultzsch, J.; Varela, M.; Hauke, F.; Hirsch, A. Fundamental Insights into the Degradation and Stabilization of Thin Layer Black Phosphorus. *J. Am. Chem. Soc.* **2017**, *139* (30), 10432–10440.

(9)   Buzaglo, M.; Bar, I. P.; Varenik, M.; Shunak, L.; Pevzner, S.; Regev, O. Graphite-to-Graphene: Total Conversion. *Adv. Mater.* **2017**, *29* (8), 1–5.

(10)   Castellanos-Gomez, A.; Barkelid, M.; Goossens, A. M.; Calado, V. E.; Van Der Zant, H. S. J.; Steele, G. A. Laser-Thinning of MoS 2: On Demand Generation of a Single-Layer Semiconductor. *Nano Lett.* **2012**, *12* (6), 3187–3192.

(11)   He, R.; Sucharitakul, S.; Ye, Z.; Keiser, C.; Kidd, T. E.; Gao, X. P. A. Laser Induced Oxidation and Optical Properties of Stoichiometric and Non-Stoichiometric Bi2Te3 Nanoplates. *Nano Res.* **2015**, *8* (3), 851–859.

(12)   Lu, J.; Wu, J.; Carvalho, A.; Ziletti, A.; Liu, H.; Tan, J.; Chen, Y.; Castro
         Neto, A. H.; Özyilmaz, B.; Sow, C. H. Bandgap Engineering of
         Phosphorene by Laser Oxidation toward Functional 2D Materials. *ACS
         Nano* **2015**, *9* (10), 10411–10421.

(13)   Chae, S. H.; Jin, Y.; Kim, T. S.; Chung, D. S.; Na, H.; Nam, H.; Kim, H.;
         Perello, D. J.; Jeong, H. Y.; Ly, T. H.; et al. Oxidation Effect in Octahedral
         Hafnium Disulfide Thin Film. *ACS Nano* **2016**, *10* (1), 1309–1316.

(14)   Lloret, V.; Rivero-Crespo, M. Á.; Vidal-Moya, J. A.; Wild, S.; Doménech-
         Carbó, A.; Heller, B. S. J.; Shin, S.; Steinrück, H.; Maier, F.; Hauke, F.; et
         al. Few Layer 2D Pnictogens Catalyze the Alkylation of Soft Nucleophiles
         with Esters. *Nat. Commun.* **2019**, *10* (1), 509.

(15)   Ares, P.; Aguilar-Galindo, F.; Rodríguez-San-Miguel, D.; Aldave, D. A.;
         Díaz-Tendero, S.; Alcamí, M.; Martín, F.; Gómez-Herrero, J.; Zamora, F.
         Mechanical Isolation of Highly Stable Antimonene under Ambient
         Conditions. *Adv. Mater.* **2016**, *28* (30), 6332–6336.

(16)   Zhang, S.; Zhou, W.; Ma, Y.; Ji, J.; Cai, B.; Yang, S. A.; Zhu, Z.; Chen, Z.;
         Zeng, H. Antimonene Oxides: Emerging Tunable Direct Bandgap
         Semiconductor and Novel Topological Insulator. *Nano Lett.* **2017**, *17* (6),
         3434–3440.

Chapter 4: A systematic study towards the Liquid-Phase Exfoliation of Antimony
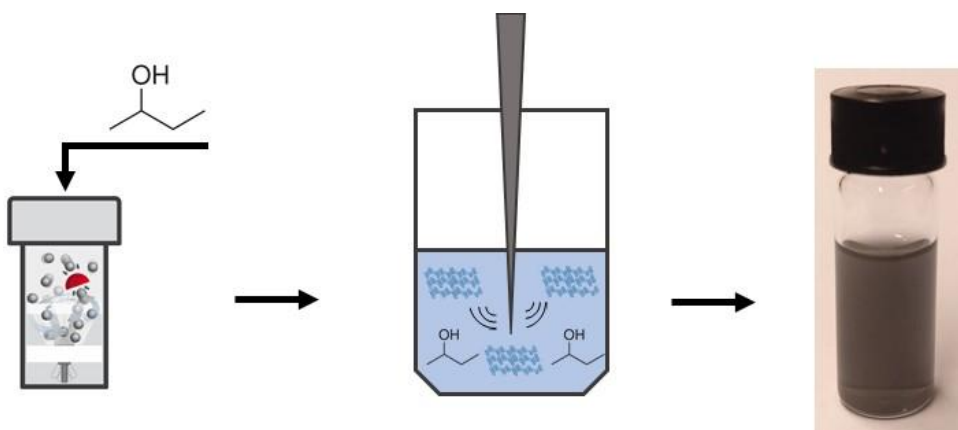
Chapter 4: A systematic study towards the Liquid-Phase Exfoliation of Antimony

4.1. Introduction

LPE techniques have been widely used to produce suspensions of many 2D inorganic layered materials mainly because are the most appropriate technique to produce single or few-layer in large-scale[1]. Besides they are considered easy methods, suitable for industrial scale-up and based on the solubility parameters theory.

In Chapter 2, it is explained in detail how it was achieved, for the first time, the isolation of FLAs by means of LPE techniques. Even though the FLAs obtained in that work have an excellent quality, it is also true that an enhancement on the concentration of the suspensions can contribute to spread its potential applications. LPE processes are dramatically affected by the features of the crystal size of the starting material, solvent selection and source of energy to assist the exfoliation process[2].

Herein, it is carried out a systematic analysis of the most relevant parameters that govern LPE process, in order to rationalize the production of FLA suspensions. Thus, it is evaluated the outcome in the LPE of antimony crystals of: i) the initial crystal size, ii) solvent used and iii) ultrasound parameters.

In order to accomplish this fundamental study, it is proposed a strategy based on three enchained steps that have been optimized by maximizing the concentration and the "dimensional anisotropy" (DA) ratio of the FLAs contained in the samples. The DA ratio is a parameter defined as the ratio between the length value and height value of the nanosheets, and offers a good approximation of their morphology. Thus, the higher the DA ratio is, the thinner and larger the nanosheets are. It is worth to remark here that in the case of FLA, the short out-of-plane atom-to-atom distances result in strong interlayer interactions, and pose an additional limitation for the exfoliation.

Results derived from this work confirm that the concentration of FLAs can be enhanced up to 30 times, *ca.* 0.368 g·L⁻¹, compared to the topmost concentration value reported so far[3], *ca.* 0.014 g·L⁻¹. This result is achieved using a pre-processing step of the bulk antimony crystals based on a wet-ball milling process in 2-butanol, followed by a LPE step in a NMP/H_2O (4:1) mixture promoted with a sonication tip. Regarding the DA ratio of the obtained FLAs, it is observed that it became larger when using 2-butanol as a solvent in the LPE step (DA ~ 27.6), keeping good concentration values (*ca.* 0.279 g·L⁻¹).

4.2. Results and Discussion

The strategy designed to optimize the LPE process to obtain FLA suspensions is summarized in Figure 4.1.
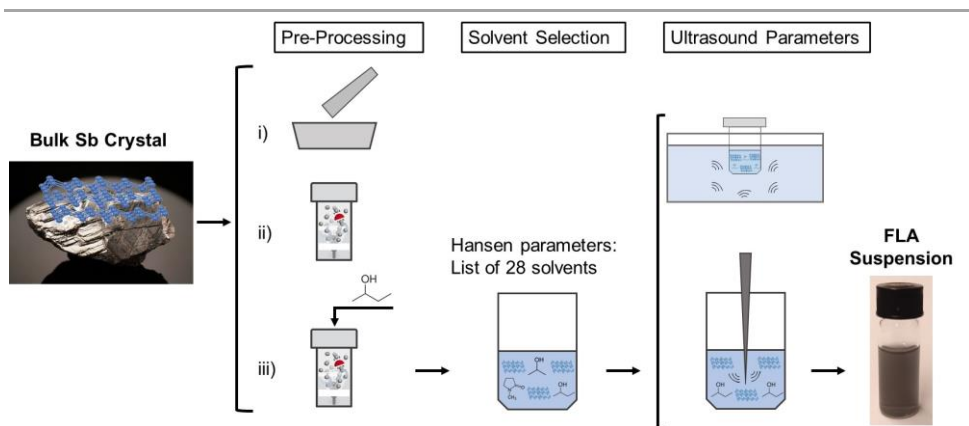

Figure 4.1 Schematic illustration of the strategy followed to optimize the LPE process to obtain FLA suspensions, involving different enchained steps. Firstly, the pre-processing using different approaches: i) grinding the bulk Sb crystals, ii) dry ball-milling the bulk Sb crystals, and iii) wet ball-milling the bulk Sb crystals. Secondly, a solvent selection based on the Hansen parameters using 28 different solvents, and thirdly, a comparison of ultrasound parameters, involving bath and tip sonication. The arrows highlight the optimum route for obtaining FLA suspensions with the highest concentration. The optical image shows a typical highly concentrated FLA suspension.

As it can be observed in Figure 4.1, this study is done attending to the three most important parameters that influence the LPE of bulk antimony crystals: i) the initial crystal size, ii) solvent used and iii) ultrasound parameters.

4.2.1. Pre-processing of bulk antimony crystals

With the aim of opening up the possibilities of application of FLAs obtained by LPE techniques, one issue that needs to be solved is the low value of the final concentration of the suspensions.

In order to enhance the FLA concentration is critical the way to process the bulk antimony crystals before the LPE process begins. Thus, in this first step, the goal is to investigate the effect of the initial particle size of the bulk antimony crystals in the final concentration of FLAs suspensions.

In this section, it is analysed three different methods of pre-processing bulk antimony crystals and how they affect in the final concentration of the FLA suspensions obtained after the LPE process. These three approaches have been selected based on previous research in this field[3,4,5,6]: i) grinding the bulk antimony crystals, ii) dry ball-milling the bulk antimony crystals and iii) wet ball-milling the bulk antimony crystals.

For evaluating the results of this step, all of the experiments have been carried out using as reference LPE conditions to analyse the final FLA concentration the optimised conditions obtained in Chapter 2: an initial antimony concentration of 0.1 g·L-1 is mixed with a 4:1 mixture of IPA/H2O. Then, the mixture is sonicated using a tip sonicator for 40 min at 400 W and 24 kHz developing the ultrasound power in pulses of 0.5 s long every 1 s. After the sonication process, suspensions are centrifuged for 3 min at 3000 rpm.

The first analysis of the three pre-processed antimony crystals is carried out by X-Ray Powder Diffraction (XRPD) and SEM to investigate if there is any change in the structure and/or the morphology. Figure 4.2 shows the XRPD patterns of the three samples, corroborating that the structure of the obtained pre-processed antimony crystals could be categorized as rhombohedral, β-phase. There are not new peaks indicating that any of the processes favour the formation of side species as antimony oxides. Figure 4.2 also confirms no significant changes between the three XRPD patterns, indicating that these processes do not affect the crystalline structure of antimony.

The only significant change among the three XRPD patterns is the relative weakening of the peak at 23.7⁰ corresponding to the (003) facet, revealing a higher degree of exfoliation along the c-axis in the wet ball-milled sample compared to the other two (see Figure 4.2, inset).
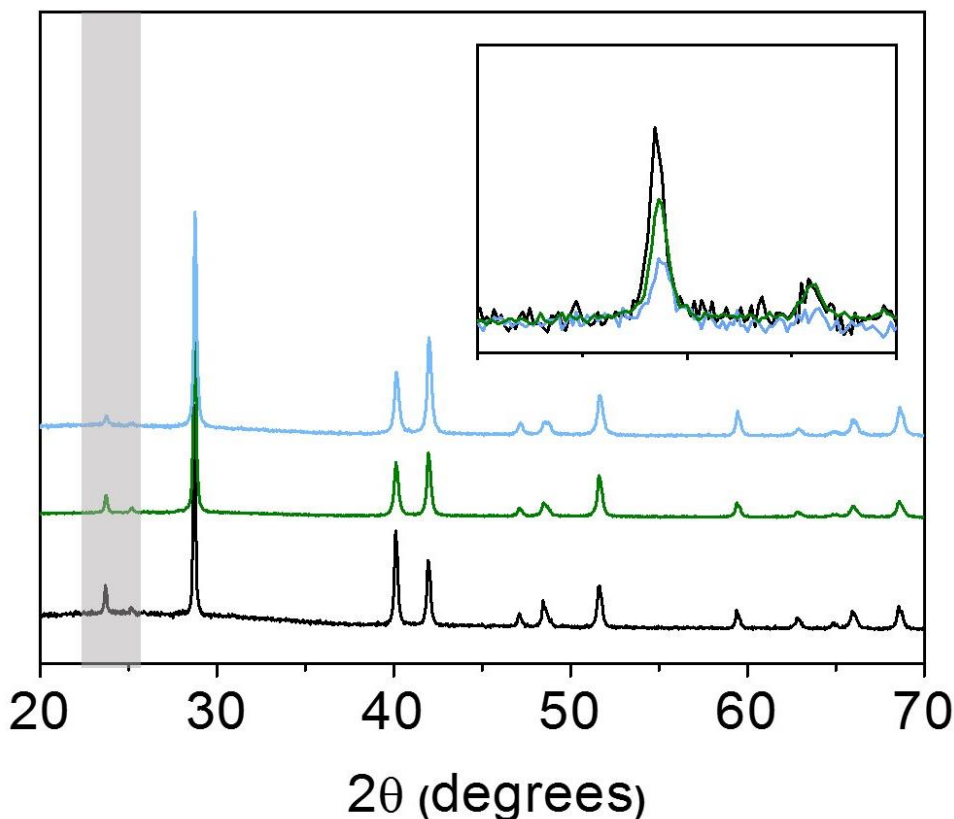

Figure 4.2 XRPD patterns of: grinded antimony crystals (black), dry ball-milled antimony crystals (green) and wet ball-milled antimony crystals in 2-butanol (blue). The inset shows a magnification of the area coloured in grey.

The morphology of the three pre-processed antimony crystals is evaluated by SEM. The analysis of the length histograms for the three samples indicates some significant differences. Thus, in the case of grinded antimony crystals (Figure 4.3a), the edges appear to be sharper than in the other two cases, and their lateral size is much larger compared to the other ones, *ca.* 5.78 µm. While for the dry ball-milled antimony crystals (Figure 4.3b) SEM images show amorphous edges and smaller lengths, *ca.* 2.07 µm, compared to the grinded ones. Remarkably, those ones obtained by wet ball-milling in 2-butanol (Figure 4.3c) presents larger lateral dimension, *ca.* 9.25 µm, but also smaller thicknesses.

Therefore, the analysis of the crystal structure and morphology of the three pre-processed antimony crystals samples, confirm that any process induced changes neither in the crystal structure nor in composition, while the particle size of the obtained antimony crystals changes from one to another.
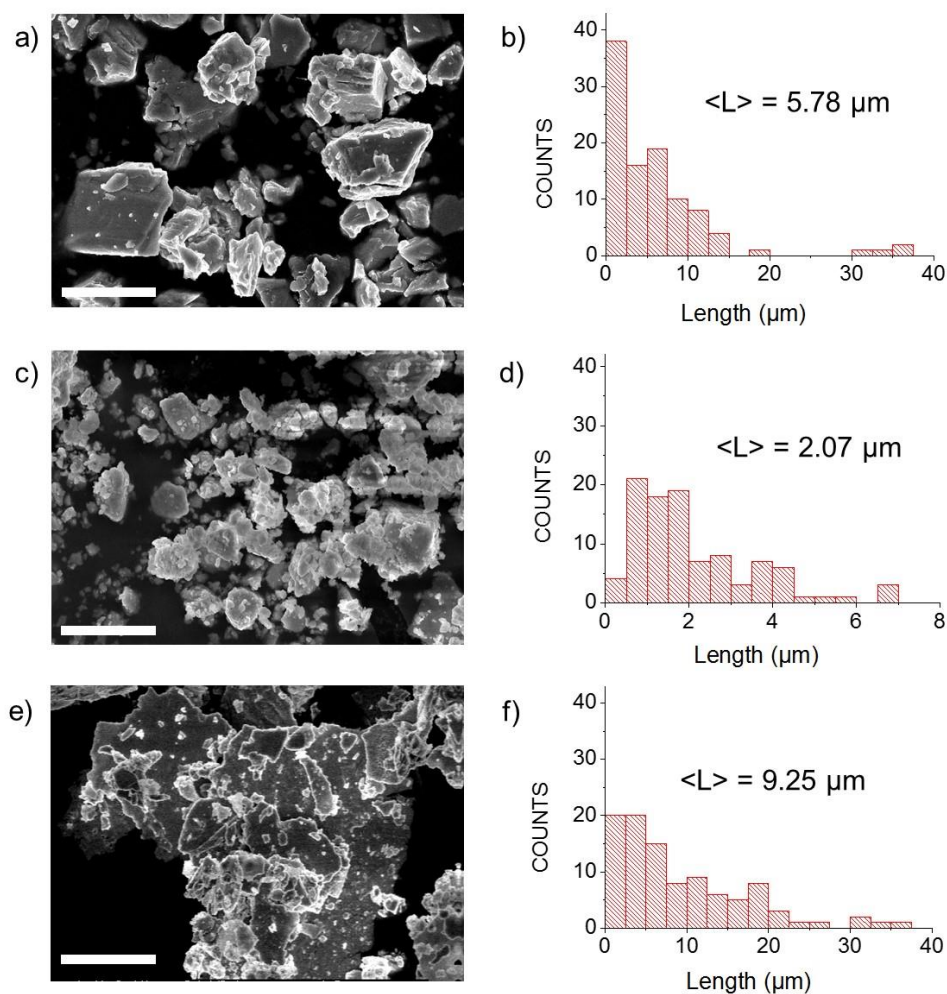
Figure 4.3 SEM images (scale bar of the SEM images equal to 5 µm) of: a) grinded antimony crystals, c) dry ball-milled antimony crystals and e) wet ball-milled antimony crystals in 2-butanol. Length histograms of the corresponding SEM images in µm of: b) grinded antimony crystals, d) dry ball-milled antimony crystals and f) wet ball-milled antimony crystals in 2-butanol.

In order to choose the best option among the different processes, the three pre-processed crystals are employed as starting material to generate suspensions in 2-butanol using the conditions described above, and then the final FLA concentration is evaluated. Figure 4.4 illustrates that the most concentrated sample is the one using the powder obtained by wet ball-milling as starting material. The concentration values are obtained by measuring the turbidity of the samples which is directly related with the concentration (Figure A4.1, page 211).

Therefore, the most appropriate pre-processing approach in order to enhance the final concentration of FLA suspensions, is the wet ball-milling of antimony crystals using 2-butanol.
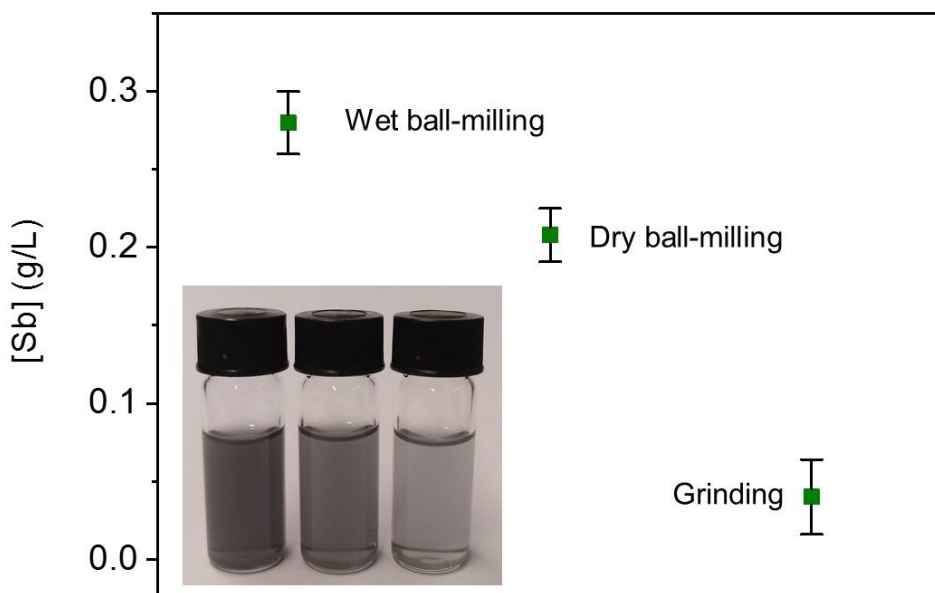

Figure 4.4 Concentration of the samples using different starting materials. The inset shows a photograph of the three different suspensions with a clear change of colour due to change on the concentration.

4.2.2. Solvent selection

It is well-known that the solvent used to exfoliate layered materials is probably the most critical parameter during the LPE process[7]. The aim of this section is to evaluate the effect of the solvent used in the LPE of antimony crystals in both, the final concentration and the DA ratio of obtained FLAs. With a focus on increasing either the concentration and/or the DA ratio of the samples, a survey of 28 pure solvents and mixtures of them with water has been tested. All the experiments are carried out using as starting material wet ball-milled antimony crystals in 2-butanol and the same reference LPE conditions used in Section 4.2.1.

It is acknowledged that in an LPE process the concentration of the suspensions is maximized when the energy cost of the exfoliation process is minimized, *i.e.* when the surface energy of the solvent matches with the surface energy of the layered crystals, as shown in Eq. (1).

$$\frac{\Delta H_{mix}}{V_{mix}} \approx \frac{2}{T_{layer}}\left(\delta_{layer} - \delta_{solvent}\right)^2 \emptyset \quad \text{Eq. (1)}$$

Where, $\delta_i = \sqrt{E_{sur}^i}$, is the square root of the component surface energy, T_{layer} is the thickness of an antimonene nanosheet and $\emptyset$ is the volume fraction.

It has been theoretically calculated a value of surface energy for antimony equal to 148.8 mJ·m^{-2} (Figure A4.2, page 212). Obviously, this theoretical value does not consider the dynamics of the LPE process, so it is expected to be reasonably higher compared to the one reported experimentally[8]. For this reason, in the initial survey are selected solvents with a wide variety of surface tensions (the surface energy of the solvents can be calculated from $\gamma = E_{sur}^{sol} - T S_{sur}^{sol}$, using an universal value for surface entropy of ~0.1 mJ·m^{-2}·K^{-1})[9], but intentionally are also included some solvents known to be good dispersants for layered materials (Table A4.3, page 213).

Every experiment has been run by triplicate and the concentration values represent the mean value of the three results. Samples prepared with SDS and SC have been discarded from the initial survey because it could not be observed Tyndall effect in their colourless suspensions, indicating that the exfoliation did not occur.

To choose the most suitable solvent from the initial survey, the focus is put at first in the final FLA concentration obtained after centrifuging the samples. Figure 4.5a shows the values of concentration, obtained using turbidity measurements as a function of the surface tension of each solvent.

Firstly, it is observed that almost all the solvents tested can disperse some amount of antimony. However, the concentration of the dispersions increased for solvents with surface tensions in the range of 23-42 mJ·m^{-2}, what means equivalent surface energy values in the range of 52-71 mJ·m^{-2}. These values are reasonably close to the calculated surface energy value for antimony, *ca.*148.8 mJ·m^{-2}. On the other hand, it is well-known that surface energy calculations overestimate the surface energy of layered materials due to the assumptions of ideality in a heterogeneous process, what is our case. This can be easily seen in the large spread of surface energy values for graphite reported in literature so far[10,11].

Even though the analysis of the concentration as a function of the surface tension is a good starting point, there is an evident problem with the data from Figure 4.5a, many solvents are included with apparently correct surface tension value, but low concentration. This issue is something commonly observed in LPE of other layered materials, indicating that some other parameters need to be considered to rationalize the effect of the solvent in the material exfoliation [12,13].

To further investigate the mechanism of the exfoliation/dispersion process, is necessary to evaluate the solute-solvents interactions, by calculating the Hansen solubility parameters (δ_H, δ_P, and δ_D), and also calculating the best well-known solubility parameter, the Hildebrand parameter (δ_T). Both group of parameters are related as shown in Eq. (2).

$$\delta_T{}^2 = \delta_H{}^2 + \delta_P{}^2 + \delta_D{}^2 \qquad \text{Eq. (2)}$$

Where δ_T is the Hildebrand parameter, δ_H is the H-bonding contribution, δ_P is the polar contribution and δ_D is the non-polar or dispersive contribution to the Hansen solubility parameters. These parameters are calculated for the initial survey of solvents and plotted them against the concentration values (Figure 4.5b-e).

Figure 4.5b shows an almost a defined peak between 22-30 MPa$^{1/2}$ for the δ_T parameter, but this result has the same problem of the surface tension, some solvents with a calculated value of δ_T within this range have low concentration. This problem can be rationalized considering that, as in the case of the surface tension, the Hildebrand parameter is too rough to fully describe the exfoliation/dispersion process. However, it can be easily observed how according to the Hansen's model, there is a defined peak for δ_D parameter close to 17 MPa$^{1/2}$, and for the other parameters it can also be found a peak between 7-22 MPa$^{1/2}$. These results clearly show that the best solvents to enhance the concentration of FLA suspensions should match with this set of Hansen solubility parameters (Table 4.1).

Table 4.1 Range of Hansen solubility parameters for promising solvents to obtain FL antimonene suspensions.

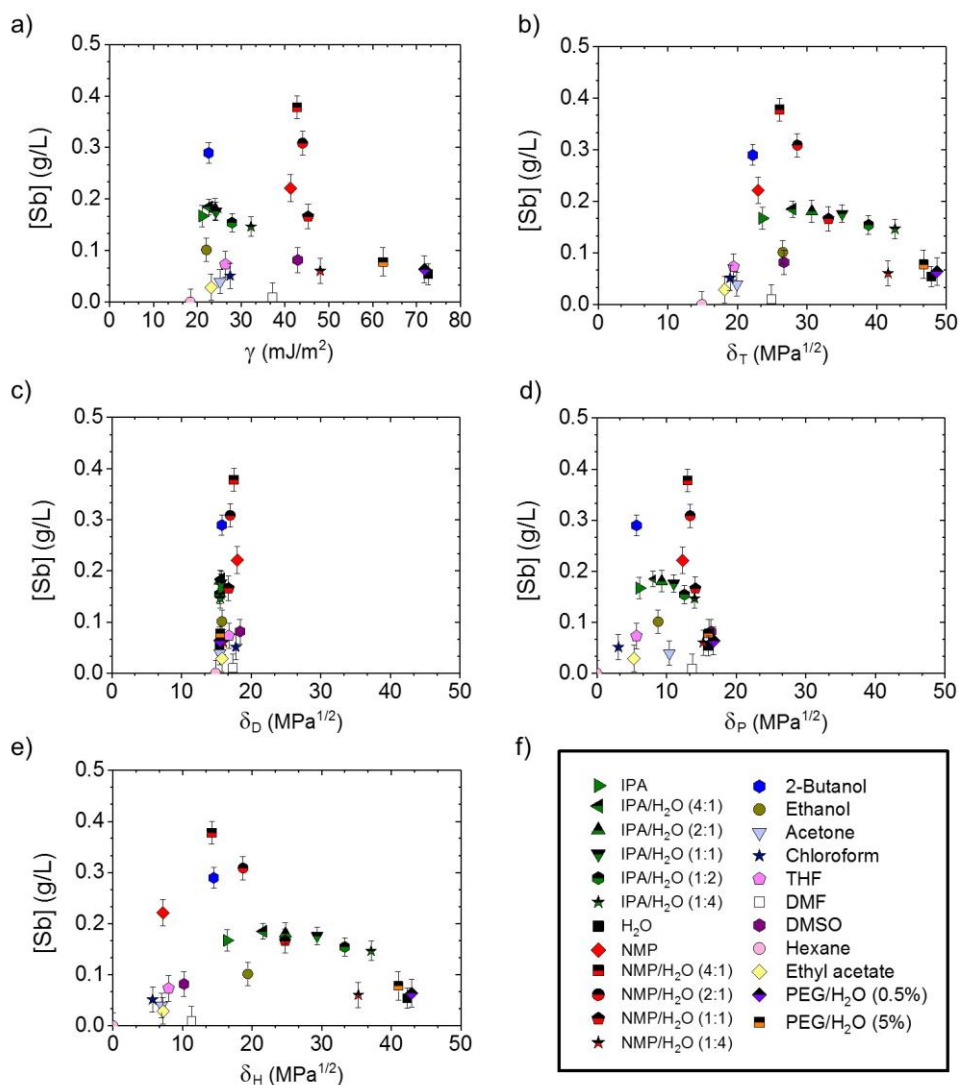| Range of δ_D (MPa$^{1/2}$)	Range of δ_P (MPa$^{1/2}$)	Range of δ_H (MPa$^{1/2}$)
16-18	7-13	7-22

Figure 4.5 Concentration of FLA in suspension after tip sonication and centrifugation, [Sb] (g/L), plotted as a function of: a) surface tension of the solvents, γ (mJ/m^2), b) Hildebrand's solubility parameter, δ_T (MPa$^{1/2}$), c) dispersive or non-polar contribution to the Hansen parameters, δ_D (MPa$^{1/2}$), d) polar contribution to the Hansen parameters, δ_P (MPa$^{1/2}$) and H-bonding contribution to the Hansen parameter, δ_H (MPa$^{1/2}$). f) Legend of solvents appearing in Figure 4.5a-e.

Taking all the discussed above into account, it is remarkable the case of NMP/H$_2$O (4:1) that gives rise a concentration value of 0.368 g·L^{-1} which is *ca.* 30 times higher than the highest previously reported for LPE of antimony crystals (*ca.* 0.014 g·L^{-1}).[3] It is also worth mentioning that the adjustment of the ratio between the organic solvent and water in the mixtures determines the optimal concentration. Thus, the 4:1 and 2:1 ratios of solvent/water mixtures, in NMP case, matches better with the set of Hansen solubility parameters described above and in consequence gives higher concentration values (Figure 4.5b-e).

Therefore, the solvents that give rise to the highest concentration values are NMP, 2-propanol (IPA) and 2-butanol, and some mixtures of them with water. This result is consequence of two factors: *i)* the rationally matching of the solvents with the surface energy of antimony and, even more remarkably, *ii)* with the set of Hansen solubility parameters.

It is obvious that another important limiting factor that determine the potential use of the FLA suspensions for several applications is their stability with time, *i.e.* particle aggregation. Therefore, the samples with the highest FLA concentration from the initial survey are measured their concentration decay at different times (1, 24, 48 and 168 h). Figure 4.6 shows that most of the suspensions evaluated undergo a decrease of its concentration of *ca.* 10-20 % and 50 % upon standing the suspension at 20 ºC for 1 or 2 days, respectively, and almost became stable for weeks after 2 days. In terms of suspensions usability, it seems a reasonably good result for most of the applications, but it is even better because it is observed that after long times of sedimentation, the suspensions recover their initial concentration values by re-sonicating them for 5 min.
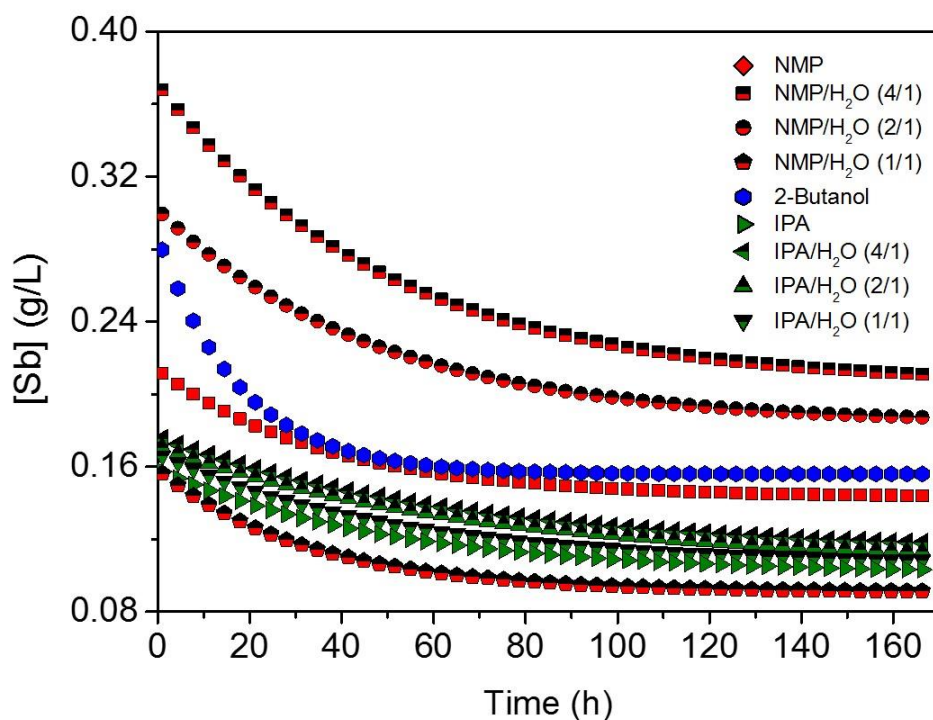
Figure 4.6 Concentration of FLA in suspension after centrifugation, [Sb] (gL^{-1}), plotted *versus* sedimentation time (h) of the samples prepared with the solvents described in the legend.

Another important issue is the effect caused in the concentration of the suspension when the solvent/water ratio is changed. Figure 4.6 shows that for the mixture NMP/H$_2$O, 4:1 and 2:1 ratio are optimum in terms of concentration compared to the other ratios, but in the case of IPA/H$_2$O the differences between using different ratios are almost neglectable.

The other aspect that has to be taken into account for the solvent selection is the DA ratio. The morphology of the nanosheets obtained in the suspensions has been evaluated using AFM.

Figure 4.7-8 show a statistical AFM analysis for the drop-casted suspensions on SiO_2 with the highest FLA concentration, based on histograms over 150 FLAs for each sample. The histograms show that the mean length, <L>, of most of FLAs contained in the samples is ~ 300 nm while the mean height, <H> is ~20 nm.
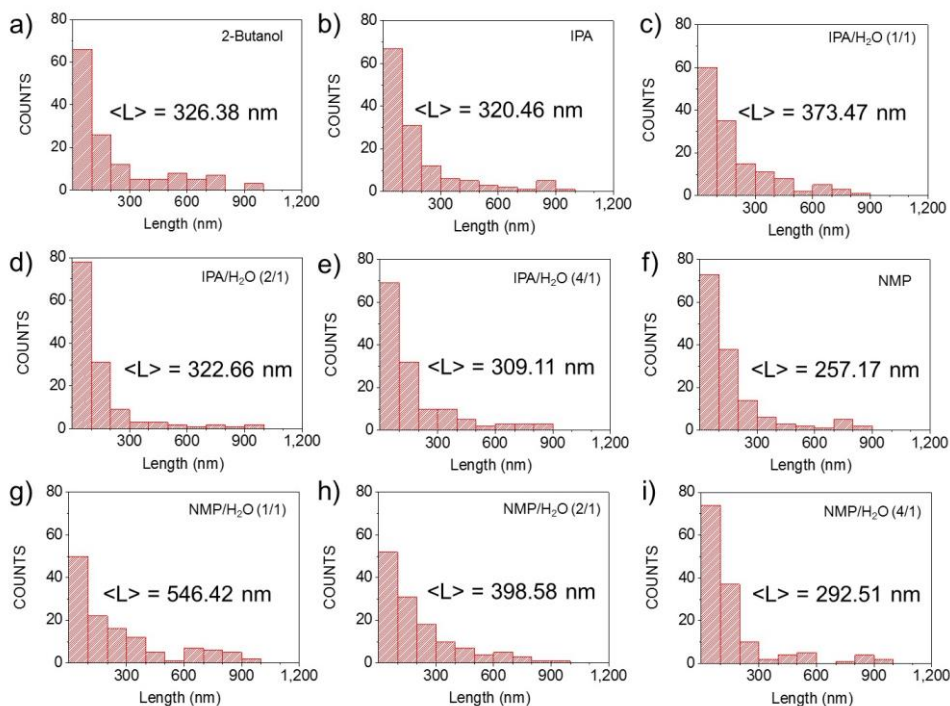

Figure 4.7 Length histogram of the FLAs contained in the different samples obtained using: a) 2-butanol, b) IPA, c) IPA/H_2O (1:1), d) IPA/H_2O (2:1), e) IPA/H_2O (4:1), f) NMP, g) NMP/H_2O (1:1), h) NMP/H_2O (2:1) and i) NMP/H_2O (4:1). <L> represents the mean length value in nm.

It has to be considered that using AFM to measure heights it is being evaluated the apparent height, which overestimate the real nanosheet thickness[14].

A closer examination of the results collected in Figure 4.8 shows a limiting minimum height coming from the LPE process which corresponds to *ca.* 4-6 nm using 2-butanol as solvent which is associated with a maximum length of *ca.* 320 nm. However, the most typical apparent heights obtained for those solvents providing good concentration values are in the range of 15-22 nm while their length almost shows similar lengths values, *ca.* 250-375 nm.
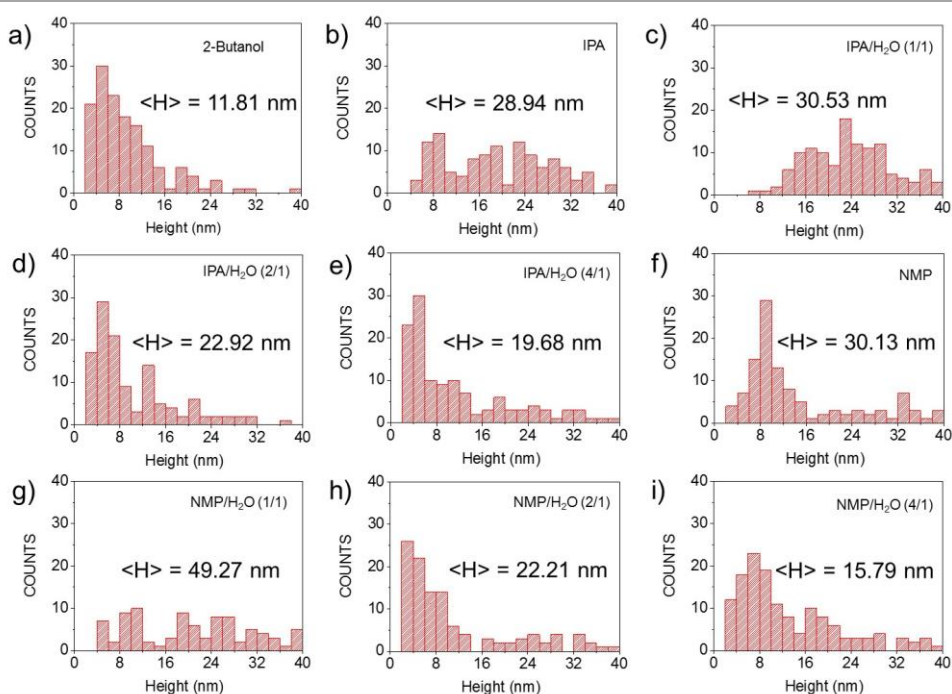

Figure 4.8 Height histogram of the FLAs contained in the different samples obtained using: a) 2-butanol, b) IPA, c) IPA/H_2O (1:1), d) IPA/H_2O (2:1), e) IPA/H_2O (4:1), f) NMP, g) NMP/H_2O (1:1), h) NMP/H_2O (2:1) and i) NMP/H_2O (4:1). <H> represents the mean height value in nm.

The highest DA ratio (Figure 4.9) correspond to the nanosheets isolated from the suspensions obtained using 2-butanol as solvent (DA *ca.* 27.6), while for the samples prepared with IPA and NMP there is an optimal proportion of the solvent/water mixture that maximizes the DA ratio, and that is the 4:1 proportion resulting in DA ratios of *ca.* 15.7 and *ca.* 18.52, respectively.
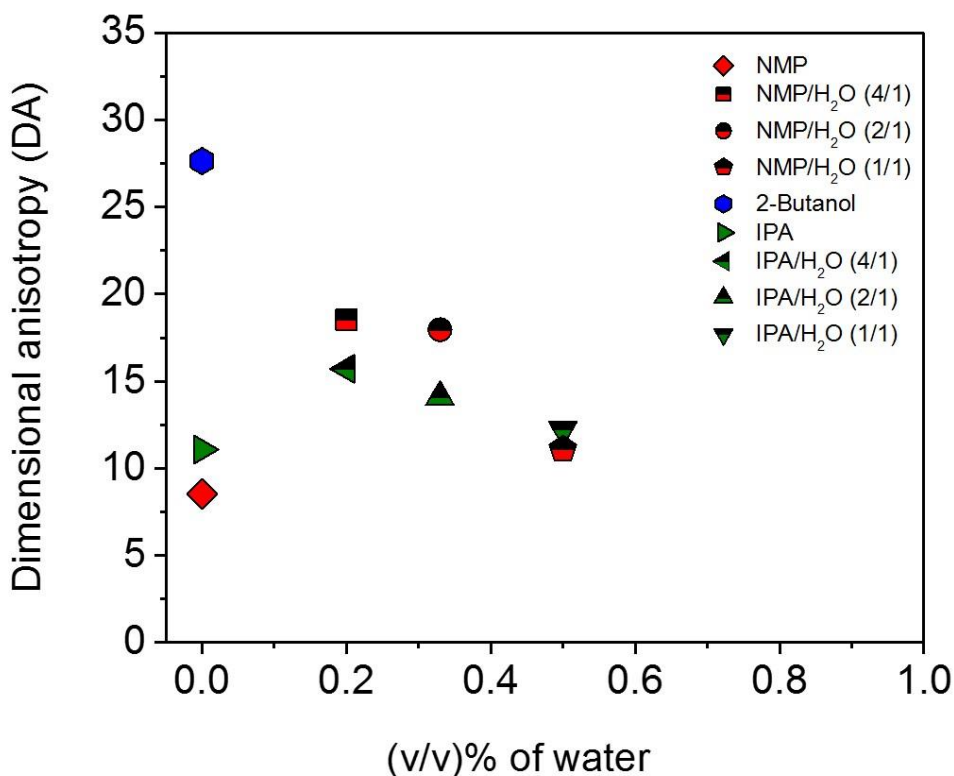

Figure 4.9 Plot of the DA ratio of the nanosheets as a function of the volume fraction (%) of water in the solvent mixtures.

Therefore, considering all the factors so far analysed, it is observed that the best results in terms of concentration, correspond to those obtained using as solvent a mixture of 4:1 NMP/H_2O, with a final concentration of 0.368 gL^{-1} and a DA ratio of *ca.* 18.52. However, 2-butanol seems to be the most suitable solvent because shows an excellent compromise between concentration, 0.279 gL^{-1}, and DA ratio, *ca.* 27.6.

4.2.3. Ultrasound parameters

Finally, in order to improve the LPE process it is evaluated the effect, on the concentration and in the DA ratio of the FLA suspensions, using different ultrasound techniques: i) sonication tip and ii) ultrasonic bath.

It is well-stablished that for layered inorganic materials, tip sonication is preferred over bath sonication mainly due to the higher production rates. However, bath sonication may offer a lower-cost alternative to tip sonication. The energy input into the sample is lower in the case of bath sonication, as it is less localized, for that reason less material fragmentation (breaking of bonds in the nanosheet) can be expected. With this technique, longer processing times are required, compared to tip sonication, to achieve an equivalent concentration of dispersed material and, in general, the process is less reproducible[15].

For this analysis is used as starting material, wet ball-milled antimony crystals in 2-butanol and also 2-butanol as LPE solvent. The rest of LPE parameters are exactly the same than in the previous two sections (0.1 gL^{-1} of antimony initial concentration, 40 min of sonication time and 3000 rpm for 3 min of centrifugation). The results showed that using ultrasonic tip the obtained concentration (~ 0.289 gL^{-1}), is higher than the one obtained using ultrasonic bath (~ 0.262 gL^{-1}).

Figure 4.10 displays the DA ratio for both samples from the mean statistic values of morphology, obtaining a much lower DA ratio using the ultrasonic-bath, *ca.* 7.76, than using the sonication tip, *ca.* 27.6. The lower DA ratio means a decrease in the lateral dimensions of the nanosheets while they show similar thicknesses (Figure 4.10). Both results can be rationalized considering the experimental differences between both techniques. Thus, while the sonication tip approach delivers energy to the dispersion medium directly, when using ultrasonic bath the energy needs to go through the solvent medium and the flask where is the material to exfoliate it[2].

Figure 4.10 Height histogram, length histogram and plot of the length as a function of the height of the FLAs contained in the samples prepared using different devices: a), b), c) sonication tip and d), e), f) ultrasonic bath.

Finally, it is also tested the effect of the ultrasonic wave amplitude of the sonication tip in the LPE process. Results show that there are not many differences in terms of concentration between using one ultrasonic wave amplitude or another.

However, it seems that the higher is the amplitude, the higher is the concentration: $[Sb]_{100\%} = 0.289$ gL^{-1}; $[Sb]_{50\%} = 0.274$ gL^{-1} and $[Sb]_{50\%} = 0.252$ gL^{-1}. While the DA ratios of the samples obtained at different ultrasonic wave amplitudes are slightly different for the nanosheets obtained at higher ultrasonic wave amplitude which showed the highest DA ratio: $DA_{100\%} = 27.6$; $DA_{50\%} = 23.2$; and $DA_{20\%} = 19.9$. Therefore, lateral dimensions are larger when decreasing the sonication amplitude but also the thicknesses (Figure 4.11).
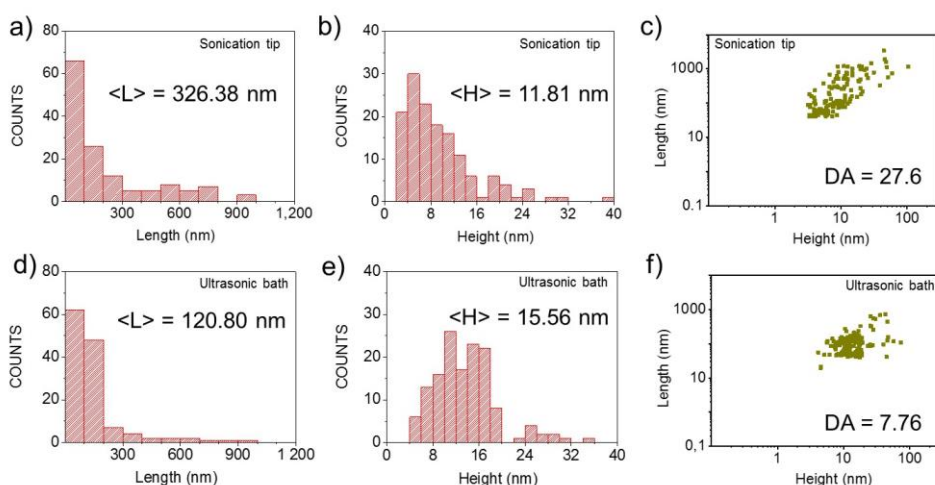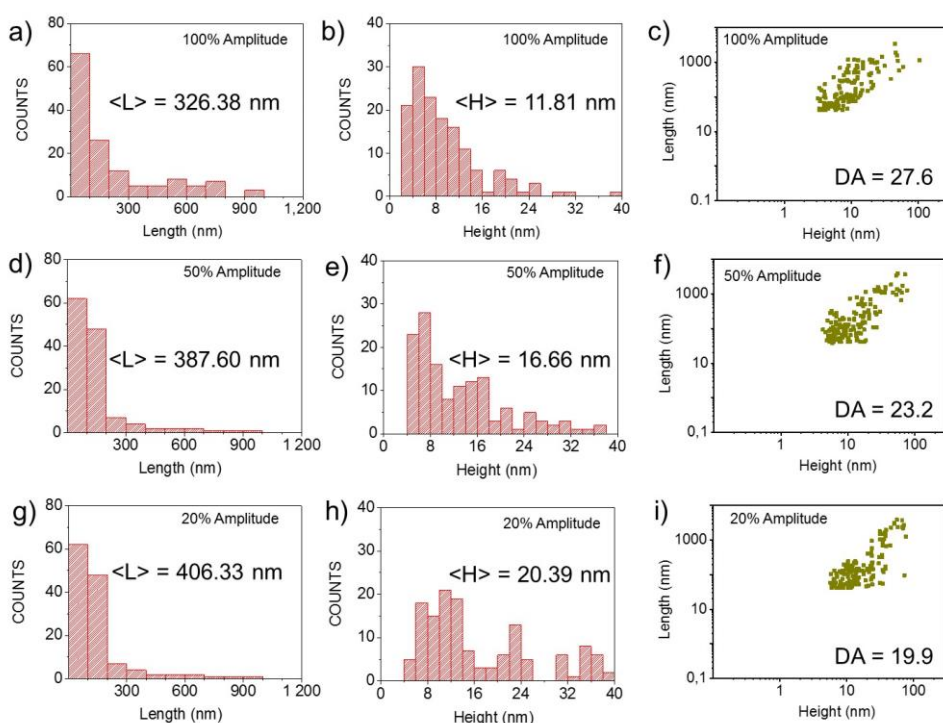

Figure 4.11 Height histogram, length histogram and plot of the length as a function of the height of the FLAs contained in the samples prepared using different wave amplitudes: a), b), c) 100%, d), e), f) 50% and g), h), i) 20%.

4.2.4. FLAs quality

The energy used to assist the exfoliation in the LPE process can affect the 2D material quality generating atomic defects in the structure of the nanosheet or generating some chemical changes, e.g. partial surface oxidization as it is described in Chapter 3. In this section, it is evaluated the quality of the FLAs isolated under the LPE optimal experimental conditions: wet ball-milled antimony crystals in 2-butanol as starting material; 2-butanol as LPE solvent with 40 min of sonication and 3000 rpm for 3 min for centrifugation using an ultrasonic tip at 100 % amplitude.

To further characterize the quality of the samples obtained using this optimal LPE parameters, it is performed SRM. The SRM mappings revealed the representative main phonon peaks, the A^1_g mode at 149.8 cm^{-1} and E_g mode at 110 cm^{-1}, even for the thinnest nanosheets *ca.* 4 nm, with no signature of oxidation (*i.e.* peaks related to the formation of Sb_2O_3 or Sb_2O_5). A phonon relaxing effect is detected when the sample thickness decreases from the bulk to *ca.* 4 nm, in good agreement with theoretical predictions and recent reports (Figure 4.12)[16,17]. The correlation between SRM and AFM shown in Figure 4.13 represents the state-of-the-art of FLA nanosheet with the smaller thickness so far reported[16,4].
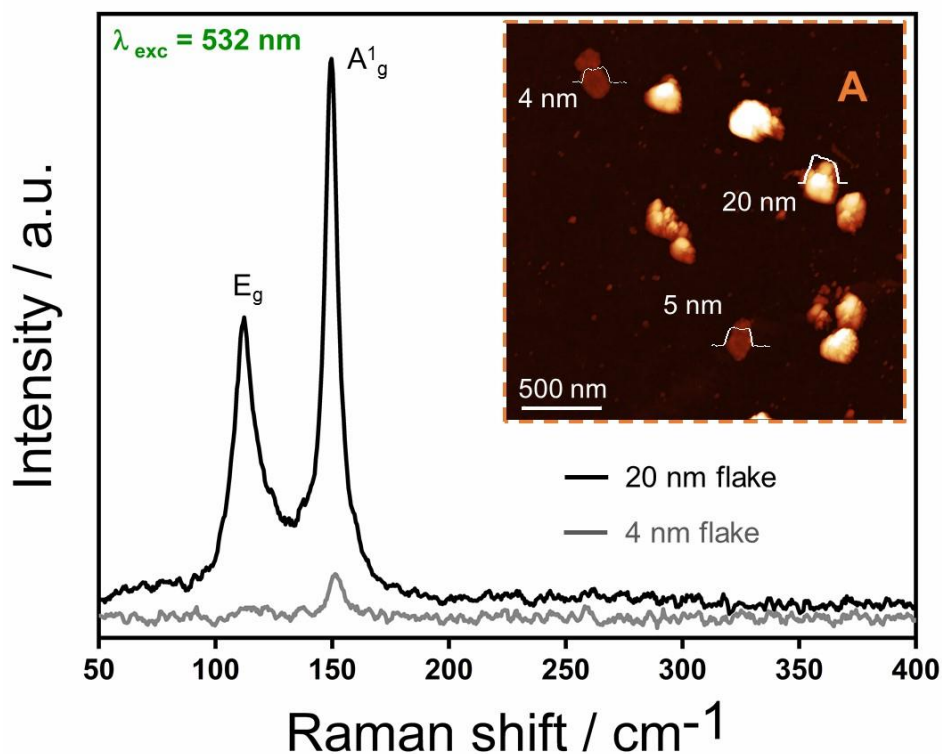
Figure 4.12 Single-point spectra measured at different thicknesses according to the topographic AFM image (inset) of the same area studied in Figure 1.13c.

Even though all FLAs shown in Figure 4.13a can be easily correlated with the A^1_g signals from Figure 4.13b, is worth mentioning that the resolution of the mapping has a broadening in the signal that could be assigned to nanosheet aggregation. However, this effect can be easily corrected by correlating it with the AFM measured distances.
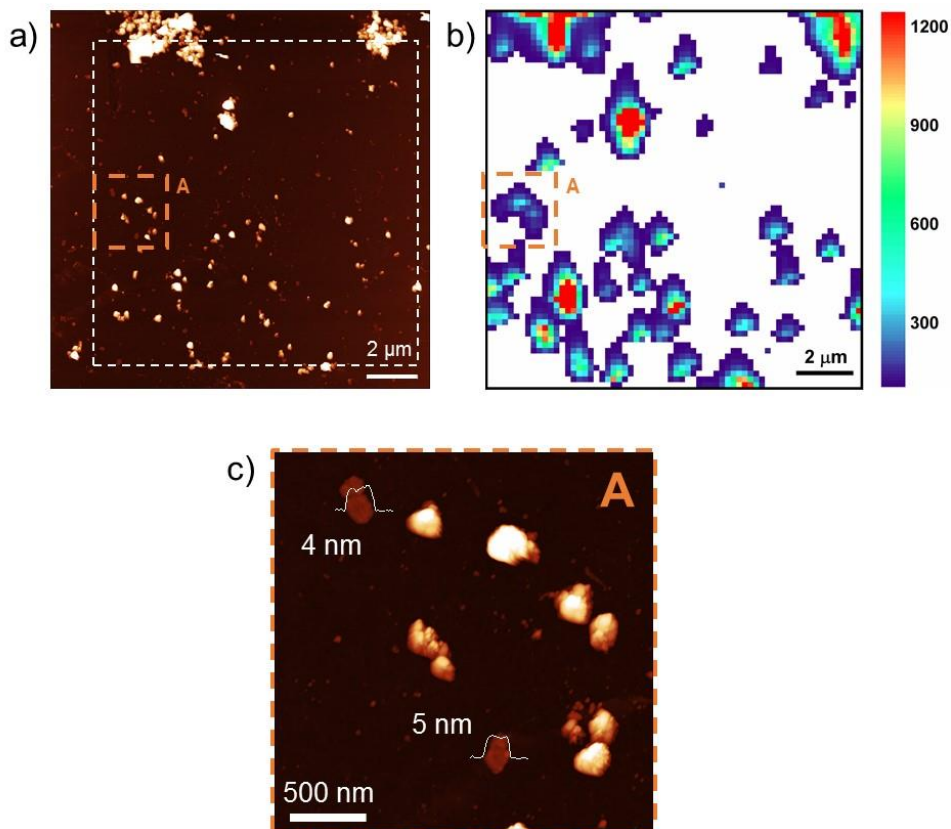
Figure 4.13 a) Representative AFM image of the FLAs obtained using the optimal parameters of the LPE process. b) The corresponding Raman A^1g (λ_{exc}=532 nm) mapping of FLAs contained in the area dotted in white in (a) (>14000 single point spectra over a surface area of 13 μm^2 using a step size of 0.2 μm). c) AFM image of the small area (A) dotted in orange in (a) and (b) showing the height profiles of *ca.* 4 and 5 nm, respectively.

The crumpled morphology observed by AFM has been further confirmed by TEM measurements, showing lateral dimensions of *ca.* 300 nm (Figure 1.14a-b). XEDS measurements of a selected area corroborated their composition, showing small signals of oxygen (Figure 1.14c).

Indeed, a careful examination of the Raman mappings reveals that for some flakes exhibiting high intensity, it is possible to detect some Raman signatures attributed to antimony oxides, *ca.* 255 cm^{-1}, tentatively related to the A_g mode of Sb_2O_3.
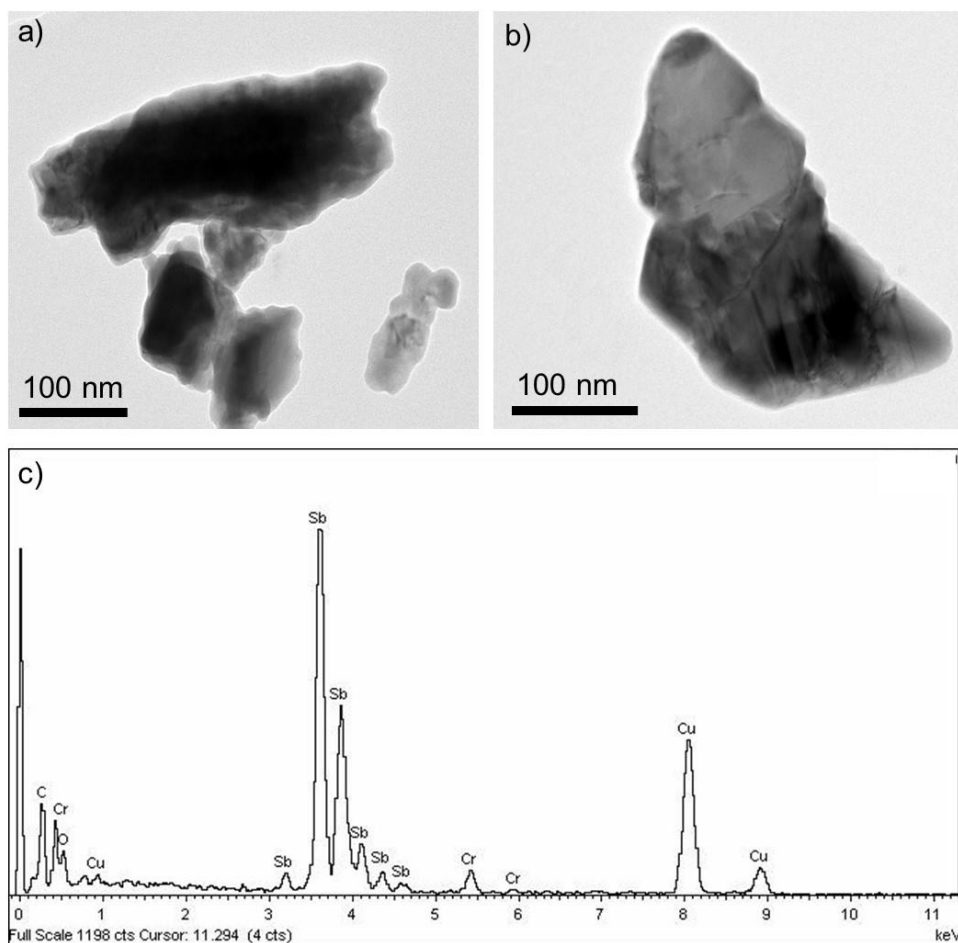

Figure 1.14 a), b) TEM image of FLAs obtained using the optimal conditions of the LPE process, c) X-Ray Energy Dispersive Spectroscopy (XEDS) microanalysis of FLAs.

In order to verify the oxidation of FLAs, this sample was investigated by XPS analysis, showing weak $3d_{3/2}$ and $3d_{5/2}$ signals of antimony in oxidation state zero at 528.8 eV for the $3d_{5/2}$ level, along with significant contributions from Sb in higher oxidation states (mainly Sb_2O_3) at around 530.8 eV (Figure 1.15). Moreover, among the solvents showing optimal Hansen parameters investigated in this work, NMP has been reported as an excellent protective solvent against oxidation for 2D materials. Along this front, other 2D-pnictogens such as black phosphorus has been successfully passivized with NMP for several days under environmental conditions[18–20]. Therefore, sample prepared with pure NMP was also analysed by XPS to investigate if it has the same effect in antimonene. Similarly to the ionic-liquid protected FLA,[21] next to the broad O 1s signal at 533 eV from the surface enriched NMP contamination, the Sb 3d region between 526 and 546 eV of the Sb-NMP sample reveals very weak Sb $3d_{3/2,5/2}$ signals at slightly lower binding energies (see inset in Figure 1.15). These results suggest a less oxidized FLA, thus, the formation of a protective NMP layer a few-nanometers thick on the surface of the FLAs.
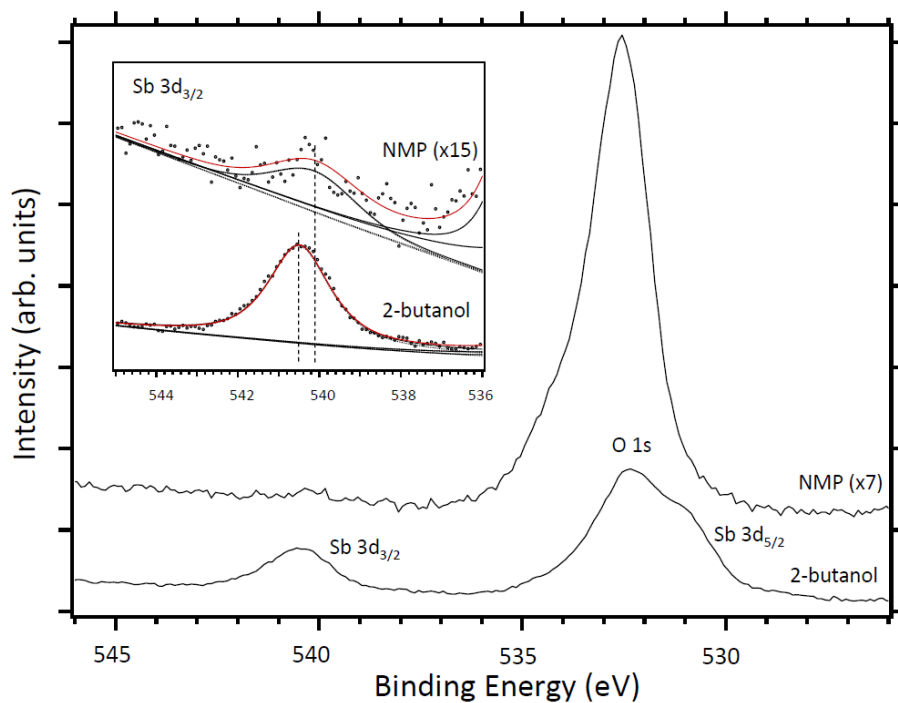
Figure 1.15 XPS Sb 3d and O 1s region of FLA samples prepared using NMP and 2-butanol, spectra are offset and rescaled for sake of clarity. The inset shows a magnification of the Sb $3d_{3/2}$ peak for both samples showing a shift to lower binding energies in the case of the sample prepared with NMP of *ca.* 0.4 eV.

4.3. Conclusions

In this chapter, it has been reported a systematic study that optimize several parameters of the exfoliation process of bulk antimony crystals with the aim to produce stable FLA suspensions with high nanosheets concentration as well as high DA ratio.

The results show that the pre-processing of the material affects importantly to the final concentration of the suspension of FLA, being the optimal pre-process the one that use "wet-ball milling" with 2-butanol.

It has also been observed that the solvent plays a crucial role in the LPE process. From the 28 solvents preselected based on the Hansen solubility parameters as well as other experimental observations, the highest concentration value is obtained using a mixture of NMP/H_2O in a (4:1) ratio, *ca.* 0.368 g/L, while largest DA value is obtained using 2-butanol, DA ratio of *ca.* 27.6. However, both solvents seem to be suitable for most of the potential applications of FLA. Characterization of the nanosheets obtained with these solvents showed that using: *i)* 2-butanol <L> = 326.38 nm, <H> = 11.81 nm with ~ 50 % of the nanosheet with heights between 2-8 nm, and lateral dimensions between 40-300 nm, being the nanosheets with smallest height those of *ca.* 3.6 nm. and lateral dimensions of *ca.* 98 nm; and *ii)* NMP/water (4:1) <L> = 292.51 nm, <H> = 15.79 nm with ~50 % of the nanosheet with heights between 2-10 nm, and lateral dimensions between 60-250 nm, being the nanosheets with smallest height those of *ca.* 4.3 nm, and lateral dimensions of *ca.* 72 nm.

Finally, it is also noticed that using a sonication tip with an ultrasonic wave amplitude of 100%, the concentration and the DA of the samples also increases. It is carefully evaluated the high quality of the antimonene isolated from this optimal experimental set up using the state-of-the-art spectroscopic, analytical and microscopic techniques.

4.3.1. Future prospects

This project has provided a complete understanding on the LPE of bulk antimony crystals. Taking into account the reported results in this study, the following step to continue with this issue would be the scale-up process of this technology. Furthermore, these results paved the way to new potential applications for antimonene-based technologies that are already being analysed.

4.4. References

(1)   Nicolosi, V.; Chhowalla, M.; Kanatzidis, M. G.; Strano, M. S.; Coleman, J. N. Liquid Exfoliation of Layered Materials. *Science* **2013**, *340* (6139), 1226419–1226419.

(2)   Backes, C.; Higgins, T. M.; Kelly, A.; Boland, C.; Harvey, A.; Hanlon, D.; Coleman, J. N. Guidelines for Exfoliation, Characterization and Processing of Layered Materials Produced by Liquid Exfoliation. *Chem. Mater.* **2017**, *29* (1), 243–255.

(3)   Martínez-Periñán, E.; Down, M. P.; Gibaja, C.; Lorenzo, E.; Zamora, F.; Banks, C. E. Antimonene: A Novel 2D Nanomaterial for Supercapacitor Applications. *Adv. Energy Mater.* **2018**, *8* (11), 1702606.

(4)   Gibaja, C.; Rodriguez-San-Miguel, D.; Ares, P.; Gómez-Herrero, J.; Varela, M.; Gillen, R.; Maultzsch, J.; Hauke, F.; Hirsch, A.; Abellán, G.; et al. Few-Layer Antimonene by Liquid-Phase Exfoliation. *Angew. Chem., Int. Ed.* **2016**, *55* (46), 14345–14349.

(5)   Sun, X.; Song, Z.; Liu, S.; Wang, Y.; Li, Y.; Wang, W.; Lu, J. Sub-5 Nm Monolayer Arsenene and Antimonene Transistors. *ACS Appl. Mater. Interfaces* **2018**, *10* (26), 22363–22371.

(6)   Tao, H.; Zhang, Y.; Gao, Y.; Sun, Z.; Yan, C.; Texter, J. Scalable Exfoliation and Dispersion of Two-Dimensional Materials – an Update. *Phys. Chem. Chem. Phys.* **2017**, *19* (2), 921–960.

(7)   Coleman, J. N.; Lotya, M.; O'Neill, A.; Bergin, S. D.; King, P. J.; Khan, U.; Young, K.; Gaucher, A.; De, S.; Smith, R. J.; et al. Two-Dimensional Nanosheets Produced by Liquid Exfoliation of Layered Materials. *Science* **2011**, *331* (6017), 568–571.

(8)   Wang, X.; He, J.; Zhou, B.; Zhang, Y.; Wu, J.; Hu, R.; Liu, L.; Song, J.; Qu, J. Bandgap-Tunable Preparation of Smooth and Large Two-Dimensional Antimonene. *Angew. Chem., Int. Ed.* **2018**, *57* (28), 8668–8673.

(9)   Hernandez, Y.; Nicolosi, V.; Lotya, M.; Blighe, F. M.; Sun, Z.; De, S.; McGovern, I. T.; Holland, B.; Byrne, M.; Gun'Ko, Y. K.; et al. High-Yield Production of Graphene by Liquid-Phase Exfoliation of Graphite. *Nat. Nanotechnol.* **2008**, *3* (9), 563–568.

(10)   Benedict, L. X.; Chopra, N. G.; Cohen, M. L.; Zettl, A.; Louie, S. G.; Crespi, V. H. Microscopic Determination of the Interlayer Binding Energy in Graphite. *Chem. Phys. Lett.* **1998**, *286* (5–6), 490–496.

(11)   Bergin, S. D.; Nicolosi, V.; Streich, P. V.; Giordani, S.; Sun, Z.; Windle, A. H.; Ryan, P.; Niraj, N. P. P.; Wang, Z. T. T.; Carpenter, L.; et al. Towards Solutions of Single-Walled Carbon Nanotubes in Common Solvents. *Adv. Mater.* **2008**, *20* (10), 1876–1881.

(12)   Hernandez, Y.; Lotya, M.; Rickard, D.; Bergin, S. D.; Coleman, J. N. Measurement of Multicomponent Solubility Parameters for Graphene Facilitates Solvent Discovery. *Langmuir* **2010**, *26* (5), 3208–3213.

(13)   Nicolosi, V.; Chhowalla, M.; Kanatzidis, M. G.; Strano, M. S.; Coleman, J. N. Liquid Exfoliation of Layered Materials. *Science* **2013**, *340* (6139), 1226419–1226419.

(14)   Nemes-Incze, P.; Osváth, Z.; Kamarás, K.; Biró, L. P. Anomalies in Thickness Measurements of Graphene and Few Layer Graphite Crystals by Tapping Mode Atomic Force Microscopy. *Carbon N. Y.* **2008**, *46* (11), 1435–1442.

(15)   Backes, C.; Higgins, T. M.; Kelly, A.; Boland, C.; Harvey, A.; Hanlon, D.; Coleman, J. N. Guidelines for Exfoliation, Characterization and Processing of Layered Materials Produced by Liquid Exfoliation. *Chem. Mater.* **2017**, *29* (1), 243–255.

(16)   Ares, P.; Palacios, J. J.; Abellán, G.; Gómez-Herrero, J.; Zamora, F. Recent Progress on Antimonene: A New Bidimensional Material. *Adv. Mater.* **2017**, *1703771*, 1–27.

(17)   Fortin-Deschênes, M.; Waller, O.; Menteş, T. O.; Locatelli, A.; Mukherjee, S.; Genuzio, F.; Levesque, P. L.; Hébert, A.; Martel, R.; Moutanabbir, O. Synthesis of Antimonene on Germanium. *Nano Lett.* **2017**, *17* (8), 4970–4975.

(18)   Hanlon, D.; Backes, C.; Doherty, E.; Cucinotta, C. S.; Berner, N. C.; Boland, C.; Lee, K.; Harvey, A.; Lynch, P.; Gholamvand, Z.; et al. Liquid Exfoliation of Solvent-Stabilized Few-Layer Black Phosphorus for Applications beyond Electronics. *Nat. Commun.* **2015**, *6*, 8563.

(19)   Kang, J.; Wood, J. D.; Wells, S. A.; Lee, J.-H.; Liu, X.; Chen, K.-S.; Hersam, M. C. Solvent Exfoliation of Electronic-Grade, Two-Dimensional Black Phosphorus. *ACS Nano* **2015**, *9* (4), 3596–3604.

(20)   Abellán, G.; Wild, S.; Lloret, V.; Scheuschner, N.; Gillen, R.; Mundloch, U.; Maultzsch, J.; Varela, M.; Hauke, F.; Hirsch, A. Fundamental Insights into the Degradation and Stabilization of Thin Layer Black Phosphorus. *J. Am. Chem. Soc.* **2017**, *139* (30), 10432–10440.

(21)   Lloret, V.; Rivero-Crespo, M. Á.; Vidal-Moya, J. A.; Wild, S.; Doménech-Carbó, A.; Heller, B. S. J.; Shin, S.; Steinrück, H.; Maier, F.; Hauke, F.; et al. Few Layer 2D Pnictogens Catalyze the Alkylation of Soft Nucleophiles with Esters. *Nat. Commun.* **2019**, *10* (1), 509.

Chapter 5: Study of Few-Layer Antimonene properties and its application

FLA
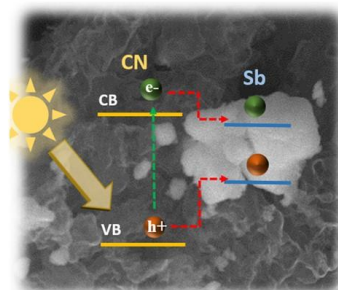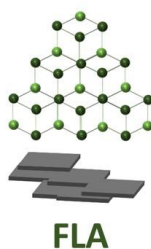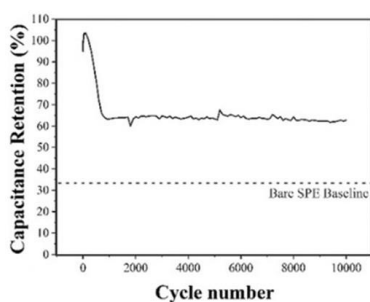
Chapter 5: Study of Few-Layer Antimonene properties and its application

5.1. Introduction

Antimonene has been recently prompted as a promising 2D material for a large variety of applications due to its outstanding expected properties. However, still only few of them have been experimentally demonstrated. This is a common question regarding the evolution period required for a novel material. For instance, if we have a look to graphene, which is a paradigmatic example in which both science and technology have made considerable efforts and resources including economical ones, it was firstly synthesized in 2004 but even today there still is a long way to walk for achieving some goals that were supposed to be already done[1]. This fact could give some light regarding the time and effort that are necessary to develop a specific application where a novel material could be applied. Nevertheless, our research group in collaboration with specialized groups has tried to demonstrate that antimonene is, in fact, this outstanding material that everyone is expecting.

In this chapter, two different works related to this issue are shown. More precisely, it is experimentally studied the electrochemical capacitive performance of FLA and its successful application as a supercapacitor.

On the other hand, it is described the formation of a 2D/2D heterostructure between graphitic carbon nitride (g-CN) and FLA, type I heterojunction, that improves the optical absorption, the charge separation under illumination, as well as the photoactivity in the degradation of organic pollutants to that showed for both pristine materials.

5.2. Results and Discussion

5.2.1. FLA based supercapacitor

It cannot be denied that the world is changing on its green energy demand. For that reason, the necessity of develop sustainable energy storage devices that fulfil the request of renewable energy sources is crucial[2].

It has been proved that electrochemical double-layer capacitors (EDLC), also called supercapacitors, are an energy storage platform with major potential due to their high power density, good operational safety, long cycling life, competitive energy density and minimum charge separation. These devices have been largely explored and are already accepted as promising for energy storage applications, such as high-power electronics and fast charging electronic devices[3]. Recent advances in nanotechnology paved the way to a further investigation on the potential applications of EDLC and their performance. More specifically, the focus has been put in the development of new nanomaterials that allowed the fabrication of electrodes with major storage capacity[4]. Actually, 2D nanomaterials have specially attracted the interest for manufacturing EDLC, due to their high specific surface area that can contribute to a high double-layer capacitance. Besides, 2D nanomaterials usually have reactive basal planes and edges that can enhance the electrochemical performance of the device, *i.e.* pseudocapacitance[5].

Graphene was the first 2D nanomaterial that was successfully applied in different energy storage devices[6]. However, other 2D layered nanomaterials have shown promising applications as electrodes in energy storage devices where ion intercalation plays an important role[7].

More recently, some studies have been successfully carried out regarding the supercapacitor application of black-phosphorus[8], paving the way of using other pnictogens for such application. It has been recently demonstrated some outstanding properties of antimonene for electrochemical energy storage applications, such as, good electrical conductivity (1.6 x 10^4 S·cm^-1)[9], larger interlayer channel size (3.73 Å)[10], and fast ion diffusion capacity[11]. Moreover, it has also been recently demonstrated as an anode material in lithium and sodium ion batteries[12], in principle, due to its ability to enable fast ionic diffusion over its surface[11].

Taking these observations as a starting point, in this work the focus has been put on the electrochemical capacitive performance of FLA and the possibility of apply this new 2D nanomaterial as a supercapacitor.

5.2.1.1. FLA preparation and characterization

In this work, FLA is obtained by introducing a modification of the LPE procedure described in Chapter 2 in order to increase the concentration of the samples. The modification consisted in processing the starting bulk antimony crystals by ball-milling for 3 h at 3000 rpm, trying to decrease the initial size of the crystals and facilitating the subsequent exfoliation. The rest of LPE conditions remained equal to those described in Chapter 2: an initial antimony concentration of 0.1 g·L^-1, a 4:1 mixture of 2-propanol/H_2O as solvent, tip sonication for 40 min at 400 W and 24 kHz, developing the ultrasound power in pulses of 0.5 s long every 1 s and centrifugation parameters of 3 min at 3000 rpm (746 g).

SEM images of the antimony crystals obtained after ball-milling step confirm the formation of microcrystals with dimensions in the range of *ca.* 1 μm (Figure 5.1a-b). Thus, confirming the successful decrease of the initial size of bulk antimony crystals (Figure 5.1c-d).
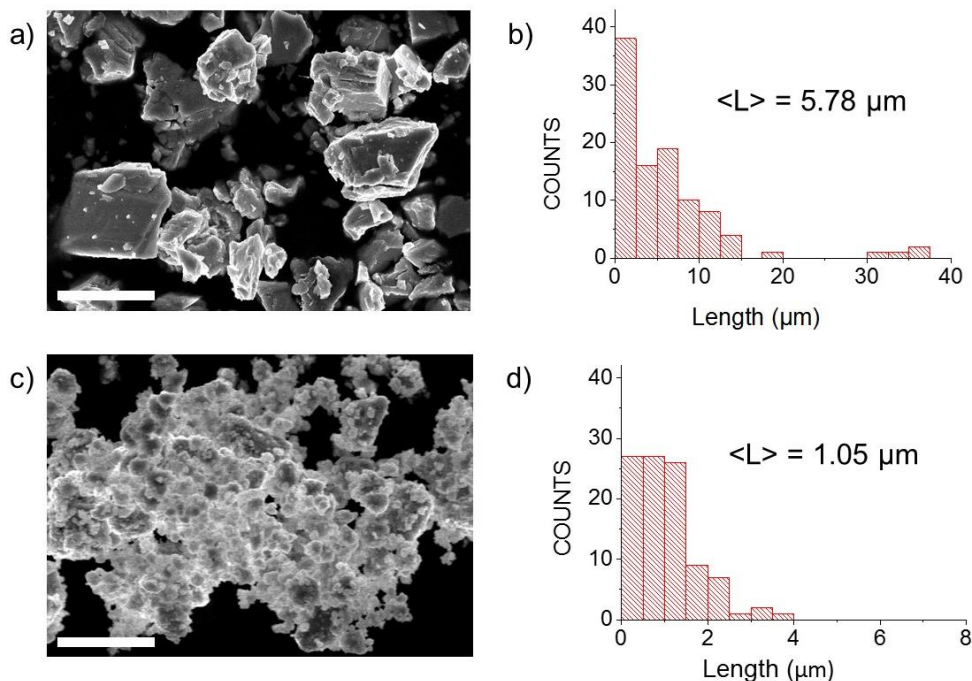
Figure 5.1 SEM images (scale bar of the SEM images equal to 5 µm) of: a) grinded antimony crystals and c) ball-milled antimony crystals for 180 min at 3000 rpm. Length histograms of the corresponding SEM images in µm of: b) grinded antimony crystals, d) ball-milled antimony crystals for 180 min at 3000 rpm.

The concentration of FLA suspensions is measured using AAS, obtaining a mean value of *ca.* 0.014 g L^{-1}, significantly higher than the one reported in Chapter 2 (*ca.* 1.74 x 10^{-3} g L^{-1}). In this case, the enhancement of the concentration and the size of the crystals are critical to get a suitable electrode deposition.

To confirm the successful exfoliation of bulk antimony crystals, AFM measurements are carried out (Figure 5.2), showing the typical topographic AFM image of FLA isolated onto SiO_2 substrates.

Analysing the height histogram (Figure 5.2b), it can be seen how FLAs have periodic step heights that are multiple of *ca.* 4 nm. In agreement with what it is described in Chapter 2. Besides, the lateral dimensions of FLAs seem to be more homogenous and smaller (*ca.* 200-500 nm) than the FLAs obtained in Chapter 2, due to the ball-milling process.
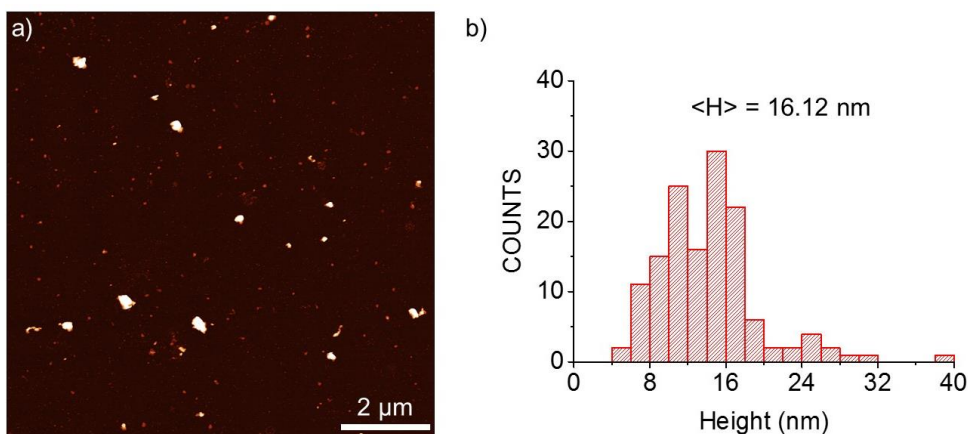
Figure 5.2 a) Representative AFM topographic image of FLAs casted onto SiO_2 substrate. b) Height histogram of 150 different FLAs showed in (a).

To further confirm the morphology and crystallinity of FLAs, TEM measurements are carried out (Figure 5.3). The morphology of FLAs showed in Figure 5.3a is in good agreement with the one obtained by AFM. In Figure 5.3b is depicted the electron diffraction pattern obtained from a magnified area of the same FLA showed in Figure 5.3a, confirming the hexagonal symmetry expected for the β-phase of antimony. Furthermore, XEDS spectra confirms the FLAs composition, which consists almost exclusively on antimony with a very low content of oxygen (Figure 5.3c).
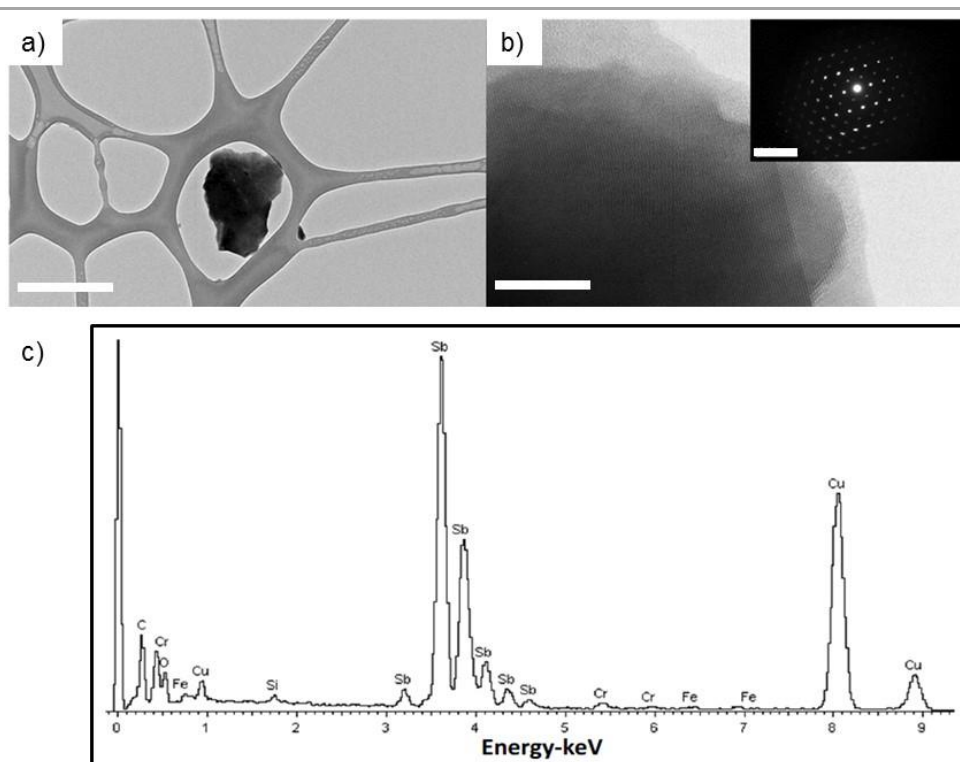
Figure 5.3 a) TEM image of an isolated FLA (scale bar equal to 500 nm). b) Magnification of same FLA in (a) showing atomic resolution (scale bar equal to 10 nm). The inset shows electron diffraction pattern, displaying the expected hexagonal symmetry for β-phase in antimony (scale bar equal to 10 nm^{-1}). c) XEDS spectra of the FLA in (a).

5.2.1.2. FLA modified Screen Printed Electrode (SPE) preparation and characterization

Modified SPE are prepared by drop-casting aliquots of prepared FLAs suspension obtained by LPE, onto the required working electrode. The solvent is let it dry until it is completely evaporated under ambient conditions. Once the solvent is evaporated, the modified SPE with FLA is used without any further modification.

In order to confirm the correct modification of the printed electrodes with FLA, they have been characterized using SEM and Raman. Attending to Figure 5.4a, it can be easily seen how the electrodes are decorated with FLAs with lateral dimensions in the range of *ca.* 200-500 nm, which agree with the morphology observed by AFM and TEM.

To further confirm that the nanosheets appearing in Figure 5.4a are indeed FLA, Raman spectroscopy measurements are carried out on modified SPEs with different amounts of FLA. Figure 5.3b confirms the existence of FLA, displaying the Raman bands associated to antimony: A^1_g and E_g vibrational modes at 149.8 cm^{-1} and at 110 cm^{-1}, respectively. The intensity of Raman bands in Figure 5.4b increases when higher amounts of FLA are drop-casted onto SPEs surface, indicating a greater coating of the electrodes, and maybe a larger thickness of the FLAs due to aggregation.
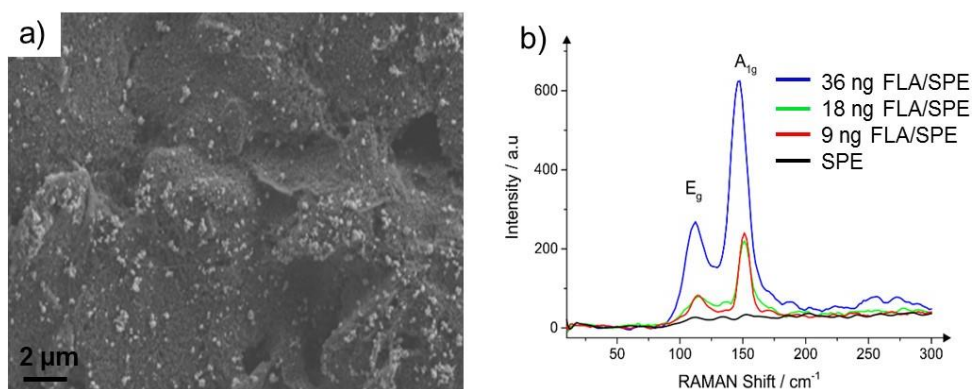

Figure 5.4 a) SEM image of modified SPE with 36 ng of FLA obtained by LPE, b) Raman spectra of bare SPE and modified SPE with different amounts of FLA.

5.2.1.3. FLA as a capacitive material

In order to provide a benchmark value, the cyclic voltammetry (CV) of bare SPEs are obtained, using a two-electrode system in 0.5 M H_2SO_4 at different scan rates. After that, it is analysed the response exhibited upon drop-casting different amounts of FLA onto the bare SPEs, ranging from 1.8 to 36 ng (Figure 5.5). The enhancement of capacitive current when small quantities of FLA are drop-casted onto the SPEs can be clearly detected. Even so, a redox process is observed at formal potential 0.0 V, which could be attributed to the oxidation and reduction of FLA, as a consequence of a Faradaic process, which also contributes considerably to the capacitance increase. The capacitance of the working electrode, C_{we}, is calculated from the corresponding voltammograms, as shown in Figure 5.5, using the following equation (Eq. 1):

$$C_{we} = \frac{\int_{V_1}^{V_2} I(V)dV}{2 \cdot \Delta V \cdot v \cdot m} \qquad \text{Eq. 1}$$

Where C_{we} is the specific capacitance exhibited by the working electrode in Faradays per gram (F·g⁻¹), $\int I(V)dV$ is the area under the intensity current function between V_2 and V_1 potentials in Coulombs (C), *i.e.* a measure of the charge stored by the capacitor device. ΔV is the potential difference between V_2 and V_1 in volts (V), v is the voltammogram scan rate in volts per second (V·s⁻¹), and m is the mass of FLA in grams.

The obtained values of capacitance are shown in Table A5.1 (page 220). These values are excellent in terms of capacitance, *ca.* 8500 F·g⁻¹, as a consequence of the combination of two factors: i) an increase of electrochemical active area, and ii) increase of the electrochemical double layer over the electrode surface as a result of the first factor.

On the other hand, the Faradaic process taking part, could also affect to these values due to the increment of the area under the current curves because of the redox peak.
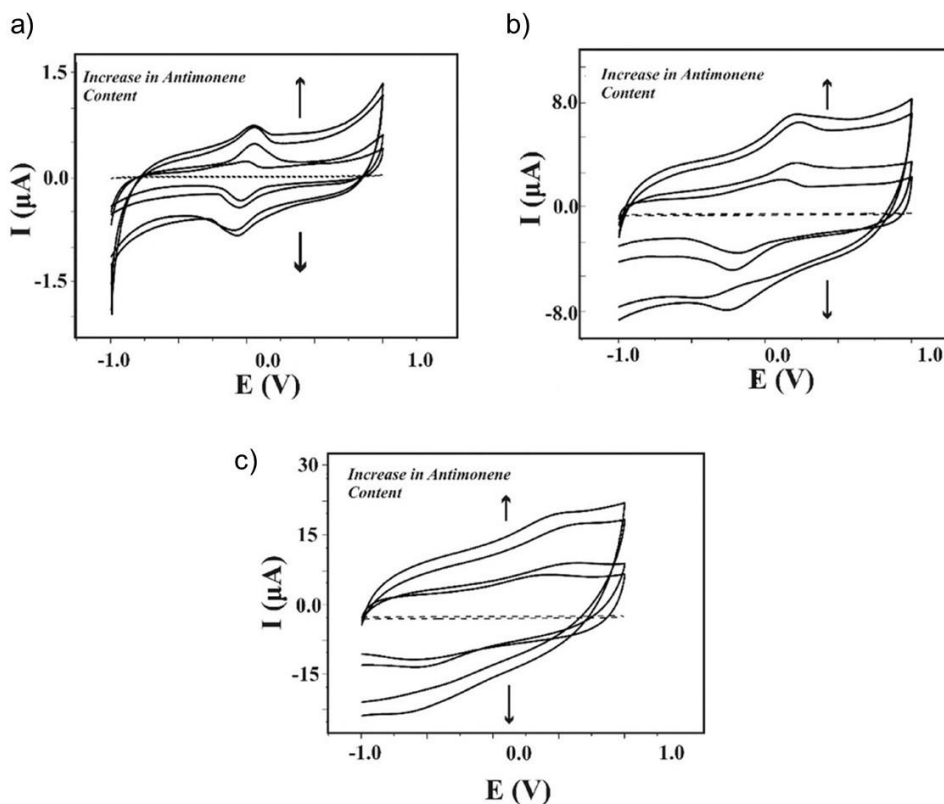
Figure 5.5 CVs obtained with a two electrodes system of SPE and different amounts of FLA (1.8, 3.6, 9, 18 and 36 ng of FLA) at a current of: a) 10 mV·s^{-1}, B) 100 mV·s^{-1}, and C) 500 mV·s^{-1} in 0.5 m H$_2$SO$_4$. It becomes clear that the integral area of the CVs, a property that is indicative of the capacitance of the system, is directly proportional to the quantity of FLA present on the SPEs.

In order to have more reliable capacitance values, galvanostatic charge/discharge analysis is accomplished using a two-electrode approach to complement the setup utilized for supercapacitors within the field.

Figure 5.6a illustrates the charge/discharge profiles obtained for bare SPE, and modified SPEs with increasing amounts of FLAs. The results clearly show that *dV/dt* decreases, which means that capacitance increases when SPE is modified with FLA. The obtained capacitance values are lower than those obtained by CV (Table A5.2, page 220), but they are considered more realistic because no Faradaic process is involved in this case. The specific capacitance value in the most suitable configuration, *i.e.* 3.6 ng FLA/SPE at a current of 14 A·g^{-1}, is 1573 F·g^{-1} (Figure 5.6c). This high value can compete with other 2D nanomaterials that are already being used for supercapacitor fabrication[13,14], and also with other kinds of materials used for such application[15]. As can be seen in Figure 5.6b, the absolute capacitance values increase with the quantity of FLA drop-casted onto the SPEs surface until a specific FLA quantity of 18.0 ng. From that mass of FLA, the absolute capacitance decreases, which could be a consequence of the nanomaterial aggregation due to a higher amount of FLA drop-casted, decreasing the electroactive surface area.

For supercapacitors, cycling stability is also an important parameter. Therefore, the charge–discharge stability was studied over 10000 galvanostatic cycles, applying a specific current of 14 A·g^{-1} on a 36 ng FLA/SPE (Figure 5.6d). The capacitance retention values establish that after a primary drop to 65 %, the following cycles retain the capacitance between 65 and 63 % of the initial capacitance over the entire range of cycles, showing the same capacitance between the scan 800 and the 10000. It is probable that the drop in the first 1000 cycles can be attributed to some of the drop-cast FLA being liberated with charge cycling.

171
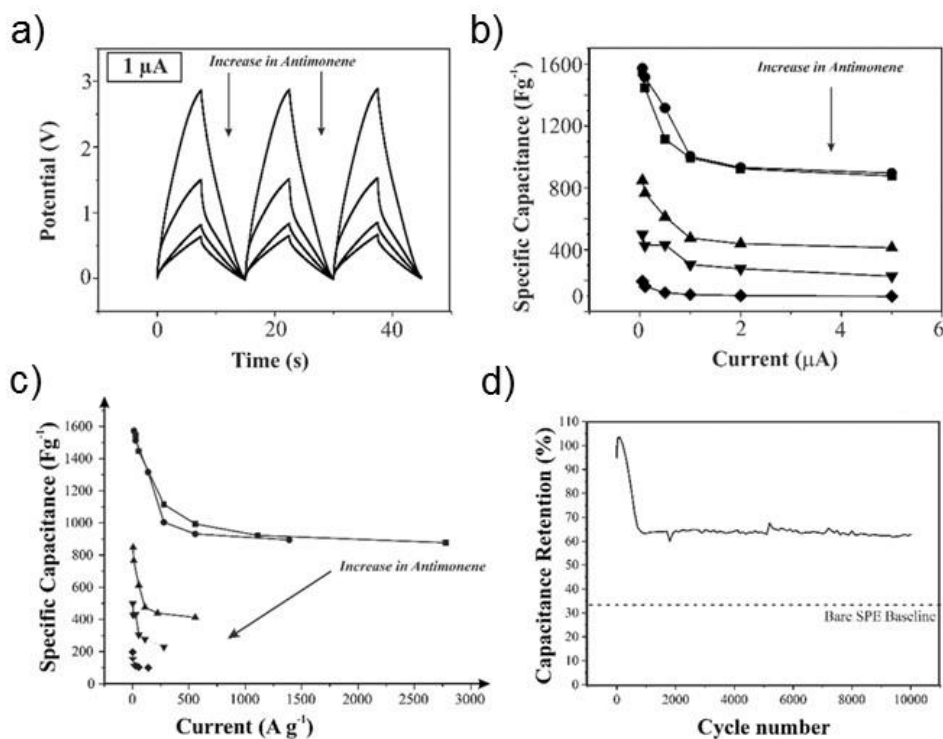
Figure 5.6 a) Representation of charge/discharge profiles obtained in 0.5 M H_2SO_4 with unmodified and FLA modified SPE (increasing the FLA quantity from 1.8 to 36.0 ng) applying 1.00 µA. b) Absolute capacitance values versus current applied obtained from charge–discharge profiles. c) Specific capacitance values versus specific current applied obtained from charge–discharge profiles. d) Relative capacitance for successive charge–discharge cycles respect the first cycle capacitance. The capacitance of the bare SPE, on its first cycle, is also indicated.

The constructed system also demonstrates a highly competitive energy and power densities of 20 mW·h·Kg^{-1} and 4.8 kW·Kg^{-1}, respectively.

5.2.2. g-CN/FLA heterostructure: structural characterization and application in photocatalysis

Graphitic carbon nitride (g-CN)[16] is considered one of the most promising novel 2D semiconductors for the future energy-related applications, due to its extraordinary electronic and chemical properties. Nowadays, it has been experimentally proved as excellent candidate for electro- and photocatalysis[17], organic pollutants degradation[18], CO_2 reduction[19] and photoelectronic devices[20]. Furthermore, its structure composed of thin layers of carbon and nitrogen atoms, allows the formation of sandwiched heterostructures with other layered materials enhancing its remarkable properties. To name a few of them, recently it has been reported heterostructures between g-CN and MOFs[21], TMDs[22] and BP[23]. The demonstration of the photocatalytic performance enhancement due to the 2D/2D heterojunctions between g-CN and other 2D materials, paved the way for the search of new ones[24]. In fact, the combination of layered materials that form this sandwich heterostructures, is an emerging research area due to the potential synergetic effect that a correct junction can create[25]. Recently, Abellán *et al.* reported the functionalization of antimonene with a perylene bisimide showing a more pronounced charge-transfer behaviour than for phosphorene[26]. This preliminary result suggests the possibility to modulate the antimonene band-gap using different molecules and other materials due to its donor character. For this reason, antimonene can be considered as a good candidate to form a new heterojunction with g-CN, which is indeed the scope of this work.

The CNSb van der Waals heterostructure is formed *via* bath sonication of ball-milled antimony crystals and g-CN in an identical weight proportion, using a 4:1 mixture of 2-propanol/H_2O as solvent to assist the process. After sonication, the so-formed dispersion is centrifuged for 10 min at 10,000 rpm giving rise to a homogeneous and stable suspension which can be easily drop-casted on substrates (see section A5.2.2 to further information, page 218).

Figure 5.8 shows a topographic AFM image of different CNSb heterostructures drop-casted onto a SiO_2 substrate. It can be easily seen how these heterostructures have a consistent morphology that is composed of a typical g-CN layer holding small FLAs on it. Normally, a typical g-CN layer shows lateral dimensions over ≈1 μm and thicknesses of ≈5 nm[17]. The g-CN layer is decorated with small FLAs of ≈100 nm in lateral dimensions and thicknesses of ≈4 nm (Figure 5.8). This morphology of FLAs is also consistent with the one observed in Chapter 4 when using bath sonication.
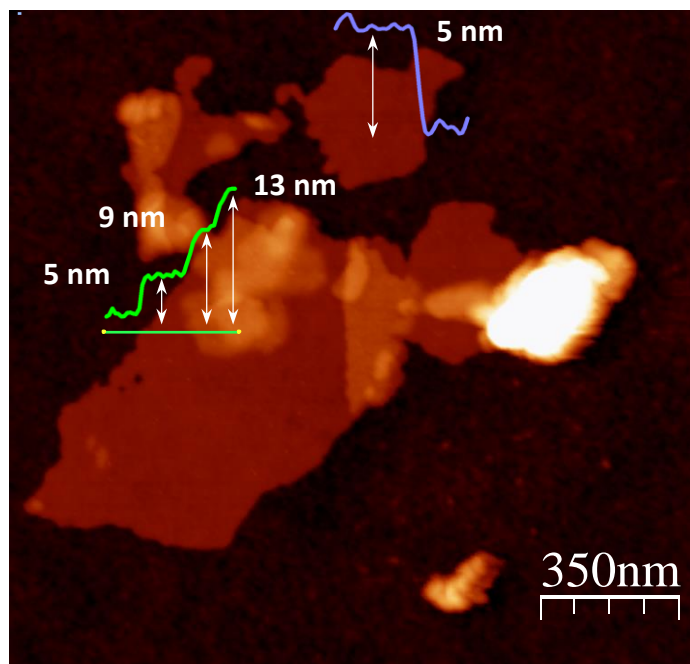
Figure 5.8 AFM topographic image of two flakes of the CNSb heterostructure with their topographic profiles, showing the typical step height of g-CN (*ca.* 5nm) and FLA (*ca.* 4 nm).

To further confirm the morphology of the CNSb heterostructure TEM measurements are carried out (Figure 5.9) TEM images show that the morphology of the CNSb heterostructure is in good agreement with the AFM images. TEM/XEDS analysis confirms that the small black flakes on the top of the heterostructure are FLAs and the large transparent flakes correspond to g-CN (Figure 5.9c).
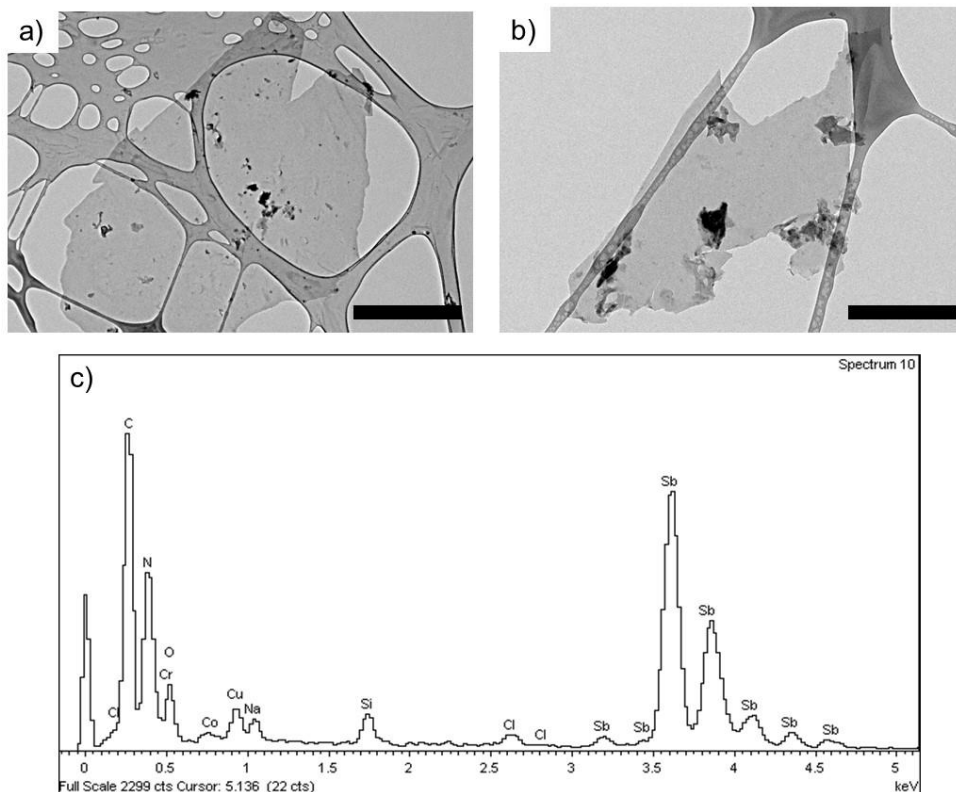
Figure 5.9 TEM image at different magnification showing diverse CNSb heterostructures: a) scale bar equal to 2 µm, b) scale bar equal to 500 nm. c) TEM/XEDS spectra of the flake showed in (b).

Furthermore, SEM analysis is carried out after drying the samples under vacuum conditions for 24 h at 60 °C, in order to eliminate the solvent and obtain a solid powder formed of several CNSb heterostructures. The drying process, give rises to the formation of large individual grains that contain small FLAs decorating g-CN layers. The SEM images, in both secondary electrons (SE) and backscattered electrons (BSE) modes, confirm the coexistence of FLA and g-CN (Figure 5.10a-b).

176

This evidence is also confirmed by elemental mapping SEM/XEDS where it can be seen that the heterostructure grains show an elemental atomic ratio of ≈ 9 % of Sb versus 91 % of g-CN (Figure 5.10 c-e).
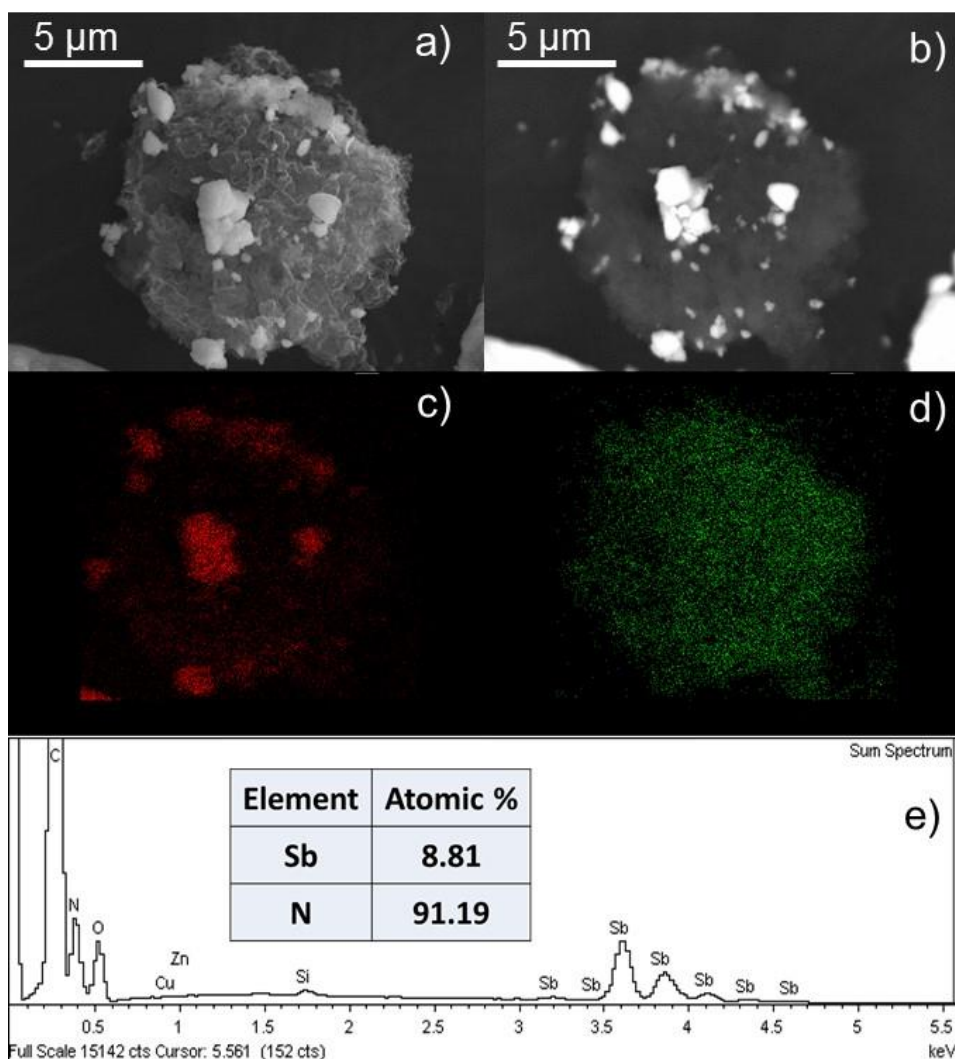
Figure 5.10 a) SEM image of a grain of CNSb heterostructure after vacuum drying 24 h at 60 °C in SE mode. b) SEM image of the same grain in (a) in BSE mode. XEDS elemental mapping of the same grain in (a) of c) Sb atoms (red) and d) N atoms (green). e) XEDS spectrum of the CNSb grain composite showed in (a) and its atomic composition.

XPS measurements of CNSb heterostructure proves the presence of both 2D materials and their interaction (Figure 5.11). C 1s spectrum displays the typical chemical states for g-CN. Three binding energies equivalent to adventitious C=C bond at 284.8 eV, C-O due to adsorbed oxygen from the environment at 286.5 eV, and one last contribution at 288.2 eV of N=C-N from the triazine units can be observed. In addition, N1s spectrum shows three different chemical species at 397.9 eV coming from C=N-C, 398.8 eV of N-(C)$_3$ groups and remaining amino groups at 400.3 eV.

Figure 5.11 XPS spectra of CNSb heterostructure for a) C 1s, b) N 1s, c) Sb 3d regions, and of FLA for d) Sb 3d peaks.

XPS spectra of the heterostructure corresponding to the Sb 3d contribution shows three bands: one at 528.2 eV corresponding to metallic Sb, other at 530.0 eV from oxidized component of Sb (Sb_2O_3), and the last one at 531.5 eV that corresponds to the peak of the O 1s component. In a related work regarding the supramolecular interaction between FLA and perylene bisimide, it has been observed that the binding energy separation between metallic and oxidized contributions for pristine Sb (*ca.* 2.26 eV) is greater than the separation of the functionalized FLA (*ca.* 1.87 eV). Thus, indicating that there is a core-level shift of *ca.* 0.4 eV induced by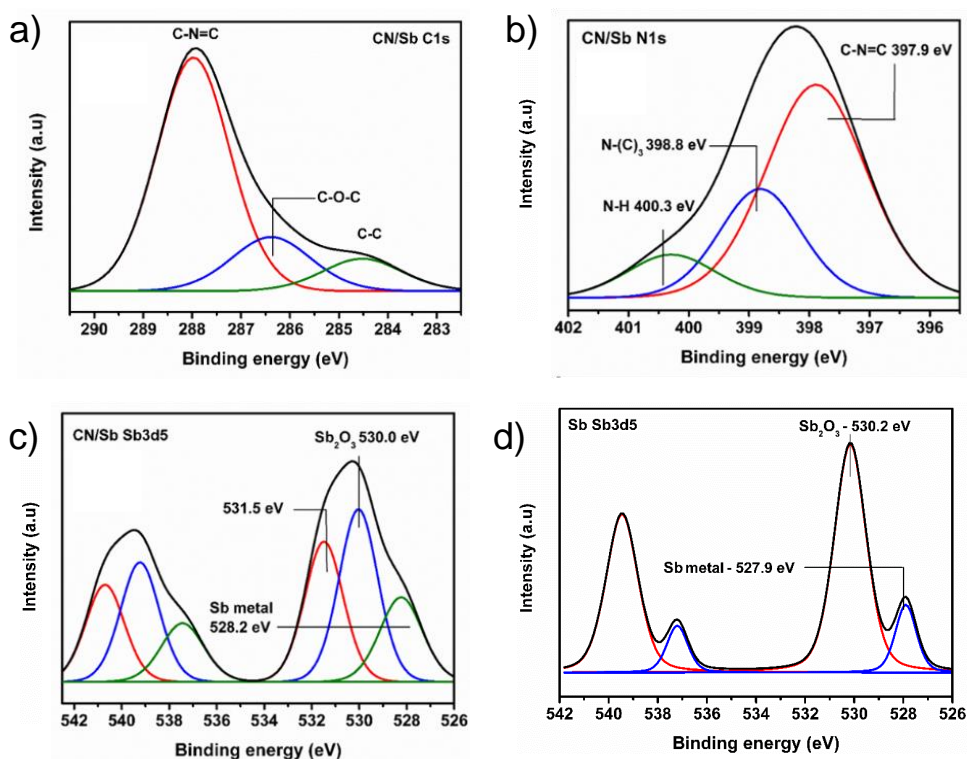 the functionalization[26]. In the case of the obtained CNSb heterostructure, the observed binding energy separation between metallic and oxidized contributions for the pristine Sb sample is *ca.* 2.3 eV (Figure 5.11d), while the difference for the CNSb sample is *ca.* 1.8 eV, and thus there is a core-level shift of about *ca.* 0.5 eV induced by charge transfer at the heterojunction between the two materials. The sign of the shift indicates that these Sb species are oxidized with respect to metallic Sb, but the charge transfer is less pronounced than in the oxide. This result indicates that the g-CN layer acts as an electron acceptor, which fits perfectly with the electron withdrawing behaviour of the g-CN layers.

To further investigate the so-formed CNSb heterostructure, different mass ratios of both starting material (from 5 to 100% in weight in comparison to g-CN) are used to generate suspensions *via* bath-sonication for 1 h in a 4:1 mixture of 2-propanol/H_2O. After generating the suspensions, they are centrifuged for 10 min at 10,000 rpm and vacuum dried at 60 ºC for 24 h to isolate the powder labelled as $CNSb_x$ (x = 0.05, 0.1, 0.2, 0.25, 0.5, 0.75, 1). Once the $CNSb_x$ powder is isolated, it is characterized by XRPD (Figure 5.12a-b).

Attending to XRPD patterns of g-CN alone, they show its typical diffraction peaks at 13.0° and 27.1° which correspond to the (100) and (200) crystal planes. The formation of the $CNSb_x$ heterostructure vanishes the contributions of g-CN due to the higher crystallinity of antimony. Interestingly, the peaks corresponding to the crystal planes of antimony[27], (003), (012), (104), and (110) are observable in the diffractograms of all the $CNSb_x$ heterostructures, while those belonging to g-CN are negligible, even so in the sample with lowest Sb content, $CNSb_{0.5}$ (Figure 5.12b).

For the sake of clarity, it is worth to point out that the label $CNSb_x$ (x = 0.05, 0.1, 0.2, 0.25, 0.5, 0.75, 1) only mentions the CN:Sb ratio used to form the heterostructure in order to further characterize it, and not to a different material.

The optical properties of the $CNSb_x$ heterostructures are measured by performing photophysical studies. Photoluminescence spectroscopy is a useful technique for identifying electronic changes such as surface states in semiconductors. It is observed that the formation of a heterostructure, normally quenches the fluorescence emission of g-CN (Figure 5.12c), and this fact proposes that there is a solid interaction between both 2D semiconductors which may lead to the creation of a heterojunction and to enhanced charge separation of the photoexcited charges due to new non-radiative recombination paths. On the other hand, UV–vis absorbance spectroscopy (Figure 5.12d) shows the typical absorption peak for g-CN at *ca.* 480 nm[28]. However, the presence of antimony in the heterostructure induces a new peak at *ca.* 650 nm, which intensity is enhanced when the amount of Sb in the CN:Sb ratio is higher.
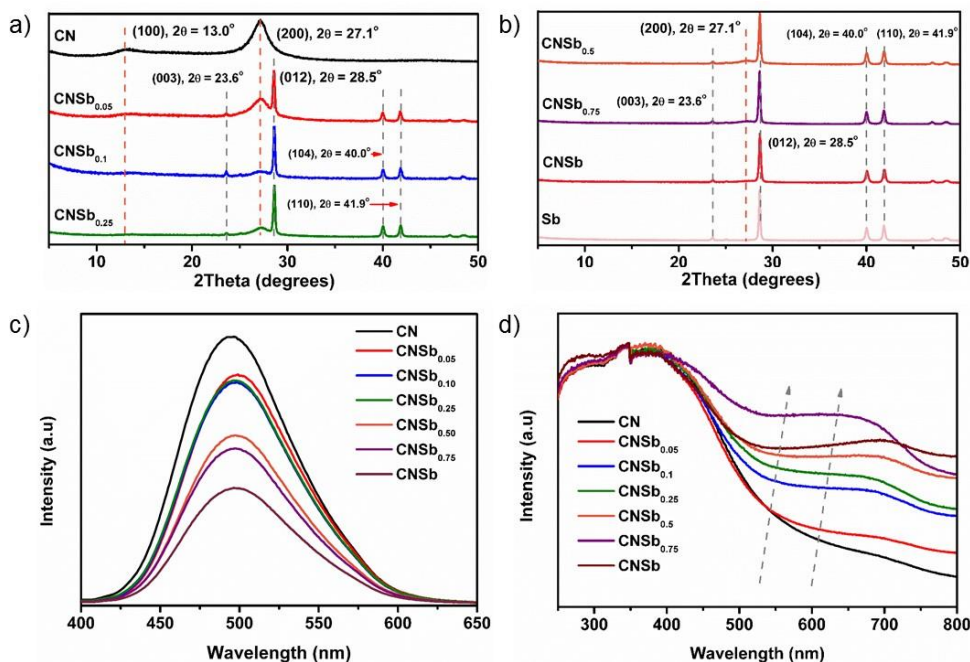
Figure 5.12 a, b) XRD patterns, c) photoluminescence spectra, and d) UV–vis absorbance spectra of CNSb$_x$ heterostructures.

In order to clarify the energy band position and, thus, the kind of heterojunction between both materials as well as the charge flow, it is combined Mott–Schottky measurements with the Tauc plot, using the theoretical bandgap value of Sb mimicking ambient conditions (1.2 eV)[10]. Tauc plot representation for g-CN (Figure 5.13a) shows a bandgap of 2.22 eV, slightly lower than the usual value of 2.7 eV due to the insertion of barbituric acid in the initial supramolecular assembly during the g-CN synthesis (see section A5.2.2, page 218)[29]. The flat band potential measured at three different frequencies (1, 2, and 3 KHz) indicate a conduction band of −0.98 eV for g-CN and −0.91 eV for Sb (Figure 5.13b–d).
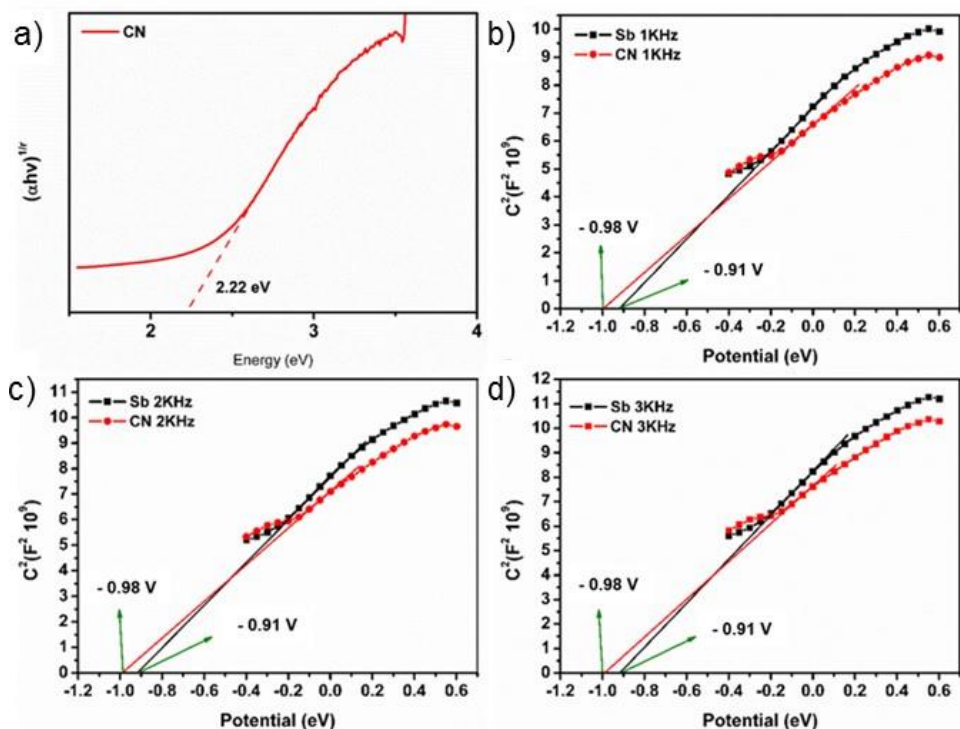
Figure 5.13 a) Tauc plot of g-CN. Mott-Schottky measurements for g-CN and Sb at b) 1 KHz, c) 2 KHz, and d) 3 KHz.

Then, it can be concluded that the interaction between both 2D semiconductors results in a heterojunction type I, where after the photoexcitation happening in g-CN, both electron and hole migrate to the conduction and valence band of Sb, respectively (Figure 5.14).
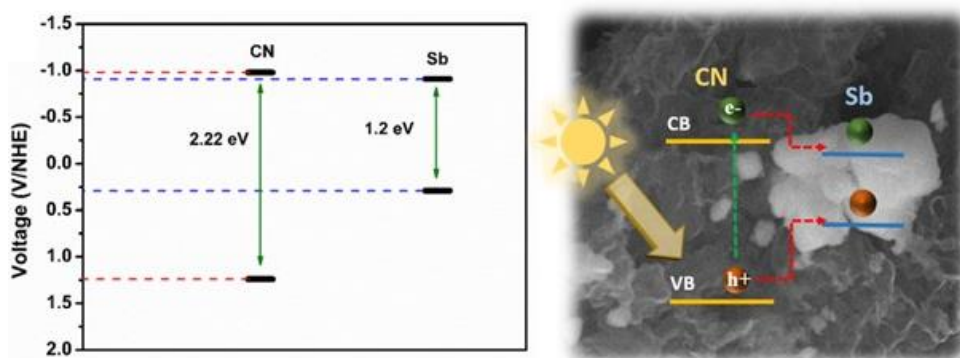
Figure 5.14 Derived band structure of the CNSbx heterostructure.

In order to check the photoactivity of the heterostructure, it was evaluated as photocatalyts for the degradation of two typical organic pollutant: rhodamine B (RhB) and of p-nitrophenol (p-NP) (Figure 5.15). The exposure of bare RhB to irradiation do not lead to any degradation of the dye. The $CNSb_x$ (x = 0.25, 0.5, 0.75, 1) heterostructures demonstrated improved photocatalytic activity compared to the pristine g-CN and Sb. In particular, using the $CNSb_{0.25}$ heterostructure, the RhB dye is fully degraded in just 20 min. The mechanism of RhB degradation was clarified by performing the experiment in the presence of a hole scavenger, triethanolamine (TEOA), and an electron acceptor, $AgNO_3$[30]. The addition of 0.1 mL TEOA, caused an important decay on the photodegradation process, while adding 0.1 mL of 0.1 m Ag^+ (aq) slightly suppressed the process. These results suggest that the photochemical degradation of RhB to the completely noncolored compound (rhodamine) occurs mostly *via* oxidation of the photogenerated holes from the valence band of g-CN. However, it seems that electrons transferred from the conduction band of g-CN to the conduction band of Sb also take part in the degradation process (Figure 5.15b).

An additional proof of the enhanced photocatalytic activity is given by the degradation of the other organic pollutant, p-NP, as a function of time under white light illumination, trying different CN:Sb ratios. Attending to Figure 5.15c, it is clear that different $CNSb_x$ heterostructures showed similar photoactivity and degraded p-NP faster than bare g-CN.
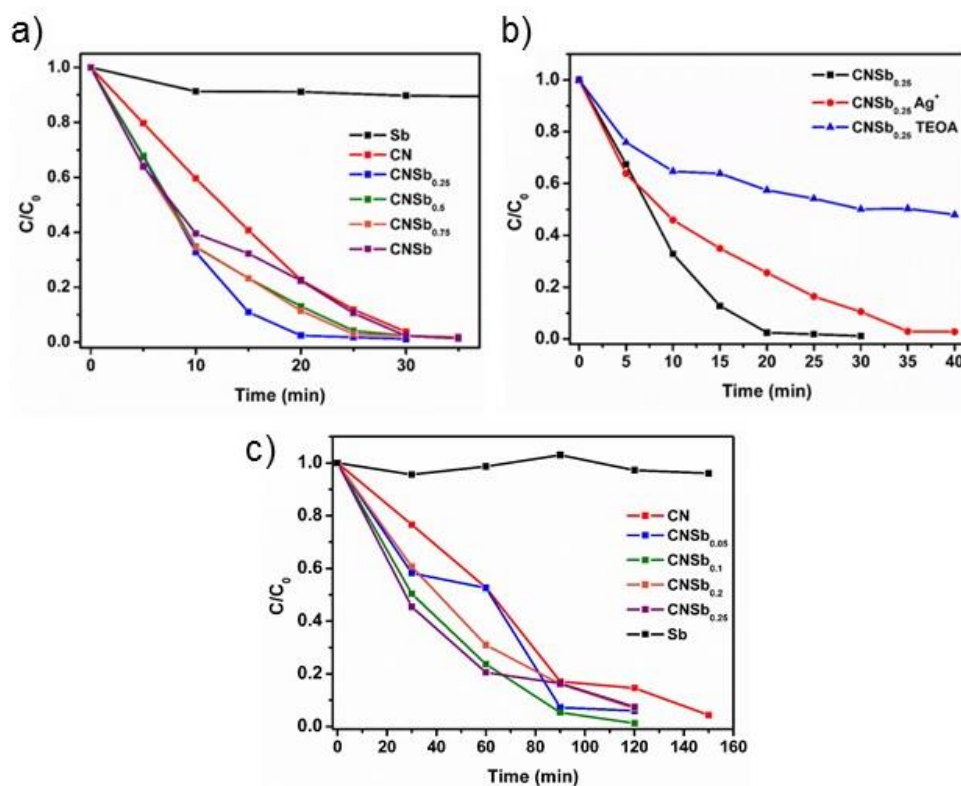
Figure 5.15 a) RhB degradation curves for $CNSb_x$ heterostructures. b) RhB degradation curves for $CNSb_{0.25}$ with different scavengers. c) p-NP degradation curves of $CNSb_x$ heterostructures.

5.3. Conclusions

In this chapter, it has been described two different studies regarding the FLAs properties and its application in different fields.

In the first presented work, FLA has been characterized for the first time as a material for application in energy storage, being used to modify a SPE for supercapacitor application. Interestingly, FLA has showed an improvement in the energy capabilities of a carbon electrode substrate in cyclic voltammetry and galvanostatic charging, proving a remarkable performance with a capacitance value of 1578 $F \cdot g^{-1}$ at a high charging current density of 14 $A \cdot g^{-1}$. Furthermore, FLA modified SPEs show a pseudocapacitive Faradaic voltammetric response, enhancing the electrochemical capacitive performance of the electrodes. Additionally, compared to a device constructed with bare graphitic electrodes the capacitive performance of the supercapacitors increases significantly when using FLA, even with small quantities as 1.8 ng of material. The built system also demonstrated a highly competitive energy and power densities of 20 $mW \cdot h \cdot Kg^{-1}$ and 4.8 $kW \cdot Kg^{-1}$, respectively.

Concerning the second work, it has been demonstrated the fabrication and characterization of a 2D/2D van der Waals heterostructure between g-CN and FLA. To achieve this result, FLA is exfoliated using LPE techniques together with g-CN, in order to create the heterojunction at the same time of the exfoliation. The interaction and close contact between both 2D nanomaterials is demonstrated by solid electron coupling within the heterostructure, resulting in an enhancement of light harvesting and charge separation properties due to the formation of a type I heterojunction.

The heterojunction also improves the photocatalytic performance of the whole structure, compared to each individual material. This work implies the first reported van der Waals heterostructure obtained using FLA and may open new possibilities in the creation of 2D/2D nanocomposites towards their photochemical application.

5.3.1. Future prospects

Both works presented in this chapter opened up two different fields where FLA can be experimentally applied. Besides, the demonstration of some of the outstanding properties of FLA paved the way to fully characterize this novel 2D material. However, is needed a deeper investigation on the potential applications of FLA in order to develop devices that could satisfy the needs that industrial production demands.

5.4. References

(1)   Ferrari, A. C.; Bonaccorso, F.; Fal'ko, V.; Novoselov, K. S.; Roche, S.; Bøggild, P.; Borini, S.; Koppens, F. H. L.; Palermo, V.; Pugno, N.; et al. Science and Technology Roadmap for Graphene, Related Two-Dimensional Crystals, and Hybrid Systems. *Nanoscale* **2015**, *7* (11), 4598–4810.

(2)   Abruña, H. D. Energy in the Age of Sustainability. *J. Chem. Educ.* **2013**, *90* (11), 1411–1413.

(3)   González, A.; Goikolea, E.; Barrena, J. A.; Mysyk, R. Review on Supercapacitors: Technologies and Materials. *Renew. Sustain. Energy Rev.* **2016**, *58*, 1189–1206.

(4)   Palaniselvam, T.; Baek, J.-B. Graphene Based 2D-Materials for Supercapacitors. *2D Mater.* **2015**, *2* (3), 032002.

(5)   Mendoza-Sánchez, B.; Gogotsi, Y. Synthesis of Two-Dimensional Materials for Capacitive Energy Storage. *Adv. Mater.* **2016**, 6104–6135.

(6)   Wen, L.; Li, F.; Cheng, H. M. Carbon Nanotubes and Graphene for Flexible Electrochemical Energy Storage: From Materials to Devices. *Adv. Mater.* **2016**, *28* (22), 4306–4337.

(7)   Balasingam, S. K.; Lee, M.; Kim, B. H.; Lee, J. S.; Jun, Y. Freeze-Dried MoS2sponge Electrodes for Enhanced Electrochemical Energy Storage. *Dalt. Trans.* **2017**, *46* (7), 2122–2128.

(8)   Hao, C.; Wen, F.; Xiang, J.; Yuan, S.; Yang, B.; Li, L.; Wang, W.; Zeng, Z.; Wang, L.; Liu, Z.; et al. Liquid-Exfoliated Black Phosphorous Nanosheet Thin Films for Flexible Resistive Random Access Memory Applications. *Adv. Funct. Mater.* **2016**, *26* (12), 2016–2024.

(9)   Ji, J.; Song, X.; Liu, J.; Yan, Z.; Huo, C.; Zhang, S.; Su, M.; Liao, L.; Wang, W.; Ni, Z.; et al. Two-Dimensional Antimonene Single Crystals Grown by van Der Waals Epitaxy. *Nat. Commun.* **2016**, *7* (1), 13352.

(10) Ares, P.; Aguilar-Galindo, F.; Rodríguez-San-Miguel, D.; Aldave, D. A.; Díaz-Tendero, S.; Alcamí, M.; Martín, F.; Gómez-Herrero, J.; Zamora, F. Mechanical Isolation of Highly Stable Antimonene under Ambient Conditions. *Adv. Mater.* **2016**, 6332–6336.

(11) Sengupta, A.; Frauenheim, T. Lithium and Sodium Adsorption Properties of Monolayer Antimonene. *Mater. Today Energy* **2017**, *5*, 347–354.

(12) Walter, M.; Erni, R.; Kovalenko, M. V. Inexpensive Antimony Nanocrystals and Their Composites with Red Phosphorus as High-Performance Anode Materials for Na-Ion Batteries. *Sci. Rep.* **2015**, *5*, 8418.

(13) Khan, A. F.; Down, M. P.; Smith, G. C.; Foster, C. W.; Banks, C. E. Surfactant-Exfoliated 2D Hexagonal Boron Nitride (2D-HBN): Role of Surfactant upon the Electrochemical Reduction of Oxygen and Capacitance Applications. *J. Mater. Chem. A* **2017**, *5* (8), 4103–4113.

(14) Gao, S.; Sun, Y.; Lei, F.; Liang, L.; Liu, J.; Bi, W.; Pan, B.; Xie, Y. Ultrahigh Energy Density Realized by a Single-Layer β-Co(OH)2 All-Solid-State Asymmetric Supercapacitor. *Angew. Chem., Int. Ed.* **2014**, *53* (47), 12789–12793.

(15) Wang, X.; Shi, B.; Fang, Y.; Rong, F.; Huang, F.; Que, R.; Shao, M. High Capacitance and Rate Capability of a Ni3S2@CdS Core-Shell Nanostructure Supercapacitor. *J. Mater. Chem. A* **2017**, *5* (15), 7165–7172.

(16) Ong, W. J.; Tan, L. L.; Ng, Y. H.; Yong, S. T.; Chai, S. P. Graphitic Carbon Nitride (g-C3N4)-Based Photocatalysts for Artificial Photosynthesis and Environmental Remediation: Are We a Step Closer to Achieving Sustainability? *Chem. Rev.* **2016**, *116* (12), 7159–7329.

(17) Shalom, M.; Gimenez, S.; Schipper, F.; Herraiz-Cardona, I.; Bisquert, J.; Antonietti, M. Controlled Carbon Nitride Growth on Surfaces for Hydrogen Evolution Electrodes. *Angew. Chem., Int. Ed.* **2014**, *53* (14), 3654–3658.

(18)   Cui, Y.; Ding, Z.; Liu, P.; Antonietti, M.; Fu, X.; Wang, X. Metal-Free Activation of H2O2 by g-C 3N4 under Visible Light Irradiation for the Degradation of Organic Pollutants. *Phys. Chem. Chem. Phys.* **2012**, *14* (4), 1455–1462.

(19)   Fang, Y.; Wang, X. Photocatalytic CO2 Conversion by Polymeric Carbon Nitrides. *Chem. Commun.* **2018**, *54* (45), 5674–5687.

(20)   Barrio, J.; Lin, L.; Amo-Ochoa, P.; Tzadikov, J.; Peng, G.; Sun, J.; Zamora, F.; Wang, X.; Shalom, M. Unprecedented Centimeter-Long Carbon Nitride Needles: Synthesis, Characterization and Applications. *Small* **2018**, *14* (21), 1–7.

(21)   Hong, J.; Chen, C.; Bedoya, F. E.; Kelsall, G. H.; O'Hare, D.; Petit, C. Carbon Nitride Nanosheet/Metal-Organic Framework Nanocomposites with Synergistic Photocatalytic Activities. *Catal. Sci. Technol.* **2016**, *6* (13), 5042–5051.

(22)   Di, T.; Zhu, B.; Cheng, B.; Yu, J.; Xu, J. A Direct Z-Scheme g-C3N4/SnS2photocatalyst with Superior Visible-Light CO2reduction Performance. *J. Catal.* **2017**, *352*, 532–541.

(23)   Zheng, Y.; Yu, Z.; Ou, H.; Asiri, A. M.; Chen, Y.; Wang, X. Black Phosphorus and Polymeric Carbon Nitride Heterostructure for Photoinduced Molecular Oxygen Activation. *Adv. Funct. Mater.* **2018**, *28* (10), 1–9.

(24)   Fu, J.; Yu, J.; Jiang, C.; Cheng, B. G-C3N4-Based Heterostructured Photocatalysts. *Adv. Energy Mater.* **2018**, *8* (3), 1–31.

(25)   Novoselov, K. S.; Mishchenko, A.; Carvalho, A.; Castro Neto, A. H. 2D Materials and van Der Waals Heterostructures. *Science* **2016**, *353* (6298).

(26)   Abellán, G.; Ares, P.; Wild, S.; Nuin, E.; Neiss, C.; Miguel, D. R.-S.; Segovia, P.; Gibaja, C.; Michel, E. G.; Görling, A.; et al. Noncovalent Functionalization and Charge Transfer in Antimonene. *Angew. Chem., Int. Ed.* **2017**, *56* (46), 14389–14394.

(27)   Tian, W.; Zhang, S.; Huo, C.; Zhu, D.; Li, Q.; Wang, L.; Ren, X.; Xie, L.; Guo, S.; Chu, P. K.; et al. Few-Layer Antimonene: Anisotropic Expansion and Reversible Crystalline-Phase Evolution Enable Large-Capacity and Long-Life Na-Ion Batteries. *ACS Nano* **2018**, *12* (2), 1887–1893.

(28)   Barrio, J.; Lin, L.; Wang, X.; Shalom, M. Design of a Unique Energy-Band Structure and Morphology in a Carbon Nitride Photocatalyst for Improved Charge Separation and Hydrogen Production. *ACS Sustain. Chem. Eng.* **2018**, *6* (1), 519–530.

(29)   Barrio, J.; Shalom, M. Ultralong Nanostructured Carbon Nitride Wires and Self-Standing C-Rich Filters from Supramolecular Microspheres. *ACS Appl. Mater. Interfaces* **2018**, *10* (46), 39688–39694.

(30)   Zhang, Y.; Zhang, N.; Tang, Z. R.; Xu, Y. J. Identification of Bi2WO6 as a Highly Selective Visible-Light Photocatalyst toward Oxidation of Glycerol to Dihydroxyacetone in Water. *Chem. Sci.* **2013**, *4* (4), 1820–1824.

Conclusions

This Thesis has been focused on the study and development of a scalable process to obtain FLA, using LPE techniques, and the exploration of its potential applications in the field of energy storage.

Indeed, one of the most important advances derived from this Thesis is the development of the first method to obtain high-quality FLAs using LPE procedures. The development of this procedure drastically opened up the possibilities regarding the application and production of FLA, as before that moment, this new 2D material had been only synthesized by micromechanical exfoliation.

In order to fully understand the insights that takes place within the exfoliation process, it has been carried out a second work focused on investigate the oxidation behaviour of FLAs obtained following the developed LPE procedure. It has been demonstrated the formation of an antimonene oxide layer (Sb_2O_3-like) on the surface of the nanosheets as a result of the LPE of bulk Sb crystals, and more interestingly, that this oxide layer could be partially removed upon annealing at moderate temperatures under UHV conditions, leaving behind a Sb_2O_3-like/antimonene heterostructure with a band gap of *ca.* 1 eV.

Additionally, in order to optimize the FLAs production, it has been done a systematic analysis of the most significant LPE parameters (i.e. initial crystal size, solvent used and ultrasound parameters) concludes that: *i)* the pre-processing of the material affects significantly to the final concentration of FLA suspensions, being the optimal pre-process the one that uses "wet-ball milling" with 2-butanol; *ii)* the use of NMP/H_2O in a 4:1 ratio as a solvent during the LPE process, produces high-quality FLA with

the highest concentration value, while using 2-butanol gives rise to the FLAs with the largest DA ratio and a decent final concentration; *iii*) the use of a sonication tip with an ultrasonic wave amplitude of 100 % enhances the concentration and the DA ratio of the FLA suspensions.

Finally, the controlled production of FLAs by LPE allows to search different potential applications. Thus, as a proof-of-concept, it has been demonstrated the electrochemical capacitive performance of FLA and its successful application as a supercapacitor. Furthermore, it has also been described the formation of a 2D/2D heterostructure between graphitic carbon nitride and FLA which enhances the optical absorption as well as charge separation under illumination.

In summary, a complete study on the LPE process of bulk antimony crystals to obtain FLAs has been developed. And thanks to that, two potential applications in the energy storage field have been experimentally demonstrated.

Conclusiones

Esta tesis se ha focalizado en el estudio y desarrollo de un proceso de obtención de FLA usando técnicas LPE y sus potenciales aplicaciones en el campo del almacenamiento de energía.

De hecho, uno de los avances más relevantes que derivan de esta tesis es el desarrollo del primer método para obtener FLAs de alta calidad, mediante el uso de técnicas LPE. El desarrollo de este procedimiento ha permitido incrementar exponencialmente las posibilidades de aplicación y producción del FLA, ya que hasta ese momento este nuevo material 2D sólo había sido sintetizado mediante exfoliación micromecánica.

Por ello, para entender y poder describir por completo todos los aspectos del procedimiento de exfoliación que se estaba llevando a cabo, se realizó un segundo trabajo centrado en investigar el proceso de oxidación que sufrían las FLAs obtenidas siguiendo el procedimiento LPE que se había desarrollado. Este segundo trabajo demostraba la formación de una capa de óxido de antimonene (del tipo Sb_2O_3) en la superficie de las nanoláminas como resultado del proceso de exfoliación que se estaba llevando a cabo. Además se descubrió que la citada capa de óxido podía ser parcialmente removida mediante un proceso de "annealing" bajo condiciones de UHV, dejando de este modo una heteroestructura del tipo Sb_2O_3/antimonene con un band gap igual a 1 eV.

Además, con el fin de optimizar la producción de FLAs, se ha realizado un análisis sistemático de los parámetros más significativos que controlan el procedimiento LPE desarrollado, como por ejemplo: el tamaño inicial del cristal, el disolvente utilizado o los parámetros de ultrasonidos empleados, que concluye que: *i)* el pre-procesado del material afecta de manera

significativa a la concentración final de FLA, siendo la molienda en base húmeda usando 2-butanol el modo de pre-procesado óptimo, *ii)* el uso como disolvente durante el proceso LPE de una mezcla NMP/H$_2$O en la proporción 4:1, da lugar al valor de concentración final de FLAs de alta calidad más elevado, mientras que el uso de 2-butanol da lugar a valores de DA más altos junto con valores aceptables de concentración *iii)* el empleo de una punta de ultrasonidos para asistir el proceso LPE con una amplitud de onda del 100 %, aumenta los valores de DA de las FLAs así como su concentración final.

Finalmente, la producción controlada de FLAs mediante técnicas LPE permite la exploración de potenciales aplicaciones. Es por esto, que a modo de prueba de concepto, se ha demostrado experimentalmente el comportamiento capacitivo del FLA así como su aplicación como supercapacitor. Además, se ha descrito también la formación de una heteroestructura 2D/2D entre nitruro de carbono grafítico y FLA, y cómo esta mejoraba la absorbancia óptica y la separación de cargas bajo iluminación.

En resumen, se ha desarrollado un estudio completo sobre el proceso de exfoliación en fase líquida de cristales de antimonio para obtener FLAs. Y gracias a ello, se han podido demostrar experimentalmente dos potenciales aplicaciones en el campo del almacenamiento de energía.

Appendix

Appendix

A1. General materials and methods

A1.1. Materials

All the general chemicals and solvents were obtained from commercial sources and used without further purification unless otherwise specified. All solutions were prepared with deionized water of resistivity not less than 18.2 MΩ·cm. The antimony crystals used in all of the works presented in here, were purchased from Smart Elements with a purity of 99.9999%.

A1.2. Methods

Atomic Force Microscopy (AFM): AFM measurements were carried out using a Cervantes Fullmode AFM from Nanotec Electronica SL, operating at room temperature in ambient air conditions. The images were processed using WSxM (freely downloadable scanning probe microscopy software from www.nanotec.es)[1]. All the topographical images shown in this work were acquired in dynamic mode. For AFM measurements, commercial Olympus OMCL-RC800PSA cantilevers were used with a nominal spring constant of 0.39 N/m and tip radius of 15 nm. Low forces of the order of 1 nN were used for imaging to ensure that the flakes would not be deformed by the tip[2].

A2. Chapter 2 methods, experimental procedures and additional data

A2.1. Methods

Atomic Absorption Spectrometry (AAS): The amount of antimony in the samples was determined by flame atomic absorption spectrometry using a ContrAA 700 high-resolution atomic absorption spectrometer (Analitik Jena, Germany). The main line for antimony at 217.5815 nm was employed for all the analysis. The atomization was performed using an air acetylene flame with an acetylene flow rate of 60 L·h^{-1} and at a 6.0 mm burner height. The aspiration rate was fixed at 5 mL·min^{-1}. All measurements were carried out in triplicate.

Transmission Electron Microscopy (TEM): Images were obtained in a JEOL JEM 2100 FX TEM system with an accelerating voltage of 200 kV. The microscope has a multiscan charge-coupled device (CCD) camera ORIUS SC1000 and an OXFORD INCA X-Ray Energy Dispersive Spectroscopy (XEDS) microanalysis system.

Scanning Transmission Electron Microscopy (STEM): Images were obtained at 80 kV in a JEOL ARM200cF equipped with a spherical aberration corrector and a Gatan Quantum EEL spectrometer. This equipment was combined with electron energy-loss spectroscopy (EELS).

Field-Emission Scanning Electron Microscopy (FESEM): Studies were performed on a Philips XL 30 S-FEG microscope operating at an accelerating voltage of 10 kV.

Raman spectroscopy: Scanning Raman Microscopy (SRM) on individual flakes was performed using a Horiba Jobin Yvon LabRAM HR Evolution confocal Raman spectrometer equipped with a microscope and an automated XYZ–table (excitation wavelengths 785, 633, 532, 473, 457 and 405 nm) with a laser spot size of ~1 µm (Olympus LMPlanFl 100x, NA 0.80). The incident laser power was kept as low as possible to avoid structural sample damage and the grating was 1800 g·mm^{-1}. The spectra were recorded under ambient conditions. Relocalization was achieved by using the optical contrast of nanomaterials deposited on opaque bilayered substrates.

DFT Calculations: The phonon frequencies at the Γ-point and Raman cross sections were calculated in the frame of density functional perturbation theory on the level of the local-density approximation (LDA) to the exchange-correlation functional as implemented in the Quantum Espresso suite[3]. The electron-ion interaction was modelled through norm conserving pseudopotentials generated with the ONCVPSP package[4], where the 4d, 5s, and 5p states were included in the set of valence electrons and applied a cutoff-energy of 1200 eV. The primitive cells of studied systems were used, i.e. of hexagonal symmetry in case of the 2D materials and rhombohedral in case of the β-phase of bulk Sb, and fully optimized the atomic positions and the lattice vectors in the periodic directions until the residual forces between atoms were smaller than 0.01 eV/ Å. Here, ABC stacking for all structures was employed. Interactions of the few-layer systems with residual periodic images due to the 3D boundary conditions were minimized by maintaining a vacuum layer of at least 25 Å. It was used 17x17x1 (17x17x17) Monkhorst-Pack k-point samplings for ground state calculations, geometry optimizations and frequency calculations for the few-layer (bulk) materials. For the Raman calculations, the grid densities were reduced to 14x14x1 (14x14x14), as the relative intensities were the interesting ones.

For the bulk system, the Raman intensities were calculated in the approximation of fixed occupation of the electronic bands, i.e. as a semiconductor.

A2.2. Experimental procedures

A2.2.1. Liquid-Phase Exfoliation of Antimony Crystals

Commercial antimony crystals were first grinded down to a fine powder using an agate mortar under ambient conditions.10 mg of grinded antimony were put on a 20 mL vial with 10 mL of a (4:1) 2-propanol/H_2O mixture. The mixture was sonicated for 40 min. at 400 W and 24 kHz delivering the ultrasound power in pulses 0.5 s long every 1 s. Then, the resulting black suspension was centrifuged at 3000 rpm (746 g) for 3 min, giving rise the so-called FLA suspensions. Sonication was performed using a Hielscher UP400S ultrasonic processor equipped with a 3 mm sonotrode. Centrifugation was carried out in a MPW-350R centrifuge using 2 mL Eppendorfs.

A2.2.2. AFM sample preparation

Prior to sample preparation, the SiO_2 (300 nm thick)/Si substrates were cleaned by ultrasonication at 380 W in acetone for 15 min and in 2-propanol for another 15 min, and then dried under an argon flow. Samples were prepared by drop-casting 20 µL of the resulting Sb suspension on a SiO_2/Si substrate at 20ºC and dried after 15 min under an argon flow.

A2.2.3. TEM sample preparation

Samples were prepared by drop-casting 20 μL of the resulting Sb suspension on copper TEM grids coated with lacey carbon film (200 mesh, EMS).

A2.3. Additional data

A2.3.1. Optimization of LPE process

- *Solvent optimization*: several pure solvents and mixtures of them with water are tested in order to achieve the liquid-phase exfoliation of bulk antimony crystals (see Table A2.1). The best solvent is chosen attending to the one that gives the highest FLAs concentration measured by AAS. Results showed that a 4:1 mixture of IPA/H_2O is the best solvent.

Table A2.1 Solvents tested with their surface tension (at 20 ºC) and their FLAs concentration (centrifugation after sonication was used to get a homogeneous suspension at 3 min and 3000 rpm).

Solvent	Surface Tension (mJ·m^{-2})	Final FLAs concentration (g·L^{-1})
Acetone	25.2	0.18×10^{-3}
NMP	41.26	0.85×10^{-3}
IPA	21.15	0.74×10^{-3}
IPA/H_2O (4:1)	22.62	1.74×10^{-3}
IPA/H_2O (2:1)	24.1	0.71×10^{-3}
IPA/H_2O (1:1)	24.25	0.57×10^{-3}
H_2O	72.7	0.01×10^{-3}

- *Sonication time optimization:* in Table A2.2 it can be see the effect of the sonication time in the final FLAs concentration, measured by AAS. Results obtained show that the concentration of FLAs increases with the sonication time up to a point (40 minutes) where the suspension is probably saturated and longer sonication times would significate a dramatic decrease of the concentration. For these experiments the solvent used is the one that gives the highest FLAs concentration (IPA/H_2O (4:1)), and the initial quantity of Sb stay fixed at 10 mg.

Table A2.2 Study of FLAs concentration (gL^{-1}) found in suspension versus sonication time (centrifugation after sonication was used to get a homogeneous suspension at 3 min and 3000 rpm).

Time	Final FLAs concentration ($g \cdot L^{-1}$)
10	1.41×10^{-3}
20	1.50×10^{-3}
30	1.59×10^{-3}
40	1.74×10^{-3}
50	1.71×10^{-3}
60	1.73×10^{-3}
120	0.86×10^{-3}

- *Initial concentration optimization:* It can be observed in Table A2.3 that an increase of the initial amount of antimony does not cause a significant effect on the final concentration of FLAs. For these experiments the solvent used and the sonication time are the ones that give the highest FLAs concentration (IPA/H_2O (4:1) and 40 min, respectively).

Table A2.3 Analysis of the initial quantity of Sb (mg) powder in the final FLAs concentration (gL^{-1}) (centrifugation after sonication was used to get a homogeneous suspension at 3 min and 3000 rpm).

Initial quantity of Sb (mg)	Final FLAs concentration (g·L^{-1})
1	1.43 x 10^{-3}
10	1.74 x 10^{-3}
20	1.56 x 10^{-3}
50	1.67 x 10^{-3}
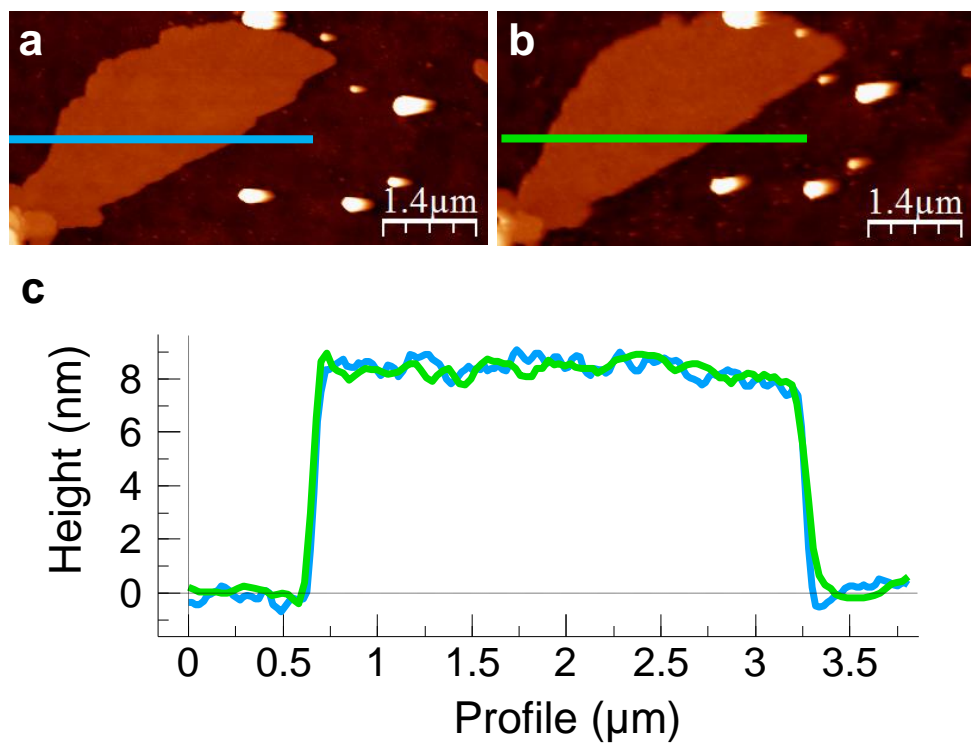
Figure A2.1. (a) AFM topographic image of a FLA nanosheet taken immediately after exfoliation. (b) Same as in (a) but two weeks later. (c) Profiles taken along the lines drawn in a- b. Please notice the similarity of the corrugation on the FLA nanosheet confirming the absence of environmental degradation.

A3. Chapter 3 methods, experimental procedures and additional data

A3.1. Methods

Raman spectroscopy: Raman spectroscopy measurements were carried out at room temperature using a Horiba LabRam HR Evolution confocal Raman microscope equipped with an automatic XYZ stage. The measurements were conducted in a backscattering configuration excited with solid state green laser (λ_{exc}=532 nm). The laser has nominal power of 14 mW that can be adjusted using filters, thus allowing a good control of the excitation laser intensity reaching the surface of the sample. The incident laser was focused using a 100× objective (0.8NA) leading to a laser spot with a diameter of *ca.* 1 μm. The backscattered light was then collected through the same objective and dispersed by a 1800 grooves per mm grating providing a spectral resolution of ~ 1 cm^{-1}. Raman mappings were recorded with the 532 nm laser (1.6 mW) using an acquisition time of 5s and a step size of 200 nm. The obtained data were processed by employing Lab Spec 5 as evaluation software, which enabled the extraction of individual intensities of A1g Raman mode from the range of 140–160 cm^{-1} subsequently used to construct Raman maps.

Optical Microscopy: Optical images of the FLA were acquired in a Zeiss Axio M1m Imager using white light illumination at normal incidence with a 100× objective (0.9NA), equipped with automated XY-stage which allows recording the exact X and Y coordinates of desired spots.

Scanning Transmission Electron Microscopy (STEM): High resolution STEM micrographs were obtained on a JEOL ARM200cF microscope equipped with a spherical aberration corrector and a Gatan Quantum electron energy loss spectrometer (EELS).

Elemental composition maps were produced using a multiple linear least square fit of the data to reference EEL spectra. All data were acquired at an accelerating voltage of 80 kV.

X-ray Photoelectron Spectroscopy (XPS): XPS characterizations were carried out using SPECS XR-50 X-ray Mg Kα (1253.7 eV) source with a pass energy of 30 eV and a spot size of 5 mm. Detection is done by a PHOIBOS 150 hemispherical energy analyser (SPECS, GmbH) and Delay Line Detector 3D-DLD4040-150. The binding energies of the XPS spectra were calibrated using Au 4f7/2 peaks. XPS peak fitting was carried out using a mixed Gaussian-Lorentzian function after a Shirley background subtraction. An area ratio of 3:2 between the Sb 3d5/2 and 3d3/2 peaks was employed in the fit with same FWHM. UPS measurements were performed with a monochrome photon energy of 21.2 eV (He I) through a toroidal mirror monochromator (SPECS GmbH). The detector utilized is the same as the one used in XPS characterizations and the experiments were performed in a chamber of base pressure better than 8×10^{-10} mbar. The UPS binding energies were calibrated and referenced to the Fermi level of a gold sample. The analysis spot size is 3×5 mm.

DFT Calculations: All calculations are performed using density functional theory (DFT) as implemented in Quantum Espresso using the local density approximation (LDA) to the exchange-correlation[3], interaction. We used ultrasoft pseudopotentials from the GBRV library with an energy cutoff of 800 eV and employed a Monkhorst-Pack grid with 14 x 14 x 1 k-points for integration in reciprocal space. To ensure that interaction between the structures is negligible, we added a vacuum layer of 20 in direction perpendicular to the two-dimensional layers. Using these parameters, we optimized the atomic positions and lattice vectors until the forces on every atom and the stresses on the unit cell were less than 0.005 eV/A and 0.01 GPa, respectively.

The phonon spectra were then calculated using a density functional perturbation theory (DFPT) approach, where we interpolated the frequencies along the high-symmetry directions from the explicitly calculated vibrations on a regular 6 x 6 x 1 q-point grid.

A3.2. Experimental procedures

A3.2.1. Liquid-Phase Exfoliation of Antimony Crystals

Commercial antimony crystals were first grinded down to a fine powder using an agate mortar under ambient conditions. 300 mg of the grinded antimony was then introduced into a 20 mL ball-mill stainless steel grinding jars (Retsch 213) charged with 30 stainless steel ball (0.5 cm diameter).

Subsequently, the mixture was treated at 30 Hz for 180 min at ambient atmosphere using a Retsch MM 400 mixer mill. 10 mg of the dry ball-milled antimony were mixed with 10 mL of a mixture of isopropanol and water in a 4:1 proportion (IPA/H_2O) and put in a 20 mL glass vial. Then, using an ultrasonic processor equipped with a 3 mm tip (Hielscher UP400S), the mixture was sonicated for a chosen time (ranging from 5 min to 45 min) at 400 W and 24 kHz delivering the ultrasound power in pulses 0.5 s long every 1 s. Temperature of the sonication process was controlled by an ice bath and kept at 0 °C to prevent unwanted evaporation of the solvent and avoid possible degradation of the material during exfoliation. The resulting suspension was then centrifuged at 3000 rpm (746 g) for 3 min to remove unexfoliated material settled to the bottom of the Eppendorf and the clear supernatant was recovered. Centrifugation was carried out in a MPW-350R centrifuge using 2 mL Eppendorf.

A3.2.2. AFM Sample preparation

Prior to sample preparation, the SiO_2 (300 nm thick)/Si substrates were cleaned by ultrasonication at 380 W in acetone for 15 min and in 2-propanol for another 15 min, and then dried under an argon flow.

Samples were prepared by drop-casting 20 µL of the resulting Sb suspension on a SiO_2/Si substrate at 20ºC and dried after 15 min under an argon flow.

A3.2.3. TEM sample preparation

Samples were prepared by drop-casting 20 µL of the resulting FLA suspension on copper TEM grids coated with lacey carbon film (200 mesh, EMS).

A3.3. Additional data
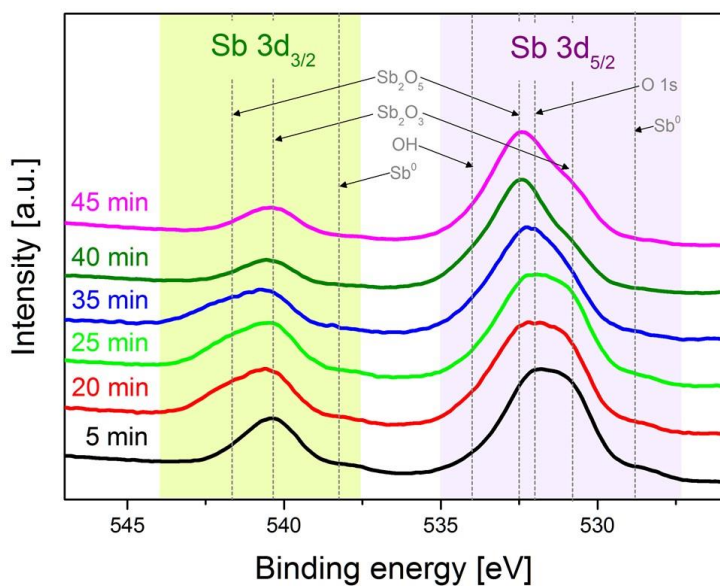
Figure A3.1 Evolution of XPS line spectra of as-prepared FLA samples as a function of sonication time ranging from 5 min to 45 min.

A4. Chapter 4 methods, experimental procedures and additional data

A4.1. Methods

Turbidimeter: Turbidity measurements were carried out using a HI-88713 Bench Top Turbidity Meter Hanna Instruments. To change between turbidity measurements to concentration values was needed to make a calibration (Figure A4.1). The real value of concentration to make the calibration was obtained by vacuum drying overnight one FLA sample and the obtained solid was weighted to know exactly the amount of antimony that was in the sample.

X-Ray Powder Diffraction (XRPD): X-ray diffraction patterns were measured on a Bruker D8 Advance with Cu Kα radiation with rapid detector (lynxeye).

Raman Spectroscopy: Raman spectra were acquired on a LabRam HR Evolution confocal Raman microscope (Horiba) equipped with an automated XYZ table using 0.80 NA objectives. All measurements were conducted using an excitation wavelength of 532 nm, with an acquisition time of 5 s and a grating of 1800 grooves/mm. To minimize the photo–induced laser oxidation of the samples, the laser intensity was kept at 10 % (1.6 mW). The step sizes in the Raman mappings were in the 0.2–0.5 µm range depending on the experiments. Data processing was performed using Lab Spec 5 as evaluation software. When extracting mean intensities of individual Sb Raman modes, it is important to keep each spectral range constant, *e.g.* from 90–110 cm^{-1} and from 140–160 cm^{-1} because otherwise the resulting value of the E_g/A^1_g – ratio can be slightly influenced.

Transmission Electron Microscopy (TEM): Images were obtained in a JEOL JEM 2100 FX TEM system with an accelerating voltage of 200 kV. The microscope has a multiscan charge-coupled device (CCD) camera ORIUS SC1000 and an OXFORD INCA X-Ray Energy Dispersive Spectroscopy (XEDS) microanalysis system.

Field-Emission Scanning Electron Microscopy (FESEM): Studies were performed on a Philips XL 30 S-FEG microscope operating at an accelerating voltage of 10 kV.

DFT Calculations: First-principles calculations within the density functional theory (DFT) formalism were carried out using the Quantum-ESPRESSO package[3]. The Perdew-Burke-Ernzerhof (PBE) functional within the generalized gradient approximation (GGA) was used[5]. For the Brillouin-zone integration, was used a Monkhorst-Pack set of special k-points[6]. A norm-conserving pseudopotential was used for Sb with electrons in a $5s^2 5p^3 4d^{10} 5d^{-1}$ configuration. The kinetic energy cutoff for the plane wave basis were 40 Ry for the wave function and 400 Ry for the charge density. Surfaces were constructed using a supercell with a thin slab of Sb (111) separated from its periodic images by a layer of vacuum. The size of this region is such that there were always ~ 20 of vacuum between the surfaces. For the Sb (111) surface a hexagonal cell with a base defined by a_0[110] and a stacking of ABCABC was used, where a_0 is the equilibrium lattice parameter. The surface energy is defined as the energy required to create a new surface. In our calculations the surface energy can be determined by taking the energy difference between the total energy of a slab and an equivalent bulk reference amount:

$$\gamma = \frac{1}{2A}\left(E_{slab}^{total} - E_{bulk}^{ref}\right)$$

Where E_{slab}^{total} and E_{bulk}^{ref} are defined as the total energy of the slab and the total energy of the bulk reference, respectively. A is the surface unit area, and the factor 1/2 is used because the E_{slab}^{total} has two surfaces.

X-ray photoelectron spectroscopy (XPS) characterization: XPS experiments were performed in an Ultra-High Vacuum (UHV) chamber. Mg Kα radiation excites core level photoelectrons, which are detected using a Specs Phoibos-150 electron analyser with a constant pass energy of 20 eV. The core level binding energies were calibrated using as references the binding energies of C 1s and Au 4f in contact with the sample. The line shape of core levels was fitted using a Shirley background and asymmetric singlet pseudo-Voigt functions. The fit was optimized using a Levenberg-Marquardt algorithm with a routine running in IGOR Pro (WaveMatrix Inc.)[7]. The quality of the fit was judged from a reliability factor, the normalized χ[2].

A4.2. Experimental procedures

A4.2.1. Dry Ball-Milling of Antimony Crystals

This procedure involves a pre-grinding process of the commercial bulk antimony crystals with an agate mortar giving rise to a so-called grinded antimony. A 20 mL ball mill reactor (IKA Ultra-Turrax Tube Drive Control) was charged with 200 mg of grinded antimony and 30 stainless steel balls, to complete a total volume of 7.5 mL. Then, the mixture stirred in the reactor for 60 min. at 3000 rpm, and the resulting antimony particles were separated from the stainless-steel balls.

A4.2.2. Wet Ball-Milling of Antimony Crystals

This step involves a pre-grinding process of the commercial bulk antimony crystals with an agate mortar giving rise to a so-called grinded antimony. After the grinding process, a stainless-steel reactor with a volume of 5 mL (Retsch 1.4112) were filled under ambient conditions with 300 mg of grinded antimony, 3 stainless steel balls of 4.74 mm diameter and 0.5 mL of 2-butanol (99.5 %, Sigma Aldrich). Subsequently, the samples were milled for 120 min. at 30 Hz in a Retsch MM 400 mixer mill. After milling, the reactors were washed with 2-butanol to obtain all of the grey metallic antimony slurry which was then centrifuged at 13000 rpm for 30 min. The sedimented antimony was dried on a hot plate at 100 ºC for 12 hours and another 24 hours in the drying oven at 75 ºC and a few mbar.

A4.2.3. Sonication Tip Exfoliation of Antimony Crystals

10 mg of "wet ball-milled" (See Appendix A4.2.2.) antimony crystals were put on a 20 mL vial with 10 mL of solvent. The mixture was sonicated for 40 min. at 400 W and 24 kHz delivering the ultrasound power in pulses 0.5 s long every 1 s. Temperature of the sonication process was controlled by an ice bath and kept at 0 °C to prevent unwanted evaporation of the solvent and avoid possible degradation of the material during exfoliation. Then, the resulting black suspension was centrifuged at 3000 rpm (746 g) for 3 min, in order to eliminate the unexfoliated crystals, and the clear supernatant was recovered. Sonication was performed using a Hielscher UP400S ultrasonic processor equipped with a 3 mm sonotrode. Centrifugation was carried out in a MPW-350R centrifuge using 2 mL Eppendorf.

213

A4.2.4. Bath Sonication Exfoliation of Antimony Crystals

10 mg of "wet ball-milled" (See Appendix A4.2.2.) antimony crystals was put on a 20 mL vial with 10 mL of solvent. The mixture was sonicated for 40 min in the ultrasonic bath at 380 W and 37 kHz. Then, the resulting black suspension was centrifuged at 3000 rpm (746 g) for 3 min, in order to eliminate the unexfoliated crystals, and the clear supernatant was recovered. Sonication was performed using an Elmasonic P300H ultrasonic bath. Centrifugation was carried out in a MPW-350R centrifuge using 2 mL Eppendorf.

A4.3. Additional data

y = 2473.1·x + 28.81
R^2 = 0.996
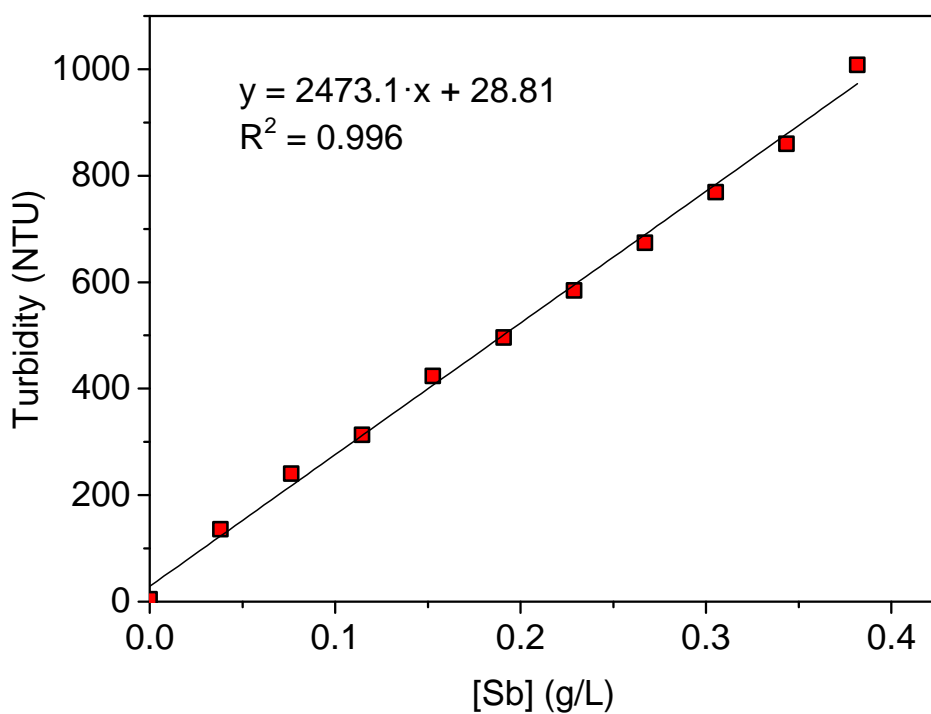
Figure A4.1. Calibration of the turbidity (NTU units) versus concentration (gL^{-1}). See Appendix A4.1 (Methods).
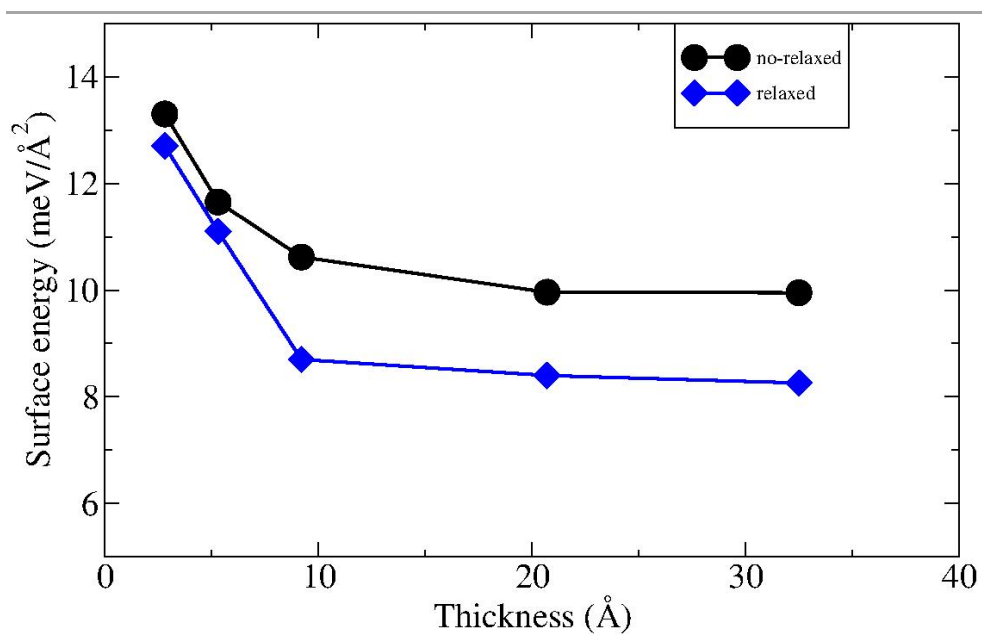
Figure A4.2 Calculated surface energies for Sb (111) slabs in both unrelaxed and fully relaxed geometries.

Table A4.3 Solvents used in the study and their surface tension (at 20 ºC).

Solvent	Surface tension (mJ/m^2)	Solvent	Surface tension (mJ/m^2)
IPA/H$_2$O (4/1)	22.62	NMP/H$_2$O (2/1)	44.01
IPA/H$_2$O (2/1)	24.1	NMP/H$_2$O (1/1)	45.26
IPA/H$_2$O (1/1)	24.25	NMP/H$_2$O (1/4)	48.05
IPA/H$_2$O (1/2)	27.92	SC/H$_2$O (2 g/L)	57.5
IPA/H$_2$O (1/4)	32.26	SC/H$_2$O (4 g/L)	53.1
H$_2$O	72.7	SC/H$_2$O (6 g/L)	51.24
IPA	21.15	DMF	37.1
2-Butanol	22.6	DMSO	42.9
Ethanol	22.1	Hexane	18.43
Acetone	25.2	Ethyl acetate	23.2
CHCl$_3$	27.5	PEG/H$_2$O (0.5%)	71.8
THF	26.4	PEG/H$_2$O (5%)	62.37
NMP	41.26	SDS/H$_2$O (0.5%)	38.3
NMP/H$_2$O (4/1)	42.78	SDS/H$_2$O (5%)	38.3

IPA: 2-propanol, THF: Tetrahydrofuran, NMP: N-Methyl-2-pyrrolidone, SC: Sodium cholate, DMF: Dimethylformamide, DMSO: Dimethyl sulfoxide, PEG: Polyethylene glycol and SDS: Sodium dodecyl sulfate.

A5. Chapter 5 methods, experimental procedures and additional data

A5.1. Methods

A5.1.1. FLA based supercapacitor

Atomic Absorption Spectroscopy (AAS): The amount of antimony in the samples was determined by flame atomic absorption spectrometry using a ContrAA 700 high-resolution atomic absorption spectrometer (Analitik Jena, Germany). The main line for antimony at 217.5815 nm was employed for all the analysis. The atomization was performed using an air acetylene flame with an acetylene flow rate of 60 L·h^{-1} and at a 6.0 mm burner height. The aspiration rate was fixed at 5 mL·min^{-1}. All measurements were carried out in triplicate.

Transmission Electron Microscopy (TEM): TEM images were obtained in a JEOL JEM 2100 FX TEM system with an accelerating voltage of 200 kV. The microscope has a multiscan charge-coupled device camera ORIUS SC1000 and an OXFORD INCA X-Ray Energy Dispersive Spectroscopy (XEDS) microanalysis system.

Scanning Electron Microscopy (SEM): SEM images and surface element analysis of antimonene/SPE were carried on using a JEOL JSM-5600LV model equipped with an EDX microanalysis package.

Raman Spectroscopy: Raman spectroscopy analysis of antimonene modified SPE surfaces was done using a "Renishaw InVia" spectrometer with a confocal microscope (50✕ objective) spectrometer with an argon laser (514.3 nm excitation) at a very low laser power level (1.2 mW) to avoid any heating effects. Spectra were obtained using a 10 s exposure time for three accumulations.

Electrochemical characterization: All electrochemical measurements were performed with an Autolab TYPE III (Autolab, The Netherlands). It was noted that the charge–discharge curves and cyclic voltammetry for capacitances measures were obtained using a two-electrode configuration.

A5.1.2. g-CN/FLA heterostructure: structural characterization and application in photocatalysis

Transmission Electron Microscopy (TEM): TEM images were obtained in a JEOL JEM 2100 FX TEM system with an accelerating voltage of 200 kV. The microscope has a multiscan charge-coupled device camera ORIUS SC1000 and an OXFORD INCA X-Ray Energy Dispersive Spectroscopy microanalysis system.

Scanning Electron Microscopy (SEM): SEM images were acquired in a JEOL JSM 6335F equipped with a backscattering electron detector and an OXFORD X-Max XEDS microanalysis system.

X-Ray Powder Diffraction (XRPD): X-ray diffraction patterns were measured on an EMPYREAN instrument using CuKα radiation.

X-ray Photoelectron Spectroscopy (XPS): XPS results were processed by using the AVANTGE software. Electrochemical measurements were recorded using a three-electrode system on an Autolab potentiostat (Metrohm, PGSTAT 101). A Pt foil electrode and an Ag/AgCl (3 m KCl) electrode were used as the counter and reference electrode, respectively.

Optical Absorption Spectroscopy (OAS): Optical absorbance spectra were measured using a Varian Spectrophotometer equipped with an integrating sphere.

Fluorescence Spectroscopy: Fluorescence measurements were performed using a FLS920P Spectrofluorimeter.

Mott-Schotky plot: Mott–Schottky ($1/C^2$ vs V) measurements were carried out in 1 m Na2SO4 aqueous solution as the electrolyte at a frequency of 2.48 kHz. Photocurrent measurements were conducted with KOH (0.1 m) as electrolyte, saturated Ag/AgCl as reference electrode and Pt plate as counter electrode.

A5.2. Experimental procedures

A5.2.1. FLA based supercapacitor

Dry Ball-Milling of Antimony Crystals: Bulk antimony crystals were grinded with an agate mortar to initially decrease their particle size. Then, a 20 mL ball mill reactor (IKA Ultra-Turrax Tube Drive Control) was charged with 100 mg of grinded antimony and 30 stainless steel balls, to complete a total volume of 7.5 mL. Then, the mixture was stirred in the reactor for 180 min at 3000 rpm, and the resulting antimony particles were separated from the stainless-steel balls.

Sonication Tip Exfoliation of Antimony Crystals: 10 mg of the dry ball-milled antimony crystals was mixed with 10 mL of a 4:1 2-propanol: water mixture in a 20 mL vial and sonicated for 40 min at 400 W and 24 kHz, delivering the ultrasound power in pulses 0.5 s long every 1 s. The resulting suspension was centrifuged at 3000 rpm (746 g) for 3 min and the clear supernatant collected as final suspension. Sonication was performed using a Hielscher UP400S ultrasonic processor equipped with a 3 mm sonotrode. Centrifugation was carried out in a MPW-350R centrifuge using 2 mL Eppendorf.

Screen Printed Electrodes (SPE) preparation: The working electrodes used were SPEs. The SPEs, which have a 3 mm diameter working electrode, were fabricated in-house with appropriate stencil designs using a microDEK 1760RS screen-printing machine (DEK, Weymouth, UK). The SPE design was previously reported[8]. For the case of each fabricated electrode, first a graphite ink formulation (Product Code: C2000802P2; Gwent Electronic Materials Ltd, UK), which was utilized for the efficient connection of all three electrodes and as the ink material for both the working and counter electrodes, was screen- printed onto a polyester (Autostat, 250 mm thickness) Flexible film. After curing the screen-printed graphite layer in a fan oven at 60 °C for 30 min. Finally, a dielectric paste (Product Code: D2070423D5; Gwent Electronic Materials Ltd, UK) was then screen-printed onto the polyester substrate to cover the connections and define the active electrode areas, including that of the working electrode (3 mm diameter). After curing at 60 °C for 30 min, the SPEs were ready to be used.

FLA modified SPE electrodes: modified electrodes were prepared by drop-casting aliquots of the 0.014 g·L⁻¹ FLA suspension onto the required working electrode with a micropipette. After a few minutes, the solvent completely evaporated (at ambient temperature) and the modified electrodes were utilized without further modification.

A5.2.2. g-CN/FLA heterostructure: structural characterization and application in photocatalysis

Dry Ball-Milling of Antimony Crystals: Bulk antimony crystals were grinded with an agate mortar to initially decrease their particle size. Then, a 20 mL ball mill reactor (IKA Ultra-Turrax Tube Drive Control) was charged with 100 mg of grinded antimony and 30 stainless steel balls, to complete a total volume of 7.5 mL. Then, the mixture was stirred in the reactor for 180 min at 3000 rpm, and the resulting antimony particles were separated from the stainless-steel balls.

Synthesis of g-CN: Photoactive g-CN was synthesized as described in the literature[9]. A supramolecular assembly was prepared by using a 1:1:0.1 (molar ratio) of cyanuric acid:melamine:barbituric acid (CMB) in 50 mL of an acidified solution with 5% (v/v) of HCl 37%. The complex was mixed for 4 h with an automatic shaker and centrifuged for 5 min at 6000 rpm. The resulting powder was dried overnight at 60 °C in a vacuum oven and then calcined at 500 °C for 4 h (heating rate: 2.3 °C min⁻¹) under an inert nitrogen atmosphere.

Preparation of CNSb heterostructure: A mixture of 10 mg of g-CN, and 10 mg of ball-milled Sb in 10 mL of 2-propanol: water (4:1 v/v) was first mixed with a Vortex, in order to produce a homogeneous suspension incorporating both materials to the liquid media. The mixture was then exfoliated using bath sonication (380 w, 37 KHz, Elmasonic P 300H) for 1 h, and centrifuged 10 min at 10 000 rpm in order to remove residual larger aggregates resulting in colloidal suspensions with high transparency.

Organic pollutants photodegradation: The photocatalytic activity was evaluated by the degradation of RhB and p-NP under white light irradiation. In a typical photocatalytic degradation experiment, RhB or p-NP (20 mL, 20 mg·L^{-1} in H$_2$O) and CNSbx composite were mixed in a glass vial and exposed to sonication in a water bath for 30 min and then kept in darkness with continuous stirring until the adsorption–desorption equilibrium between the dye and the catalyst is obtained. After turning on the light, aliquots were withdrawn from the suspension at a given time interval. The concentration of remaining RhB or p-NP in the solution was spectrophotometrically monitored by optical absorption values (at 554 nm of UV–vis absorption spectra for RhB and 314 nm for p-NP) on a UV–vis spectrophotometer during the photodegradation process.

A5.3. Additional data

Table A5.1 Specific capacitance data at F g^{-1} obtained during CVs measurements using different amounts of FLA onto the modified SPEs at different scan rates.

Scan rate (V/s)	Antimonene mass (ng)				
	1.8	3.6	9.0	18.0	36.0
0.025	8549	6747	2816	2789	1587
0.050	8361	6091	2679	2536	1442
0.075	8246	5790	2537	2365	1347
0.100	8187	5609	2428	2249	1277
0.250	7975	5075	2113	1909	1102
0.500	7538	4498	1843	1617	957

Table A5.2 Specific capacitance values (Fg^{-1}) obtained from charge-discharge profiles for different amounts of FLA onto the modified SPEs at different specific currents (Ag^{-1}).

1.8 ng Antimonene		3.6 ng Antimonene		9.0 ng Antimonene		18.0 ng Antimonene		36.0 ng Antimonene	
I (Ag^{-1})	C (Fg^{-1})	I (Ag^{-1})	C (Fg^{-1})	I (Ag^{-1})	C (Fg^{-1})	I (Ag^{-1})	C (Fg^{-1})	I (Ag^{-1})	C (Fg^{-1})
28	1547	14	1573	6	848	3	499	1	196
56	1446	28	1514	11	765	6	427	3	163
278	1115	139	1316	56	613	28	433	14	123
556	994	278	1005	111	475	56	304	28	111
1111	923	556	932	222	439	111	277	56	104
2778	878	1389	895	556	413	278	229	139	99

A6. References

(1) Horcas, I.; Fernández, R.; Gómez-Rodríguez, J. M.; Colchero, J.; Gómez-Herrero, J.; Baro, A. M. <scp>WSXM</Scp> : A Software for Scanning Probe Microscopy and a Tool for Nanotechnology. *Rev. Sci. Instrum.* **2007**, *78* (1), 013705.

(2) Nemes-Incze, P.; Osváth, Z.; Kamarás, K.; Biró, L. P. Anomalies in Thickness Measurements of Graphene and Few Layer Graphite Crystals by Tapping Mode Atomic Force Microscopy. *Carbon N. Y.* **2008**, *46* (11), 1435–1442.

(3) Giannozzi, P.; Baroni, S.; Bonini, N.; Calandra, M.; Car, R.; Cavazzoni, C.; Ceresoli, D.; Chiarotti, G. L.; Cococcioni, M.; Dabo, I.; et al. QUANTUM ESPRESSO: A Modular and Open-Source Software Project for Quantum Simulations of Materials. *J. Phys. Condens. Matter* **2009**, *21* (39).

(4) Hamann, D. R. Optimized Norm-Conserving Vanderbilt Pseudopotentials. *Phys. Rev. B - Condens. Matter Mater. Phys.* **2013**, *88* (8), 1–10.

(5) Perdew, J. P.; Burke, K.; Ernzerhof, M. Generalized Gradient Approximation Made Simple. *Phys. Rev. Lett.* **1996**, *77* (18), 3865–3868.

(6) Monkhorst, H. J.; Pack, J. D. Special Points for Brillouin-Zone Integrations. *Phys. Rev. B* **1976**, *13* (12), 5188–5192.

(7) Schmid, M.; Steinrück, H. P.; Gottfried, J. M. A New Asymmetric Pseudo-Voigt Function for More Efficient Fitting of XPS Lines. *Surf. Interface Anal.* **2014**, *46* (8), 505–511.

(8) Randviir, E. P.; Brownson, D. A. C.; Metters, J. P.; Kadara, R. O.; Banks, C. E. The Fabrication, Characterisation and Electrochemical Investigation of Screen-Printed Graphene Electrodes. *Phys. Chem. Chem. Phys.* **2014**, *16* (10), 4598–4611.

(9) Barrio, J.; Lin, L.; Wang, X.; Shalom, M. Design of a Unique Energy-Band Structure and Morphology in a Carbon Nitride Photocatalyst for Improved Charge Separation and Hydrogen Production. *ACS Sustain. Chem. Eng.* **2018**, *6* (1), 519–530.

List of publications

Publications discussed in this dissertation

(1) Gibaja, C.; Rodriguez-San-Miguel, D.; Ares, P.; Gómez-Herrero, J.; Varela, M.; Gillen, R.; Maultzsch, J.; Hauke, F.; Hirsch, A.; Abellán, G.; Zamora, F.; Few-Layer Antimonene by Liquid-Phase Exfoliation. *Angew. Chemie Int. Ed.* **2016**, *55* (46), 14345–14349.

(2) *Assebban, M.; *Gibaja, C.; Fickert, M.; Torres, I.; Weinreich, E.; Wolff, S.; Gillen, R.; Maultzsch, J.; Varela, M.; Tan, S. J. R.; Loh, K. P.; Michel, E. G.; Zamora, F.; Abellán, G.; Unveiling the oxidation behavior of liquid-phase exfoliated few-layer antimonene. *J. Am. Chem. Soc.* **2019** (Submmited).

(3) *Gibaja, C.; *Asseban, M.; Torres, I.; M.; Fickert, Sanchis-Gual. R.; Brotons, I.; S. Paz, W.; Palacios, J. J.; Michel, E. G.; Abellán, G.; Zamora, F.; Liquid Phase Exfoliation of Antimony: a systematic study to isolate Few-Layer Antimonene. *ACS Nano.* **2019** (Submmited).

(4) Martínez-Periñán, E.; Down, M. P.; Gibaja, C.; Lorenzo, E.; Zamora, F.; Banks, C. E. Antimonene: A Novel 2D Nanomaterial for Supercapacitor Applications. *Adv. Energy Mater.* **2018**, *8* (11), 1702606.

(5) *Barrio, J.; *Gibaja, C.; Tzadikov, J.; Shalom, M.; Zamora, F.; 2D/2D Graphitic Carbon Nitride/Antimonene Heterostructure: Structural Characterization and Application in Photocatalysis. *Adv. Sustainable Syst.* **2019**, *3* (2), 1800138.

*Researchers noted with (*), contributed equally to the work.

Other publications during Ph.D.

(1) Azani, M. R.; Hassanpour, A.; Carcelén, V.; Gibaja, C.; Granados, D;.; Mas-Ballesté, R.; Zamora, F.; Highly concentrated and stable few-layers graphene suspensions in pure and volatile organic solvents. *Appl. Mat. Today.* **2016**, *2*, 17-23.

(2) Abellán, G.; Ares, P.; Wild, S.; Nuin, E.; Neiss, C.; Rodriguez-San-Miguel, D.; Segovia, P.; Gibaja, C.; Michel, E. G.; Görling, A.; et al. Noncovalent Functionalization and Charge Transfer in Antimonene. *Angew. Chem. Int. Ed.* **2017**, *56* (46), 14389–14394.

List of abbreviations

2D: Two-dimensional

3D: Three-dimensional

AFM: Atomic Force Microscopy

AMQDs: Antimonene Quantum Dots

BP: Black Phosphorus

COF: Covalent Organic Frameworks

DA: Dimensional Anisotropy

DFT: Density Functional Theory

DLS: Dynamic Light Scattering

DMF: N,N-dimethylformamide

DMSO: Dimethylsulfoxide

EDLC: Electrochemical Double-Layer Capacitors

EELS: Electron Energy Loss Spectroscopy

EQE: External Quantum Efficiency

FESEM: Field Emission Scanning Electron Microscopy

FET: Field-Effect Transistor

FFT: Fast Fourier Transform

FLA: Few-Layer Antimonene

FLAs: Few-Layer Antimonene Flakes/Sheets

g-CN: Graphitic Carbon Nitride

HAADF-STEM: High Angle Annular Dark Field - Scanning Transmission Electron Microscopy

h-BN: Hexagonal Boron Nitride

HOPG: Highly Oriented Pyrolytic Graphite

HRTEM: High Resolution Transmission Electron Microscopy

HTL: Hole Transport Layer

ICP-MS: Inductively Coupled Plasma Mass Spectrometry

IPA: 2-propanol

LDHs: Layered Double Hydroxides

LOD: Limit of Detection

LPE: Liquid-Phase Exfoliation

MBE: Molecular Beam Epitaxy

MOF: Metal Organic Frameworks

MOSFETs: Metal Oxide Semiconductor Field-Effect Transistor

MOX: Transition Metal Oxyhalides

NMP: N-Methyl-2-pyrrolidone

PEG: Polyethylene Glycol

p-NP: p-nitrophenol

PTA: Photothermal Agents

PTCEs: Photothermal Conversion Efficacies

RhB: Rhodamine B

SANs: Semiconducting Antimonene Nanosheets

SbNS: Antimony Nanosheets

SEM: Scanning Electron Microscopy

SIB: Sodium Ion Batteries

SPE: Screen Printed Electrode

SRM: Scanning Raman Microscopy

STM: Scanning Tunneling Microscopy

STEM: Scanning Transmission Electron Microscopy

TEM: Transmission Electron Microscopy

TFETs: Tunnelling Field Effect Transistor

THF: Tetrahydrofuran

TMDs: Transition Metal Dichalcogenide

TPV: Thermophotovoltaic

UHV: Ultra High Vacuum

UPS: Ultraviolet Photoelectron Spectroscopy

UV-Vis: Ultraviolet-Visible Spectroscopy

vdWE: van der Waals Epitaxy

XEDS: X-ray Energy Dispersive Spectroscopy

XPS: X-ray Photoelectron Spectroscopy

XRPD: X-ray Powder Diffraction

Agradecimientos

Han sido muchas las personas que han estado implicadas a lo largo de estos años, de manera directa o indirecta, en los trabajos que han conducido a elaborar esta tesis doctoral. A todas ellas les quiero agradecer su apoyo y colaboración, sin los cuales no habría sido posible la realización de la misma.

En primer lugar deseo dejar constancia y testimonio de agradecimiento al Prof. Félix Zamora por su papel como director de tesis. Más que un director, Félix ha sido un mentor y orientador constante a lo largo de estos años. Me diste la oportunidad de conocer de tu mano el mundo de la investigación y lo apasionante y duro que puede llegar a ser. Me apoyaste y tuviste en cuenta mi opinión en cada uno de los proyectos que iban surgiendo, hasta el punto de ofrecerme y confiarme la responsabilidad de emprender una nueva y próxima aventura en el ámbito empresarial. Además, siempre has sido una fuente de inspiración y sosiego en los momentos más complejos y delicados del proceso de elaboración de la tesis. Por todo ello, te doy las gracias y confío en poder estar a la altura de las expectativas marcadas.

También me gustaría agradecer su colaboración a otros profesores e investigadores de la UAM que han contribuido de manera notable en mi formación durante estos años. A los profesores Julio Gómez-Herrero y Cristina Gómez-Navarro, a los doctores Miriam Moreno y Pablo Ares, y a los doctorandos Diego y Yolanda porque siempre han sido una fuente de consejos y de conocimiento en cualquiera de las dudas que me iban surgiendo en mi trabajo relacionadas con los diversos aspectos del mundo de la física. Y a la Prof. Pilar Amo, cuya mano amiga siempre era bien recibida dentro y fuera del laboratorio.

Otro grupo de personas del que no puedo olvidarme son mis compañeros del grupo de investigación, en especial del Dr. David Rodríguez San Miguel, ya que con él comencé esta andadura en el mundo de los materiales 2D y fue a la persona que me ayudó a desenvolverme en el laboratorio cuando entré, y Miguel Ángel, sin cuya ayuda y saber hacer habría sido imposible acabar esta tesis. Del mismo modo dar las gracias a la Dra. Carmen Montoro y a los doctorandos Verónica, Pablo y Javier, que recorrieron el camino de sus respectivos proyectos de investigación y tesis doctorales conmigo y a los cuáles les mando todo mi apoyo para lo que les queda por delante. A las nuevas incorporaciones al grupo (Dra. Ana Platero, Nacho, Noelia, Jesús, Javier, etc...), también me gustaría agradecerles el apoyo que han demostrado durante este tiempo. Y por último dentro de este grupo, me gustaría agradecer a los doctorandos Jesús e Iñigo en particular, al primero por animarme y solucionarme los momentos de dificultad, y al segundo porque ha sido mi apoyo durante este último año y continúa la investigación de la que trata esta memoria.

By the way, I would never forget about Prof. Hirsch group at FAU in Germany, where I had the opportunity to do a short researching stay for three months and I met a lot of wonderful people like Prof. Hauke, Stefan, Michi, Oliver, Milan, Aleksa and specially to M'hammed and Vicent without whom I would have had a really hard time there.

Del mismo modo, me gustaría dar las gracias a una serie de profesores e investigadores no pertenecientes a la UAM cuya aportación a mi formación y a esta tesis ha sido significativa. En primer lugar, al Dr. Gonzalo Abellán y su grupo mixto del ICMol y la FAU, que me brindó la oportunidad de colaborar con ellos durante estos últimos meses de tesis y cuya opinión crítica y apoyo me ha ayudado de manera inmejorable a lo largo de ella.

Por otro lado, también le quiero dar las gracias al doctorando Jesús Barrio de la BGU, que empezó en nuestro grupo y siempre me ha motivado a generar nuevas colaboraciones relacionando nuestras dos líneas de investigación.

En un ámbito más personal y menos académico me gustaría agradecer a mi familia: a mi hermano y a mis padres todo el apoyo y comprensión que me han brindado desde que nací y especialmente durante estos últimos años. Como profesionales de la enseñanza que son, mis padres siempre han estado a mi lado y han apoyado en todos los sentidos las decisiones relacionadas con mi formación. Finalmente también quiero recordar a mi grupo de amigos, en especial a mis recientes compañeros de piso (Sergio y David) que han tenido que soportar mis monólogos cuando cada noche llegaba del laboratorio y no dejaba de hablar de los avatares relacionados con la elaboración de la tesis.

A todos los citados, y también a aquellos que no he citado, muchas gracias por vuestra ayuda.